MICROPOROUS MATERIALS FABRICATED FROM DISCRETE MOLECULAR CAGES

BY

TIMOTHY PATRICK MONEYPENNY II

DISSERTATION

Submitted in partial fulfillment of the requirements
for the degree of Doctor of Philosophy in Chemistry
in the Graduate College of the
University of Illinois at Urbana-Champaign, 2018

Urbana, Illinois

Doctoral Committee:

Professor Jeffrey S. Moore
Professor Kenneth S. Suslick
Professor Jianjun Cheng
Associate Professor Alison Fout

Abstract

In the context of materials science, an interesting relationship exists between the properties of solid materials and the existence of void spaces within them. In fact, whether the presence of voids is desired or not tends to depend on one's perception of the effects that voids induce. In densified materials, for example, the presence of voids can be detrimental to structural integrity. Thus, such materials that contain voids are considered defective. On the other hand, when voids are desirable, their presence in certain materials is essential to material behavior. In zeolites, for example, the size, shape, and connectivity of void spaces regulate catalytic activity. In reality, however, and at some finite length scale, *all real materials* contain intrinsic void space; a consequence of the imperfect packing arrangements of atoms. Thus, it is necessary not only to elucidate what effects voids have on the properties of materials, but also to investigate methods that provide control of void features within solid materials.

While all materials possess *intrinsic* voids, the ability to introduce *intentional* voids in solids presents multiple difficulties. The statement "nature abhors a vacuum" is a familiar quip that reflects this challenge of designing open pore spaces in solid materials, as porous frameworks with open void spaces are often higher in energy relative to their more dense structural counterparts. Nonetheless, during the last few decades, technology has advanced such that scientists have significant control over the size, shape, and position of voids within solids. Materials such as zeolites, metal-organic frameworks (MOFs), and covalent-organic frameworks (COFs) all demonstrate the profound ability to position pores of various shapes and sizes with molecular precision in a solid framework. This control over pore design has led to significant materials applications for porous materials including adsorption, catalysis, and molecular separation.

Despite the successes of porous networks such as zeolites, MOFs, and COFs, there remains a need for greater molecular diversity and tunable microenvironments that are precise in molecular design. Moreover, there is a need for fundamental understanding of the relationship between characteristics of voids derived from molecular species and the behavior these entities exhibit within solid materials. Herein, we test the hypothesis that discrete molecular cages with non-collapsible pores are building blocks for porous solids by preparing molecular cages via alkyne metathesis. We demonstrate that molecular pores can be rationally synthesized from tritopic

organic precursors in a single step and assembled in the solid state to afford permanently porous materials. Featuring organic synthesis and modular packing, our methodology provides molecular control for the fabrication of functional porous materials with precise microenvironments.

First, a non-intuitive precursor design principle for synthesizing molecular cages via alkyne metathesis is described. By subjecting a series of precursors with varying bite angles to AM, it is experimentally demonstrated that the product distribution and convergence towards product formation is strongly dependent on precursor bite angle. Furthermore, it was discovered that precursors with the ideal tetrahedron bite angle (60º) do not afford the most efficient pathway to the product. These results lend credence to the underlying systemic issues facing the synthesis of 3D architectures via dynamic covalent chemistry, where variations in precursor geometry lead to significant deviation of product distributions away from discrete products.

Next, a systematic study of the effects of molecular shape-persistence on the porosity of molecular solids is discussed. Three molecular cages synthesized via alkyne metathesis and post-synthetic modifications were designed to provide controlled, stepwise adjustments in molecular shape-persistence. Experimental measurements of nitrogen adsorption taken from rapidly and slowly crystallized solids of each cage demonstrated a trend in porosity that correlated with shape-persistence. Molecular dynamic simulations that modeled cage motion corroborated the trend seen in the experimental data and emphasized that shape-persistence governs the microporosity of these materials. Our integrated synthetic and computational approach demonstrates that the microporosity of this class of molecular solids can be controlled through fine-tuning at both the atomic and microscales.

Lastly, the fabrication and characterization of a novel solid-state lithium electrolyte nanocomposite derived from a porous molecular cage is discussed. A solid-liquid electrolyte nanocomposite (SLEN) fabricated from an electrolyte system and a porous organic cage exhibits ionic conductivity on the order of 1×10^{-3} S cm^{-1}. With an experimentally measured activation barrier of 0.16 eV, this composite is characterized as a superionic conductor. Furthermore, the SLEN displays excellent oxidative stability up to 4.7 V vs. Li/Li^{+}. This simple three-component system enables the rational design of electrolytes from tunable, discrete molecular architectures that possess intrinsic void space.

Acknowledgements

As you'll see in this dissertation, Nature really does abhor a vacuum. Along these lines and whether we like it or not, scientific progress is never truly performed in a vacuum either. Science is achieved with the assistance of several individuals, either directly or indirectly, that each contribute critical input; the lack of which would otherwise eliminate any possibility for advancement. The research to be presented in this dissertation is no exception to this rule, and although it may be potentially impossible to name all of those individuals who have helped, inspired, and pushed me along the way, I will certainly attempt to do so. While my teachings and studies have taught me that I cannot be certain about the exact position and momentum of an electron, I am 100 % certain that without those individuals mentioned in this section, I would not be the person or scientist that I am today.

I have always considered the study of chemistry as a blank canvas in which researchers are the creators and where limitations only exist in one's own mind. Joining Jeff's research group has only supported this hypothesis. Throughout my time in Jeff's group, he has allowed me limitless freedom to explore those topics which interested me. Even though this freedom was initially quite daunting, it allowed me to find my own way and take full responsibility for any failures (and successes) that may have resulted. My time in Jeff's group has taught me many important lessons: 1) be selective in my pursuit of ideas, 2) perform those experiments that will test the hypothesis as soon as possible, and perhaps the most important 3) to have fun! For these lessons, and for numerous others, I thank you, Jeff. I am also thankful for the opportunities and support that Jeff has given me: allowing me to attend many conferences (sometimes out of the country!), writing letters of recommendation, and nominating me for departmental awards. These are all gestures that I truly appreciate and I am honored to have such a kind and supportive advisor. Thank you, Jeff, for everything you have done for me.

To my thesis committee, Prof. Ken Suslick, Prof. Alison Fout, and Prof. Jianjun Cheng: thank you for all of your comments, suggestions, and advice throughout my studies. You have all been extremely supportive and I am grateful to learn from you.

To my wife, Molly: thank you for all of your encouragement, affection, and resilience while I've been in graduate school. I realize it was not always easy for us when we lived apart, and I am thankful for your unwavering support throughout that time. You were the foundation that kept me

grounded under times of stress and frustration, and I think it is safe to assume that you will continue to be my foundation in years to come. I will always cherish the memories we have made throughout the last four years: holidays, England, Iceland, our wedding, moving you in, rescuing Daisy, and transforming the condo into a home. I am extremely thankful to have you in my life and I look forward to our future together.

To my family: thank you for providing me with the opportunities in life to allow me to get to this point. To you, mom: thank you for always encouraging me to become a better version of myself. I have not forgotten all of those days growing up when you helped me with homework and pushed me to do better in school when I was slacking. Thank you for being patient and understanding with me during those awkward teen years. Thank you for making me understand the value of education. Thank you for your unconditional love. To dad: thank you for showing me the value of hard work. Even as a kid, I recognized how much effort you put toward improving our lives. I noticed how early you would get up and go to work and how late you stayed. Thank you for being a great role model and supporting me in all of my efforts. Thank you both for always wanting the best for Matt and me as kids. Thank you for putting us in great schools, placing us in wonderful homes and neighborhoods, and always providing for us. To my brother, Matt: thank you for being my best friend. Thank you for being your silly self and for showing me that laughing makes life better. To the Hohmans: thank you all for being so caring and supportive throughout graduate school. You guys are my second family and I couldn't have done it without you.

To my friends, both new and old: thank you for having an impact on my life. To those from my childhood and teen years, thank you for your lasting friendship and support after all this time: Andrew Naylor, Josh Holahan, Kyle Hill, Mike Lostoski, and Marc Salopek. To my friends from UIUC, thank you for making graduate school enjoyable and not all work and no play: Ryan Rooney, Zach Goldsmith, Michael Drummond, Jack Killion, Josh Francis, Elena Monoto-Blanco, Kali Serrano, Kimberly Basset, Siraj Ali, Chris Bemis, Emma Southgate, Dan Holycross, Carrie Levinn, Connor Delaney, Aaron Roth, Dan McCurry, Amit Patel, Sarah Perlmutter, Jason Varnell, Gabe Espinosa Martinez, and Erin Nissen.

To the Moore group, both new and old: thank you for all of your welcoming support, advice, edits, friendship, mentorship, and great discussions. I have been lucky to have magnificent colleagues: Semin Lee, Anna Yang, Huiying Liu, Kristen Hutchins, Maxwell Robb, Shijia Tang, Jun Li, Ian Robertson, Catherine Casey, Nag Gavvalapalli, Kevin Cheng, Etienne Chenard, Olivia

Lee, Shawn Miller, Anderson Coates, Josh Grolman, Josh Kaitz, Windy Santa Cruz, Ke Yang, Abby Halmes, Jose Zavala, Hao Yu, Chris Pattillo, Morgan Cencer, Oleg Davydovich, Gabe Rudebusch, Lily Robertson, Xiaocun Lu, Yun Liu, Xing Jiang, and Yu Cao.

To my collaborators: thank you for helping with the work presented in this dissertation. To Semin Lee and Anna Yang: thank you guys for being a great research team. Thanks also goes out to: Prof. Yang Zhang, Prof. Andrew Gewirth, Prof. Ralph Nuzzo, Nathan Walter, Zhikun Cai, Dr. Danielle Gray, Dr. Toby Woods, Yu-Run Miao, Jordan Hinman, Bruno Giuliano Nicolau, and Aaron Petronico. I have learned significantly from my interactions with all of you.

To my favorite high school teacher, Mr. Sawan: thank you for introducing chemistry to me. Your classes laid the foundation for the rest of my studies. Thank you for giving me the opportunity to take both honors and AP chemistry.

A special thanks goes out to those who have helped on the administration front: Ashley Trimmell, Beth Myler, Theresa Struss, Katie Trabaris, Karen Watson, Kara Metcalf, Staci Ryan, Lori Johnson, Connie Knight, and Star Murray. You have all helped me along the way and I am grateful for all of your help. To Ashley Trimmell, you have been a serious help to the entire Moore group, including myself. Without you, the Moore group would cease to exist. Also, I'd like to thank Patricia Simpson for helping me prepare for my job search.

Thank you to the National Science Foundation and the Beckman Institute for Advanced Science and Technology for funding the research in this dissertation.

Lastly, I'd like to thank you, reader. I hope you find the results in this dissertation both informative and interesting. May it encourage you to search for new ideas and make new discoveries.

TABLE OF CONTENTS

Chapter 1

Introduction

1.1 Porous Materials

Porous materials, or solids which exhibit permanent porosity as a result of interconnected voids, have been utilized by society throughout history. Natural porous materials such as charcoal, dried plants, and terracotta have been used since antiquity for filtration and purification of water. Even in modern times, the life of the average citizen is greatly improved by the properties of porous materials. Activated carbon in current water purification products is used to filter out ions and other impurities from our drinking water, porous solids of poly(lactic acid) are used as biomedical scaffolds for tissue engineering, and porous poly(olefin) films are used as separators between electrodes in lithium ion batteries used to power handheld devices.

Recently, significant research has led to the development of many new types of synthetic porous materials just within the past two decades. Materials such as zeolites, metal-organic frameworks, and covalent-organic frameworks have demonstrated the synthetic ability of scientists to construct solids of various porous topologies. The extensive amount of research in the field of porous materials has enabled various technological applications including selective adsorption, molecular separation, and catalysis. Collectively, these materials are extended solids comprised of molecular units that are linked together in an infinite lattice by strong covalent or coordinative bonds. As such, these materials suffer from inherent limitations in design, synthesis, and materials processing. In this dissertation, I will present research efforts of a relatively new type of porous material: porous molecular cages. The research presented herein will discuss efforts toward rational design and synthesis (Chapter 2), understanding porosity in molecular cage solids (Chapter 3), and utilizing their unique nanopores for materials applications (Chapter 4). The

following chapter is designed to place the field of molecular cages in the context of porous materials and to provide a brief overview of the various porous materials reported in the literature.

1.2 Network Porous Materials

Within the study of synthetic porous materials, there arises a few distinct classes that deserve mention. Among the various classes that one can distinguish, no other class has made greater impact in society than that of network porous materials, or network solids. The defining feature of network solids is that they are chemical compounds bonded by covalent or coordinative bonds in a continuous, infinite lattice arrangement. As such, these materials tend to be extremely durable, chemically stable, and thermally stable while also providing various technologically-important applications. In this section, I will discuss those network solids which I have deemed extremely impactful to society.

1.2.1 Zeolites

Undoubtedly, no other porous network material has made a bigger societal impact than zeolites. Zeolites are a class of porous, crystalline aluminosilicates that are comprised of tetrahedrons linked together at the corners to form a three-dimensional network material.[1] The tetrahedra are built from Si or Al atoms at the center bonded to four adjacent oxygen atoms at the corners and are arranged in such a way to afford open porous frameworks that are comprised of cavities of molecular dimensions (ca. 3−15 Å).[1] When the central atom is Al, this bonding arrangement imparts an overall negative charge on the Al atom, which provides sites throughout the framework for cation-exchange. If the counter cation is H^+, the framework becomes extremely acidic and the material can be used for a variety of acid-catalyzed reactions. When comprised of other cations such as K^+, zeolites can be used for ion exchange and various other applications. In this fashion, millions of zeolite structures have been predicted based on the possible arrangements and chemical makeup of tetrahedra. To date, only ca. 216 structures have been discovered either naturally or synthetically.[2] Nonetheless, these materials have become industrially and academically significant for their applications including heterogeneous catalysis[1,3-8] and ion exchange[9]. With the large body of work on zeolites present in the literature, it would be inappropriate to provide a detailed review. The interested reader is instead directed to reviews on the subject.[2,10-14] Rather than delving into a thorough summary of the zeolites, I will discuss in the following section a representative zeolite that has found significant utility in industry.

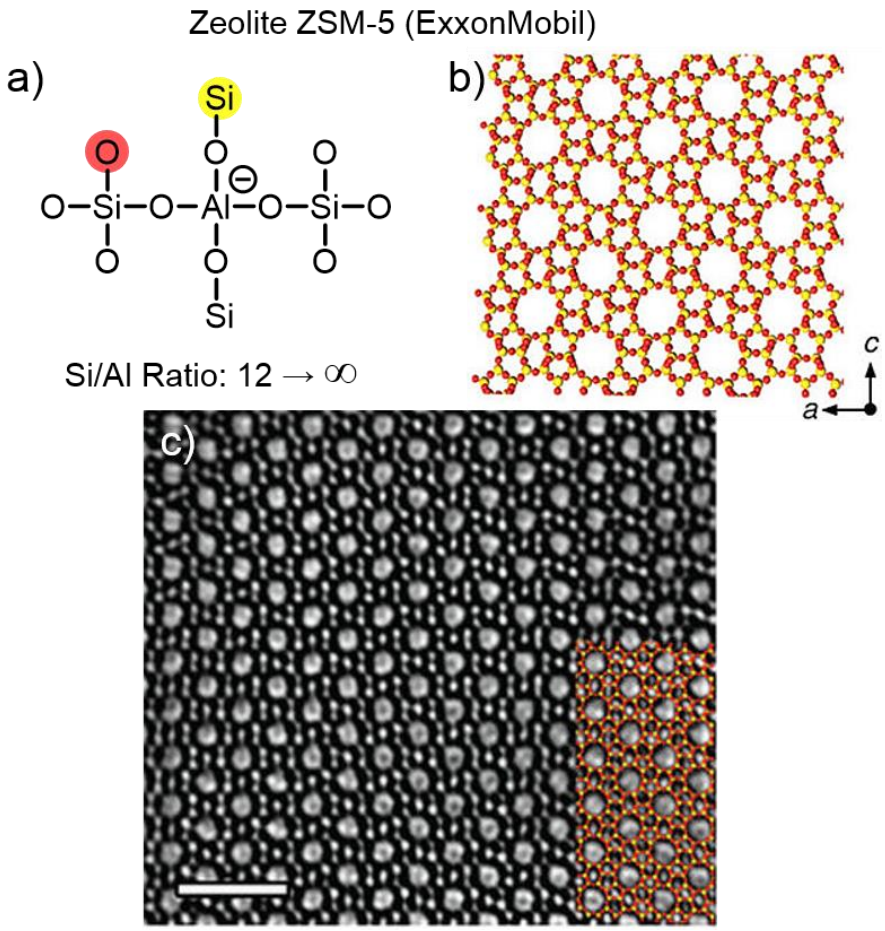

Figure 1.1*: Atomic and molecular structure of ZSM-5. a) Simplistic chemical bonding arrangement drawing showing that each Si or Al atom is bonded to four adjacent O atoms. b) MFI crystal structure along b-axis. c) HR-TEM image, along the c-axis, of an MFI nanosheet with an overlaid crystal structure in the [010] direction (scale bar is 1 nm). Panels b and c are adapted with permission from ref. 15.*

The most industrially significant zeolite is ZSM-5 (Zeolite Socony Mobil-5), first developed and patented by Mobil in 1975.[5] ZSM-5 is an aluminosilicate zeolite of the MFI framework type with a chemical formula of $Na_nAl_nSi_{96-n}O_{192}\bullet 16H_20$ where $0<n<27$. The general packing structure of ZSM-5 is illustrated in Figure 1.1. The structure consists of pentasil units, or eight five-membered rings, connected together in a framework by oxygen bridges to form pleated sheets. The sheets are connected by oxygen bridges to afford a structure like that shown in Figure 1.1c. Thus, the packing arrangement affords pore channels with apertures on the order of 5.5 Å.[15] At high temperatures, ZSM-5 crystallizes in the orthorhombic Pnma space group,

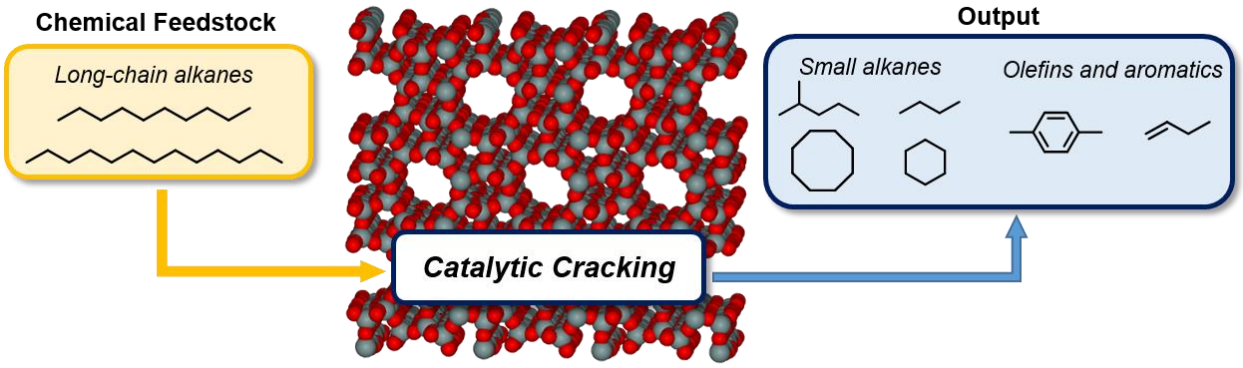

***Figure 1.2**: Illustration of catalytic cracking through ZSM-5.*

however, it has been shown that the structure can undergo a phase transition to monoclinic $P2_1/n$ at lower temperatures.[16]

Since ZSM-5 is extremely acidic when protons are the cation in the framework, this material has been used for a variety of acid-catalyzed reactions. Typical reactions using ZSM-5 include hydrocarbon isomerization,[17-20] alkylation,[21-23] and cracking.[5,8] Reactivity in this system can be described as examples of shape selectivity.[24] Zeolites exhibit three types of shape selective catalysis as a result of their pores to afford specific products: 1) Reactant shape selectivity, or selectivity based on the size of the reactants (reactants larger than the pores in the zeolite cannot enter). 2) Transition state shape selectivity, or selectivity based on the size and shape of intermediates that exist during the transition state of a reaction (molecules that are too big have a much lower probability of forming). 3) Product shape selectivity (large products will desorb at much slower rates due to limited diffusivity). In this fashion, only specific products will be formed as a result of sieving through a zeolite.[24].

While zeolites have found widespread use in industry, a significant challenge in this field is the rational design and synthesis of novel structures. In general, zeolites are synthesized via hydrothermal methods where reactive gels comprised of silica and alumina are heated between 80 and 200 ºC in alkaline media. As a result, the chemical bond formation and overall architecture construction occur in the same step. Unfortunately, it can be quite difficult to have much control over the resulting framework. To further illustrate this point, I quote Cundy and Cox: "The major pathway to all [zeolites] is that of hydrothermal synthesis. It is unfortunately fairly common to see in the scientific literature…that this process is still at an empirical stage, or poorly understood, or even steeped in some form of alchemical mystery."[25] The outlook in this excerpt, albeit taken from

a 2003 review article, is still relevant today as only 216 architectures have been discovered out of millions predicted. Indeed, with the interest in hierarchal and mesoporous zeolites in the current literature, a deep understanding of the mechanism of crystallite growth and heterogeneous nucleation must be determined to advance this field from empirical and alchemical-like to a science rooted in rational design.

1.2.2 Metal-Organic Frameworks

Metal-organic frameworks (MOFs) are synthetic porous materials constructed from linking inorganic and organic units by strong coordinative bonds.[26-29] Inorganic units known as secondary building units (SBUs) are bonded with organic linkers to afford an open crystalline framework with permanent porosity. Typically, organic linker molecules are di- or multi-topic carboxylic acids that can be readily synthesized if not already commercially available. With the vast amount of organic and inorganic units that can be reacted, an ever increasing amount of MOFs have been synthesized with more than 20,000 already reported in the literature.[30] Additionally, the ability to change the size of MOF structures using different linkers without altering the overall topology engenders isoreticular principles.[31] The significant interest and research performed in this field has made MOFs the most porous class of materials to date, with typical surface areas ranging from 1000 to 10,000 m^2/g.[30]

1.2.3 Covalent-Organic Frameworks

Covalent-organic frameworks (COFs) are a relatively new and emerging class of crystalline network materials formed solely from organic precursors. Typically, these materials are synthesized via reactions between rigid organic building blocks that afford crystalline 2-D or 3-D frameworks comprised of strong covalent bonds. The predictable reactivity of organic precursors allows precise control over composition, topology, and porosity of the resulting material. Furthermore, the strong covalent bonding arrangements provide chemical and thermal stability to the framework. As a result, many applications have been explored including adsorption,[32-34] energy storage,[35,36] catalysis,[37,38] sensing,[39,40] and optoelectronic devices.[41-43] Although the study of COFs closely resembles, at least on a conceptual level, that of MOFs, there are distinct and significant differences that prompt many interesting and exciting challenges.

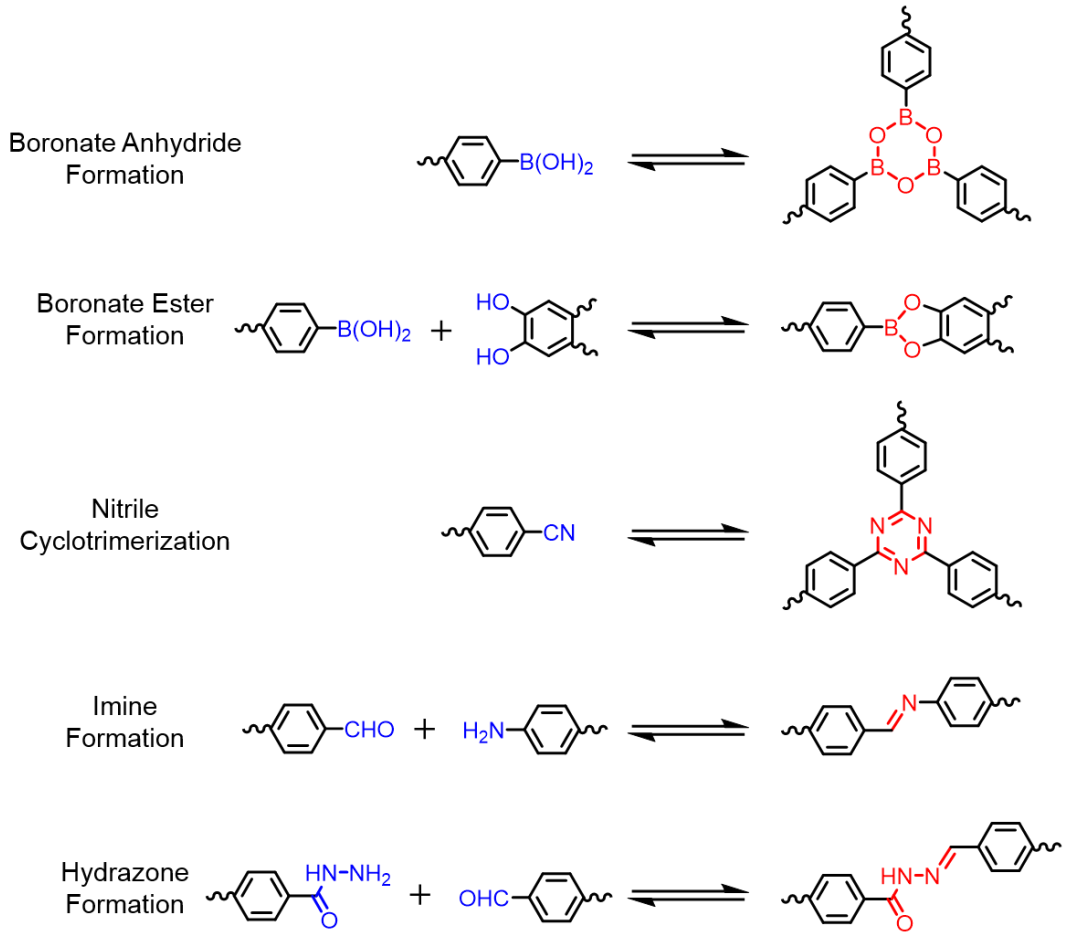

***Figure 1.3**: The most common covalent reactions used to synthesize COFs.*

Typically, the synthesis of COFs is performed via condensation reactions. The most common synthetic methods to synthesize COFs have been via boronate anhydride formation,[44,45] boronate ester formation,[46,47] borosilicate formation,[48,49] nitrile cyclotrimerization,[50] imine condensation,[51,52] and hydrazone formation.[53-55] Figure 1.3 provides a summary of the various covalent reactions utilized to form COFs. In general, reactions used to synthesize COFs must be reversible (i.e. dynamic) in order to provide error correction during framework formation. Additionally, the organic precursors used in the reaction must be rigid to provide structural regularity and integrity of the resulting framework.

Given the plethora of COF research in the literature, it may be perceived that the synthesis of COFs is a simple task that only requires heating a mixture of multitopic organic precursors with orthogonal functional groups. As a few examples have determined, even when the prerequisites of dynamics and rigidity are met, there is no guarantee that a certain mixture of organic precursors will afford a structurally regular, crystalline COF. Such difficulty in synthesis has hindered rational

design and continues to be a significant challenge. Fortunately, studies from Dichtel[47] and others are shedding light on the complex equilibria and kinetic factors of COF formation. These examples are poised to elucidate hidden reaction requirements and advance the field of COFs.

1.3 Molecular Porous Materials

1.3.1 Porous Molecular Solids

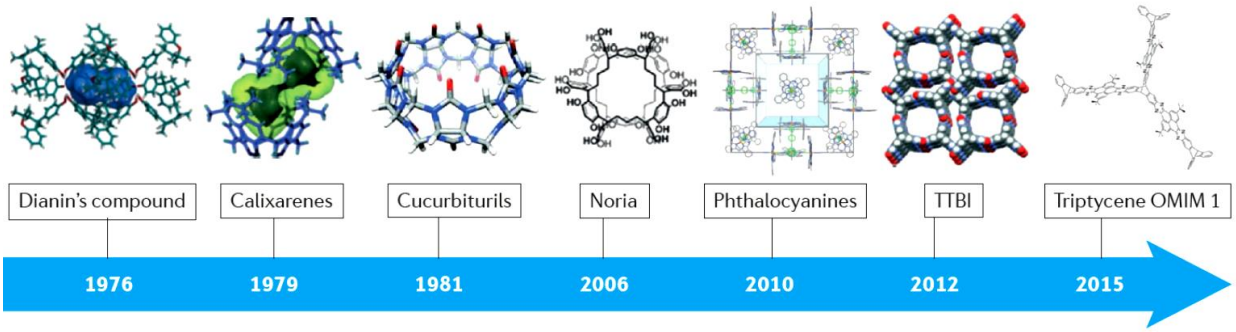

***Figure 1.4**: Historical view of molecular porous solids.[56] Reproduced from ref. 56 with permission from Springer Nature.*

What unifies all of the aforementioned materials is that they are *frameworks* or extended solids constructed either by strong covalent or coordinative bonds. Consequently, the crystal lattice energy or extended solid packing is dominated by these strong interactions. Such interactions provide structural robustness to the framework during desolvation or guest removal from the lattice, allowing them to be sorbent to gases and liquids. Another class of porous materials that have been extensively studied are porous solids which are constructed from discrete molecules. Such materials have been termed "porous molecular solids." These solids are much rarer to encounter in the literature than framework solids, as small discrete molecules have a tendency to pack densely in order to maximize attractive intermolecular interactions and thus prevent interconnected open pore space.[57,58] Furthermore, because their crystal lattices are dominated by weak van der Waals interactions, they are often unstable to solvent removal. For these reasons, the interest to discover molecular solids has been historically overshadowed by the interest in framework solids. Nonetheless, a variety of molecular solids have been discovered and proven to be effective porous materials, as shown in Figure 1.4.

The first molecular porous solid was reported by Barrer and Shanson (termed Dianin's compound) as early as 1976;[59] nearly two decades before the discovery of MOFs. They discovered that the solid of Dianin's compound readily adsorbs a plethora of gases including Ar, Kr, and Xe among various other gases. They further claimed that this compound behaved like an "organic zeolite" and made the observation that the structure of the solid is *less rigid* than that of a zeolite such that "guest molecules can penetrate into the cavities, even though wide windows giving access to these cavities do not exist."[59] In the context of porous molecular solids, lattice flexibility is often thought of as a defining feature that sets these materials apart from framework solids.[60-63] Indeed, it is the weak van der Waals interactions between molecules within these solids that prompts this response to adsorbates.

Since the study by Barrer and Shanson, many other porous molecular solids have been reported. Notable examples include calixarenes pioneered by Atwood,[64-71] and awkwardly-shaped organic molecules that are designed to prevent efficient packing in the solid state.[72-76] Collectively, these materials exhibit *extrinsic* porosity, or porosity that arises due to the inefficient packing arrangement of these molecules. Current challenges in this field involve the discovery of novel molecules that pack in such an arrangement that affords accessible surface topologies for adsorption. Unfortunately, rational design of such materials is challenging because small changes in molecular structure often have unpredictable effects on crystal packing; thus, it is not trivial to predict novel porous molecular solids. It is for this reason, as discussed by Schon and Jansen, that "design" in solid-state chemical synthesis has been considered as an illusion.[77]

1.3.2 Porous Molecular Cages

A more recent field of study involves the synthesis and porosity of molecular cage molecules, or molecules with *intrinsic* porosity due to their inherent molecular cavities. While various molecular cages have been reported, as shown by the groups of Fujita,[78-81] Atwood,[82-84] Newkome,[85,86] Nitschke,[87-90] Rebek,[91-93] and others,[94-96] it wasn't until a study by Cooper in 2009 that demonstrated permanent porosity in solids of organic molecular cages.[97] This contribution revealed for the first time that solids of molecular cages can remain permanently porous upon removal of enclatherated solvent.

The initial molecular cage system provided a means to systematically study the effects on porosity of various synthetic alterations on the cage framework. Varying the diamine linker, for

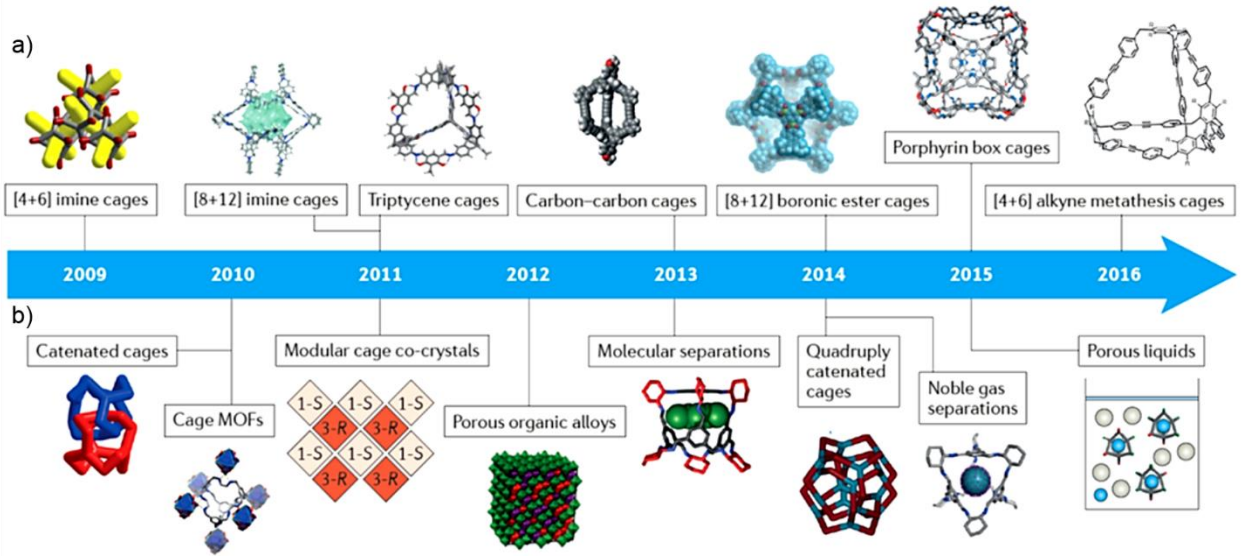

Figure 1.5*: Timeline and progression of the field of porous molecular cages.*[56] *Reproduced from ref. 56 with permission from Springer Nature.*

example, provokes different packing arrangements in the solid state and thus changes the adsorption properties.[97] The readily soluble nature of these discrete cages also provides the means to synthesize different polymorphs with the *same cage*. Hence, the same molecular cage can be packed in the solid state in a variety of different ways, depending on the crystallization conditions used to prepare the solid. In this fashion, Cooper determined that the same cage can be induced to pack in such a way to be porous or non-porous by using specific crystallization conditions.[97] Even solids of the same packing arrangement (space group) can exhibit different adsorption capacities due to the presence of crystal defects.[58,97] Furthermore, solubility allows the opportunity for mix-and-match strategies and co-crystallization techniques.[98-102] Cages of opposite chirality, for example, have been shown to pack in a more dense fashion than those of the same chirality.[103] This strategy has been extended to systems that are comprised of binary or tertiary co-crystals (two or three different cages, respectively) and organic alloys; a method that is analogous to the construction of multivariate MOFs.[103]

Undeniably, a plethora of organic cages have been synthesized and characterized since the seminal study by Cooper. Figure 1.5 provides a succinct overview of the field throughout the last eight years that highlights some important findings. With a diverse and widespread interest in these materials, many interesting applications have surfaced; the most interesting of which involve using organic molecular cage solids for molecular catalysis,[104-106] molecular separations,[107-110] proton conductivity,[111] and porous liquids.[112,113] While relatively less interest has been paid in this

research field as compared to framework materials, the characteristic features of molecular cages open up new possibilities that are otherwise unavailable with other current porous materials. The development of porous liquids, for example, will prove to be a defining application for porous molecular cages, as the solubility of porous molecular species is a requirement. Nonetheless, the major challenges in the field of molecular cages include 1) targeting potential cage structures which give rise to permanent porosity, 2) the efficient synthesis of targeted organic molecular cages, and 3) understanding the porosity in molecular cage solids as a function of cage structure and packing.

1.4 Synthesis of Molecular Cages

1.4.1 Overview

The synthesis of organic molecular cages is, in principle, performed using two different synthetic methods. Although less common, organic molecular cages have been synthesized via a step-wise, irreversible process that involves the use of kinetically controlled reactions. In this context, researchers have used cross-coupling,[114-116] nucleophilic aromatic substitution,[117] ester condensation,[118] and azide-alkyne Huisgen cycloaddition[119] to construct desired architectures. Such methods usually entail many synthetic steps and result in low overall yields of the desired product. While irreversible processes tend to be more difficult, the resulting cages are often quite thermally and chemically stable as a result of the strong bonds that are formed. The most prevalent route to synthesize organic molecular cages, and the route that I will focus most of the following section on, involves the use of dynamic covalent chemistry (DCC).[120] The common view of DCC reactions is that they proceed under thermodynamic control and allow for error-correction and reversibility of intermediates. Thus, the most thermodynamically-stable products are often, but not always, formed in high yields. Since molecular cages are entropically favored over oligomeric or polymeric products, DCC systems are regularly utilized for molecular cage synthesis. Organic molecular cages have been synthesized using imine condensation, boronic ester condensation, disulfide formation, aldehyde condensation, olefin metathesis, and alkyne metathesis. Out of these, the most utilized DCC reactions to synthesize organic molecular cages are imine condensation and boronic ester condensation.

1.4.2 Imine Condensation

In the context of organic molecular cages, imine condensation is unquestionably the most utilized reaction. Imines are generally prepared by the condensation of primary amines and aldehydes. Mechanistically, an imine condensation reaction proceeds by an initial nucleophilic addition to afford a hemiaminal intermediate which is then followed by an elimination of water to yield the imine. It terms of equilibrium, the system typically favors the starting reagents (the carbonyl compound and amine), thus is it necessary to remove the water formed in the reaction. The dynamic nature of the imine bond make it an attractive reaction to synthesize molecular cages. While a large number of cages have been constructed using imine condensation, only a cursory review will be given here that covers some of the most impactful work.

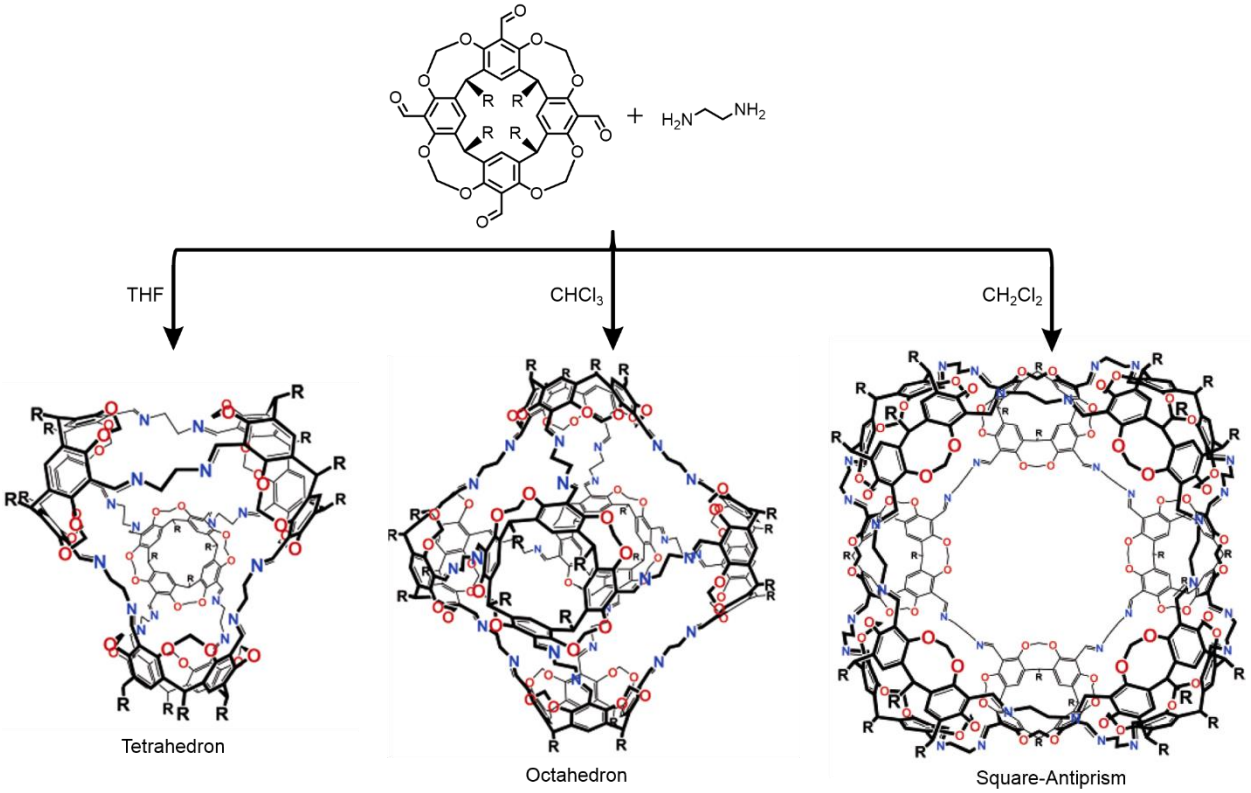

***Figure 1.6**: Synthesis of three different molecular cages using imine condensation.*

Imine condensation has been utilized to construct 3-D capsule-like molecules since the research of Cram and Quan in their synthesis of hemicarcerands. It wasn't until the work of Warmuth and co-workers that imine condensation was used to synthesis organic cages (Figure 1.6).[121-124] They discovered that a hemicarcerand resembling those synthesized by Cram and coworkers, when reacted with 1,2-diaminoethane, forms an octahedral molecular cage when

reacted in chloroform with catalytic trifluoroacetic acid (TFA).[124] Furthermore, they also discovered that the resulting cage structure that forms is dependent on the solvent used for the reaction. In chloroform, the octahedral molecular cage forms, in dichloromethane, a square-antiprism forms, and when tetrahydrofuran is used, a tetrahedron forms.[124] These initial studies on imine cage systems set the stage for subsequent cage research that eventually lead to permanently porous materials.

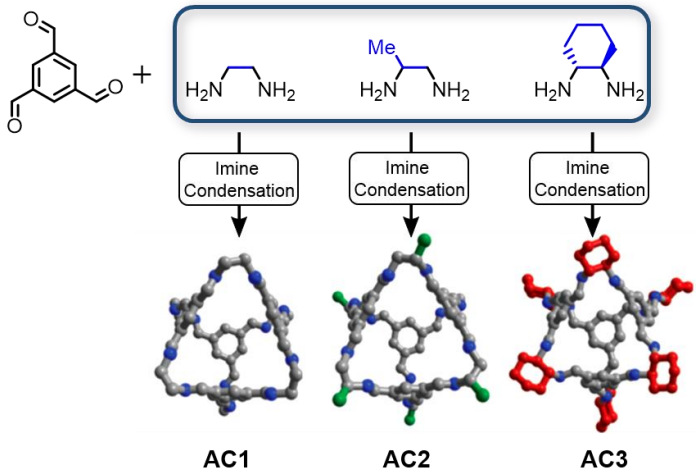

Figure 1.7*: Synthesis of three analogous porous organic cages via imine condensation between 1,3,5-triformylbenzene and 1,2-diamines.*

Cooper and coworkers also use imine condensation to synthesize molecular cages. As shown in Figure 1.7, they discovered that when 1,3,5-triformalbenzene is reacted with 1,2-diaminoethane derivatives, various analogous [4+6] tetrahedral cages are formed.[97] Extensive research has proven that this method can be extended to other related systems where either the amine linker or aldehyde linker can be altered (or both).[125-128] A great example of the generality of this method can be seen in a recent article that describes the synthesis of extended, trigonal prismatic cages as shown in Figure 1.8.[98]

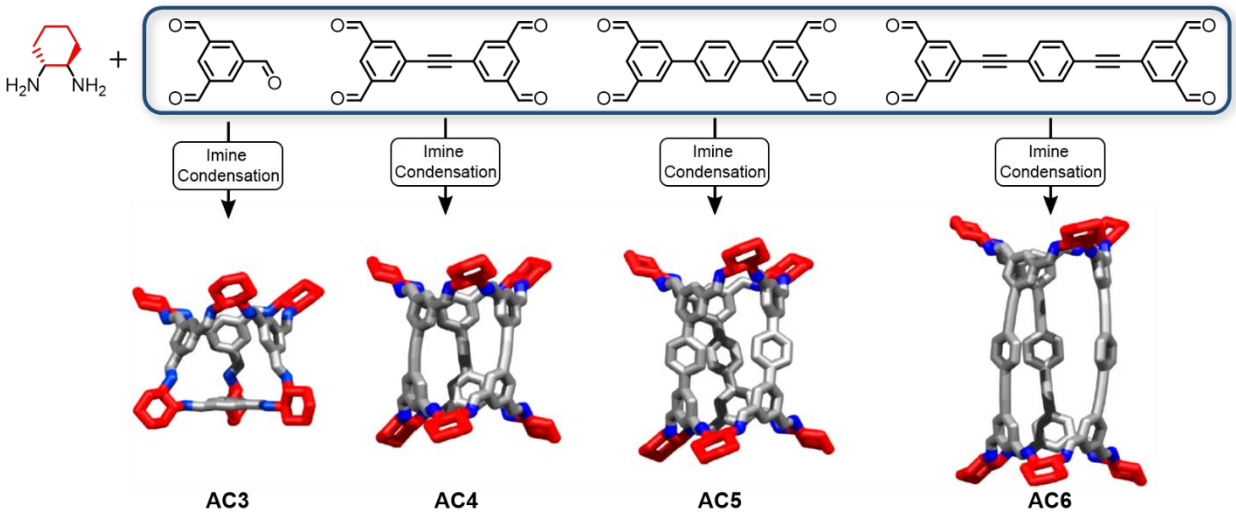

***Figure 1.8**: Prismatic imine molecular cages synthesized via imine condensation of R,R-1,2-cyclohexyldiamine and various multifunctional aldehyde linkers.*

1.4.3 Boronic Ester Condensation

In terms of molecular cage synthesis, boronic ester condensation is the second most used reaction to construct organic molecular cages. Boronic esters, also named boronate esters, are readily prepared from boronic acids and alcohols or diols. The reaction also releases water as a byproduct that is typically removed to drive the reaction forward. The benefit of using boronic ester formation over imine condensation is the rigidity that the boronate ester bond induces. As a result, extremely large cages can be formed that are stable to guest removal. One disadvantage to using this chemistry, however, is that boronate esters are extremely sensitive to moisture. Thus, cages formed with boronate esters are characteristically not stable. Nonetheless, many examples in the literature have used this chemistry as a means to construct organic molecular cages. Again, only a brief summary of those structures will be discussed.

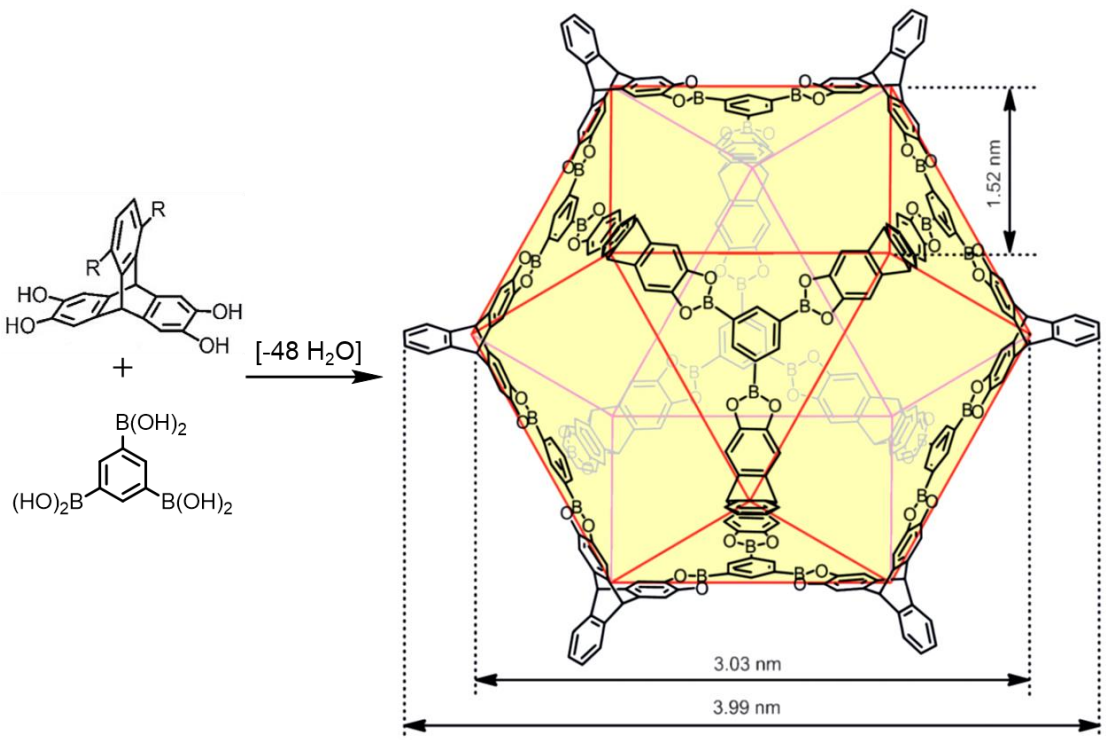

***Figure 1.9**: A cuboctahedral [8+12] cage synthesized via boronic ester condensation.*

The largest porous organic cage in the literature was synthesized using boronic ester condensation. As shown by Mastalerz and coworkers (Figure 1.9), a cuboctahedral [8+12] cage can be synthesized by condensation of twelve molecules of triptycene tetraol and eight molecules of the 1,3,5-tris(boronic acid)benzene.[129] The cuboctahedron has a pore diameter of ca. 3.03 nm, making it the largest known molecular cage to date. The molecular packing of this cage results in a permanently porous solid with a BET specific surface area of 3758 m^2/g, which surpasses even well-known MOFs, COFs, and zeolites.[129]

Beuerle and coworkers extended cage synthesis via boronic ester condensation to include shape-controlled self-sorting.[130] They described a system that can exhibit both narcissistic and social self-sorting depending on the organic precursors added to the reaction. Using a simple thermodynamic argument, they rationalized and synthesized a variety of different cages using one catacol and three different difunctional boronic acids. This example is the first report describing self-sorting in a cage-forming systems via boronic ester condensation. Their approach opens the door for rational control over the resulting structures formed during DCC synthesis.

1.4.4 Challenges in Molecular Cage Synthesis

Given the amount of successful molecular cage synthesis reported, it may be perceived that designing and constructing novel molecular organic cages is a trivial matter that only requires multitopic amines and aldehydes or boronic acids and alcohols. Unfortunately, this is not the case. Even though DCC is a powerful and proven synthetic tool for such a task, DCC reactions initially form oligomeric intermediates as kinetic products which can sometimes precipitate and be removed from equilibrium. Furthermore, while DCC is commonly believed to be thermodynamically controlled, this view can be misleading. As shown in a few cases, kinetics may intervene and dominate the product distribution, ultimately affording other undesirable structures. Additionally, the desired architecture may not even be the thermodynamic product in the system. Too much reversibility may lead to denser structures such as catenated cages that are difficult to separate and purify. Lastly, even if a cage is successfully synthesized, there is no guarantee that molecular solids constructed from it will give rise to permanent porosity. Since porosity is a function of cage structural stability and solid packing arrangement, just synthesizing a molecular cage is not sufficient to guarantee a porous material.

1.5 Alkyne Metathesis

While other DCC reactions have proven to be useful for synthesizing covalent organic architectures, they are often unstable to moisture or acidic environments. Furthermore, most dynamic systems require multiple precursors in the same reaction for successful architecture formation. Imine condensation, for example, requires two precursors (an aldehyde and an amine) to form a structure that consists of acid-labile imines. Boronic ester condensation requires a boronic acid and a catechol to afford a product that consists of moisture-sensitive boronic esters. To alleviate the difficulties in current DCC approaches, we sought to use alkyne metathesis for architecture formation. Since alkyne metathesis involves the scrambling of strong and chemically stable carbon-carbon triple bonds (ca. 200 kcal/mol) with a linear geometry, we hypothesized that it is an effective DCC reaction for successful covalent organic architecture formation.

1.5.1 Origins and Mechanism

The origin of alkyne metathesis is rooted in heterogeneous catalysis. Early work showed that solids synthesized by immobilizing early transition metal oxides of W and Mo on silica are able to catalyze 2-pentyne into 2-butyne and 3-hexyne.[131,132] Unfortunately, the high reaction

temperatures (between 200-450 ºC) required for this transformation delayed widespread use, as these reaction conditions favored substrate polymerization rather than productive metathesis (i.e. scrambling). Mortreux and Blanchard eventually discovered that a mixture of $[Mo(CO)_6]$ and resorcinol could scramble internal alkynes at temperatures of 160 ºC, giving rise to the first homogeneous alkyne metathesis catalyst, albeit with an unknown active species.[133] Still, the reaction temperature seriously limited this transformation and engendered only a narrow functional-group tolerance.

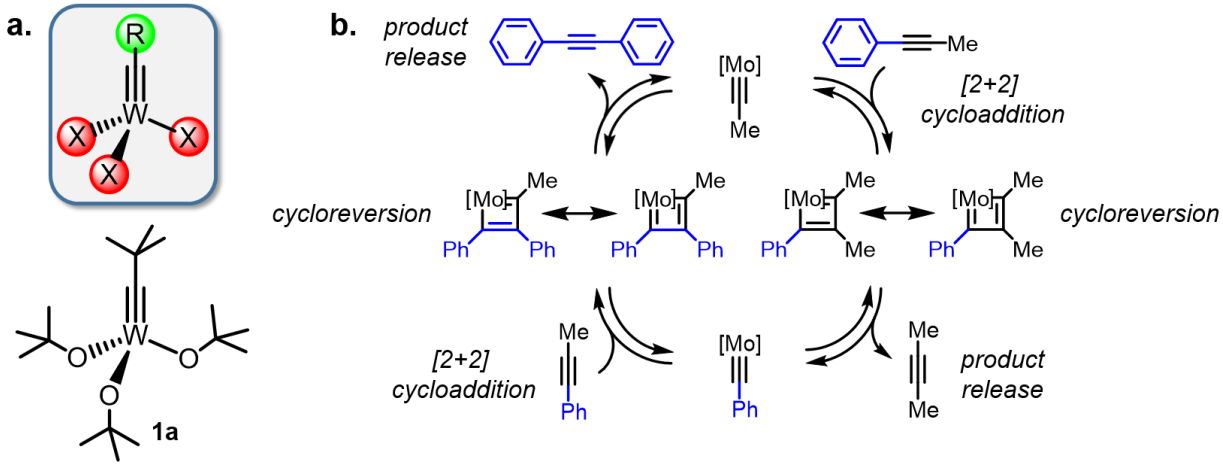

***Figure 1.10**: a) Classical alkyne metathesis structure where R is either an alkyl or aromatic substitutent and X is an ancillary ligand. b) Metathesis reaction mechanism for the formation of diphenylacetylene.*

While the mechanism of this reaction was postulated early on by Katz and McGinnis (i.e. the Chauvin cycle of olefin metathesis),[134] it wasn't until several classical studies from the Schrock group that experimental evidence for this mechanism was observed.[135-137] The mechanism is shown in Figure 1.10b for the reaction of 1-phenyl-1-proyne catalyzed with a Mo species to afford diphenylacetylene and 2-butyne. In this catalyst cycle, the alkylidyne species combines with the substrate in a formal [2+2] cycloaddition reaction to form metallocyclobutadiene. This species undergoes cycloreversion followed by product release to afford another catalytically active species, which subsequently follows the same steps to complete the turnover and afford the product. Product release from the metallacyclobutadiene is rate limiting.[138]

1.5.2 Catalyst Development and Synthesis

Much of the current knowledge on catalyst design has stemmed from early experiments reported by Schrock and coworkers. In fact, active alkyne metathesis catalysts (with only two recent exceptions)[139] are high-valent alkylidyne Schrock catalysts. The metal center is in its highest oxidation state and the alkylidyne moiety is trianionic.[135] Hence, the most popular species used for this transformation are carbyne d^0 complexes of Mo(VI), W(VI), and Re(VII). In the "classic" sense, an alkyne metathesis catalyst can be illustrated by the complexes $[X_3W{\equiv}CR]$ (Figure 1.10a). Developed by Schrock, complexes of this type were the first well-defined molecular catalysts for alkyne metathesis.[140]

The basic structure and design of the ligands used in catalyst design is best illustrated by complex 1a in Scheme X, where R and X are different substituents. The substituent, R, has minor effect on the activity of the system, since it is removed upon the first turnover of the cycle. The electronic structure of substituent R will, however, affect catalyst initiation rates, as shown in a recent study by Fischer and coworkers who observed a moderately positive Hammett reaction constant for initiation.[141] The sterics of R has also recently been shown to affect polymer topology in ring-opening metathesis polymerization.[142] Additionally, the most important characteristic of R is that the nature of this substituent will affect ease of preparation and catalyst benchtop stability.[143]

The most important factor in catalyst activity, however, is the anionic ancillary ligands, X. Both the sterics and electronics of these ligands affect activity and stability of the overall system. The metathesis catalytic cycle is rather demanding with respect to electronics, as opposing ligand characteristics are needed at different points in the catalytic cycle. Substrate uptake in the form of a [2+2] cycloaddition to afford the metallocyclobutadiene requires lewis acidity at the metal center, while cycloreversion and product release necessitate electron density at the metal center.[143] We can see this, for example, when comparing catalysts comprised of Mo versus those comprised of W, as W catalysts tend to be more acidic; correspondingly, product release with these systems tend to be more difficult to achieve. The electronic demands make it difficult to finely-tune the electronic nature of the catalyst species to meet these demands. This difficulty is best illustrated by the poor substrate scope seen in the earlier catalytic systems, where ligand design was much less understood. With respect to ligand sterics, a balance must be found. Ligand bulk provides protection for the metal center toward nucleophilic attack. In addition, bulky ligands help to prevent metal dimerization via oxo bridges and limit bimolecular decomposition during turnover.

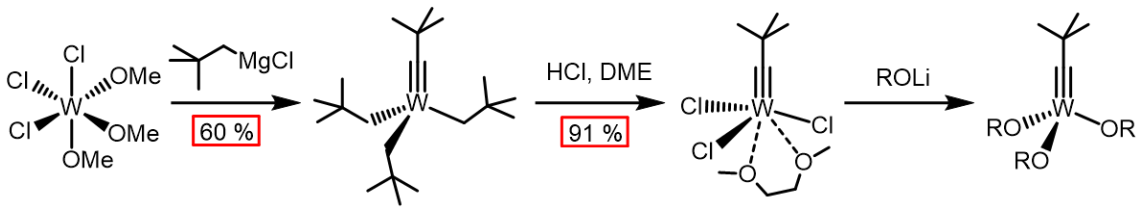

Scheme 1.1*: Classical Schrock synthesis of high-valent tungsten alkylidyne complexes.*

From the groundwork laid by Schrock, the Cummins lab advanced the field of alkyne metathesis by introducing an alternative synthetic route to high valent Mo complexes;[144,145] as the synthesis of such complexes was plagued with low yields via the classical Schrock method. Rather than performing exhaustive alkylation of the Mo (VI) species as in the Schrock method, Cummins pioneered a high-valent route starting with the reduction of $MoCl_5$ using tin in tetrahydrofuran (Scheme 1.2).[144] Treatment of the resulting *mer*-$MoCl_3(THF)_3$ with 2 equiv of Li[N(*t*-Bu)Ar](OEt_2) in ether affords the highly useful trivalent species, Mo[N[*t*-Bu]Ar]$_3$, in good yields.

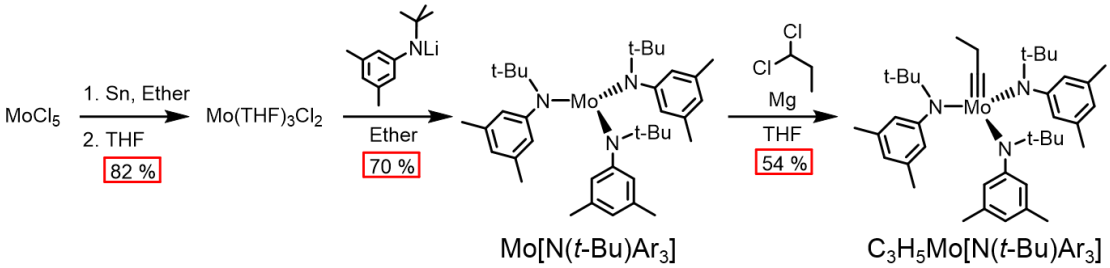

Scheme 1.2*: Synthesis of high valent Molybdenum alkylidyne pre-catalyst adapted from Cummins and Zhang.*

With respect to the work presented herein, the catalyst system used for our experiments was developed by Wei Zhang during his graduate studies.[146-148] Catalyst development began with the reaction of Mo[N(*t*-Bu)Ar]$_3$ (Ar = 3,5-$C_6H_3Me_2$) with dichloromethane to yield a mixture of ClMo[N(*t*-Bu)Ar]$_3$ and HCMo[N(*t*-Bu)Ar]$_3$.[149] The addition of Mg and replacement of dichloromethane with 1,1-dichloropropane to this reaction mixture resulted in the formation of pre-catalyst C_3H_5Mo[N(*t*-Bu)Ar]$_3$ (the last synthetic step in Scheme 1.2).[148] While initial ligands used to activate the pre-catalysts included nitrophenol derivatives, we utilize silanolates as the ligands in our catalytic system, as they have proven to have enhanced activity and stability.[150,151]

Silanolate ligands, as shown by Furstner,[150,151] provide many benefits to catalytic system. While triphenylsilanolate (Ph_3SiO) may be perceived as being too bulky, X-ray structural data support that this ligand does not hinder substrate binding, yet is still bulky enough to prevent an associative mechanism. In terms of electronics, the donor capacity of silanolates depends

significantly on the Mo−O−Si bond. When this bond angle is close to 180º, both electron pairs on the oxygen atom are able to participate in O→Mo bonding and the acidity at the metal center decreases. When the Mo−O−Si bond angle decreases, only one lone pair of electrons from the oxygen atom can participate in overlap with the Mo d-orbital, increasing lewis acidity.[150] As a result of these properties, silanolates can accommodate the opposing electronic demands at the metal center during the catalytic cycle.

1.6 Kinetically Trapped Tetrahedral Cages via Alkyne Metathesis

In the common view, dynamic covalent chemistry (DCC) proceeds reversibly under thermodynamic control.[120] As such, it is expected that such reaction systems will allow error correction during the formation of intermediates and ultimately afford the most thermodynamically stable products after equilibrations. In light of this view, one might expect cage formation under DCC to be relatively trivial. Unfortunately, kinetic considerations and difficulties that arise from them are often overlooked in the field. Since DCC involves the breaking and forming of strong covalent bonds, it is possible that significant kinetic barriers must be overcome to locate the thermodynamic product. Consequently, the progress toward equilibrium may become impeded due to extended intermediate lifetimes or intermediates that become kinetically trapped in the dynamic system.

Although kinetic traps are typically thought of as hindrances, in a few specific examples they have afforded useful or desired architectures. As demonstrated by Sanders and coworkers, hydrazone-based macrocycles become kinetically trapped in a dynamic system once they form.[152] The kinetic stability allows these macrocycles to be used as anion receptors. Another example of this phenomenon is described by Otto and coworkers where disulfide-based six-membered macrocycles become trapped while self-assembling into tubular stacks.[153] This self-assembly creates a driving force for the hexacycles to be form preferentially over other macrocycles.

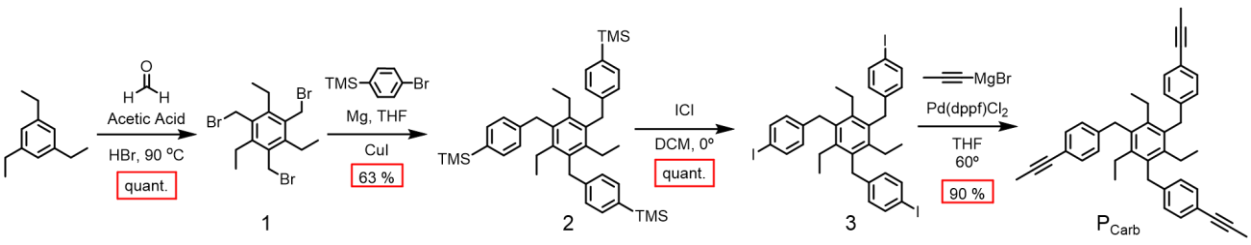

***Scheme 1.3**: Synthesis of cage precursor, P_{Carb}.*

In our first contribution to the field of molecular cages, we discovered a cage-forming system utilizing tritopic precursors and alkyne metathesis.[154] Tritopic precursors were synthesized as shown in Scheme 1.3. Briefly, P_{Carb} was synthesized in four steps in high yields starting from a copper(I)-catalyzed coupling to transform **1** to tribenzyl compound **2**. Iodination of **2** by treatment with ICl in dichloromethane afforded **3** in nearly quantitative yields. Lastly, kumada coupling of **3** with propyne magnesium bromide using $Pd(dppf)Cl_2$ as the catalyst afforded P_{Carb} in high yields. A similar protocol was followed to synthesize a precursor with the same framework but contained isopentoxy solubilizing groups instead of ethyl (P_B).

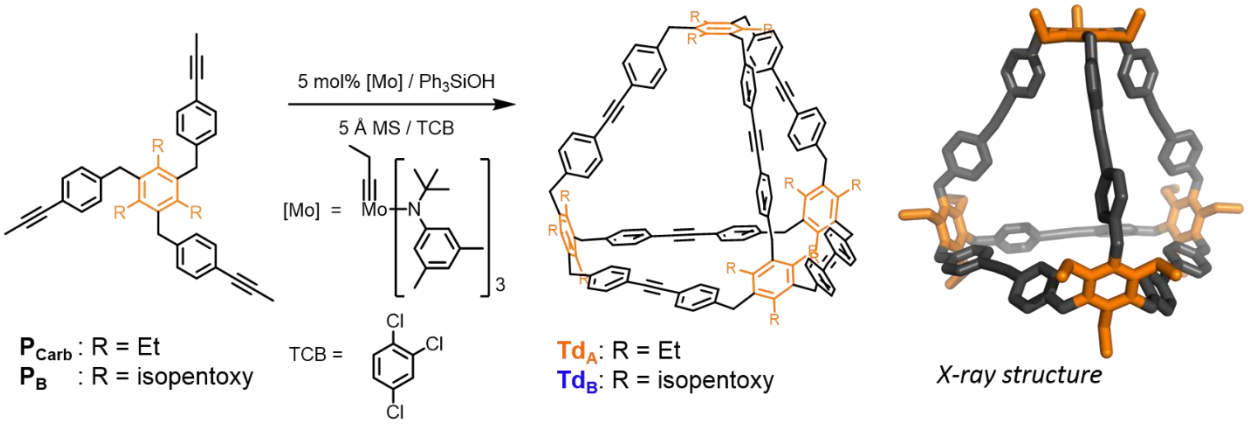

***Scheme 1.4**: Synthesis of tetrahedral organic cages via alkyne metathesis.*

Both precursors, P_{Carb} and P_B, were subjected to alkyne metathesis conditions using 5 mol % [Mo] catalyst, 30 mol % Ph_3SiOH, 5 Å molecular sieves (800 mg/mmol of propyne groups), at 10 mM concentration for 12 hours at 70 ºC in 1,2,4-trichlorobenzene. Under these reaction conditions, both precursor afforded a tetrahedral cage in nearly quantitative yields. Crystallization of Td_A from a mixture of chloroform and toluene afforded crystals in the $I4_1/a$ space group and unambiguously determines the tetrahedral geometry of the compound. Interestingly, the angle between benzylic edges and the central benzene moiety on the vertices was found to be 117.3º on average, which is smaller than the ideal 125.2º angle for a tetrahedron.

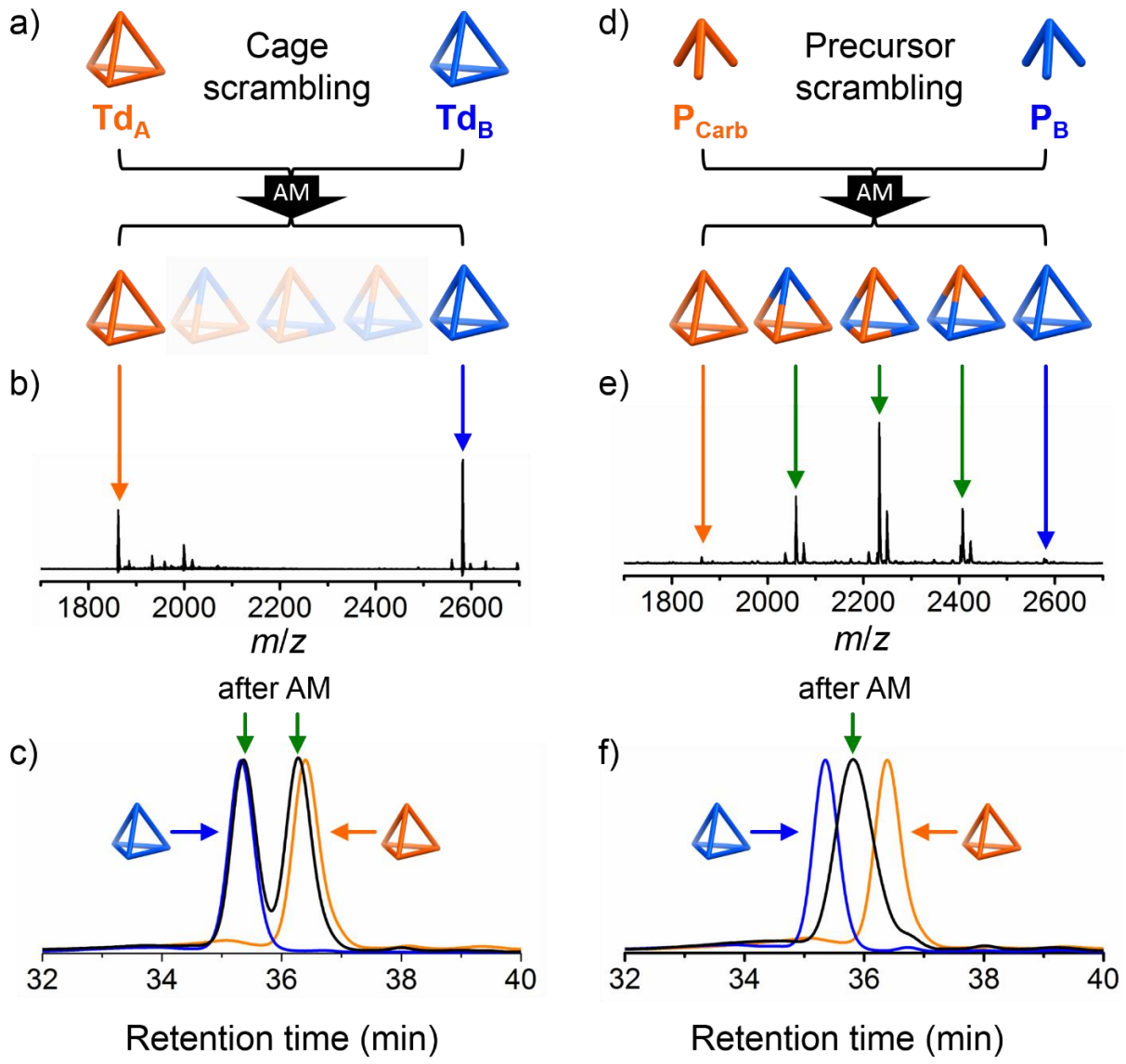

Figure 1.11*: Results from mixing experiments. a) Cage mixing experiment. b) MALDI-MS analysis of the cage mixing experiment. c) GPC trace of the cage mixing experiment overlaid with GPC traces from each cage separately. d) Precursor mixing experiment. e) MALDI-MS spectrum of the precursor mixing experiment. f) GPC trace of the precursor mixing experiment overlayed with the GPC traces of each cage separately. Figure reprinted (adapted) with permission from ref. 154. Copyright (2016) American Chemical Society.*

Given that such high yields were observed for this complex system, it was hypothesized that cage formation represented a kinetic trap within this dynamic system. To test this hypothesis, dynamic scrambling experiments were performed to determine the nature of the system (Figure 1.11). First, an equimolar mixture of the two precursors, P_{Carb} and P_B, was subjected to metathesis

with 4x the original concentration of [Mo] catalyst. Characterization of this mixture by GPC and MALDI-MS revealed that a statistical mixture of cages formed as a result of the scrambling. Then, a mixing experiment was performed with equimolar amounts of each cage (Td_A and Td_B) under similar conditions. Characterization of this mixture indicated that the same two cages were recovered in quantitative yields after the reaction. The results from these two experiments allowed us to conclude that the tetrahedral cages are kinetically trapped once they are formed under these reaction conditions.

1.7 References

Notes: Parts of this chapter are adopted from Lee, S.; Yang, A.; Moneypenny II, T. P.; Moore, J. S. *J. Am. Chem. Soc.* **2016**, *138*, 2182-2185. The materials are reproduced/adapted with permission.

(1) Liang, J.; Liang, Z.; Zou, R.; Zhao, Y. *Adv. Mater.* **2017**, *29*, 1701139.

(2) Lu, P.; Villaescusa, L. A.; Camblor, M. A. *Chem. Rec.*, *0*.

(3) Mynsbrugge, J. V. d.; Janda, A.; Lin, L. C.; Speybroeck, V. V.; Head-Gordon, M.; Bell, A. T. *ChemPhysChem* **2018**, *19*, 341.

(4) Pan, D.; Song, X.; Yang, X.; Gao, L.; Wei, R.; Zhang, J.; Xiao, G. *Applied Catalysis A: General* **2018**, *557*, 15.

(5) Ji, Y.; Yang, H.; Yan, W. *Catalysts* **2017**, *7*, 367.

(6) Gang, Y.; Xianli, Z. *Current Catalysis* **2017**, *6*, 146.

(7) Dehghan, R.; Anbia, M. *Fuel Process. Technol.* **2017**, *167*, 99.

(8) Blay, V.; Louis, B.; Miravalles, R.; Yokoi, T.; Peccatiello, K. A.; Clough, M.; Yilmaz, B. *ACS Catalysis* **2017**, *7*, 6542.

(9) Kulkarni, A. R.; Zhao, Z.-J.; Siahrostami, S.; Norskov, J. K.; Studt, F. *Catalysis Science & Technology* **2018**, *8*, 114.

(10) Reeve, P. J.; Fallowfield, H. J. *Journal of Environmental Management* **2018**, *205*, 253.

(11) Feliczak-Guzik, A. *Microporous Mesoporous Mater.* **2018**, *259*, 33.

(12) Liu, Z.; Hua, Y.; Wang, J.; Dong, X.; Tian, Q.; Han, Y. *Materials Chemistry Frontiers* **2017**, *1*, 2195.

(13) Li, Y.; Li, L.; Yu, J. *Chem* **2017**, *3*, 928.

(14) Fellinger, T.-P.; Thomas, A.; Yuan, J.; Antonietti, M. *Adv. Mater.* **2013**, *25*, 5838.

(15) Kumar, P.; Agrawal, K. V.; Tsapatsis, M.; Mkhoyan, K. A. *Nat. Commun.* **2015**, *6*, 7128.

(16) Grau-Crespo, R.; Acuay, E.; Ruiz-Salvador, A. R. *Chem. Commun.* **2002**, 2544.

(17) Cho, Y.-H.; Kim, C. H.; Lee, S. H.; Han, J.; Kwon, T. S.; Lee, K.-Y. *Fuel* **2018**, *221*, 399.

(18) Gołąbek, K.; Tarach, K. A.; Góra-Marek, K. *Spectrochimica Acta Part A: Molecular and Biomolecular Spectroscopy* **2018**, *192*, 361.

(19) Pebriana, R.; Mujahidin, D.; Syah, Y. M. *Materials Research Express* **2017**, *4*, 044004.

(20) Farahani, S. H.; Alavi, S. M.; Falamaki, C. *RSC Advances* **2017**, *7*, 34012.

(21) Chen, L.; Xue, T.; Wu, H.; Wu, P. *RSC Advances* **2018**, *8*, 2751.

(22) Wang, Q.; Han, W.; Lyu, J.; Zhang, Q.; Guo, L.; Li, X. *Catalysis Science & Technology* **2017**, *7*, 6140.

(23) Hu, H.; Lyu, J.; Rui, J.; Cen, J.; Zhang, Q.; Wang, Q.; Han, W.; Li, X. *Catalysis Science & Technology* **2016**, *6*, 2647.

(24) Wei, Y.; Parmentier, T. E.; de Jong, K. P.; Zecevic, J. *Chem. Soc. Rev.* **2015**, *44*, 7234.

(25) Cundy, C. S.; Cox, P. A. *Chem. Rev.* **2003**, *103*, 663.

(26) Deng, H.; Doonan, C. J.; Furukawa, H.; Ferreira, R. B.; Towne, J.; Knobler, C. B.; Wang, B.; Yaghi, O. M. *Science* **2010**, *327*, 846.

(27) Tranchemontagne, D. J.; Hunt, J. R.; Yaghi, O. M. *Tetrahedron* **2008**, *64*, 8553.

(28) Sudik, A. C.; Cote, A. P.; Wong-Foy, A. G.; O'Keeffe, M.; Yaghi, O. M. *Angew. Chem. Int. Ed. Engl.* **2006**, *45*, 2528.

(29) Eddaoudi, M.; Kim, J.; Rosi, N.; Vodak, D.; Wachter, J.; O'Keeffe, M.; Yaghi, O. M. *Science* **2002**, *295*, 469.

(30) Furukawa, H.; Cordova, K. E.; O'Keeffe, M.; Yaghi, O. M. *Science* **2013**, *341*, 1230444.

(31) Furukawa, H.; Ko, N.; Go, Y. B.; Aratani, N.; Choi, S. B.; Choi, E.; Yazaydin, A. O.; Snurr, R. Q.; O'Keeffe, M.; Kim, J.; Yaghi, O. M. *Science* **2010**, *329*, 424.

(32) Yu, J.-T.; Chen, Z.; Sun, J.; Huang, Z.-T.; Zheng, Q.-Y. *J. Mater. Chem.* **2012**, *22*, 5369.

(33) Furukawa, H.; Yaghi, O. M. *J. Am. Chem. Soc.* **2009**, *131*, 8875.

(34) Doonan, C. J.; Tranchemontagne, D. J.; Glover, T. G.; Hunt, J. R.; Yaghi, O. M. *Nat. Chem.* **2010**, *2*, 235.

(35) Das, S. K.; Bhunia, K.; Mallick, A.; Pradhan, A.; Pradhan, D.; Bhaumik, A. *Microporous Mesoporous Mater.* **2018**, *266*, 109.

(36) Zhou, J.; Wang, B. *Chem. Soc. Rev.* **2017**, *46*, 6927.

(37) Pachfule, P.; Acharjya, A.; Roeser, J.; Langenhahn, T.; Schwarze, M.; Schomäcker, R.; Thomas, A.; Schmidt, J. *J. Am. Chem. Soc.* **2018**, *140*, 1423.

(38) Diercks, C. S.; Lin, S.; Kornienko, N.; Kapustin, E. A.; Nichols, E. M.; Zhu, C.; Zhao, Y.; Chang, C. J.; Yaghi, O. M. *J. Am. Chem. Soc.* **2018**, *140*, 1116.

(39) Qian, H.-L.; Dai, C.; Yang, C.-X.; Yan, X.-P. *ACS Appl. Mater. Interfaces* **2017**, *9*, 24999.

(40) Peng, Y.; Huang, Y.; Zhu, Y.; Chen, B.; Wang, L.; Lai, Z.; Zhang, Z.; Zhao, M.; Tan, C.; Yang, N.; Shao, F.; Han, Y.; Zhang, H. *J. Am. Chem. Soc.* **2017**, *139*, 8698.

(41) Wan, S.; Guo, J.; Kim, J.; Ihee, H.; Jiang, D. *Angew. Chem. Int. Ed.* **2008**, *47*, 8826.

(42) Spitler, E. L.; Dichtel, W. R. *Nat. Chem.* **2010**, *2*, 672.

(43) Ding, X.; Chen, L.; Honsho, Y.; Feng, X.; Saengsawang, O.; Guo, J.; Saeki, A.; Seki, S.; Irle, S.; Nagase, S.; Parasuk, V.; Jiang, D. *J. Am. Chem. Soc.* **2011**, *133*, 14510.

(44) Smith, M. K.; Northrop, B. H. *Chem. Mater.* **2014**, *26*, 3781.

(45) Côté, A. P.; Benin, A. I.; Ockwig, N. W.; O'Keeffe, M.; Matzger, A. J.; Yaghi, O. M. *Science* **2005**, *310*, 1166.

(46) Smith, B. J.; Parent, L. R.; Overholts, A. C.; Beaucage, P. A.; Bisbey, R. P.; Chavez, A. D.; Hwang, N.; Park, C.; Evans, A. M.; Gianneschi, N. C.; Dichtel, W. R. *ACS Central Science* **2017**, *3*, 58.

(47) Smith, B. J.; Dichtel, W. R. *J. Am. Chem. Soc.* **2014**, *136*, 8783.

(48) Lan, J.; Cao, D.; Wang, W. *J. Phys. Chem. C* **2010**, *114*, 3108.

(49) Hunt, J. R.; Doonan, C. J.; LeVangie, J. D.; Côté, A. P.; Yaghi, O. M. *J. Am. Chem. Soc.* **2008**, *130*, 11872.

(50) Wang, Y.; Li, J.; Yang, Q.; Zhong, C. *ACS Appl. Mater. Interfaces* **2016**, *8*, 8694.

(51) Zhao, Y.; Guo, L.; Gándara, F.; Ma, Y.; Liu, Z.; Zhu, C.; Lyu, H.; Trickett, C. A.; Kapustin, E. A.; Terasaki, O.; Yaghi, O. M. *J. Am. Chem. Soc.* **2017**, *139*, 13166.

(52) Bhunia, S.; Das, S. K.; Jana, R.; Peter, S. C.; Bhattacharya, S.; Addicoat, M.; Bhaumik, A.; Pradhan, A. *ACS Appl. Mater. Interfaces* **2017**, *9*, 23843.

(53) Stegbauer, L.; Schwinghammer, K.; Lotsch, B. V. *Chem. Sci.* **2014**, *5*, 2789.

(54) Bunck, D. N.; Dichtel, W. R. *J. Am. Chem. Soc.* **2013**, *135*, 14952.

(55) Uribe-Romo, F. J.; Doonan, C. J.; Furukawa, H.; Oisaki, K.; Yaghi, O. M. *J. Am. Chem. Soc.* **2011**, *133*, 11478.

(56) Hasell, T.; Cooper, A. I. *Nat. Rev. Mater.* **2016**, *1*, 16053.

(57) Desiraju, G. R. *Angew. Chem. Int. Ed.* **1995**, *34*, 2311.

(58) Hasell, T.; Culshaw, J. L.; Chong, S. Y.; Schmidtmann, M.; Little, M. A.; Jelfs, K. E.; Pyzer-Knapp, E. O.; Shepherd, H.; Adams, D. J.; Day, G. M.; Cooper, A. I. *J. Am. Chem. Soc.* **2014**, *136*, 1438.

(59) Barrer, R. M.; Shanson, V. H. *J. Chem. Soc., Chem. Commun.* **1976**, 333.

(60) Manurung, R.; Holden, D.; Miklitz, M.; Chen, L.; Hasell, T.; Chong, S. Y.; Haranczyk, M.; Cooper, A. I.; Jelfs, K. E. *J. Phys. Chem. C* **2015**, *119*, 22577.

(61) Holden, D.; Jelfs, K. E.; Trewin, A.; Willock, D. J.; Haranczyk, M.; Cooper, A. I. *J. Phys. Chem. C* **2014**, *118*, 12734.

(62) Jiang, S.; Jelfs, K. E.; Holden, D.; Hasell, T.; Chong, S. Y.; Haranczyk, M.; Trewin, A.; Cooper, A. I. *J. Am. Chem. Soc.* **2013**, *135*, 17818.

(63) Holden, D.; Jelfs, K. E.; Cooper, A. I.; Trewin, A.; Willock, D. J. *J. Phys. Chem. C* **2012**, *116*, 16639.

(64) Thallapally, P. K.; Peter McGrail, B.; Dalgarno, S. J.; Schaef, H. T.; Tian, J.; Atwood, J. L. *Nat. Mater.* **2008**, *7*, 146.

(65) Dalgarno, S. J.; Thallapally, P. K.; Barbour, L. J.; Atwood, J. L. *Chem. Soc. Rev.* **2007**, *36*, 236.

(66) Thallapally, P. K.; Dalgarno, S. J.; Atwood, J. L. *J. Am. Chem. Soc.* **2006**, *128*, 15060.

(67) Thallapally, P. K.; Wirsig, T. B.; Barbour, L. J.; Atwood, J. L. *Chem. Commun.* **2005**, 4420.

(68) Thallapally, P. K.; Lloyd, G. O.; Wirsig, T. B.; Bredenkamp, M. W.; Atwood, J. L.; Barbour, L. J. *Chem. Commun.* **2005**, 5272.

(69) Atwood, J. L.; Barbour, L. J.; Jerga, A. *Angew. Chem. Int. Ed.* **2004**, *43*, 2948.

(70) Atwood, J. L.; Barbour, L. J.; Jerga, A.; Schottel, B. L. *Science* **2002**, *298*, 1000.

(71) Atwood, J. L.; Barbour, L. J.; Jerga, A. *Science* **2002**, *296*, 2367.

(72) Kohl, B.; Rominger, F.; Mastalerz, M. *Chem. Eur. J.* **2015**, *21*, 17308.

(73) Taylor, R. G. D.; Carta, M.; Bezzu, C. G.; Walker, J.; Msayib, K. J.; Kariuki, B. M.; McKeown, N. B. *Org. Lett.* **2014**, *16*, 1848.

(74) Chong, J. H.; Ardakani, S. J.; Smith, K. J.; MacLachlan, M. J. *Chem. Eur. J.* **2009**, *15*, 11824.

(75) Kohl, B.; Rominger, F.; Mastalerz, M. *Org. Lett.* **2014**, *16*, 704.

(76) Taylor, R. G. D.; Bezzu, C. G.; Carta, M.; Msayib, K. J.; Walker, J.; Short, R.; Kariuki, B. M.; McKeown, N. B. *Chem. Eur. J.* **2016**, *22*, 2466.

(77) Jansen, M.; Schön, J. C. *Angew. Chem. Int. Ed.* **2006**, *45*, 3406.

(78) Schmidt, B. M.; Osuga, T.; Sawada, T.; Hoshino, M.; Fujita, M. *Angew. Chem. Int. Ed.* **2016**, *55*, 1561.

(79) Fujii, S.; Tada, T.; Komoto, Y.; Osuga, T.; Murase, T.; Fujita, M.; Kiguchi, M. *J. Am. Chem. Soc.* **2015**, *137*, 5939.

(80) Bruns, C. J.; Fujita, D.; Hoshino, M.; Sato, S.; Stoddart, J. F.; Fujita, M. *J. Am. Chem. Soc.* **2014**, *136*, 12027.

(81) Sun, Q. F.; Sato, S.; Fujita, M. *Angew. Chem. Int. Ed.* **2014**, *53*, 13510.

(82) McKinlay, R. M.; Thallapally, P. K.; Atwood, J. L. *Chem. Commun.* **2006**, 2956.

(83) McKinlay, R. M.; Thallapally, P. K.; Cave, G. W. V.; Atwood, J. L. *Angew. Chem. Int. Ed.* **2005**, *44*, 5733.

(84) Atwood, J. L.; Barbour, L. J.; Hardie, M. J.; Raston, C. L.; Statton, M. N.; Webb, H. R. *CrystEngComm* **2001**, *3*, 18.

(85) Xie, T.-Z.; Endres, K. J.; Guo, Z.; Ludlow, J. M.; Moorefield, C. N.; Saunders, M. J.; Wesdemiotis, C.; Newkome, G. R. *J. Am. Chem. Soc.* **2016**, *138*, 12344.

(86) Xie, T. Z.; Guo, K.; Guo, Z.; Gao, W. Y.; Wojtas, L.; Ning, G. H.; Huang, M.; Lu, X.; Li, J. Y.; Liao, S. Y.; Chen, Y. S.; Moorefield, C. N.; Saunders, M. J.; Cheng, S. Z. D.; Wesdemiotis, C.; Newkome, G. R. *Angew. Chem. Int. Ed.* **2015**, *54*, 9224.

(87) McConnell, A. J.; Aitchison, C. M.; Grommet, A. B.; Nitschke, J. R. *J. Am. Chem. Soc.* **2017**, *139*, 6294.

(88) Brenner, W.; Ronson, T. K.; Nitschke, J. R. *J. Am. Chem. Soc.* **2017**, *139*, 75.

(89) Castilla, A. M.; Ronson, T. K.; Nitschke, J. R. *J. Am. Chem. Soc.* **2016**, *138*, 2342.

(90) Meng, W.; Clegg, J. K.; Thoburn, J. D.; Nitschke, J. R. *J. Am. Chem. Soc.* **2011**, *133*, 13652.

(91) Daver, H.; Harvey, J. N.; Rebek, J.; Himo, F. *J. Am. Chem. Soc.* **2017**, *139*, 15494.

(92) Tzeli, D.; Theodorakopoulos, G.; Petsalakis, I. D.; Ajami, D.; Rebek, J. *J. Am. Chem. Soc.* **2012**, *134*, 4346.

(93) Hou, J.-L.; Ajami, D.; Rebek, J. *J. Am. Chem. Soc.* **2008**, *130*, 7810.

(94) Hart-Cooper, W. M.; Sgarlata, C.; Perrin, C. L.; Toste, F. D.; Bergman, R. G.; Raymond, K. N. *Proc. Natl. Acad. Sci.* **2015**, *112*, 15303.

(95) Hong, C. M.; Kaphan, D. M.; Bergman, R. G.; Raymond, K. N.; Toste, F. D. *J. Am. Chem. Soc.* **2017**, *139*, 8013.

(96) Fiedler, D.; Pagliero, D.; Brumaghim, J. L.; Bergman, R. G.; Raymond, K. N. *Inorg. Chem.* **2004**, *43*, 846.

(97) Tozawa, T.; Jones, J. T. A.; Swamy, S. I.; Jiang, S.; Adams, D. J.; Shakespeare, S.; Clowes, R.; Bradshaw, D.; Hasell, T.; Chong, S. Y.; Tang, C.; Thompson, S.; Parker, J.; Trewin, A.; Bacsa, J.; Slawin, A. M. Z.; Steiner, A.; Cooper, A. I. *Nat. Mater.* **2009**, *8*, 973.

(98) Slater, A. G.; Little, M. A.; Pulido, A.; Chong, S. Y.; Holden, D.; Chen, L.; Morgan, C.; Wu, X.; Cheng, G.; Clowes, R.; Briggs, M. E.; Hasell, T.; Jelfs, K. E.; Day, G. M.; Cooper, A. I. *Nat. Chem.* **2016**, *9*, 17.

(99) Little, M. A.; Briggs, M. E.; JonesJames, T. A.; Schmidtmann, M.; Hasell, T.; Chong, S. Y.; Jelfs, K. E.; Chen, L.; Cooper, A. I. *Nat. Chem.* **2015**, *7*, 153.

(100) Mitra, T.; Jelfs, K. E.; Schmidtmann, M.; Ahmed, A.; Chong, S. Y.; Adams, D. J.; Cooper, A. I. *Nat. Chem.* **2013**, *5*, 276.

(101) Hasell, T.; Chong, S. Y.; Jelfs, K. E.; Adams, D. J.; Cooper, A. I. *J. Am. Chem. Soc.* **2012**, *134*, 588.

(102) Jones, J. T. A.; Hasell, T.; Wu, X.; Bacsa, J.; Jelfs, K. E.; Schmidtmann, M.; Chong, S. Y.; Adams, D. J.; Trewin, A.; Schiffman, F.; Cora, F.; Slater, B.; Steiner, A.; Day, G. M.; Cooper, A. I. *Nature* **2011**, *474*, 367.

(103) Hasell, T.; Chong, S. Y.; Schmidtmann, M.; Adams, D. J.; Cooper, A. I. *Angew. Chem. Int. Ed.* **2012**, *51*, 7154.

(104) Zhang, Y.; Xiong, Y.; Ge, J.; Lin, R.; Chen, C.; Peng, Q.; Wang, D.; Li, Y. *Chem. Commun.* **2018**, *54*, 2796.

(105) Qiu, L.; McCaffrey, R.; Jin, Y.; Gong, Y.; Hu, Y.; Sun, H.; Park, W.; Zhang, W. *Chem. Sci.* **2018**, *9*, 676.

(106) Sun, J.-K.; Zhan, W.-W.; Akita, T.; Xu, Q. *J. Am. Chem. Soc.* **2015**, *137*, 7063.

(107) Hasell, T.; Miklitz, M.; Stephenson, A.; Little, M. A.; Chong, S. Y.; Clowes, R.; Chen, L.; Holden, D.; Tribello, G. A.; Jelfs, K. E.; Cooper, A. I. *J. Am. Chem. Soc.* **2016**.

(108) Slater, A. G.; Cooper, A. I. *Science* **2015**, *348*.

(109) Kewley, A.; Stephenson, A.; Chen, L.; Briggs, M. E.; Hasell, T.; Cooper, A. I. *Chem. Mater.* **2015**, *27*, 3207.

(110) Chen, L.; Reiss, P. S.; Chong, S. Y.; Holden, D.; Jelfs, K. E.; Hasell, T.; Little, M. A.; Kewley, A.; Briggs, M. E.; Stephenson, A.; Thomas, K. M.; Armstrong, J. A.; Bell, J.; Busto, J.; Noel, R.; Liu, J.; Strachan, D. M.; Thallapally, P. K.; Cooper, A. I. *Nat. Mater.* **2014**, *13*, 954.

(111) Liu, M.; Chen, L.; Lewis, S.; Chong, S. Y.; Little, M. A.; Hasell, T.; Aldous, I. M.; Brown, C. M.; Smith, M. W.; Morrison, C. A.; Hardwick, L. J.; Cooper, A. I. *Nat. Commun.* **2016**, *7*, 12750.

(112) Zhang, F.; Yang, F.; Huang, J.; Sumpter, B. G.; Qiao, R. *J. Phys. Chem. B* **2016**, *120*, 7195.

(113) Giri, N.; Del Pópolo, M. G.; Melaugh, G.; Greenaway, R. L.; Rätzke, K.; Koschine, T.; Pison, L.; Gomes, M. F. C.; Cooper, A. I.; James, S. L. *Nature* **2015**, *527*, 216.

(114) Avellaneda, A.; Valente, P.; Burgun, A.; Evans, J. D.; Markwell-Heys, A. W.; Rankine, D.; Nielsen, D. J.; Hill, M. R.; Sumby, C. J.; Doonan, C. J. *Angew. Chem. Int. Ed.* **2013**, *52*, 3746.

(115) Wu, Z.; Lee, S.; Moore, J. S. *J. Am. Chem. Soc.* **1992**, *114*, 8730.

(116) Zhang, C.; Chen, C.-F. *J. Org.Chem.***2007**, *72*, 9339.

(117) Zhang, C.; Wang, Z.; Tan, L.; Zhai, T. L.; Wang, S.; Tan, B.; Zheng, Y. S.; Yang, X. L.; Xu, H. B. *Angew. Chem. Int. Ed.* **2015**, *54*, 9244.

(118) Ono, K.; Johmoto, K.; Yasuda, N.; Uekusa, H.; Fujii, S.; Kiguchi, M.; Iwasawa, N. *J. Am. Chem. Soc.* **2015**, *137*, 7015.

(119) Zhang, J.; Li, Y.; Yang, W.; Lai, S.-W.; Zhou, C.; Liu, H.; Che, C.-M.; Li, Y. *Chem. Commun.* **2012**, *48*, 3602.

(120) Rowan, S. J.; Cantrill, S. J.; Cousins, G. R. L.; Sanders, J. K. M.; Stoddart, J. F. *Angew. Chem. Int. Ed.* **2002**, *41*, 898.

(121) Sun, J.; Warmuth, R. *Chem. Commun.* **2011**, *47*, 9351.

(122) Sun, J.; Bennett, J. L.; Emge, T. J.; Warmuth, R. *J. Am. Chem. Soc.* **2011**, *133*, 3268.

(123) Xu, D.; Warmuth, R. *J. Am. Chem. Soc.* **2008**, *130*, 7520.

(124) Liu, X.; Warmuth, R. *J. Am. Chem. Soc.* **2006**, *128*, 14120.

(125) Culshaw, J. L.; Cheng, G.; Schmidtmann, M.; Hasell, T.; Liu, M.; Adams, D. J.; Cooper, A. I. *J. Am. Chem. Soc.* **2013**, *135*, 10007.

(126) Giri, N.; Davidson, C. E.; Melaugh, G.; Del Popolo, M. G.; Jones, J. T. A.; Hasell, T.; Cooper, A. I.; Horton, P. N.; Hursthouse, M. B.; James, S. L. *Chem. Sci.* **2012**, *3*, 2153.

(127) Jiang, S.; Bacsa, J.; Wu, X.; Jones, J. T. A.; Dawson, R.; Trewin, A.; Adams, D. J.; Cooper, A. I. *Chem. Commun.***2011**, *47*, 8919.

(128) Jelfs, K. E.; Wu, X.; Schmidtmann, M.; Jones, J. T. A.; Warren, J. E.; Adams, D. J.; Cooper, A. I. *Angew. Chem. Int. Ed.* **2011**, *50*, 10653.

(129) Zhang, G.; Presly, O.; White, F.; Oppel, I. M.; Mastalerz, M. *Angew. Chem. Int. Ed.* **2014**, *53*, 1516.

(130) Klotzbach, S.; Beuerle, F. *Angew. Chem. Int. Ed.* **2015**, *54*, 10356.

(131) Mortreux, A.; Petit, F.; Blanchard, M. *J. Mol. Catal.* **1980**, *8*, 97.

(132) Mortreux, A.; Dy, N.; Blanchard, M. *J. Mol. Catal.* **1976**, *1*, 101.

(133) Mortreux, A.; Blanchard, M. *J. Chem. Soc., Chem. Commun.* **1974**, 786.

(134) Katz, T. J.; McGinnis, J. *J. Am. Chem. Soc.* **1975**, *97*, 1592.

(135) Schrock, R. R. *Acc. Chem. Res.* **1986**, *19*, 342.

(136) Pedersen, S. F.; Schrock, R. R.; Churchill, M. R.; Wasserman, H. J. *J. Am. Chem. Soc.* **1982**, *104*, 6808.

(137) Wengrovius, J. H.; Sancho, J.; Schrock, R. R. *J. Am. Chem. Soc.* **1981**, *103*, 3932.

(138) Churchill, M. R.; Ziller, J. W.; Freudenberger, J. H.; Schrock, R. R. *Organometallics* **1984**, *3*, 1554.

(139) Bai, W.; Wei, W.; Sung, H. H. Y.; Williams, I. D.; Lin, Z.; Jia, G. *Organometallics* **2018**, *37*, 559.

(140) Fürstner, A. *Angew. Chem. Int. Ed.* **2013**, *52*, 2794.

(141) von Kugelgen, S.; Sifri, R.; Bellone, D.; Fischer, F. R. *J. Am. Chem. Soc.* **2017**, *139*, 7577.

(142) von Kugelgen, S.; Bellone, D. E.; Cloke, R. R.; Perkins, W. S.; Fischer, F. R. *J. Am. Chem. Soc.* **2016**, *138*, 6234.

(143) Furstner, A. *Angew. Chem. Int. Ed.* **2013**, *52*, 2794.

(144) Tsai, Y.-C.; Diaconescu, P. L.; Cummins, C. C. *Organometallics* **2000**, *19*, 5260.

(145) Blackwell, J. M.; Figueroa, J. S.; Stephens, F. H.; Cummins, C. C. *Organometallics* **2003**, *22*, 3351.

(146) Zhang, W.; Kraft, S.; Moore, J. S. *J. Am. Chem. Soc.* **2004**, *126*, 329.

(147) Zhang, W.; Lu, Y.; Moore, J. S. In *Organic Syntheses*; John Wiley & Sons, Inc.: 2003.

(148) Zhang, W.; Kraft, S.; Moore, J. S. *Chem. Commun.* **2003**, 832.

(149) Fürstner, A.; Mathes, C.; Lehmann, C. W. *J. Am. Chem. Soc.* **1999**, *121*, 9453.

(150) Heppekausen, J.; Stade, R.; Kondoh, A.; Seidel, G.; Goddard, R.; Fürstner, A. *Chem. Eur. J.* **2012**, *18*, 10281.

(151) Heppekausen, J.; Stade, R.; Goddard, R.; Fürstner, A. *J. Am. Chem. Soc.* **2010**, *132*, 11045.

(152) Beeren, S. R.; Sanders, J. K. M. *Chem. Sci.* **2011**, *2*, 1560.

(153) Li, J.; Carnall, J. M. A.; Stuart, M. C. A.; Otto, S. *Angew. Chem. Int. Ed.* **2011**, *50*, 8384.

(154) Lee, S.; Yang, A.; Moneypenny, T. P.; Moore, J. S. *J. Am. Chem. Soc.* **2016**, *138*, 2182.

Chapter 2

Evidence for a Kinetic Bottleneck in Multitopic Alkyne Metathesis†

2.1 Introduction

Dynamic covalent chemistry (DCC)[1,2] has proven to be a powerful synthetic method to construct molecular architectures such as macrocycles,[3-5] cages,[6-11] and covalent organic frameworks.[12-14] DCC reactions proceed via thermodynamic control which allows for error correction and convergence towards thermodynamically-stable products. These reactions provide the ability to synthesize large, complex molecules in one step with high yields on gram scales.[1] Additionally, DCC reactions provide the ability to re-equilibrate the product distribution of a system by simply changing the reaction conditions.[1] As such, DCC has emerged as the most viable method to synthesize large, complex molecular architectures comprised solely of covalent bonds.

Implicit in this thermodynamically-controlled scenario, but not frequently investigated in the literature, is the fact that dynamic systems must necessarily explore a multitude of intermediate structures and molecular arrangements before locating an energy minimum and corresponding product distribution. Since DCC reactions involve the breaking and forming of strong covalent bonds (ca. 835 kJ/mol for −C≡C−), there arises significant kinetic considerations and difficulties

that must be overcome to achieve successful architecture formation. These difficulties are borne out of finite catalyst lifetimes, slower rates of reactions, and potential kinetic bottlenecks in comparison to coordination complexs.[1] Whereas kinetically labile metal-ligand coordination systems siphon through intermediates on the order of seconds,[15,16] DCC systems may take up to several days to reach equilibrium.[11,17-20] Consequently, the progress of equilibration may become impeded due to extended intermediate lifetimes which afford undesired structures including intractable mixtures and complex precipitates that halt the reaction completely.[7,11,21,22]

As it relates to the synthesis of covalent molecular cages via DCC, the typical synthetic approach relies on a heuristic method to design precursors. With this approach, researchers depend on the topicity, geometry, and directionality of precursors to propose a reasonable thermodynamically-stable structural outcome and expect this structure to be thermodynamically favored in the reaction conditions. While such an approach is tempting to use, especially with the success of its implementation in the field of coordination complexes,[23-25] it frequently fails to produce the desired structural outcome or yields no discernible products at all in DCC systems. Especially in complex, multitopic scenarios (greater than three reactive functional groups per precursor) where the number of possible intermediates greatly increases and kinetic factors may heavily intervene, this approach becomes unreliable. Thus, there is a need to determine reliable precursor design rules to alleviate kinetic burdens in multitopic DCC syntheses.

In this context, it is useful to frame the problem of reaching a desired product not just in terms of a single reaction pathway, but rather in terms of a reaction energy landscape, where each point on the landscape corresponds to a molecular entity with a specific internal free energy.[26] Thus, multitopic DCC equilibration is more accurately described as a process which progresses through an ensemble of various structural intermediates and reaction pathways en route toward the thermodynamic product distribution. Consequently, the systems that fail to reach a single discrete product suggest that the energy landscape governing the reaction is in either one of two categories: 1) the landscape is too flat, leading to an analogous "Levinthal's paradox" where there is insufficient time to reach the thermodynamic product, or 2) the landscape is too rough, leading to premature kinetic trapping at intermediate stages.[26] It is because of these scenarios that precursor design considerations must take into account not only the thermodynamics of products but also that the energy landscape provides pathways to these products on reasonable timescales. With these considerations in mind, there is a need for a deeper understanding of how the DCC energy

landscape depends on geometric attributes of precursors. Only when a dynamic system proceeds along a smooth energy landscape, or a landscape which does not allow intermediates to irreversibly fall into deep energy minima, will the thermodynamic product be achieved in appreciable yields. Accordingly, precursors must be designed with geometric attributes that direct product distribution along smooth energy landscapes.

Although many covalent organic cages have been prepared via DCC,[8,27] there are few reports on unsuccessful attempts from which much could be learned. Furthermore, researchers in this field generally only provide enthalpic arguments to support (or refute) their observations and fail to address kinetic or reaction pathway considerations. While there are no clear set of design principles to form molecular cages, the literature hints that subtle environmental effects or structural changes in precursor geometry result in the non-intuitive formation of cage products with unexpected architectures. For example, Warmuth and coworkers discovered a solvent dependent cage-forming system using imine condensation, where one precursor selectively formed an octahedron, a tetrahedron, or a square anti-prism depending on the solvent used in the reaction.[28] Cooper and co-workers developed a strategy to determine odd-even effects in the synthesis of imine cages where the products from the reactions with an even α,ω-alkanediamine carbon chain length afforded tetrahedral [4+6] cages and the products from the reactions with an odd chain length afforded [2+3] cage structures.[29] To support their experimental observations, they performed DFT calculations to determine relative structural energies of each cage and found that these calculations supported their odd-even rule hypothesis. Zhang and co-workers devised a study on altering the size of precursor units.[30] They designed multiple tritopic precursors with ca. 90º carbazole arms, varied the size of the central panel, and observed that the size of the building blocks plays a significant role in determining the resulting structural outcome. Precursors with smaller panels tended to form D_2h tetramers, while precursors with larger panels tended to form dimers. These results collectively indicate that multitopic DCC energy landscapes are complex and their product distributions are affected by various reaction parameters that are not always intuitive. Furthermore, these studies illustrate the widespread absence of any kinetic or reaction pathway considerations in the literature of this field.

To understand multitopic DCC landscapes more completely and probe the reaction pathway, we sought to perform systematic studies that experimentally discern design principles for tetrahedral organic cages synthesized via dynamic alkyne metathesis (AM).[31] Since this

example forms a tetrahedral cage product in nearly quantitative yields, we supposed it would be a key system to investigate the effects of minor adjustments in precursor geometry on the DCC energy landscape. Taking inspiration from work by Fujita,[24,32,33] we hypothesized that precursor bite angle (or the angle between phenylene-containing arms) governs the dynamic energy landscape and resulting product distribution in multitopic AM.

We tested this hypothesis by synthesizing a series of analogous tritopic precursors with different bite angles—one with a tight bite angle, one with a medium bite angle, and one with a bite angle that perfectly matches the ideal angle of a tetrahedron (60°)—to deliberately alter the DCC energy landscape. Subjecting each precursor to identical AM conditions and characterizing the resulting mixtures demonstrates that precursors with ideal bite angles are not the most efficient at forming a tetrahedral molecular cage. Monitoring reaction progress via gel permeation chromatography (GPC) provides evidence that slight changes in bite angle induce restructuring of the dynamic energy landscape. Our results demonstrate that even minor adjustments in precursor geometry significantly bias the DCC energy landscape. DCC cage formation is thus reminiscent of other reactive systems that venture through multiple intermediates, some of which are on a pathway to the target, while others have strayed from a pathway directed to the target.[24,33]

2.2 Precursor Design and Synthesis

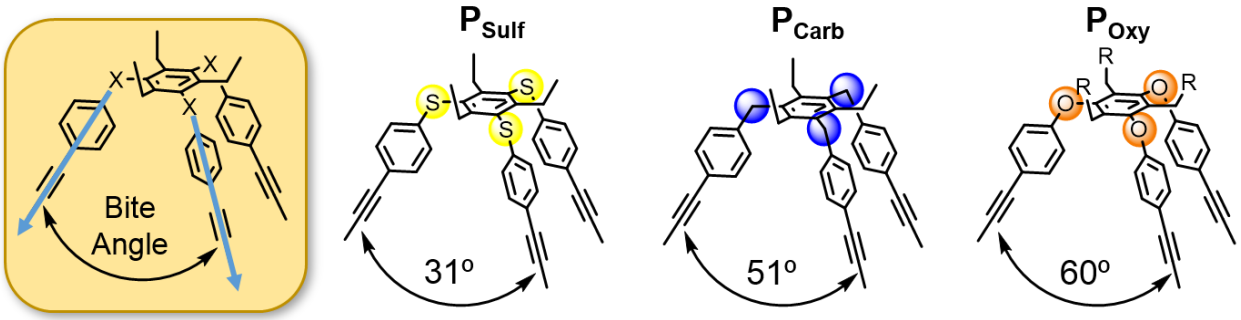

***Figure 2.1**: A series of analogous tritopic precursors synthesized in this study. The bite angle is defined as the angle between phenylene-containing arms and is determined via X-ray crystallography. R = 4-tert-butylbenzene.*

In this study, precursor bite angle is defined as the angle between phenylene containing arms as depicted in Figure 2.1. Bite angles were calculated using coordinates from single crystal XRD structures (Figure 2.2). Two atoms on each precursor arm were selected and defined as points

in three-dimensional Euclidean space. Vectors were defined from the coordinates of these points and the angle between vectors was calculated with the equation shown in Figure 2.3. The final bite angle for each precursor was calculated as the average of three angles.

Precursors synthesized in this study were designed to have similar geometry and only differ in bite angle. To alter precursor bite angle, we chose to change the atoms at each of the three benzylic positions in the precursor such that the $C_{Ar}{-}X_{Benzylic}{-}C_{Ar}$ bond would either increase or decrease relative to P_{Carb}. It was hypothesized that the $C_{Ar}{-}X_{Benzylic}{-}C_{Ar}$ bond angle is decreased by replacing $–CH_2–$ with −S− and increased by replacing with −O−. Using VSEPR, one can use an electronegativity argument to understand trends in bite angle as a result of changing the $C_{Ar}{-}X_{Benzylic}{-}C_{Ar}$ bond. In situations where the outer atoms remain the same (C_{Ar}) and the central atom is changed ($–CH_2–$, −S−, or −O−), the electronegativity of the central atom determines the angle of this bond. Changing the central atom to sulfur (electronegativity of 2.58) introduces lone pairs and lone pair−lone pair repulsions which have the net effect of decreasing the bond angle. In the case of oxygen, which has a much higher electronegativity (3.44), it exerts a stronger pull on the electron lone pairs toward itself, thus increasing bonding pair−bonding pair repulsions while also decreasing lone pair−lone pair repulsions. The net effect is an increase in the bond angle. Examples of this effect has also been shown in the literature for both sulfur and oxygen.[34,35]

The original precursor, P_{Carb}, was synthesized according to the previous method.[31] The precursor representing a tight bite angle, P_{Sulf}, was synthesized in four steps as shown in Scheme 2.1. First, 1,3,5-triethylbenzene was exhaustively brominated at the central benzene core using bromine catalyzed with iron powder to obtain **1** in 98 % yield.[36] Then, **1** was reacted with sodium thiophenolate in 1,3-dimethyl-2-imidazolidinone at 140 ºC to afford **2** in 72 % yield. Bromination of each phenyl ring at the para-position was accomplished using N-bromosuccinimide in a 2:1 (v/v) mixture of dichloromethane and acetonitrile to afford **3** in 74 % yield. Last, Kumada coupling of **3** with propynylmagnesium bromide using [1,1'-Bis(diphenylphosphino)ferrocene]dichloropalladium (II) as the catalyst afforded P_{Sulf} in 90 % yield.

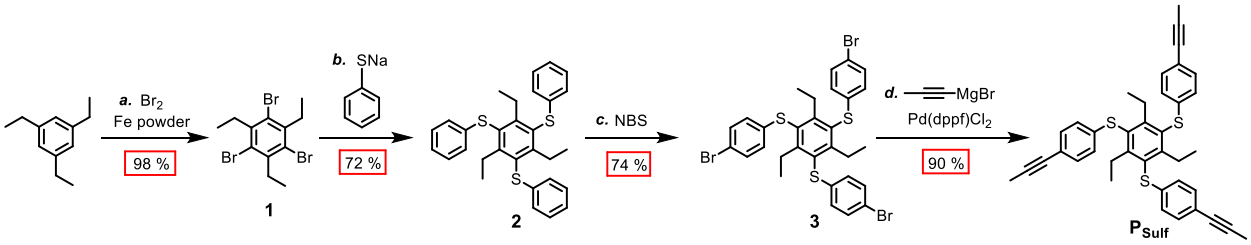

***Scheme 2.1**: Synthesis of P_{Sulf}. Reagents and conditions: (a) bromine (5 equiv), Fe powder (0.3 equiv), 10 min, rt, 98 %; (b) sodium thiophenolate (7 equiv), DMI, 140 ºC, 3 d, 72 %; (c) NBS (3.3 equiv), DCM/MeCN 2:1 (v/v), 0 ºC, 15 min then rt, 2 d, 74 %; (d) propynyl magnesium bromide (5 equiv), $Pd(dppf)Cl_2$ (0.06 equiv), THF, 65 ºC, 2 d, 90 %. DMI = 1,3-dimethyl-2-imidazolidinone, NBS = N-bromosuccinimide.*

The precursor representing a wide bite angle, P_{Oxy}, was synthesized in good yields from eight synthetic steps as shown in Scheme 2.2. First, 1,3,5-trimethoxybenzene was bromomethylated using paraformaldehyde and HBr in acetic acid to afford **4** in 38 % yield after crystallization.[37] A Grignard reaction using 4-tertbutylphenylmagnesium bromide afforded **5** in 70 % yield. Demethylation of **5** using boron tribromide in dichloromethane afforded **6** in near quantitative yields. Then, **6** was reacted with 4-fluoro-1-nitrobenzene and cesium carbonate in a nucleophilic aromatic substitution reaction affording **7** in 84 % yield. The nitro groups were hydrogenated using palladium/carbon (0.10 mass equiv) and hydrogen to afford **8** in near quantitative yields. Intermediate **8** was transformed to the corresponding tris(1-aryl-3,3-dialkyltriazene), **9**, in 93 % yield by first forming a tris(diazonium) salt *in situ* and protecting with pyrrolidine under basic conditions. Iodine-promoted transformation of **9** to the corresponding iodinated product, **10**, was performed using diiodomethane in a 90 % yield.[38] Lastly, Sonogashira coupling of propyne and **10** was performed using copper (I) iodide, bis(triphenylphosphine)palladium (II) dichloride, and trimethylamine to afford P_{Oxy} in 77 % yield.

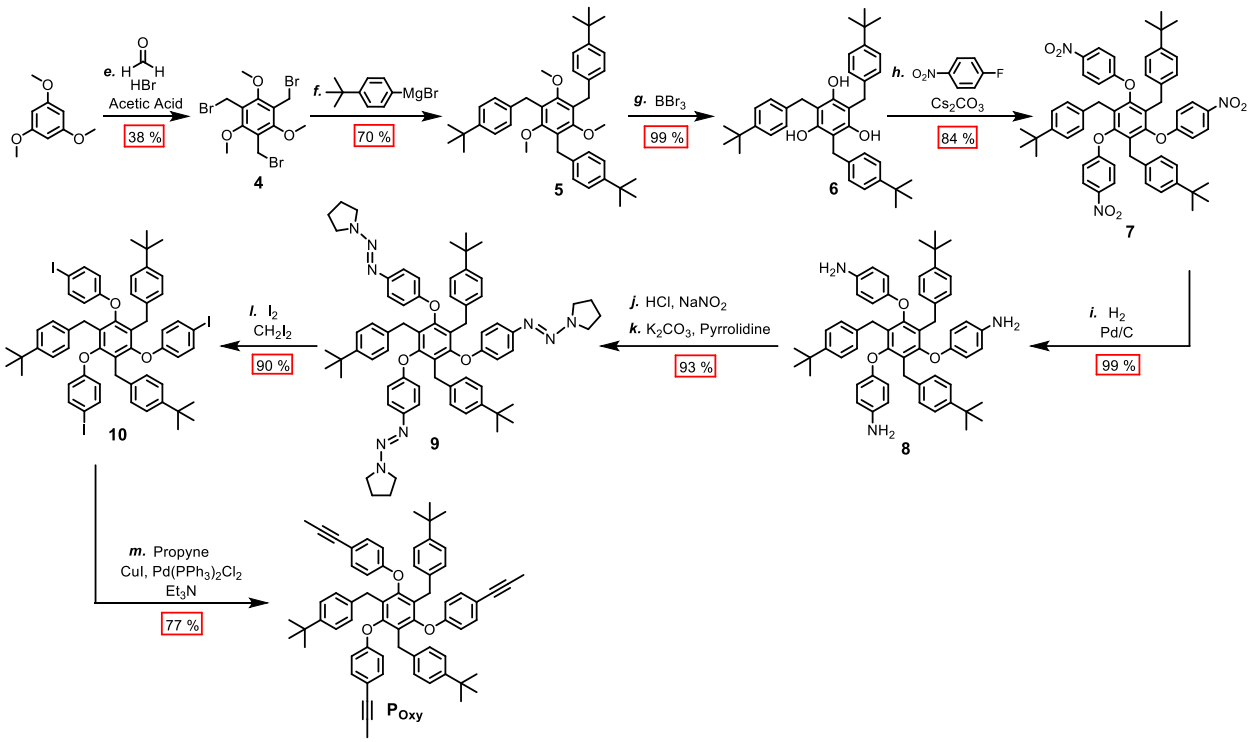

Scheme 2.2: *Synthesis of P_{Oxy}. Reagents and conditions: (e) Paraformaldehyde (9 equiv), HBr in acetic acid (9.4 equiv), 85 ºC, 38 %; (f) 1-bromo-4-tert-butylbenzene (5 equiv), Mg (10 equiv), benzene, 100 ºC, 16 hr, 70 %; (g) BBr_3 (4.3 equiv), DCM, 0 ºC → rt, 14 hr, 99 %; (h) 1-fluoro-4-nitrobenzene (5 equiv), Cs_2CO_3 (5 equiv), DMF, 90 ºC, 3 hr, 84 %; (i) Pd/C (0.10 mass equiv), hydrogen atmosphere, EtOAc, rt, 24 hr, 99 %; (j) HCl (12 equiv), $NaNO_2$ (4.5 equiv), MeCN/H_2O 2:1 (v/v), 0 ºC, 30 mins; (k) K_2CO_3 (15.6 equiv), pyrrolidine (7.5 equiv), MeCN/H_2O 1:1 (v/v), 0 ºC → rt, 1 hr, 93 % over two steps; (l) iodine (3.1 equiv), diiodomethane, 80 ºC, 4 hr, 90 %; (m) propyne atmosphere, CuI (0.1 equiv), $Pd(PPh_3)_2Cl_2$ (0.08 equiv), Et_3N/THF 5:1 (v/v), rt, 12 hr, 77 %. BBr_3 = boron tribromide.*

2.3 Bite Angle Determination

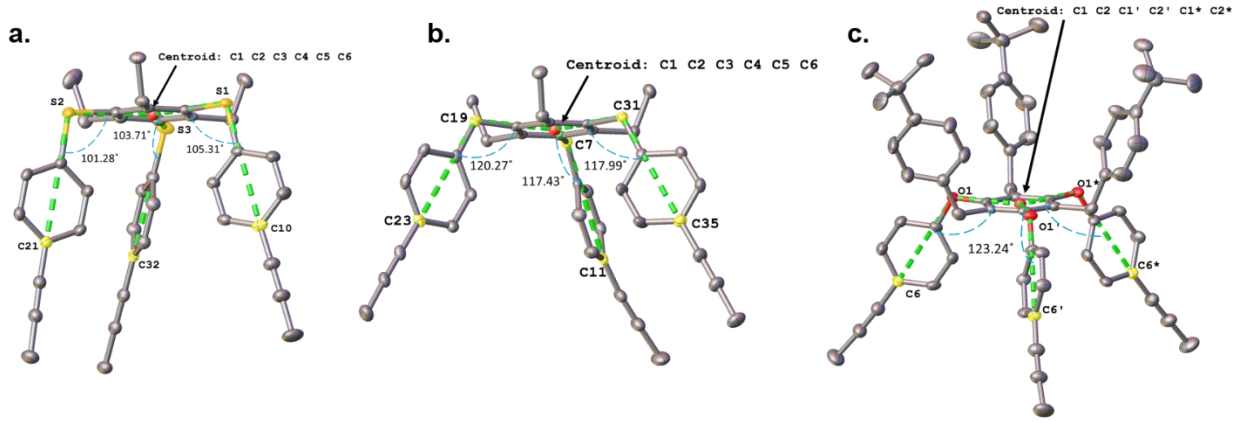

***Figure 2.2**: Crystal structures of (a) P_{Sulf}, (b) P_{Carb}, and (c) P_{Oxy}. Green dotted lines represent vectors drawn from respective labeled atoms. Centroids were calculated from atoms of the central benzene ring. Bond angles are labeled and calculated using the centroid and the C_{Ar} atom in each structure (i.e. from centroid to C_{21}, C_{32}, or C_{10} in P_{Sulf}).*

In order to accurately determine the bite angle of each precursor, single crystal X-ray diffraction analysis was used. Single crystal structures of each precursor are shown in Figure 2.2. Single crystals of P_{Sulf} were grown from slow evaporation of a 1:1 mixture of dichloromethane and methanol and crystallized in the monoclinic space group $P2_1/n$. Intensity data were collected on a Bruker D8 Venture equipped with a four-circle kappa diffractometer and Photon 100 detector. An Iμs microfocus Mo (λ = 0.71073 Å) source with a multilayer mirror monochromator provided the incident beam. The sample was mounted on a 0.3 mm loop with the minimal amount of Paratone-N oil. Data was collected as a series of φ and/ or ω scans. Data was collected at 100K in a cold stream of $N_{2(g)}$. The X-ray crystal structure exhibits an alternating up-down orientation of the central hexasubstituted benzene ring. The angle between benzylic edges and the central benzene moiety (using a centroid) was found to be 103.4º on average.

Single crystals of $\mathbf{P_{Carb}}$ were grown by slow diffusion of methanol into a solution of ethyl acetate and crystallized in the monoclinic space group $P2_1/n$. Intensity data were collected on a Bruker D8 Venture equipped with a four-circle kappa diffractometer and Photon 100 detector. An Iμs microfocus Mo (λ = 0.71073 Å) source with a multilayer mirror monochromator provided the incident beam. The sample was mounted on a 0.3mm loop with the minimal amount of Paratone-N oil. Data was collected as a series of φ and/ or ω scans. Data was collected at 100K in a cold stream of $N_{2(g)}$.The crystal structure exhibits the expected alternating up-down orientation of

hexasubstituted benzenes. The X-ray crystal structure shows that the angle between the benzylic edges and the central benzene moiety was 118.6º on average.

Lastly, single crystals of **P_{Oxy}** grew by slow diffusion of methanol into a solution of dichloromethane and crystallized in the hexagonal space group P-3c1. Intensity data were collected on a Bruker D8 Venture equipped with a four-circle kappa diffractometer and Photon 100 detector. An Iμs microfocus Mo (λ = 0.71073 Å) source with a multilayer mirror monochromator provided the incident beam. The sample was mounted on a 0.3mm loop with the minimal amount of Paratone-N oil. Data was collected as a series of φ and/ or ω scans. Data was collected at 100K in a cold stream of $N_{2(g)}$. This structure also exhibits the expected alternating up-down configuration about the center hexasubstituted benzene. The angle between the benzylic edges and the central benzene moiety was found to be 123.2º on average.

Bite angles were calculated using coordinates from single crystal XRD structures. Two atoms on each precursor arm were selected (as indicated with red circles in Figure 2.3) and defined as points in three-dimensional Euclidean space. Vectors were defined from the coordinates of these points. The angle between vectors was calculated with the equation shown in Figure 2.3. The final bite angle for each precursor was calculated as the average of three angles. In this fashion, the bite angles for P_{Sulf}, P_{Carb}, and P_{Oxy} were determined to be 31º, 51º, and 60º, respectively. It is important to note that with a bite of 60º, P_{Oxy} represents the precursor with a bite angle that matches the ideal angle for a tetrahedron.

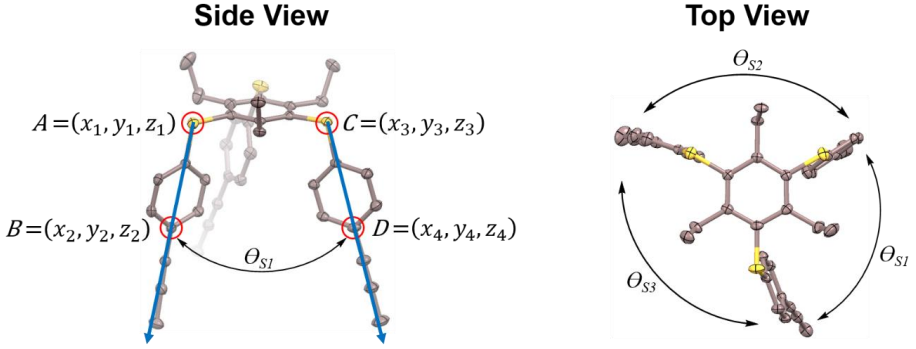

$$\overrightarrow{AB} = \vec{V}_1 = \langle x_2 - x_1, y_2 - y_1, z_2 - z_1 \rangle$$
$$\overrightarrow{CD} = \vec{V}_2 = \langle x_4 - x_3, y_4 - y_3, z_4 - z_3 \rangle$$

$$\theta_{S1} = arccosine \frac{\vec{V}_1 \cdot \vec{V}_2}{\|\vec{V}_1\| \cdot \|\vec{V}_2\|} \qquad Bite\ Angle = \frac{1}{3}(\theta_{S1} + \theta_{S2} + \theta_{S3})$$

***Figure 2.3**: Bite angle calculation for P_{Sulf}.*

2.4 Precursor Metathesis Experiments

To test the original hypothesis that precursor bite angle controls the product distribution in multitopic alkyne metathesis, single precursor metathesis experiments were performed with each precursor being subjected to identical reaction conditions. Initial AM experiments were performed in an argon-filled glovebox at 70 ºC with 10 mM precursor concentration in 1,2,4-trichlorobenzene (TCB) for 12 hours using a molybdenum catalyst ([Mo], 5 mol %), triphenylsilanol ligand (30 mol %), and molecular sieves (5 Å, 800 mg/mmol of propynyl groups) to sequester the 2-butyne byproduct. After 12 hours, the reaction vial was removed from the glovebox and the vial was opened to air immediately. The reaction was filtered to remove the molecular sieves, the reaction mixture was collected, and then methanol was added to precipitate the product mixture. Reaction mixtures were characterized by NMR, MALDI-MS, and GPC.

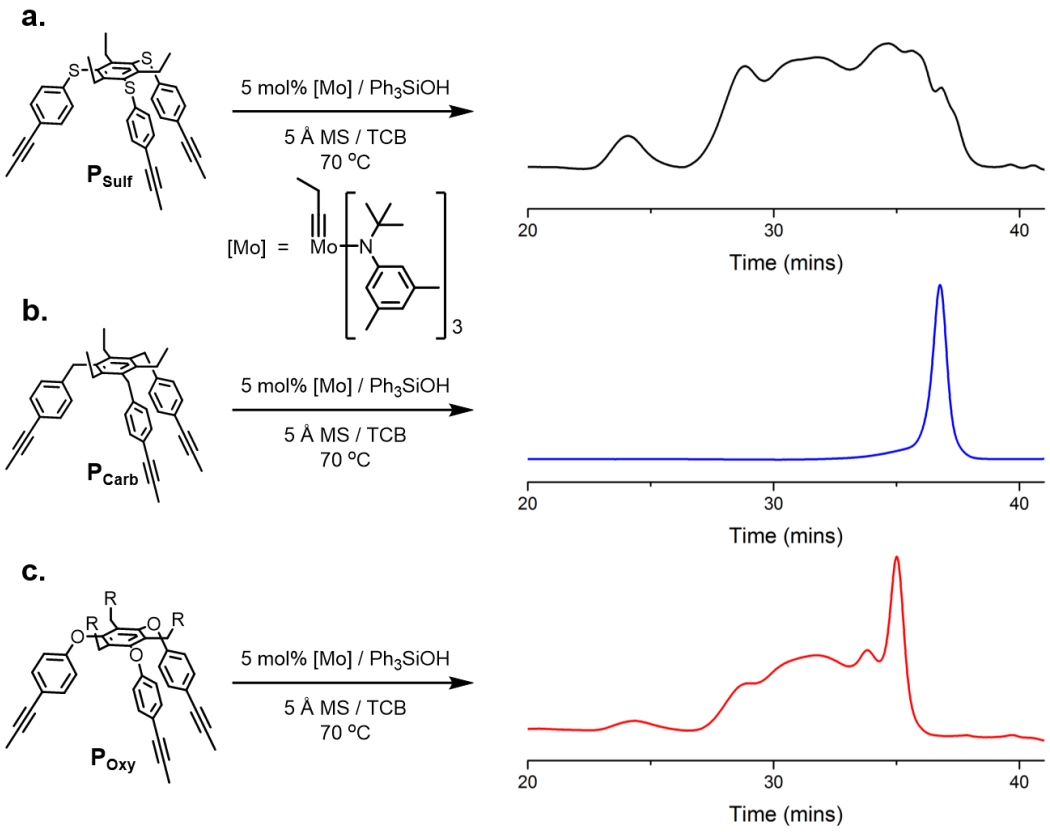

***Figure 2.4**: GPC chromatograms of the product distributions afforded after AM of (a) **P_{Sulf}**, (b) **P_{Carb}**, and (c) **P_{Oxy}** at 70 ºC for 12 hours.*

AM of **P_{Sulf}** affords a product distribution exhibiting a mixture of ill-defined oligomers, as shown by the GPC trace (Figure 2.4). The ^{1}H NMR spectrum of this mixture exhibits broad

resonances, typical of oligomerization (Figure 2.56). Subjecting $\mathbf{P_{Carb}}$ to AM at 70 ºC for 12 hours affords a very narrow product distribution, and forms exclusively the desired tetrahedral cage. The GPC trace exhibits one sharp peak with a narrow PDI of 1.02. The ^{1}H NMR exhibits sharp peaks, indicative of a highly symmetric, discrete product. Characterization by MALDI-MS and single crystal XRD analysis confirms the formation of a tetrahedral cage in near quantitative yield. Repeating this experiment at room temperature for 12 hours affords an identical product distribution with similar yield. Subjecting $\mathbf{P_{Oxy}}$ to AM at 70 ºC affords a product distribution that exhibits signs of both oligomers and a discrete structure as shown by the GPC trace in Figure 2.4.

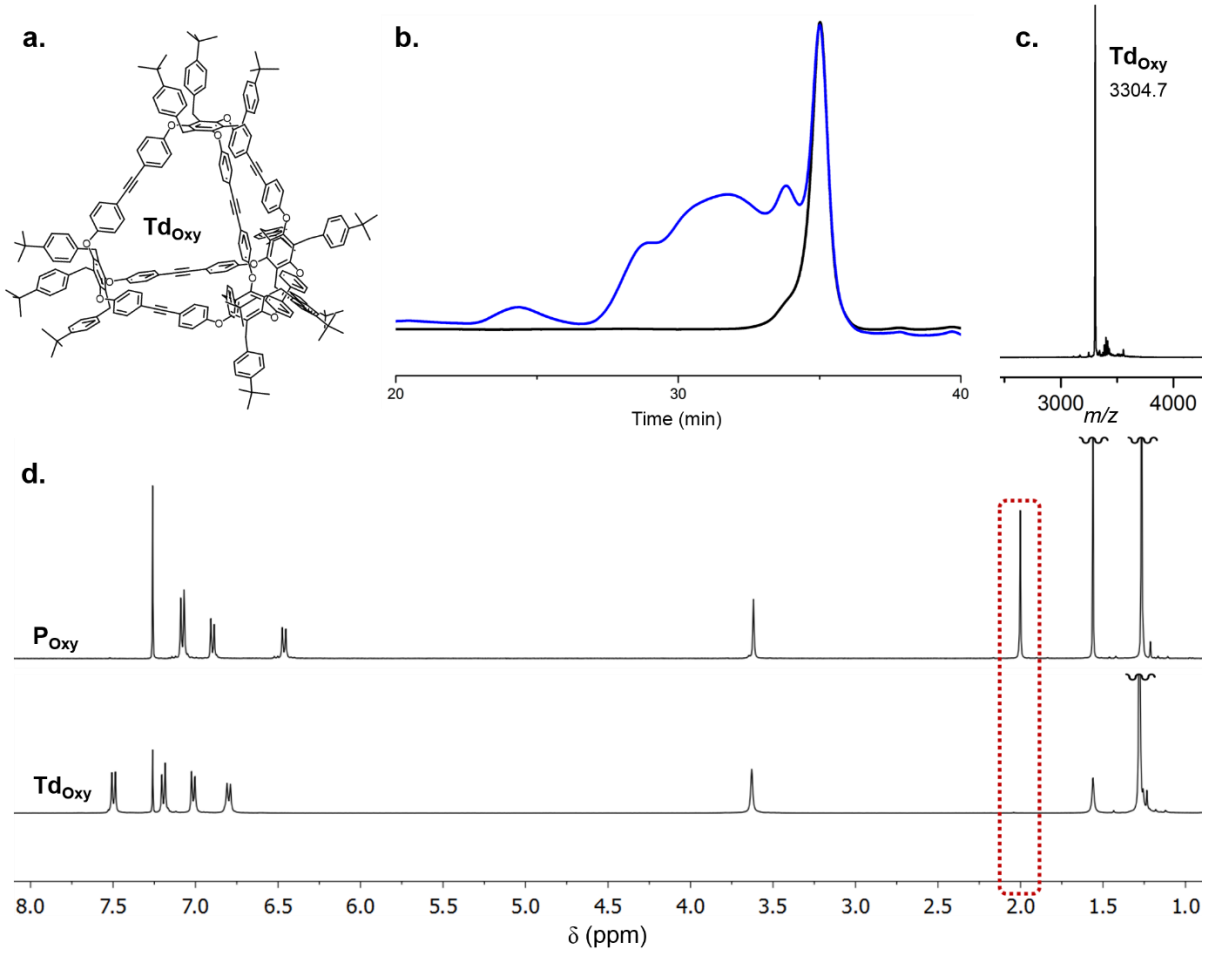

Figure 2.5*: Purification of the product distribution afforded from subjecting* $\boldsymbol{P_{Oxy}}$ *to AM at 70 ºC. (a) Structure of* $\boldsymbol{Td_{Oxy}}$*. (b) GPC traces before (blue) and after (black) purification. (c) MALDI-MS spectrum of purified product using a DCTB matrix. (d)* ^{1}*H NMR (400 MHz, d-chloroform) comparison of* $\boldsymbol{P_{Oxy}}$ *and* $\boldsymbol{Td_{Oxy}}$*. The red dotted box corresponds to the propynyl proton resonance.*

The ^{1}H NMR spectrum of this mixture exhibits sharp peaks indicative of a highly symmetric molecule as well as broad resonances at the baseline due to the presence of oligomers (Figure 2.57). Flash chromatography of this mixture affords a new cage, **Td$_{Oxy}$**, in 23% yield (Figure 2.5). Characterization of the resulting product by NMR and MALDI-MS reveals a highly symmetric compound with a mass corresponding to a tetramer, confirming the formation of **Td$_{Oxy}$**.

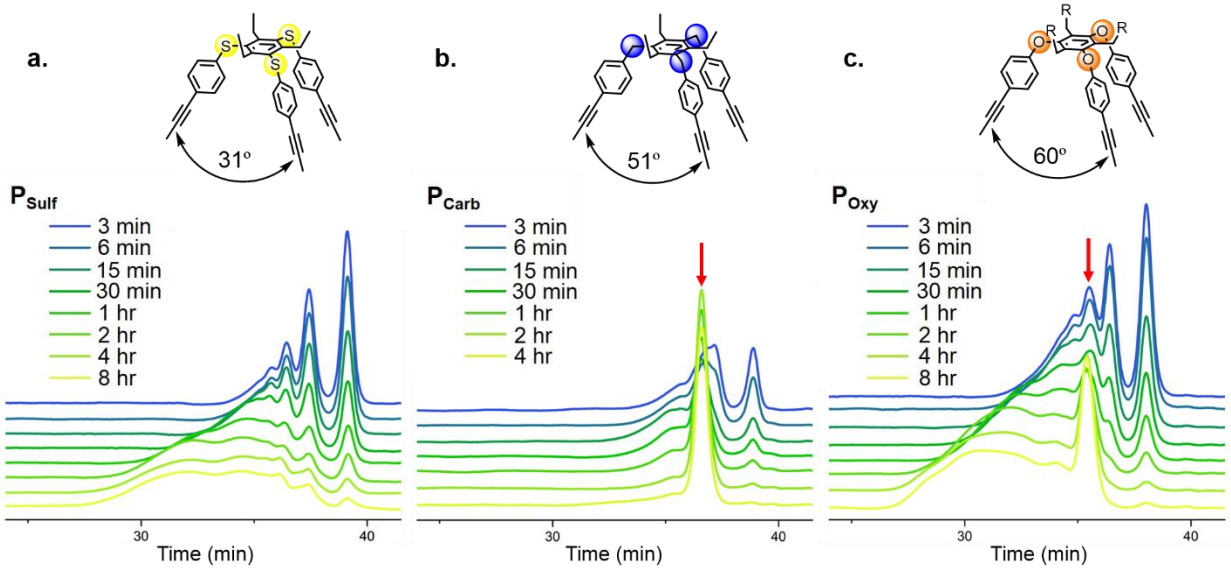

***Figure 2.6**: GPC chromatograms taken after various time points of AM of (a) **P$_{Sulf}$**, (b) **P$_{Carb}$**, and (c) **P$_{Oxy}$** at room temperature with 5 mol % [Mo] catalyst. Red arrows denote cage products.*

To investigate how each system behaves over time, the reaction progress was monitored by GPC over the course of eight hours. Each precursor was subjected to alkyne metathesis in chloroform at room temperature using a molybdenum catalyst ([Mo], 5 mol %), triphenylsilanol ligand (30 mol %), and molecular sieves (5 Å, 800 mg/mmol of propynyl groups) and aliquots of the reactions were taken at various time points. The aliquots were then quenched with hydrated chloroform and the product mixtures were characterized via GPC. The results obtained from these experiments are shown in Figure 2.6. Room temperature reaction conditions were chosen to better sample early reaction progress. Chloroform was used as the solvent to allow direct injection into the GPC. There were negligible solvent effects on product distribution during AM of these precursors within these reaction conditions (see Figure 2.20, Experimental).

In the case of **P$_{Sulf}$**, the system progresses through a series of intermediates within the first three minutes of the reaction as shown in Figure 2.6a. As the reaction proceeds, however, the product distribution broadens and enters a regime where formed intermediates are unable to locate

a single thermodynamically-stable product. As such, the reaction results in a broad product distribution of ill-defined oligomers within eight hours of reaction time. In the case of **P$_{Carb}$** (Figure 2.6b), initially this precursor forms smaller and larger oligomers, similar to **P$_{Sulf}$**. As the reaction progresses, however, all of the oligomeric intermediates funnel toward **Td$_{Carb}$**, until the entirety of the dynamic mixture converges within 4 hours. The **P$_{Oxy}$** system starts in a similar fashion as the previous two cases, initially forming a mixture of oligomers (Figure 2.6c). Some intermediates are able to form **Td$_{Oxy}$** and the concentration of cage increases steadily over time. Other intermediates, however, enter a regime where they continuously grow larger and these intermediates are unable to locate the cage product within eight hours.

The results from these experiments provide evidence to validate the hypothesis that precursor bite angle governs dynamic covalent energy landscapes. As shown by **P$_{Sulf}$**, it was observed that tightening the bite angle directs intermediates to off-target pathways. The result is a broad, ill-defined product distribution with undetectable cage formation under the reaction conditions and allotted reaction time. Precursor **P$_{Sulf}$** thus has a bite angle that is simultaneously too tight to form a tetrahedron and too wide to form a closed dimer under these conditions. Thus, the dynamic system drifts into an oligomeric regime of the energy landscape.

The results from **P$_{Oxy}$** are counterintuitive to heuristic design principles based on the geometrically ideal bite angle. Although the bite angle of **P$_{Oxy}$** is ideal for a tetrahedron, the early-time product distribution indicates that the system initially ventures off the target pathway. Additionally, while some intermediates are able to form **Td$_{Oxy}$**, the majority of the dynamic system continues to progress along off-target pathways within eight hours. Hence, precursor **P$_{Oxy}$** provides an example where the bite angle still allows the system to converge toward a discrete cage product, but the rate of convergence is decreased relative to **P$_{Carb}$**. If the reaction is allowed to proceed for 24 hours, however, the product distribution ultimately funnels toward **Td$_{Oxy}$** in near-quantitative yields (See Figure 2.19).

Finally, precursors with a slightly tighter bite angle than the mathematically ideal angle for a tetrahedron provide the most direct convergence to the cage. While the bite angle of **P$_{Carb}$** is about 9^{o} tighter than the optimum for a tetrahedron, the dynamic mixture achieves nearly quantitative yields of the cage within four hours at room temperature. We deduce that the dynamic energy landscape in this case has a "funneled" surface, allowing the intermediates to siphon toward the most thermodynamically-stable product while avoiding other off-target pathways.

2.5 Precursor Mixing Experiments

Although $\mathbf{P_{Sulf}}$ was not able to form detectable quantities of cage during AM, we hypothesized it is possible to incorporate it into a cage structure using a mixture of the other precursors. Additionally, these mixing experiments are expected to provide knowledge of a lower limit bite angle threshold for cage formation, which would prove very helpful for future experiments testing novel precursor geometries. To test this hypothesis, we performed mixing experiments between the various precursors. Precursor mixing experiments were performed between $\mathbf{P_{Sulf}}$ and $\mathbf{P_{Carb}}$, $\mathbf{P_{Sulf}}$ and $\mathbf{P_{Oxy}}$, $\mathbf{P_{Carb}}$ and $\mathbf{P_{Oxy}}$, and between all three in one pot. The experiments were performed with 10 mM concentration of precursors (total), using 5 mol % [Mo], 30 mol % Ph_3SiOH, and 5 Å MS in TCB for 12 hours at room temperature. The GPC traces from the mixtures afforded by these experiments are shown in Figure 2.7 (cage composition is denoted in molar ratios by [$\mathbf{P_{Sulf}:P_{Carb}:P_{Oxy}}$]).

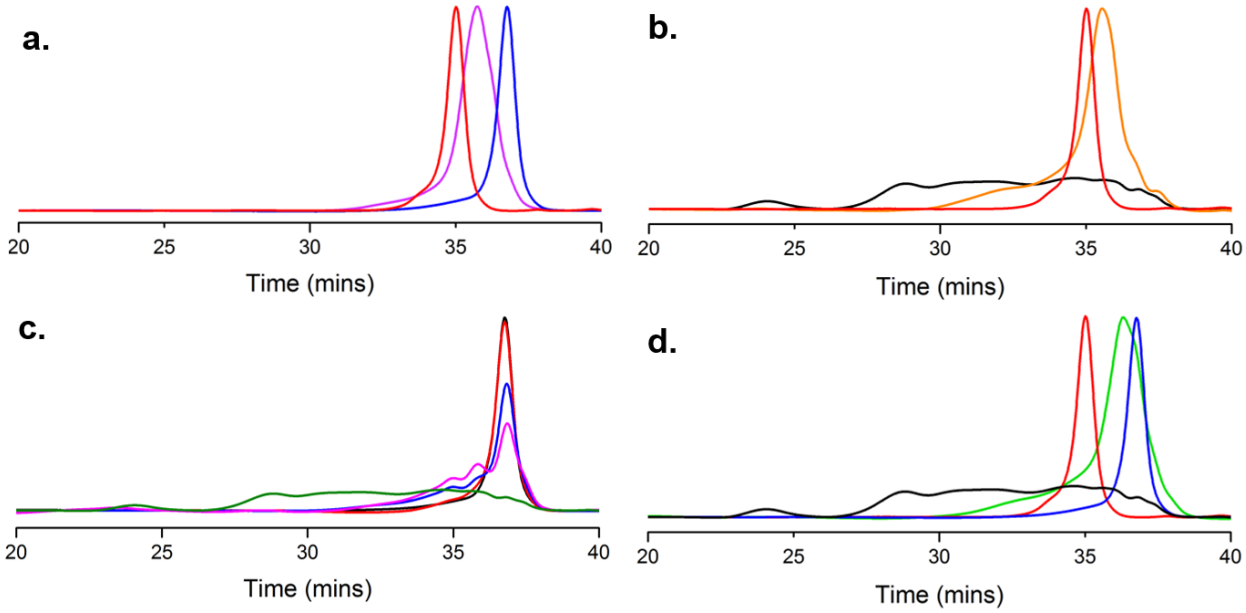

***Figure 2.7**: GPC chromatograms of the product distribution afforded from mixing experiments. (a) GPC traces of $\mathbf{Td_{Carb}}$ (blue), $\mathbf{Td_{Oxy}}$ (red), and the 1:1 mixture of $\mathbf{P_{Carb}}$ and $\mathbf{P_{Oxy}}$ (pink). (b) GPC traces of $\mathbf{Td_{Oxy}}$ (red), the product distribution from AM of $\mathbf{P_{Sulf}}$ (black), and the 1:1 mixture of $\mathbf{P_{Oxy}}$ and $\mathbf{P_{Sulf}}$ (orange). (c) normalized GPC traces of $\mathbf{Td_{Carb}}$ (black), the 1:3 mixture (pink), the 1:1 mixture (blue), the 3:1 mixture (red) of $\mathbf{P_{Carb}}$ and $\mathbf{P_{Sulf}}$, respectively, and the product distribution of $\mathbf{P_{Sulf}}$ (green). (d) GPC traces of $\mathbf{Td_{Carb}}$ (blue), $\mathbf{Td_{Oxy}}$ (red), the product distribution after AM of $\mathbf{P_{Sulf}}$ (black), and the 1:1:1 mixture of $\mathbf{P_{Sulf}}$, $\mathbf{P_{Carb}}$, and $\mathbf{P_{Oxy}}$ (green).*

We first investigated the product distribution formed from mixing $\mathbf{P_{Carb}}$ and $\mathbf{P_{Oxy}}$. Subjecting a 1:1 by mole mixture of $\mathbf{P_{Carb}}$ and $\mathbf{P_{Oxy}}$ to AM afforded a well-behaved product distribution containing a molecular weight between that of $\mathbf{Td_{Carb}}$ and $\mathbf{Td_{Oxy}}$ (Figure 2.7a). Characterization of this mixture by ^{1}H NMR indicated that a distribution of mixed cage products was obtained (Figures 2.61 and 2.63). MALDI-MS analysis confirmed the formation of three mixed cage species [0:3:1], [0:2:2], [0:1:3] (Figure 2.22). A similar result was obtained when precursors $\mathbf{P_{Oxy}}$ and $\mathbf{P_{Sulf}}$ were mixed in a 1:1 molar ratio (Figure 2.7b). Characterization by MALDI-MS confirmed the formation of $\mathbf{Td_{Oxy}}$ ([0:0:4]) and the mixed [1:0:3], [2:0:2], and [3:0:1] cages (Figure 2.21). Additionally, precursors $\mathbf{P_{Carb}}$ and $\mathbf{P_{Sulf}}$ were mixed in various molar ratios (1:3, 2:2, and 3:1, respectively) and the product distributions were characterized (Figure 2.7c). Characterization of each mixture via MALDI-MS confirmed the formation of the [3:1:0], [2:2:0], and [1:3:0] mixed cages (Figures 2.23 and 2.24). As a final experiment, all three precursors were mixed in a single reaction. As shown by the GPC trace in Figure 2.7d, a broad product distribution was obtained. Characterization by MALDI-MS confirmed the formation of various cages, including the [2:1:1], [1:2:1], and [1:1:2] mixed cages (Figures 2.25 and 2.26). All combination of cages were detected from mixing experiments using MALDI-MS except for the cage comprised solely of $\mathbf{P_{Sulf}}$ precursors.

The obtained results allow us to deduce characteristics of this dynamic system. Although bite angle deviations greatly affect the DCC energy landscape, they do not favor self-sorting of the various multitopic components. Secondly, precursor $\mathbf{P_{Sulf}}$ is incorporated into cage architectures provided the other precursors in the architecture can accommodate the angle strain. In each mixing experiment, $\mathbf{P_{Sulf}}$ was successfully incorporated into a molecular cage architecture.

2.6 DFT Calculations

To further understand the process of cage formation, we performed DFT calculations to determine the relative structural enthalpies (ΔE) between the final open tetramer (OT) intermediate (one edge open) and the tetrahedral cage (Td) for each precursor system. In our calculations, the OT intermediate contained two methyl-capped acetylene moieties and the Td cages were all minimized with one 2-butyne molecule as the side product. The DFT calculations were performed in VASP using the PBE functional, with 2000 minimization steps.

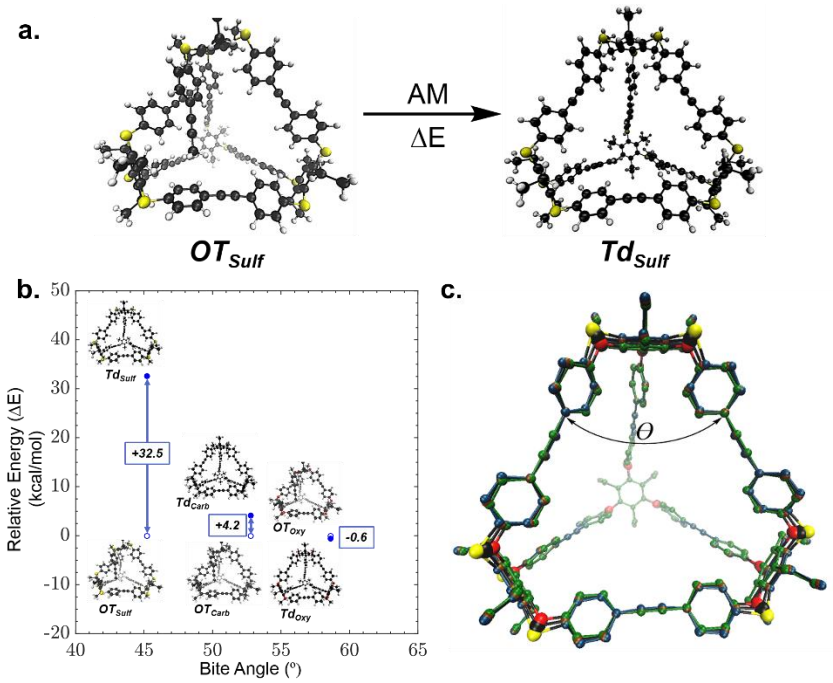

Figure 2.8*: Results from DFT calculations. (a) Representative "cage closing" metathesis reaction starting from the open tetramer of* $\mathbf{P_{Sulf}}$ *(*$\mathbf{OT_{Sulf}}$*) to form* $\mathbf{Td_{Sulf}}$*. (b) Plot of calculated relative structural energies,* ΔE *(relative to the open tetramer) vs. bite angle (calculated from DFT) of each system. All values in kcal/mol. (c) Overlay of the energy minimized structures of* $\mathbf{Td_{Sulf}}$ *(blue),* $\mathbf{Td_{Carb}}$ *(orange), and* $\mathbf{Td_{Oxy}}$ *(green). Hydrogen atoms are removed for clarity. From these structures, the bite angles (*Θ*) were calculated as 45.1°, 52.8°, and 58.5° for* $\mathbf{Td_{Sulf}}$*,* $\mathbf{Td_{Carb}}$*, and* $\mathbf{Td_{Oxy}}$ *respectively. DFT, PBE functional, 2000 minimizations steps.*

The results from these calculations, as shown in Figure 2.8, allow rationalization of the experimentally observed product distributions for each system. In the $\mathbf{P_{Sulf}}$ system, the corresponding closed cage, $\mathbf{Td_{Sulf}}$, is 32.5 kcal/mol higher in enthalpy than the open tetramer ($\mathbf{OT_{Sulf}}$). Thus, the final "cage-closing" step in the $\mathbf{P_{Sulf}}$ system results in significant structural strain energy for $\mathbf{Td_{Sulf}}$ and is not enthalpically favored. To further illustrate this point, the average bite angle in the calculated structure for $\mathbf{Td_{Sulf}}$ of 45.1° (Figure 2.8c) is ca. 14° larger than the bite angle calculated from the crystal structure of $\mathbf{P_{Sulf}}$, indicating that the precursor must widen its bite angle significantly for successful Td cage formation. In the $\mathbf{P_{Carb}}$ system, the tetrahedral cage ($\mathbf{Td_{Carb}}$) is only 4.2 kcal/mol higher in enthalpy than the corresponding open tetramer ($\mathbf{OT_{Carb}}$), indicating that the cage-closing step results in minor cage strain. This strain energy is evident in the crystal structure of $\mathbf{Td_{Carb}}$,[26] where the acetylene moieties are slightly bent inwards toward the

center ca. 17º from a linear geometry. Lastly, in the **P$_{Oxy}$** system, the tetrahedral cage (**Td$_{Oxy}$**) is 0.6 kcal/mol *lower* in enthalpy than the corresponding open tetramer (**OT$_{Oxy}$**). These results are not surprising, as this precursor was designed to have a bite angle that closely resembled the ideal angle for a tetrahedral cage.

Our calculations support the argument that enthalpic considerations alone are insufficient to describe the experimental observations from DCC reactions. Comparison between the **P$_{Carb}$** system and the **P$_{Oxy}$** system demonstrates this point: although **Td$_{Oxy}$** is more enthalpically favored to form than **Td$_{Carb}$** (with respect to their corresponding OT intermediates), our experimental results show that **Td$_{Carb}$** forms via a more efficient pathway. We hypothesize that this discrepancy is reconciled by kinetic considerations in that there are significant differences in the relative energy barriers for formation of the last metallacyclobutadiene intermediate in the final "cage-closing" step. If correct, this final step becomes a kinetic bottleneck on the DCC energy landscape and this putative bottleneck is governed by the precursor bite angle. Further molecular modeling analysis will be performed in future studies to test this hypothesis.

2.7 Conclusions

In conclusion, a systematic study investigating the effects of precursor bite angle on the DCC energy landscape of multitopic AM was performed. Three precursors were synthesized with bite angles ranging from 31º to 60º, and each was subjected to dynamic AM. It was observed that tightening the bite angle, as illustrated by AM of **P$_{Sulf}$**, effectively biased the DCC energy landscape and prevented the system from funneling toward a discrete architecture. On the other hand, widening the bite angle to the ideal tetrahedron geometry, as evidenced by **P$_{Oxy}$**, surprisingly biased the DCC energy landscape so as to lengthen the required time for the system to locate the desired cage product. It was also observed that precursors with angles slightly tighter than the ideal bite angle for a tetrahedron (**P$_{Carb}$**) afford the desired cage architecture most efficiently. DFT calculations of relative structural enthalpies allowed us to validate that there exists a discrepancy between our experimental observations and simple, idealized geometric predictions. Given added complexities in DCC systems such as kinetic bottlenecks, an intuitive approach toward designing DCC molecular cage precursors is thus not always predictive.

Detailed pathway analyses are likely to supply the missing insight to overcome the design challenges in DCC.

Our results lend credence to the underlying systemic issues facing the synthesis of 3D architectures via DCC, where variations in precursor geometry lead to significant deviation of product distributions away from discrete products. Such behavior considerably challenges rational design and limits synthesis of novel covalent organic cage targets. These experiments demonstrate that precursor bite angle dominates multitopic DCC energy landscapes and product distributions in multitopic AM. Geometric control of dynamic energy landscapes provides insight toward essential precursor design parameters for successful architecture formation. Our results suggest that to synthesize novel covalent organic cages in high yields via multitopic DCC, one must design and synthesize precursors with slightly smaller bite angles than that of the theoretically optimum angle for the targeted structure. We envision the information learned from this study will alleviate difficulties in novel architecture synthesis via DCC and contribute to rational precursor design rules that allow *a priori* targeting of structures with specific architectural features.

2.8 Experimental

General. All air or moisture-sensitive manipulations were performed under an atmosphere of nitrogen using standard Schlenk techniques or in an argon-filled glove box. Analytical TLC was performed on Kieselgel F-254 precoated silica gel plates and visualization was performed with UV light (254 nm) or a CAM stain. Column chromatography was performed on Biotage Isolera using Silicycle Siliasep HP flash cartridges. All metathesis reactions were prepared in an argon-filled glove box and run under an inert atmosphere. Reaction vessels were 20 mL I-CHEM vials fitted with PTFE/Silicone septa purchased from VWR International unless specified otherwise.

Materials. Unless otherwise stated, all starting materials and reagents were purchased from Sigma Aldrich and used without further purification. Bis(triphenylphosphine)palladium(II) dichloride was purchased from Strem Chemicals, Inc. and 1,1'-bis(diphenylphosphino)ferrocenepalladium (II) dichloride was purchased from AK Scientific. The following compounds were prepared according to literature procedure: 1,3,5-Tris(4-propynylbenzyl)-2,4,6-triethylbenzene (**P_{Carb}**),[31] molybdenum(IV) propylidyne precatalyst **[Mo]**.[39,40] Tetrahydrofuran (THF), dichloromethane

(DCM), Benzene, and triethylamine (TEA) were obtained from a Solvent Delivery System (SDS) equipped with activated neutral alumina columns under argon.

Characterization. ^{1}H and ^{13}C NMR spectra were recorded on Varian Unity 400 MHz, Varian Unity 500 MHz, and Varian VXR 500 MHz at room temperature (298 K). All spectra were recorded in $CDCl_3$ unless specified otherwise. Chemical shifts are reported in δ (ppm) and referenced by TMS or residual solvent peaks ($CDCl_3$: 7.26 for ^{1}H, 77.16 for ^{13}C). Coupling constants (J) are expressed in hertz (Hz). Splitting patterns are designated as: s (singlet), d (doublet), t (triplet), q (quartet), m (multiplet). EI and ESI mass spectra were recorded on a Micromass 70-VSE spectrometer and Micromass Q-TOF Ultima spectrometer. MALDI mass spectra were recorded on a Bruker Daltonics UltrafleXtreme MALDI TOF spectrometer. Analytical gel permeation chromatography (GPC) analyses were performed on an Agilent 1260 Infinity in THF or chloroform at 25 °C. The instrument was equipped with a series of 4 Waters HR Styragel columns (7.8 x 300mm, HR1, HR3, HR4, and HR5) and was calibrated using monodisperse polystyrene standards.

Synthesis of Precursors

Note: The synthesis of ***P_{Carb}*** *followed a procedure previously reported by our group.*

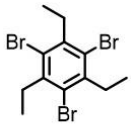

1

Preparation of 1,3,5-triethyl-2,4,6-tribromobenzene (1): To an oven-dried, two-neck round bottom flask fitted with an addition funnel and a bubbler was added a stir bar, iron powder (100 mg, 1.8 mmol, 0.3 equiv), and bromine (4.92 g, 1.59 mL, 30.8 mmol, 5 equiv). To the addition funnel was added 1,3,5-triethylbenzene (1.00 g, 1.16 mL, 6.16 mmol, 1 equiv) and this liquid was added dropwise over the course of 30 mins. During the addition, the bubbler was dipped in a 10 % (w/v) solution of NaOH to quench the evolved HBr gas. After the addition, the reaction was allowed to stir for 10 mins before 30 mL of a 10 % (w/v) sodium hydroxide solution was added. The mixture was extracted 3x with 30 mL of chloroform. The organic layers were collected, washed with water (3 x 20 mL) and brine (1 x 20 mL), then dried over magnesium sulfate before being filtered. The volatiles were removed using a rotavap affording an off-white powder (2.40 g, 6.01 mmol, 98 % yield). ^{1}H NMR (500 MHz, $CDCl_3$): δ = 3.13 (q, J = 7.45, 6H), 1.18 (t, J = 7.47,

9H) ppm. ^{13}C NMR (125 MHz, $CDCl_3$): δ = 142.64, 124.41, 32.82, 12.35. HRMS-EI: $C_{12}H_{15}Br_3$ Calcd. 395.8724, found 395.8712.

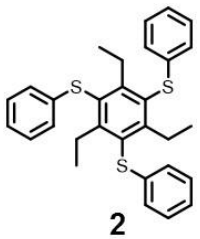

2

Preparation of 2: To an oven-dried round bottom flask was added **1** (0.50 g, 1.25 mmol, 1 equiv) and 10 mL of DMI. Argon was bubbled through the solution for 10 mins before sodium thiophenolate (1.16 g, 8.77 mmol, 7 equiv) was added all at once. The flask was sealed with a septum and the reaction was then heated to 140º C and stirred for 3 days at this temperature under nitrogen. The reaction was allowed to cool to room temperature before 30 mL of a 10% potassium carbonate solution was added. The contents were extracted with 30 mL of EtOAc 3x and washed with water (3 x 20 mL) and brine (1 x 20 mL). The organic layers were collected and dried over magnesium sulfate before being filtered. The solvent was evaporated via rotavap. Flash chromatography running a gradient from 100:0 – 85:15 of Hexane and DCM afforded a colorless oil which solidified upon standing (0.438, 0.90 mmol, 72 % yield). ^{1}H NMR (500 MHz, $CDCl_3$): δ = 7.21 (t, J = 7.69, 6H), 7.07 (t, J = 7.37, 3H), 6.90 (d, J = 7.32, 6H), 3.15 (q, J = 7.36, 6H), 1.10 (t, J = 7.37, 9H) ppm. ^{13}C NMR (125 MHz, $CDCl_3$): δ = 158.60, 139.42, 130.31, 129.08, 125.20, 124.92, 29.27, 15.76. HRMS-EI: $C_{30}H_{30}S_3$ Calcd. 486.1510, found 486.1499.

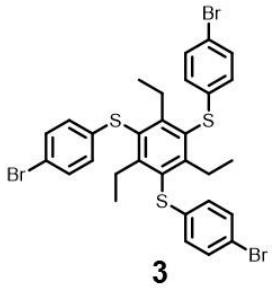

3

Preparation of 3: To an oven-dried round bottom flask was added **2** (0.100 g, 0.205 mmol, 1 equiv) and 25 mL of a 2:1 (v/v) mixture of acetonitrile and DCM. The flask was allowed to cool to 0º C in an ice bath before NBS (0.121 g, 0.677 mmol, 3.3 equiv) was added all at once. The reaction was taken off the ice bath after the addition and allowed to stir at room temperature for 2 days. Then, 30 mL of water was added to the reaction mixture and the contents were extracted 3x

with 25 mL of DCM. The organic layers were collected, washed with water (3 x 20 mL) and brine (1 x 20 mL) and dried over magnesium sulfate before being filtered. The volatiles were removed under vacuum. Flash chromatography running a gradient of 100:0 – 90:10 of Hexane and DCM afforded a colorless oil (0.110 g, 0.152 mmol, 74 % yield). ^{1}H NMR (500 MHz, $CDCl_3$): δ = 7.33 (d, J = 8.64, 6H), 6.74 (d, J = 8.65, 6H), 3.09 (q, J = 7.35, 6H), 1.08 (t, J = 7.37, 9H) ppm. ^{13}C NMR (125 MHz, $CDCl_3$): δ = 158.79, 138.42, 132.18, 130.23, 126.68, 118.67, 29.29, 15.75. HRMS-EI: $C_{30}H_{27}Br_3S_3$ Calcd. 719.8825, found 719.8827.

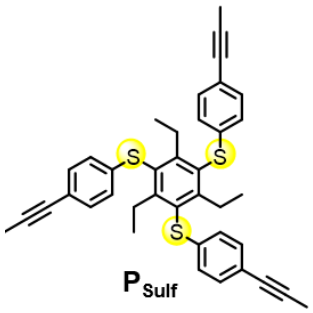

P$_{Sulf}$

Preparation of P$_{Sulf}$: To an oven-dried round bottom flask was added **3** (0.090 g, 0.124 mmol, 1 equiv) and Pd(dppf)Cl_2 (0.0054 g, 0.007 mmol, 6 mol %). The flask was sealed with a septum and purged 3x with dry N_2. Approximately 10 mL of dry THF was added and the contents were heated to 65º C and stirred for 5 mins before a solution of propynyl magnesium bromide (0.5 M, 1.24 mL, 0.622 mmol, 5 equiv) in THF was added dropwise. The reaction was allowed to stir at this temperature for 2 days. Then, 20 mL of 5 % (w/v) HCl solution was added. The contents were extracted with 15 mL of EtOAc (3 x 15 mL). The organic layers were washed with water (3 x 20 mL) and brine (1 x 20 mL). The organic layers were collected and dried over magnesium sulfate before being filtered. The volatiles were removed under vacuum. Flash chromatography running a gradient from 100:0 – 90:10 of Hexane and EtOAc afforded a light yellow solid product (0.067 g, 0.112 mmol, 90 % yield). ^{1}H NMR (500 MHz, $CDCl_3$): δ = 7.22 (d, J = 8.42, 6H), 6.78 (d, J = 8.44, 6H), 3.10 (q, J = 7.27, 6H), 2.03 (s, 9H), 1.07 (t, J = 7.36, 9H) ppm. ^{13}C NMR (125 MHz, $CDCl_3$): δ = 158.75, 138.89, 132.15, 130.11, 124.91, 120.66, 86.18, 79.42, 29.28, 15.71, 4.53. HRMS-EI: $C_{39}H_{36}S_3$ Calcd. 600.1979, found 600.1986.

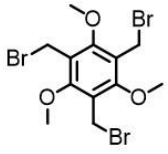

4

Preparation of 4: 1,3,5-trimethoxybenzene (5.00 g, 29.73 mmol, 1 equiv), paraformaldehyde (8.03 g, 268 mmol, 9 equiv), HBr in acetic acid (5.7 M, 48.9 mL, 279 mmol, 9.4 equiv), and a stir bar were added to an oven-dried, glass tube fitted with a Teflon cap and stirred at 85 ºC for 5 hours. The contents were cooled to room temperature, then extracted with dichloromethane (3 x 100 mL). The organic layers were washed with water (3 x 30 mL) then a saturated brine solution (1 x 30 mL). The organic layers were collected, dried over magnesium sulfate, filtered, and the volatiles were evaporated using a rotavap. Isopropyl alcohol (100 mL) and dichloromethane (15 mL) were added to the crude mixture, then this solution was placed in a freezer overnight. The product crystallized as white needles and was collected by filtration (5.1 g, 38 % yield). ^{1}H NMR (500 MHz, $CDCl_3$): δ = 4.60 (s, 6H), 4.14 (s, 9H) ppm. ^{13}C NMR (125 MHz, $CDCl_3$): δ = 160.21, 123.44, 62.81, 22.62. HRMS-EI: $C_{12}H_{15}O_3Br_3$ Calcd. 443.8571, found 443.8566.

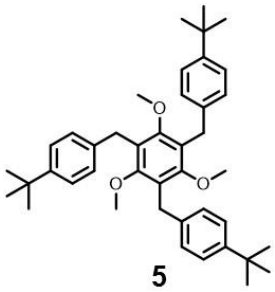

5

Preparation of 5: To an oven-dried round bottom flask was added Mg shavings (1.63 g, 67.1 mmol, 10 equiv) and a stir bar. The flask was then fitted with a septum, and the contents were evacuated and back-filled 3x with nitrogen gas. Then, 15 mL of dry THF was added via cannula, and the contents were stirred vigorously. A small amount of iodine (<5 mg) was added to the stirred mixture for activation. After the red-brown color dissipated completely, a solution of 1-bromo-4-tert-butylbenzene (7.15 g, 33.5 mmol, 5 equiv) in 10 mL of dry THF was added dropwise to the reaction mixture over the course of 10 mins. The mixture was allowed to stir at room temperature for 1.5 hrs. At this time, stirring was stopped and the mixture was allowed to settle for 5 mins. The solution was then transferred to a separate oven-dried, nitrogen-purged, two-necked round bottom flask equipped with a stir bar, a short-path distillation apparatus on one arm, and a septum on the other. Then, 15 mL of dry benzene was added and THF was distilled off under vacuum at 0.30 torr at 50 ºC. The reaction mixture was heated to 100 ºC, then a solution of **4** (3.00 g, 6.71 mmol, 1 equiv) in 5 mL of benzene was added and the reaction was allowed to stir at this temperature for 16 hrs. The reaction was cooled to room temperature, worked up with 30 mL of

10 % HCl solution, and extracted 3x with 30 mL of ethyl acetate. The organic layers were collected, washed with water (3 x 20 mL) and brine (1 x 20 mL), dried over $MgSO_4$, and then filtered. The volatiles were removed using a rotavap. Flash chromatography using a hexane and dichloromethane gradient from 80:20 to 50:50 afforded a white solid (2.85 g, 4.69 mmol, 70 % yield). ^{1}H NMR (500 MHz, $CDCl_3$): δ = 7.29 (d, J = 8.30, 6H), 7.13 (d, J = 8.33, 6H), 4.04 (s, 6H), 3.52 (s, 9H), 1.31 ppm (s, 27H) ppm. ^{13}C NMR (125 MHz, $CDCl_3$): δ = 157.43, 148.42, 138.53, 127.92, 125.19, 124.18, 61.73, 34.44, 31.57, 29.97. HRMS-EI: $C_{42}H_{54}O_3$ Calcd. 606.4073, found 606.4094.

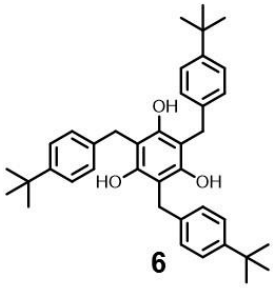

6

Preparation of 6: To an oven-dried round bottom flask was added **5** (2.73 g, 4.50 mmol, 1 equiv) and a stir bar. The flask was fitted with a septum and the contents were evacuated and back-filled with nitrogen 3x. Then, 30 mL of dry dichloromethane was added via cannula and the contents stirred until everything dissolved. The solution was cooled to 0 ºC and a solution of boron tribromide (1.0 M, 19.3 mL, 19.3 mmol, 4.3 equiv) was added dropwise over the course of 10 mins. The reaction stirred for 14 hrs, eventually reaching room temperature. The reaction was quenched with 30 mL of DI water and extracted 3x with dichloromethane (15 mL). The organic layers were washed with water (3 x 20 mL) and brine (1 x 20 mL), then collected, and dried over $MgSO_4$. The volatiles were removed using a rotavap affording a yellow solid product (2.54 g, 4.50 mmol, >99 % yield). ^{1}H NMR (500 MHz, $CDCl_3$): δ = 7.35 (d, J = 8.29, 6H), 7.20 (d, J = 8.04, 6H), 4.78 (s, 3H), 4.01 (s, 6H), 1.33 (s, 27H) ppm. ^{13}C NMR (125 MHz, $CDCl_3$): δ = 152.05, 149.52, 136.38, 127.88, 125.96, 106.91, 34.55, 31.51, 28.95. HRMS-EI: $C_{39}H_{48}O_3$ Calcd. 564.8103, found 564.8145.

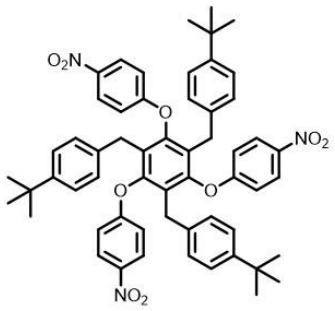

7

Preparation of 7: To a round bottom flask was added a stir bar, **6** (1.00 g, 1.77 mmol, 1 equiv), 1-fluoro-4-nitrobenzene (1.25 g, 8.85 mmol, 5 equiv), and Cs_2CO_3 (2.88 g, 8.85 mmol, 5 equiv). The flask was fitted with a septum and the contents of the flask were then evacuated and back-filled 3x with nitrogen. Then, 10 mL of dry DMF was added to the flask and the reaction mixture was heated to 90 ºC and stirred for 3 hrs at this temperature. After cooling to rt, 50 mL of water was added to the reaction mixture and the contents were extracted 3x with 15 mL of ethyl acetate. Flash chromatography using an eluent gradient of 100:0 hexane:ethyl acetate to 85:15 hexane:ethyl acetate afforded a white powder (1.40 g, 1.50 mmol, 84 % yield). ^{1}H NMR (500 MHz, $CDCl_3$): δ = 7.97 (d, J = 8.55, 6H), 7.07 (d, J = 8.27, 6H), 6.85 (d, J = 8.22, 6H), 6.61 (d, J = 8.77, 6H), 3.67 (s, 6H), 1.21 (s, 27H) ppm. ^{13}C NMR (125 MHz, $CDCl_3$): δ = 162.29, 150.76, 149.66, 142.57, 134.79, 128.17, 127.98, 125.84, 125.38, 115.02, 34.45, 31.46, 30.66. HRMS-EI: $C_{57}H_{57}N_3O_9Na$ Calcd. 950.3993, found 950.3973.

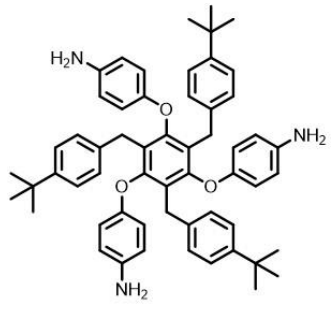

8

Preparation of 8: A round bottom flask was charged with **7** (2.80 g, 3.02 mmol), 300 mg of Pd/C, and a stir bar. Dry ethyl acetate (20 mL) was added and the flask was equipped with a septum. The contents of the vial were then evacuated and back-filled with hydrogen gas 3x. The contents were stirred vigorously for 24 hrs under hydrogen. Chloroform (50 mL) was added to the mixture and the contents were filtered through a pad of silica (with additional washing using 100 mL of

chloroform). The volatiles were removed under vacuum affording a beige powder (2.50 g, 2.98 mmol, 99 % yield). ^{1}H NMR (500 MHz, $CDCl_3$): δ = 7.12 (d, J = 8.25, 6H), 6.98 (d, J = 8.25, 6H), 6.43 (m, 12H), 3.67 (s, 6H), 3.36 (s, 9H), 1.28 (s, 27H) ppm. ^{13}C NMR (125 MHz, $CDCl_3$): δ = 151.81, 151.24, 148.14, 140.43, 137.20, 128.50, 127.23, 124.85, 116.30, 115.57, 34.39, 31.60, 30.51. HRMS-EI: $C_{57}H_{64}N_3O_3$ Calcd. 838.4935, found 838.4948.

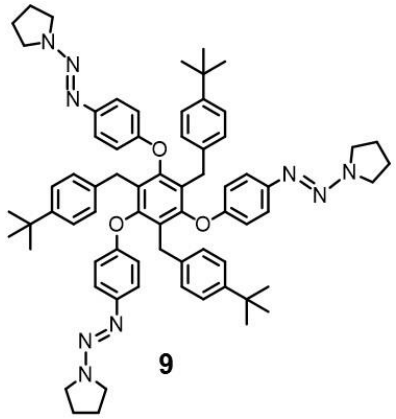

9

Preparation of 9: A solution of **8** (520 mg, 0.620 mmol, 1 equiv) in a mixture of 30 mL of acetonitrile and 5 mL of DI water was cooled to 0 ºC. Then, HCl (12 M, 0.64mL, 7.44 mmol, 12 equiv) was added dropwise over the course of 10 mins during which everything dissolved. After stirring for 10 mins, a solution of $NaNO_2$ (193 mg, 2.80 mmol, 4.5 equiv) in 10 mL of DI water was added dropwise over the course of 10 mins. The reaction was allowed to stir 30 mins, before adding it dropwise to a stirred solution of pyrrolidine (330 mg, 4.65 mmol, 7.5 equiv) and K_2CO_3 (1.33 g, 9.67 mmol, 15.6 equiv) in 30 mL DI water at 0 ºC. After the addition was complete, the reaction was allowed to warm to room temperature and stir at this temperature for 1 hr. Then, the reaction was extracted 3x with 30 mL of ethyl acetate. The combined organic layers were washed with water (3x40 mL), collected and dried over $MgSO_4$, and filtered. The volatiles were removed using a rotavap. Flash chromatography using an eluent of 85:15 hexane/ethyl acetate afforded an off-white solid (625 mg, 0.576 mmol, 93 % yield). ^{1}H NMR (500 MHz, $CDCl_3$): δ = 7.16 (d, J = 9.01, 6H), 7.09 (d, J = 8.33, 6H), 6.97 (d, J = 8.31, 6H), 6.56 (d, J = 8.81, 6H), 3.74 (s, 12H), 3.69 (s, 6H), 2.00 (m, 12H), 1.24 (s, 27H) ppm. ^{13}C NMR (125 MHz, $CDCl_3$): δ = 155.90, 151.66, 148.33, 146.02, 136.97, 128.58, 127.55, 125.06, 121.40, 115.17, 34.50, 31.67, 30.67, 24.10. HRMS-EI: $C_{69}H_{81}N_9O_3$ Calcd. 1083.6440, found 1083.6462.

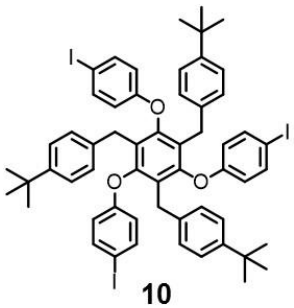

10

Preparation of 10: A 20 mL scintillation vial was charged with **9** (250 mg, 0.231 mmol, 1 equiv), iodine (181 mg, 0.715 mmol, 3.1 equiv), a stir bar, and 5 mL of diiodomethane. The contents were degassed by bubbling argon through the solution for 10 mins. The reaction mixture was then heated at 80 ºC for 4 hrs. After this period, the reaction was allowed to cool to room temperature, the solvent was removed under vacuum, and then the contents were quenched with 10 % sodium bisulfite solution and extracted 3x with 10 mL of ethyl acetate. The organic layers were collected, dried over magnesium sulfate, filtered, and the volatiles were removed using a rotavap to afford a white solid (243 mg, 0.208 mmol, 90 % yield). ^{1}H NMR (500 MHz, $CDCl_3$): δ = 7.31 (d, J = 8.50, 6H), 7.09 (d, J = 8.29, 6H), 6.89 (d, J = 8.29, 6H), 6.30 (d, J = 8.50, 6H), 3.62 (s, 6H), 1.28 (s, 27H) ppm. ^{13}C NMR (125 MHz, $CDCl_3$): δ = 157.90, 151.09, 148.96, 138.36, 136.08, 128.40, 127.74, 125.23, 117.23, 84.25, 34.57, 31.75, 30.65. HRMS-EI: $C_{57}H_{57}O_3I_3$ Calcd. 1170.1415, found 1170.1442.

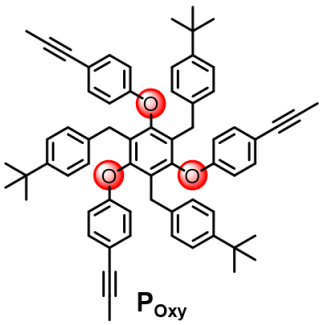

P_{Oxy}

Preparation of P_{Oxy}: To an oven-dried, sealed glass tube fitted with a teflon screw cap was added **10** (0.23 g, 0.196 mmol, 1 equiv), 1 mL of THF, 5 mL of triethylamine, and a stir bar. The contents were purged by bubbling with argon for 10 mins before copper (I) iodide (0.0037 g, 0.0196 mmol, 10 mol %) and bis(triphenylphosphino)palladium (II) dichloride (0.011 g, 0.0157 mmol, 8 mol %) were added at once. Propyne gas was then bubbled through the solution for ca. 3 mins before the tube was sealed with the screw cap. The reaction stirred at rt for 12 hrs. At this time, the tube was opened, and the reaction was quenched with the addition of 10 mL of saturated ammonium chloride

solution. The mixture was extracted with ethyl acetate (3 x 20 mL) and the organic layers were collected and washed with water (3 x 20 mL) and saturated brine solution (1 x 20 mL). The organic layers were collected, dried over magnesium sulfate, filtered, and the volatiles were evaporated using a rotavap. The contents were dry-loaded onto a column and purified running an eluent of 100:0 hexane:ethyl acetate to 90:10 hexane:ethyl acetate to afford a white powder (0.137 g, 0.151 mmol, 77 % yield). ^{1}H NMR (500 MHz, $CDCl_3$): δ = 7.08 (d, J = 8.20, 12H), 6.90 (d, J = 8.20, 6H), 6.46 (d, J = 8.60, 6H), 3.62 (s, 6H), 2.00 (s, 6H), 1.27 (s, 27H) ppm. ^{13}C NMR (125 MHz, $CDCl_3$): δ = 157.24, 151.11, 148.61, 136.23, 132.80, 128.36, 127.56, 125.05, 117.42, 114.81, 84.63, 79.35, 34.41, 31.53, 30.56, 4.39. HRMS-EI: $C_{66}H_{67}O_3$ Calcd. 907.5090, found 907.5079.

Generalized Metathesis Conditions:

Note: *Metathesis was performed in either chloroform or 1,2,4-trichlorobenzene (TCB). In our hands, solvent had a negligible effect on AM product distributions (see Figure 2.20).*

In an argon-filled glove box, precursor (0.05 mmol), 5 Å molecular sieves powder (800 mg/mmol of propynyl groups) and solvent (2.5 mL) were added to a reaction vial (vial 1) containing a stir bar. A solution of molybdenum (VI) alkylidyne precatalyst, **[Mo]** (0.0025 mmol) and Ph_3SiOH (0.015 mmol) in solvent (2.5 mL) was stirred in a separate vial (vial 2) for 5 min then added to vial 1. The reaction mixture was stirred at the specified temperature in the glovebox for the specified time. The reaction was removed from the glovebox and the vial was opened to air immediately. The reaction mixture was then filtered through 0.45 μm membrane filter paper or syringe filter. The filtrate was collected, MeOH (50 mL) was added to the solution and this solution stirred for 10 mins. The precipitates were filtered using a 0.45 μm membrane filter paper and washed extensively with MeOH. The resulting powder was dried under vacuum.

Generalized Precursor Mixing Metathesis Conditions: Precursors A and B (total of 0.073 mmol, 1 equiv), a stir bar, 204 mg of 5 Å molecular sieves, and 3.65 mL of solvent were added to a reaction vial (vial 1). A solution of molybdenum (VI) alkylidyne precatalyst, **[Mo]** (0.00365 mmol, 0.05 equiv) and Ph_3SiOH (0.0219 mmol, 0.30 equiv) in chloroform or 1,2,4-trichlorobenzene (3.65 mL) was stirred in a separate vial (vial 2) for 5 min then added to vial 1. The reaction mixture was stirred at rt in the glovebox for 12 hrs. The reaction was removed from the glovebox and the vial was opened to air immediately. The reaction mixture was then filtered through 0.45 μm membrane filter paper or a syringe filter. The filtrate was collected, MeOH (50 mL) was added to the solution, the mixture was stirred vigorously for 10 mins, and the precipitates

were collected using a 0.45 μm membrane filter paper and washed extensively with MeOH. The resulting powder was dried under vacuum.

AM of P_{Sulf}: This reaction followed the General Metathesis Conditions procedure. In an argon-filled glove box, **P_{Sulf}** (0.030 g, 0.050 mmol, 1 equiv) and 143 mg of 5Å molecular sieves were added to a reaction vial (vial 1) along with a stir bar and TCB (2.5 mL). In a separate reaction vial (vial 2) was added [Mo] (1.7 mg, 0.0025 mmol, 0.05 equiv), Ph_3SiOH (4.15 mg, 0.015 mmol, 0.30 equiv), and TCB (2.5 mL). The contents of vial 2 were agitated until complete dissolution. This catalyst solution was then added to vial 1 and the reaction was sealed with a screw cap and left to stir for 12 hours at 70 ºC. After 12 hours, the vial was taken out of the glove box and opened to air. The contents were filtered with either a 0.45 μm membrane filter paper or syringe filter, and the filtrate was collected. Methanol (100 mL) was added to the filtrate and the mixture was stirred at rt for 10 mins. The contents were filtered with 0.45 μm membrane filter paper and the solids were collected and dried under vacuum to afford 25.8 mg of a white powder.

AM of P_{Carb}: This reaction follows the General Metathesis Conditions procedure using **P_{Carb}** (0.027 g, 0.050 mmol, 1 equiv), 143 mg of 5Å molecular sieves, [Mo] (1.7 mg, 0.0025 mmol, 0.05 equiv), Ph_3SiOH (4.15 mg, 0.015 mmol, 0.30 equiv), and TCB (5 mL). The reaction afforded 23.2 mg of **Td_{Carb}** as a white powder (99 % yield).

AM of P_{Oxy}: This reaction followed the General Metathesis Conditions procedure. **P_{Oxy}** (0.045 g, 0.050 mmol, 1 equiv), 143 mg of 5Å molecular sieves, [Mo] (1.7 mg, 0.0025 mmol, 0.05 equiv), Ph_3SiOH (4.15 mg, 0.015 mmol, 0.30 equiv), and TCB (5 mL) were used. The reaction afforded 41.2 mg (99 % crude yield) of a white powder. Flash chromatography of this mixture running an eluent of 1:2:97 (*v/v/v*, DCM/ethyl acetate/hexane) affords **Td_{Oxy}** in ca. 23 % yield (9.5 mg). If the reaction is run at rt for 24 hrs in chloroform, then **Td_{Oxy}** is afforded in 98 % yield. ^{1}H NMR (500 MHz, $CDCl_3$): δ = 7.49 (d, J = 8.93, 6H), 7.19 (d, J = 8.31, 6H), 7.01 (d, J = 8.17, 6H), 6.80 (d, J = 8.27, 6H), 3.63 (s, 6H), 1.28 (s, 27H) ppm. ^{13}C NMR (125 MHz, $CDCl_3$): δ = 157.67, 151.19, 148.88, 136.20, 133.41, 128.37, 127.84, 125.24, 117.34, 114.81, 88.47, 34.48, 31.53, 30.70. MALDI-MS: $C_{66}H_{67}O_3$ Calcd. 3304.7, found 3304.7.

AM Mixing of P_{Sulf} and P_{Carb}: This reaction followed the Generalized Precursor Mixing Metathesis Conditions. Briefly, for the equimolar experiment, **P_{Sulf}** (21.97 mg, 0.0365 mmol,), **P_{Carb}** (20 mg, 0.0365 mmol), 204.5 mg of 5Å molecular sieves, a stir bar, and 3.65 mL of chloroform (or TCB) were added in a reaction vial (vial 1) in an argon-filled glove box. In a second

vial (vial 2) was added [Mo] (2.43 mg, 0.00365 mmol, 0.05 equiv), Ph_3SiOH (6.05 mg, 0.0219 mmol, 0.30 equiv), and chloroform (3.65 mL). Vial 2 was agitated until complete dissolution before the contents were added to vial 1. The reaction was sealed with a cap and allowed to stir at rt for 12 hrs. At this time, the reaction was removed from the glove box, opened to air, and filtered through either a 0.45 μm membrane filter paper or syringe filter, and the filtrate was collected. Methanol (100 mL) was added to the filtrate and the mixture was stirred at rt for 10 mins. The contents were filtered with 0.45 μm membrane filter paper and the solids were collected and dried under vacuum to afford 35.7 mg of an off-white powder. The 1:3 $\mathbf{P_{Sulf}}$ **:** $\mathbf{P_{Carb}}$ experiment was performed in a similar fashion using 10.98 mg (0.0183 mmol) of $\mathbf{P_{Sulf}}$ and 30 mg (0.0548 mmol) of $\mathbf{P_{Carb}}$. The 3:1 $\mathbf{P_{Sulf}}$ **:** $\mathbf{P_{Carb}}$ experiment was also performed in a similar fashion using 32.9 mg (0.0548 mmol) of $\mathbf{P_{Sulf}}$ and 10 mg (0.00.0182 mmol) of $\mathbf{P_{Carb}}$.

AM Mixing of $\mathbf{P_{Sulf}}$ and $\mathbf{P_{Oxy}}$: This reaction followed the Generalized Precursor Mixing Metathesis Conditions with slight adjustments in the amount of precursors used. The reaction contained $\mathbf{P_{Sulf}}$ (10.9 mg, 0.0182 mmol), $\mathbf{P_{Oxy}}$ (16.6 mg, 0.0182 mmol), 102 mg of 5Å molecular sieves, [Mo] (1.21 mg, 0.00182 mmol, 0.05 equiv), Ph_3SiOH (3.02 mg, 0.011 mmol, 0.30 equiv), and chloroform (3.62 mL). The reaction afforded 24.4 mg of an off-white powder.

AM Mixing of $\mathbf{P_{Carb}}$ and $\mathbf{P_{Oxy}}$: This reaction followed the Generalized Precursor Mixing Metathesis Conditions with slight adjustments in the amount of precursors used. The reaction contained $\mathbf{P_{Carb}}$ (10.0 mg, 0.0182 mmol), $\mathbf{P_{Oxy}}$ (16.6 mg, 0.0182 mmol), 102 mg of 5Å molecular sieves, [Mo] (1.21 mg, 0.00182 mmol, 0.05 equiv), Ph_3SiOH (3.02 mg, 0.011 mmol, 0.30 equiv), and chloroform (3.62 mL). The reaction afforded 23.1 mg of an off-white powder.

AM Mixing of $\mathbf{P_{Sulf}}$, $\mathbf{P_{Carb}}$, and $\mathbf{P_{Oxy}}$: This reaction followed the Generalized Precursor Mixing Metathesis Conditions with slight adjustments in the amount of precursors used. The reaction contained $\mathbf{P_{Sulf}}$ (11 mg, 0.0182 mmol), $\mathbf{P_{Carb}}$ (10.0 mg, 0.0182 mmol), $\mathbf{P_{Oxy}}$ (16.6 mg, 0.0182 mmol), 153.8 mg of 5Å molecular sieves, [Mo] (1.84 mg, 0.0028 mmol, 0.05 equiv), Ph_3SiOH (4.53 mg, 0.0164 mmol, 0.30 equiv), and chloroform (5.50 mL). The reaction afforded 33.0 mg of an off-white powder.

GPC Data

Note: In crude GPC data, peaks at ~43.8 mins are due to residual solvent (1,2,4-trichlorobenzene) from metathesis.

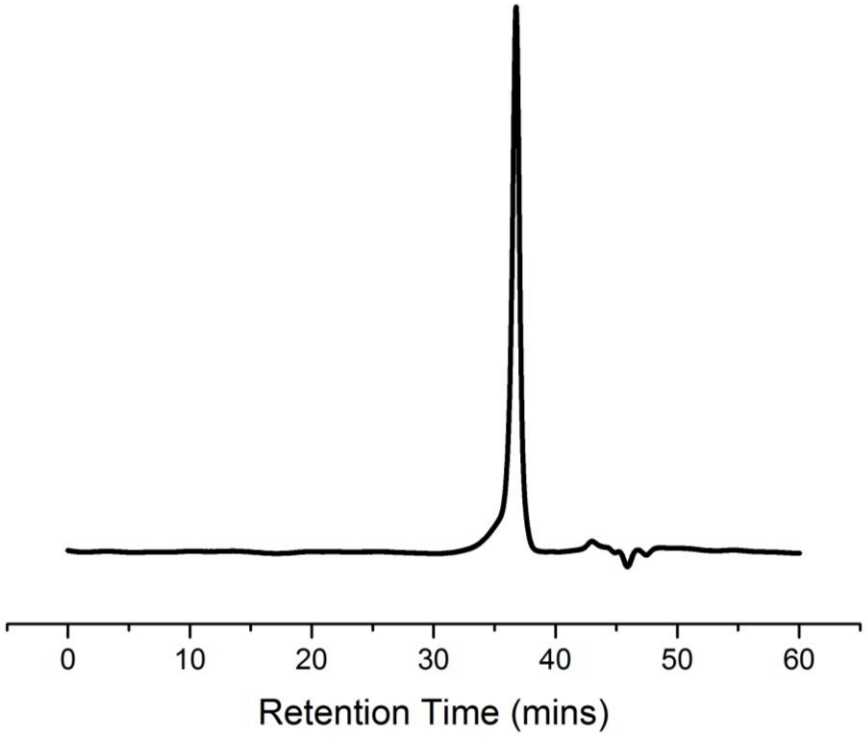

***Figure 2.9**: GPC trace of* $\mathbf{Td_{Carb}}$.

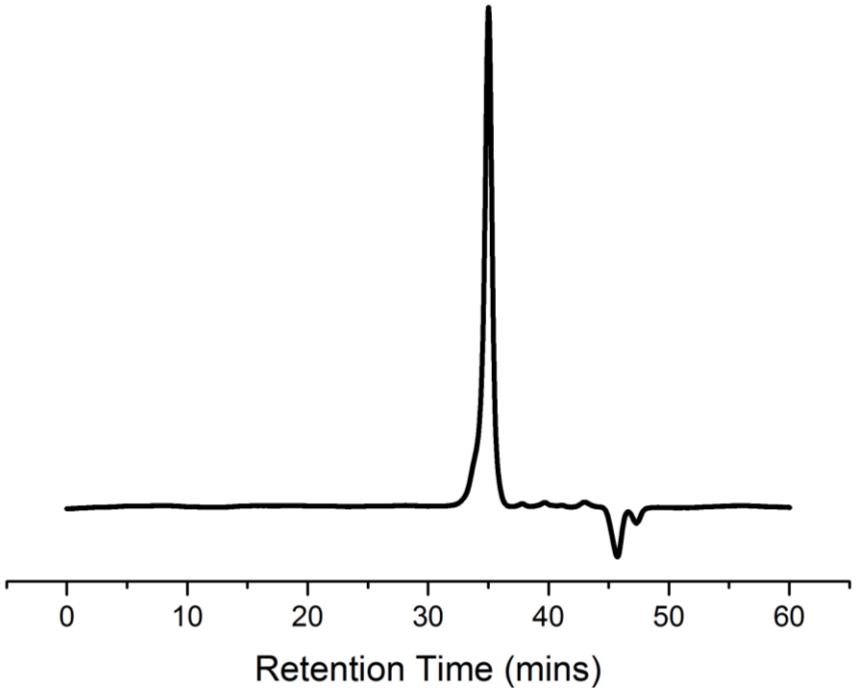

Figure 2.10: *GPC trace of* $\mathbf{Td_{Oxy}}$.

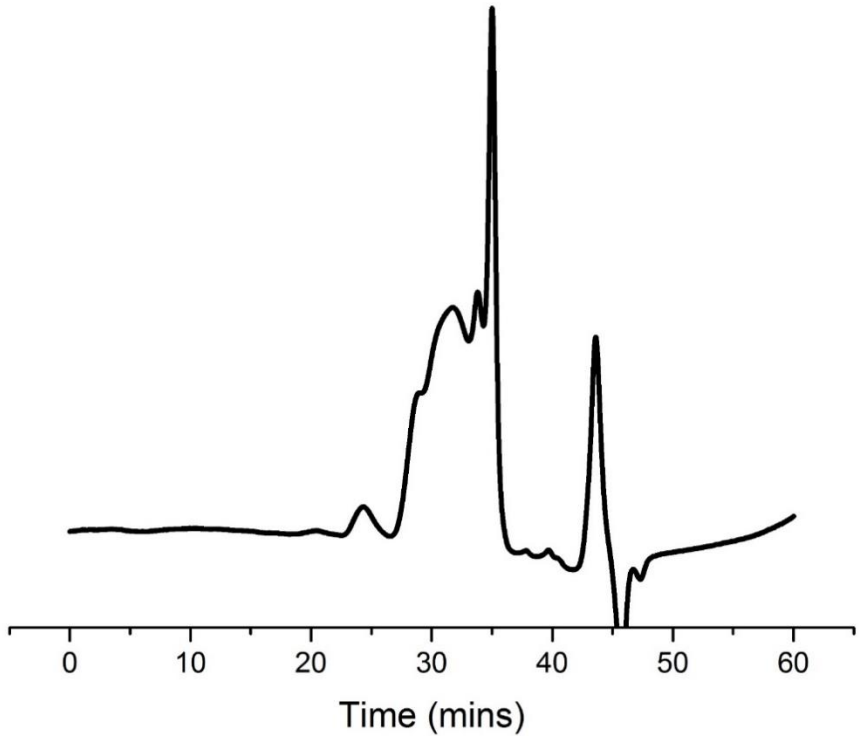

Figure 2.11: *GPC trace of the product distribution from metathesis of* $\mathbf{P_{Oxy}}$ *at 70 ºC for 12 hrs in TCB.*

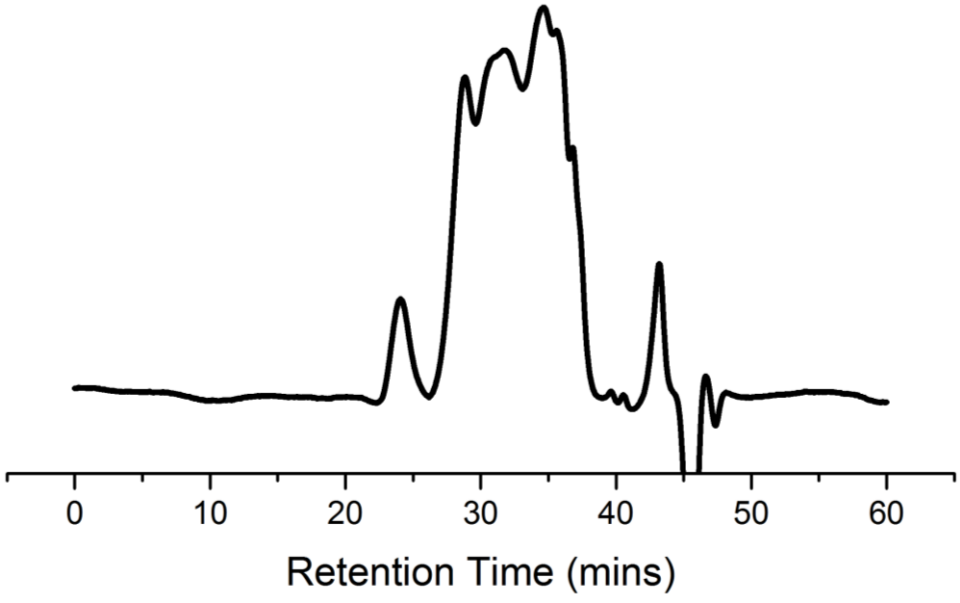

Figure 2.12: *GPC trace of the product distribution from metathesis of* $\mathbf{P_{Sulf}}$ *at 70 ºC for 12 hrs in TCB.*

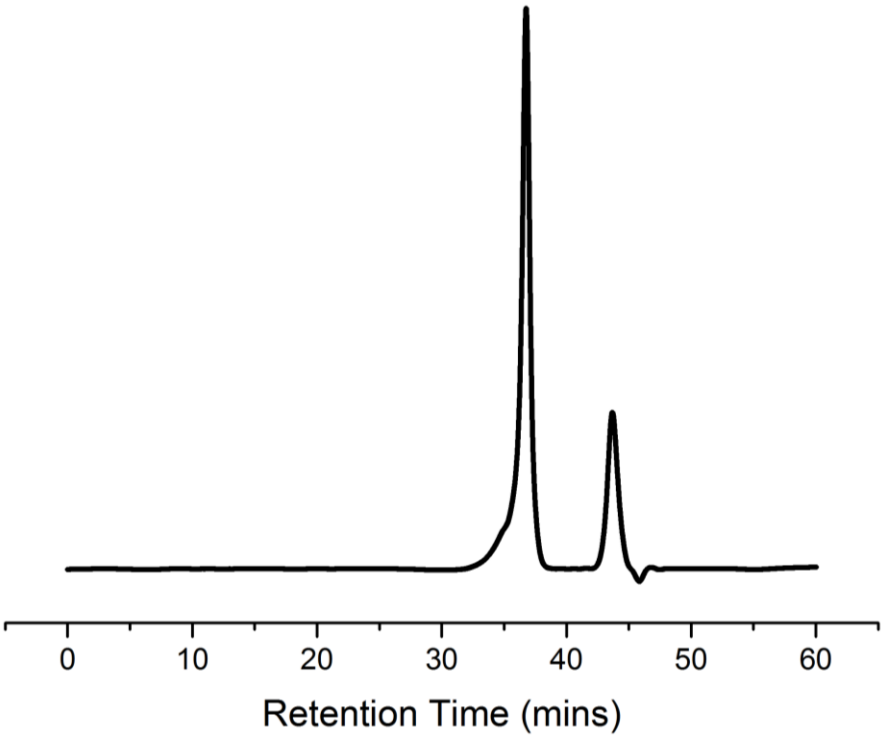

Figure 2.13: *GPC trace of the product distribution from metathesis of a 1:3 mixture of* $\boldsymbol{P_{Sulf}:P_{Carb}}$ *at rt for 12 hrs.*

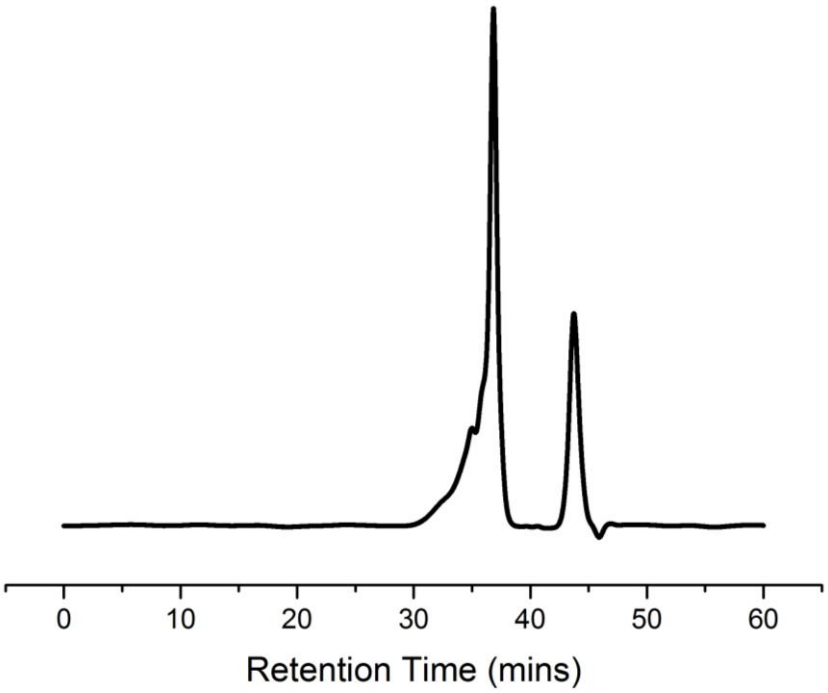

Figure 2.14: *GPC trace of the product distribution from metathesis of a 1:1 mixture of* $\boldsymbol{P_{Sulf}:P_{Carb}}$ *at rt for 12 hrs.*

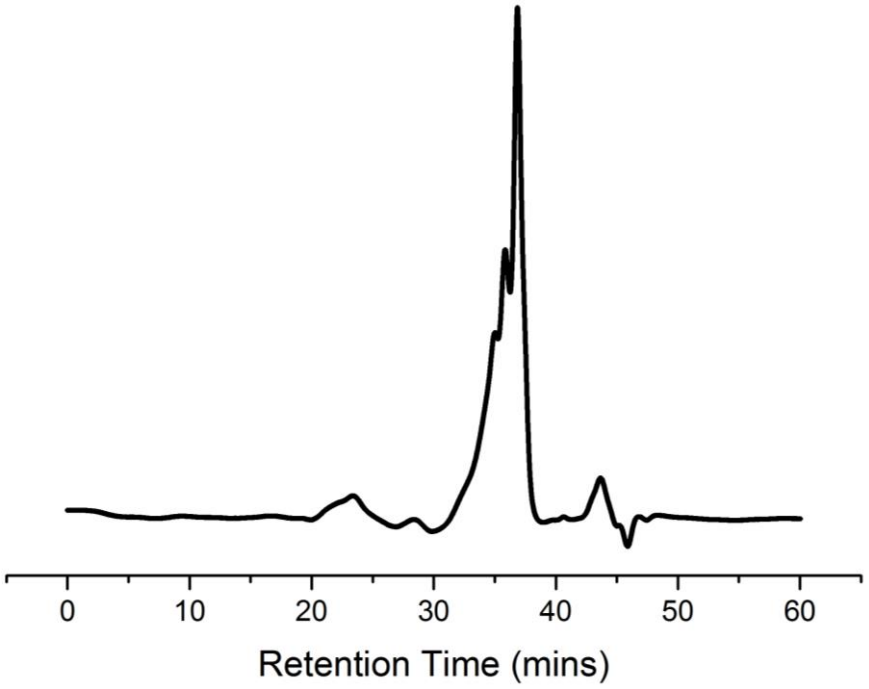

Figure 2.15: *GPC trace of the product distribution from metathesis of a 3:1 mixture of* $\boldsymbol{P_{Sulf}:P_{Carb}}$ *at rt for 12 hrs.*

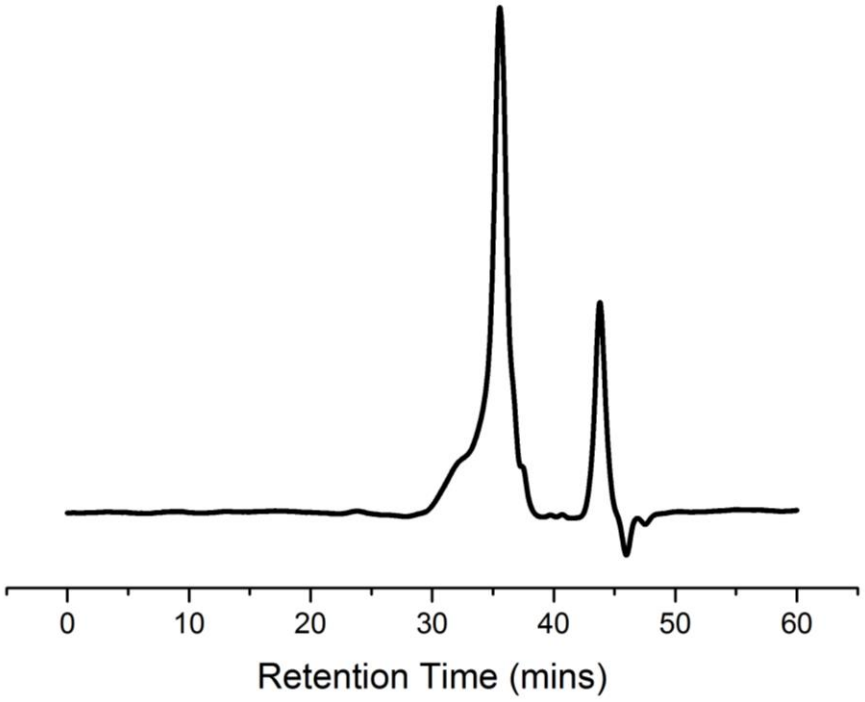

Figure 2.16: *GPC trace of the product distribution from metathesis of a 1:1 mixture of* $\boldsymbol{P_{Sulf}:P_{Oxy}}$ *at rt for 12 hrs.*

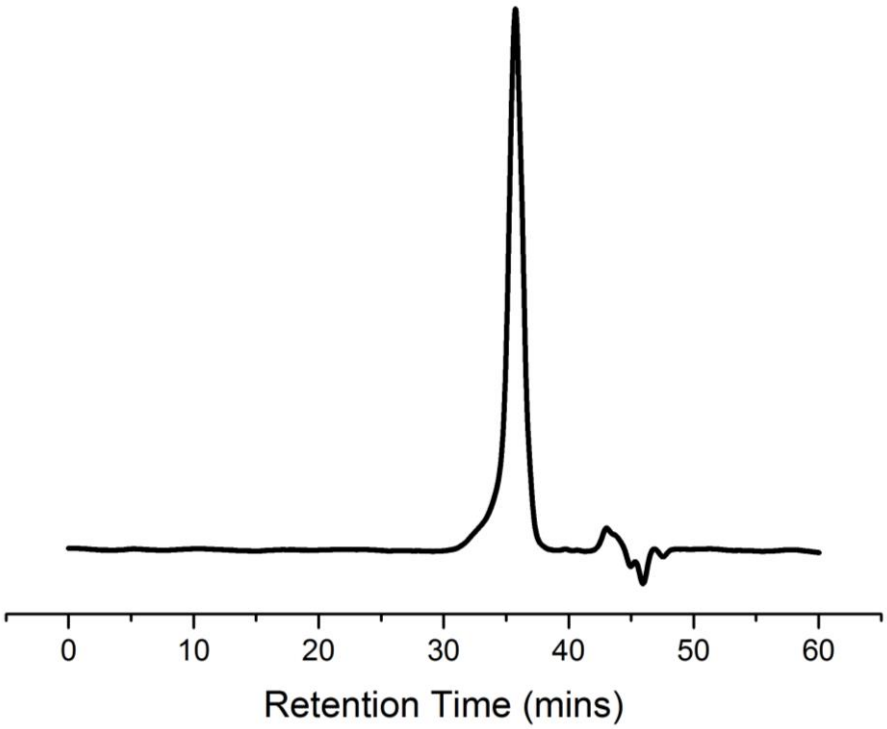

Figure 2.17: *GPC trace of the product distribution from metathesis of a 1:1 mixture of* $\boldsymbol{P_{Carb}:P_{Oxy}}$ *at rt for 12 hrs.*

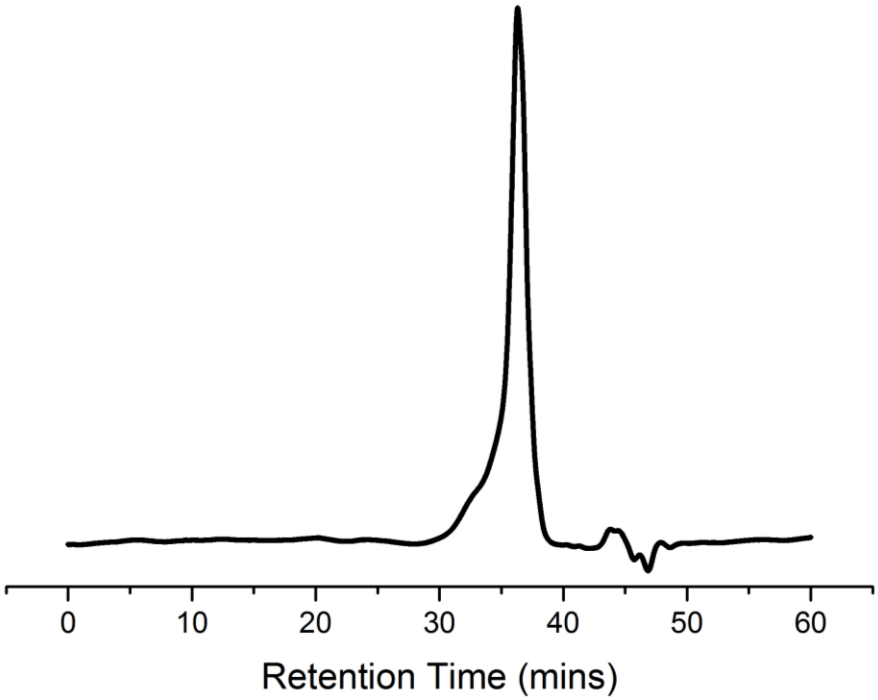

Figure 2.18: *GPC trace of the product distribution from metathesis of a 1:1:1 mixture of* $\boldsymbol{P_{Sulf}:P_{Carb}:P_{Oxy}}$ *at rt for 12 hrs.*

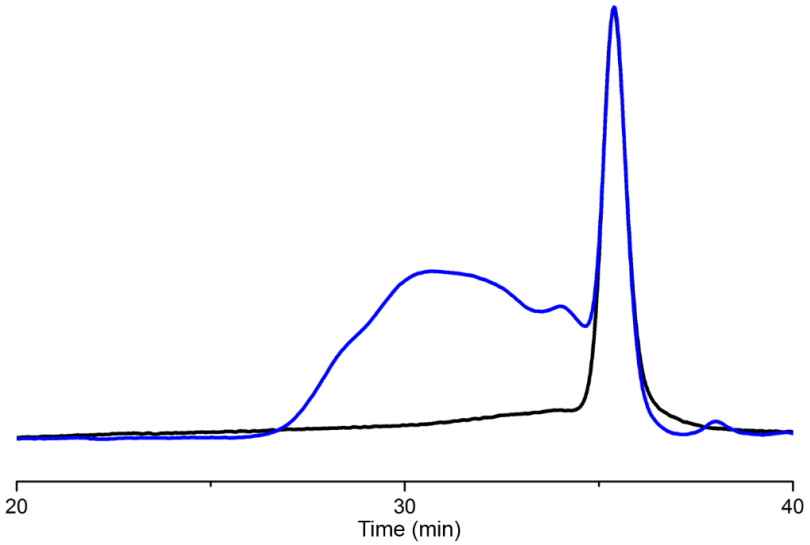

Figure 2.19: *Overlay of the GPC traces from metathesis of* $\mathbf{P_{Oxy}}$ *at rt in chloroform after 8 hrs (blue) and after 24 hrs (black).*

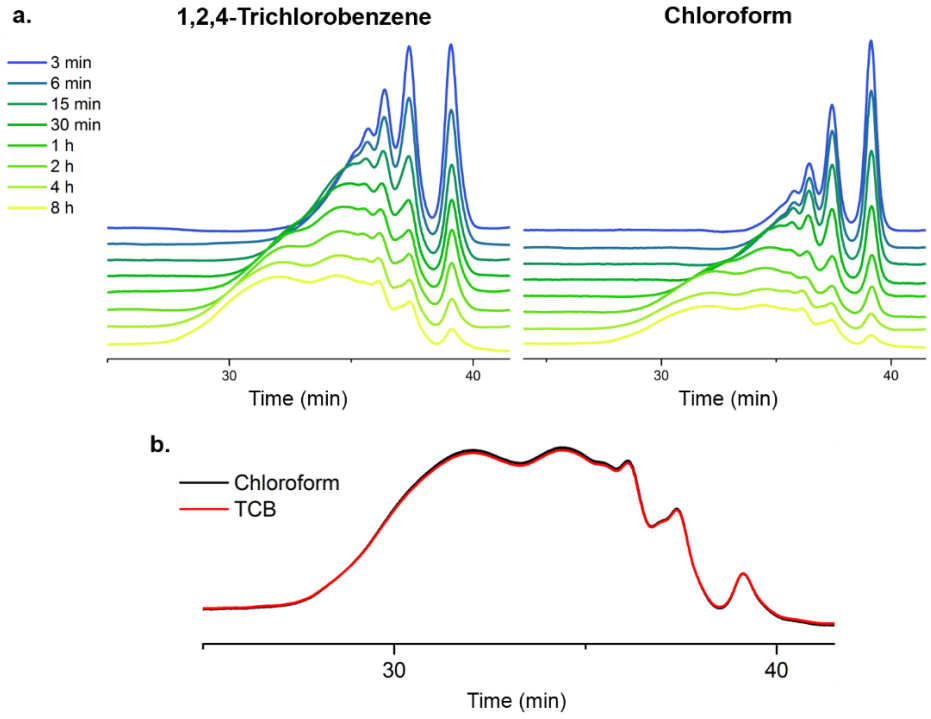

Figure 2.20: *GPC comparison of the product distribution resulting from AM of* $\mathbf{P_{Sulf}}$ *at rt using either chloroform or TCB as the solvent. a) Product distribution over time for AM using TCB and chloroform. b) Normalized GPC overlay of the product distributions at 8 h for chloroform and TCB.*

MALDI-MS Data

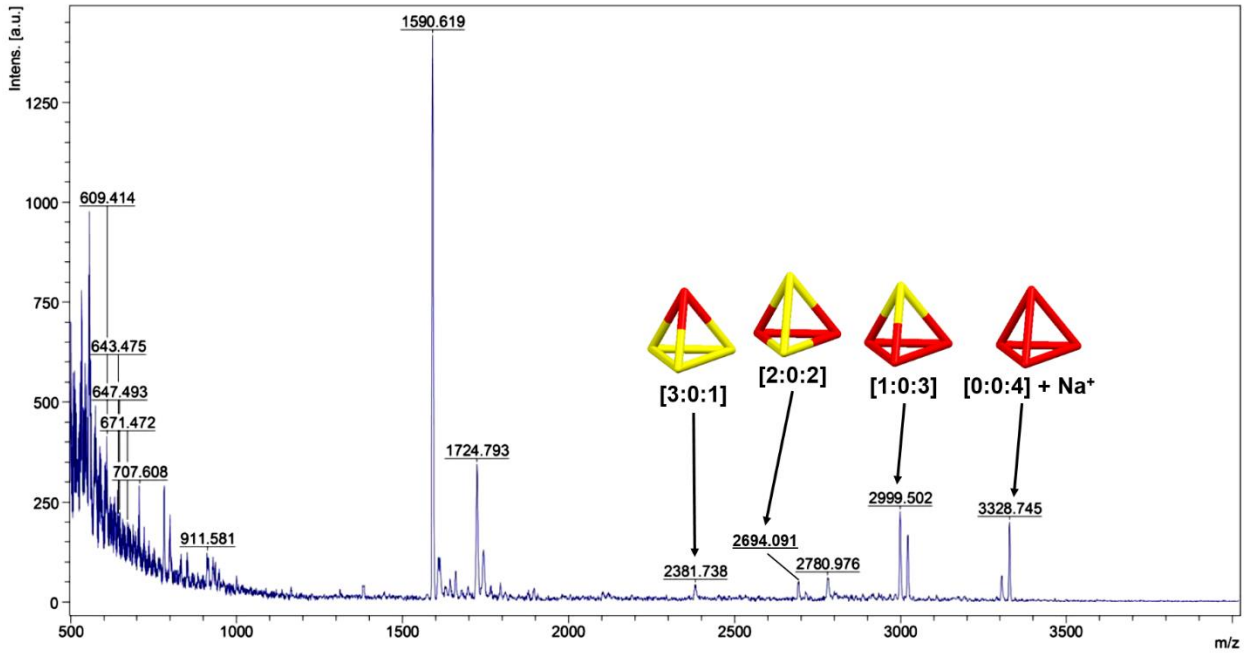

Figure 2.21: *MALDI-MS spectrum of the product distribution from metathesis of a 1:1 mixture of* $\boldsymbol{P_{Sulf}}$**:**$\boldsymbol{P_{Oxy}}$ *(DHB matrix).*

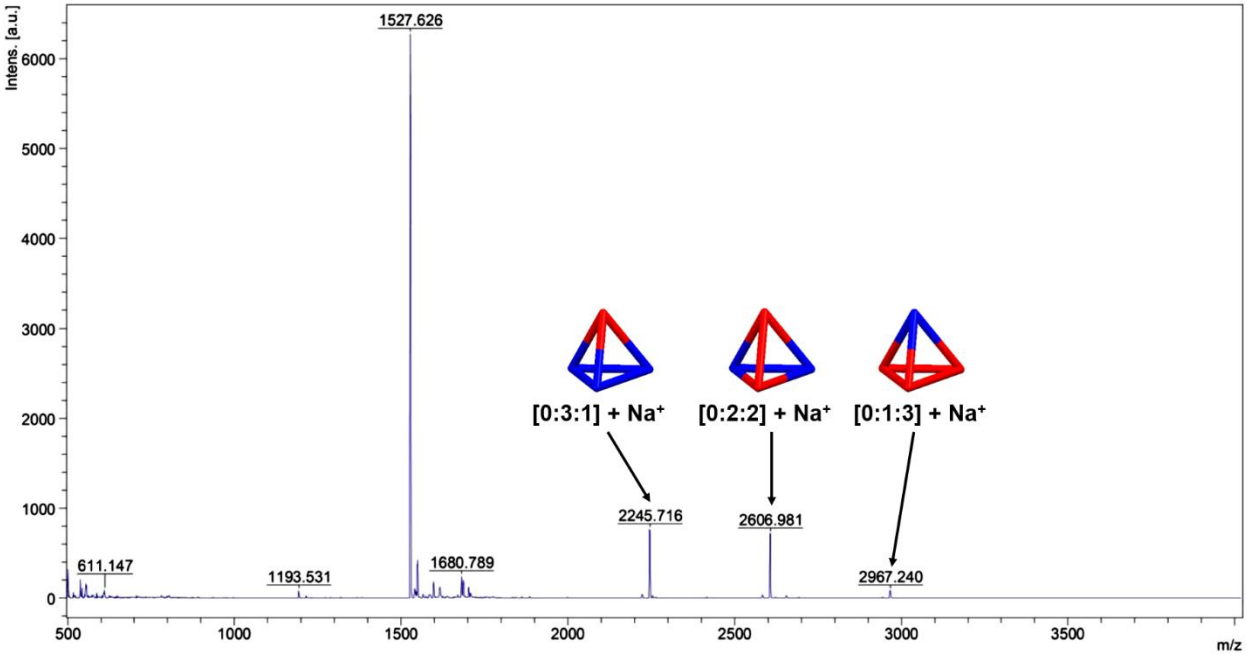

Figure 2.22: *MALDI-MS spectrum of the product distribution from metathesis of a 1:1 mixture of* $\boldsymbol{P_{Carb}}$**:**$\boldsymbol{P_{Oxy}}$ *(DHB matrix).*

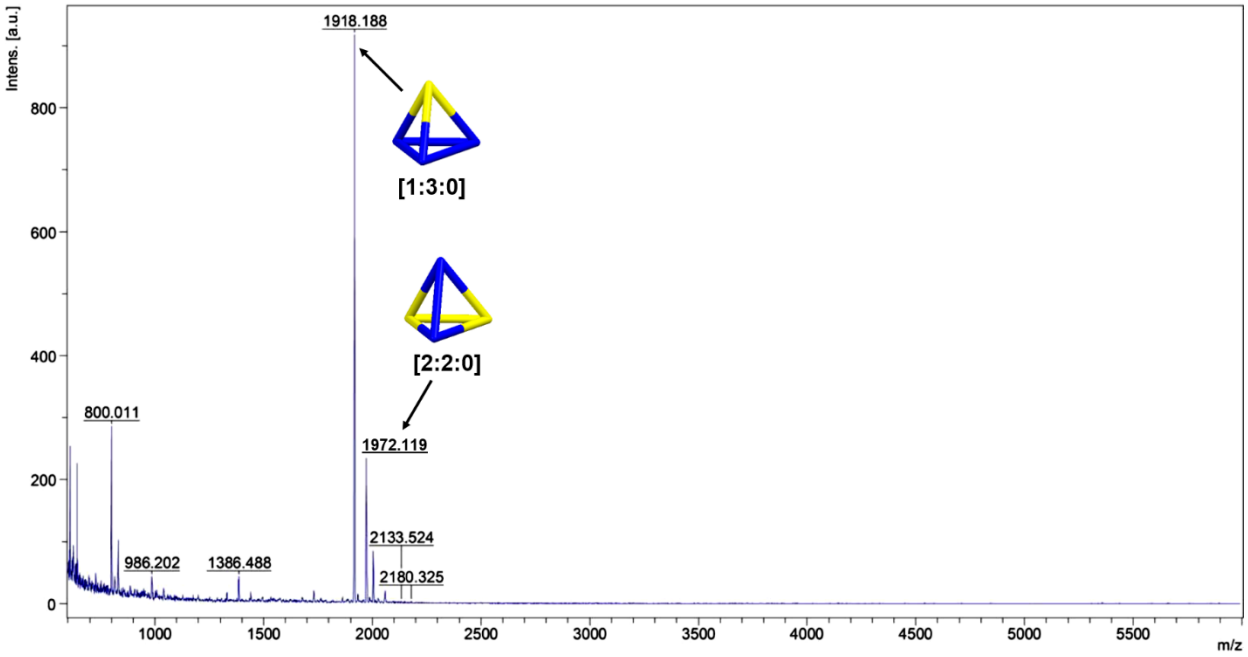

Figure 2.23: *MALDI-MS spectrum of the product distribution from metathesis of a 1:3 mixture of* $\boldsymbol{P_{Sulf}}$**:**$\boldsymbol{P_{Carb}}$ *(DHB matrix).*

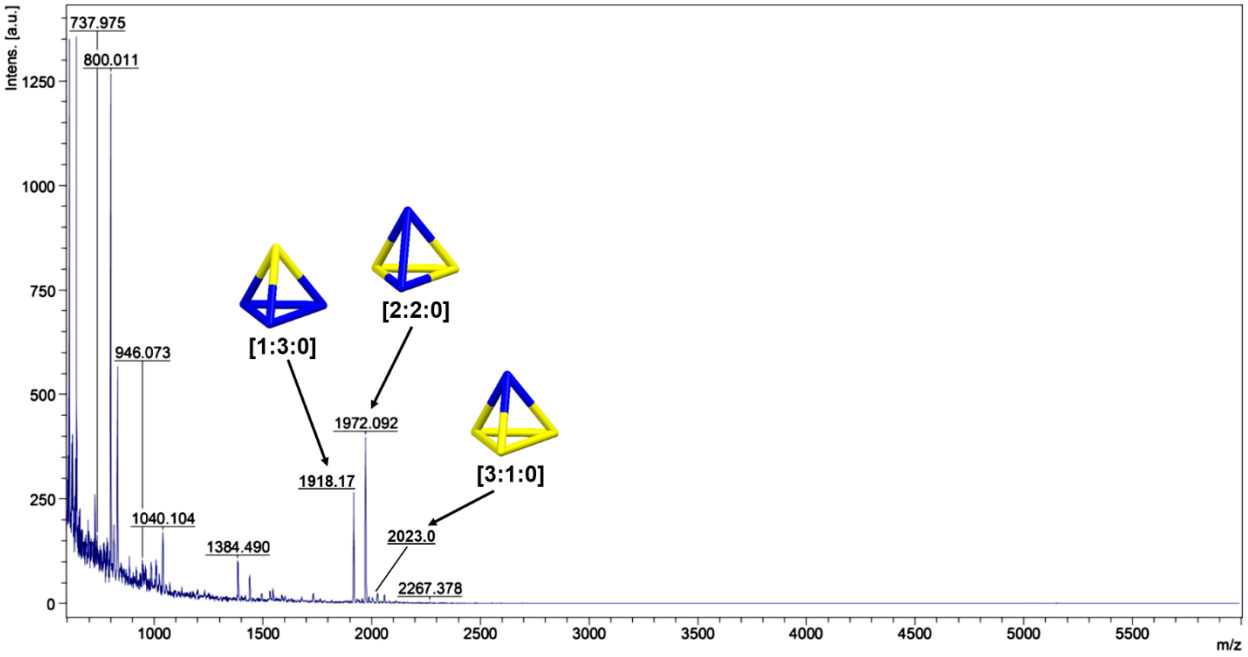

Figure 2.24: *MALDI-MS spectrum of the product distribution from metathesis of a 1:1 mixture of* $\boldsymbol{P_{Sulf}}$**:**$\boldsymbol{P_{Carb}}$ *(DHB matrix).*

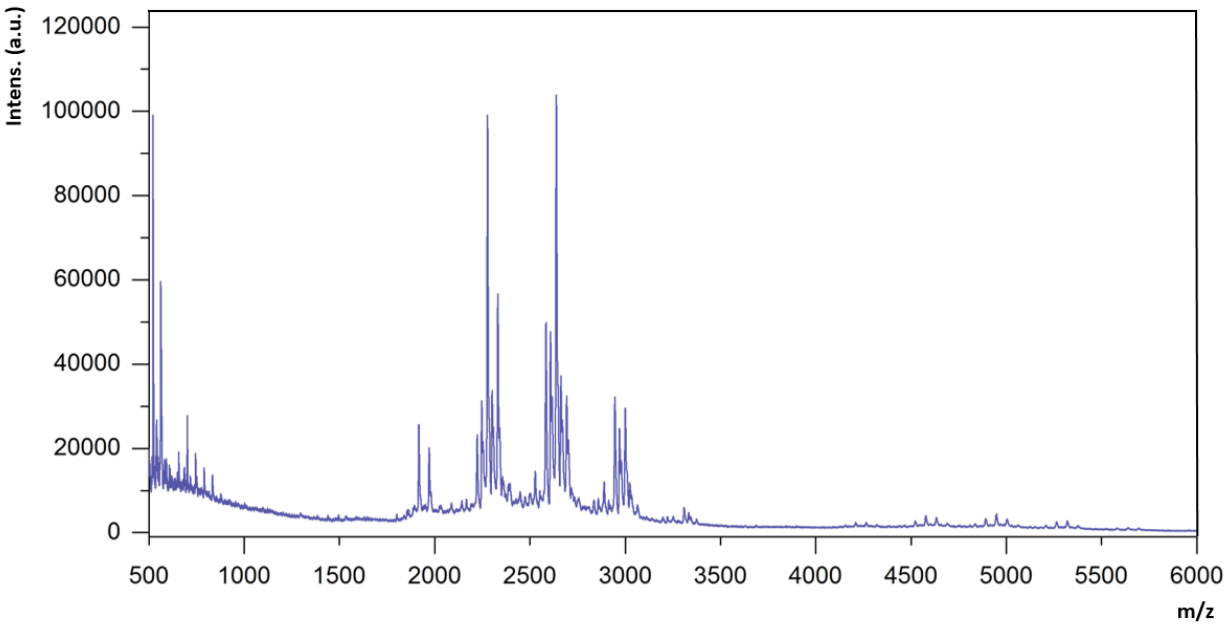

Figure 2.25: *MALDI-MS spectrum of the product distribution from metathesis of a 1:1:1 mixture of* $\boldsymbol{P_{Sulf}:P_{Carb}:P_{Oxy}}$ *(DCTB matrix).*

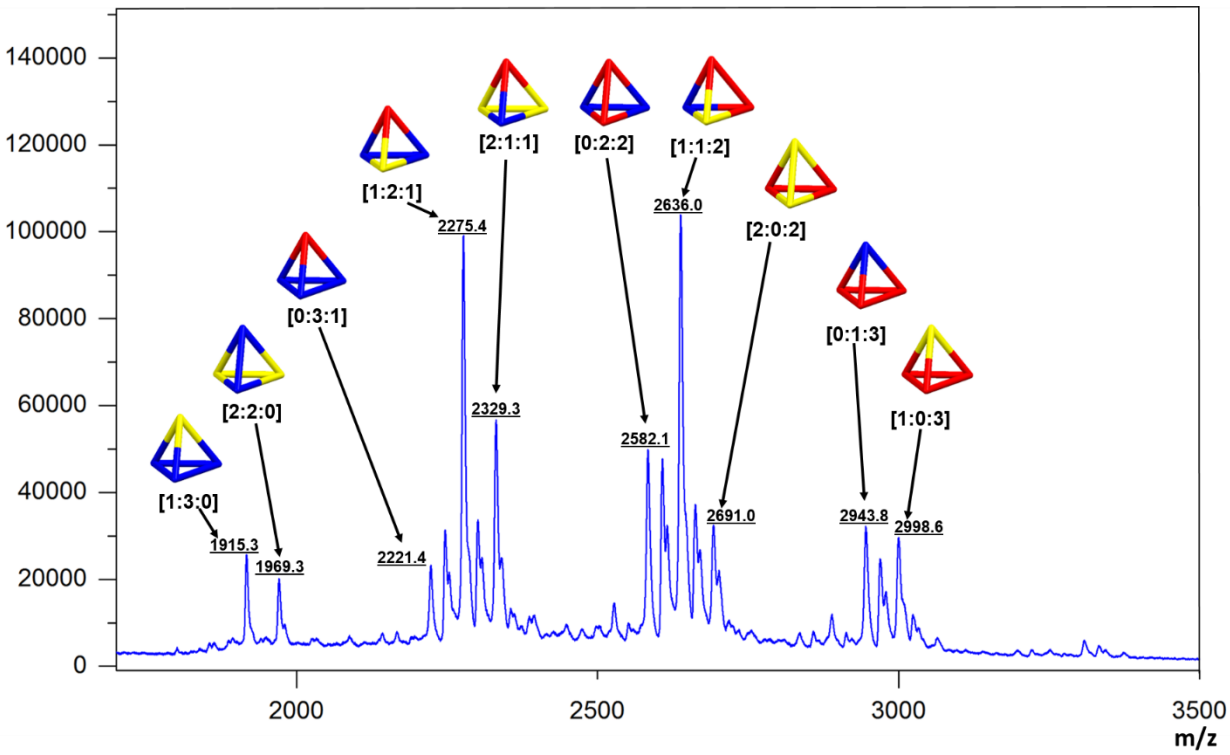

Figure 2.26: *Zoomed-in MALDI-MS spectrum of the product distribution from metathesis of a 1:1:1 mixture of* $\boldsymbol{P_{Sulf}:P_{Carb}:P_{Oxy}}$ *(DCTB matrix).*

^{1}H and ^{13}C NMR Spectra

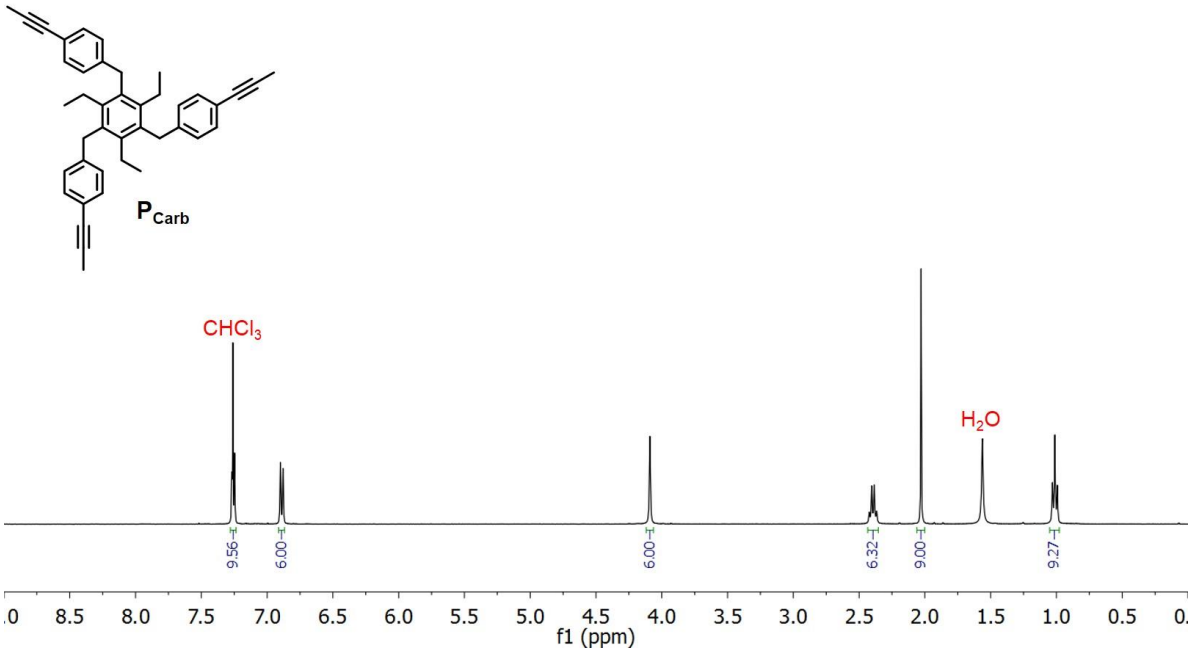

Figure 2.27: *^{1}H NMR of **P_{Carb}** (400 MHz, $CDCl_3$).*

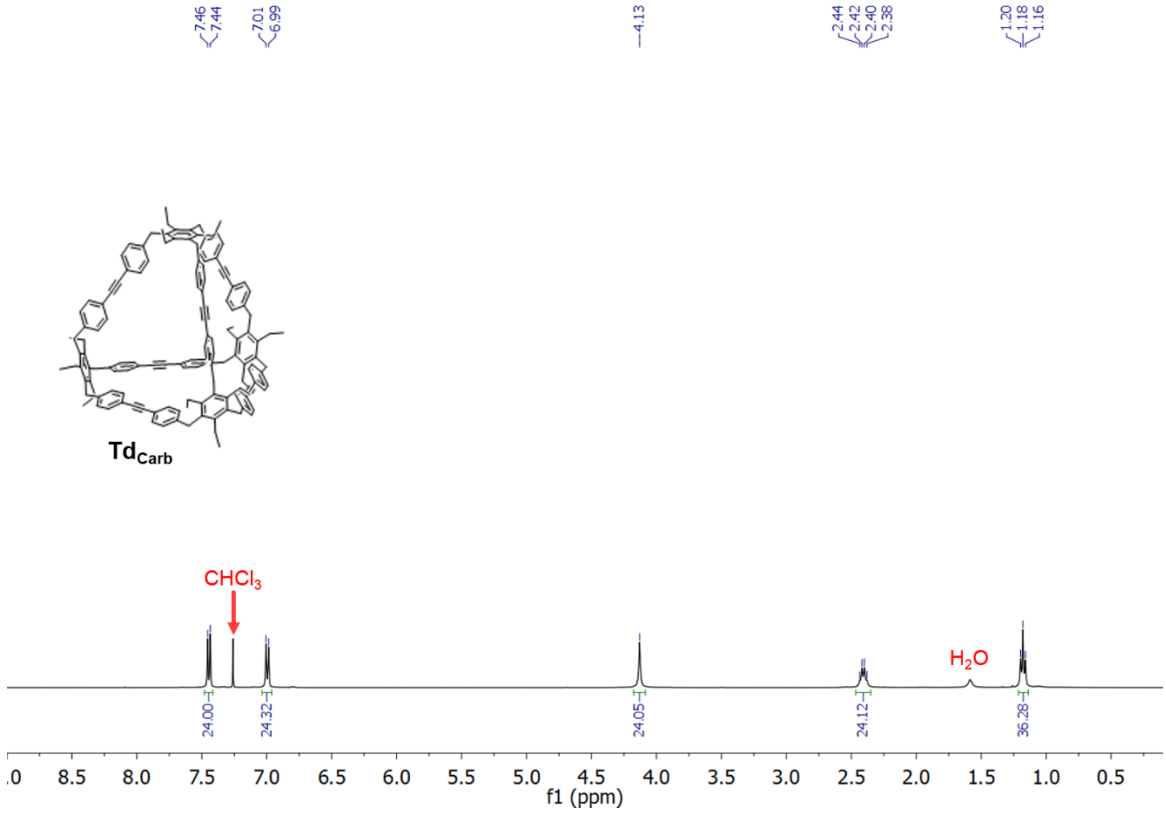

Figure 2.28: *^{1}H NMR of **Td_{Carb}** (400 MHz, $CDCl_3$).*

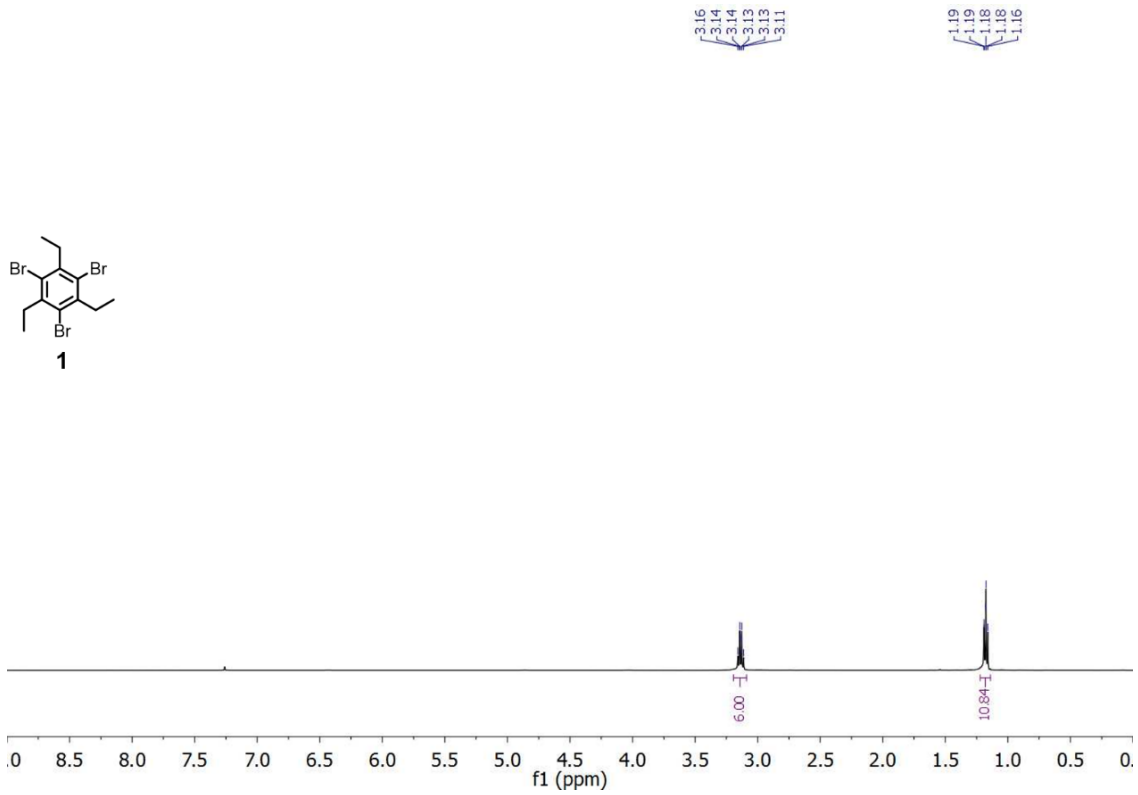

Figure 2.29: *^{1}H NMR of **1** (400 MHz, $CDCl_3$).*

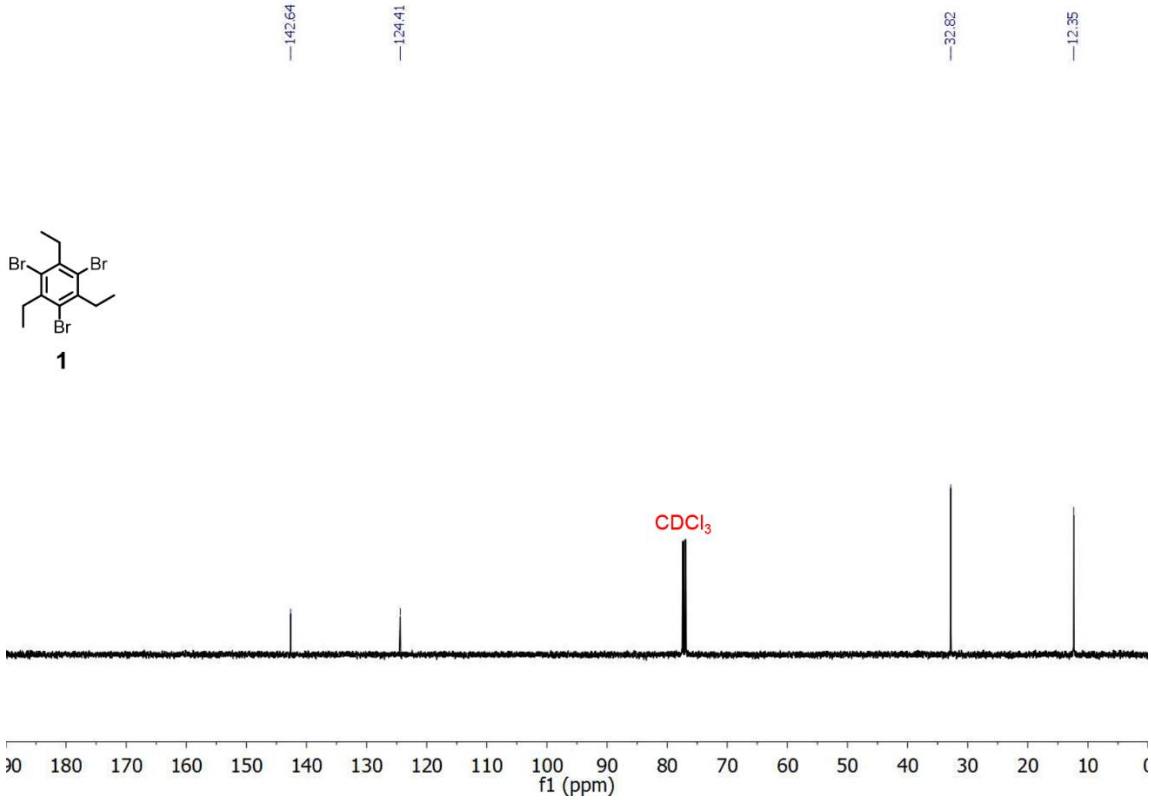

Figure 2.30: *^{13}C NMR of **1** (125 MHz, $CDCl_3$).*

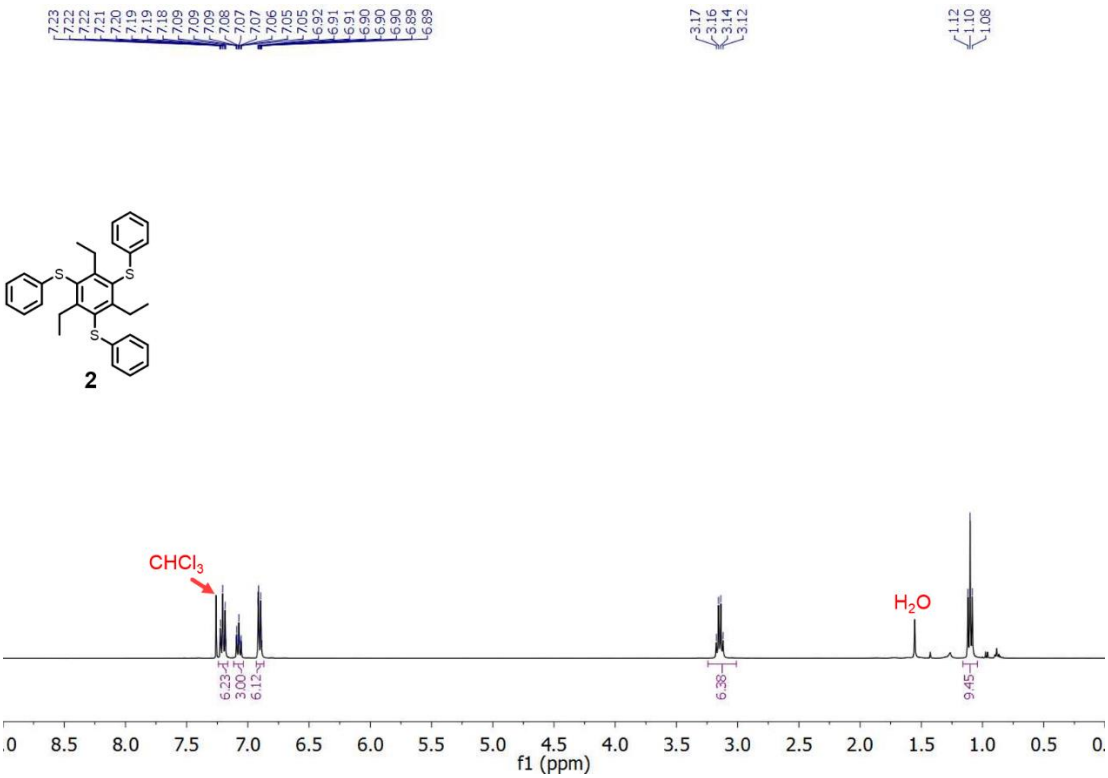

Figure 2.31: *^{1}H NMR of **2** (400 MHz, $CDCl_3$).*

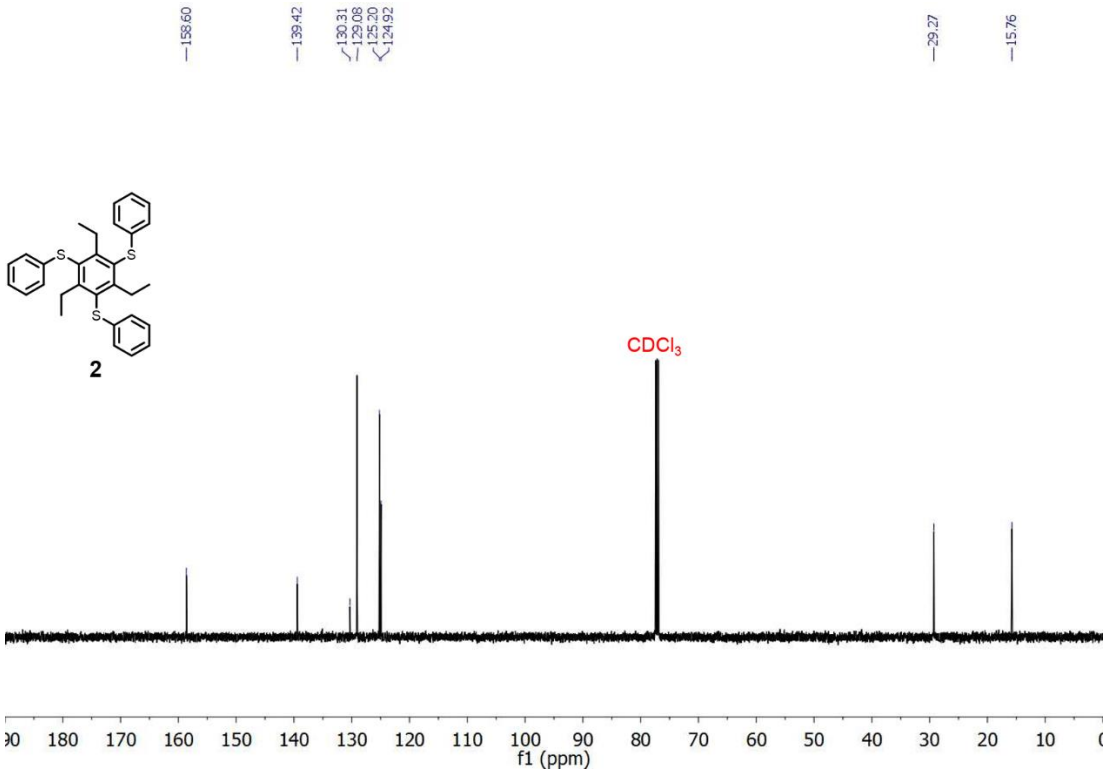

Figure 2.32: *^{13}C NMR of **2** (125 MHz, $CDCl_3$).*

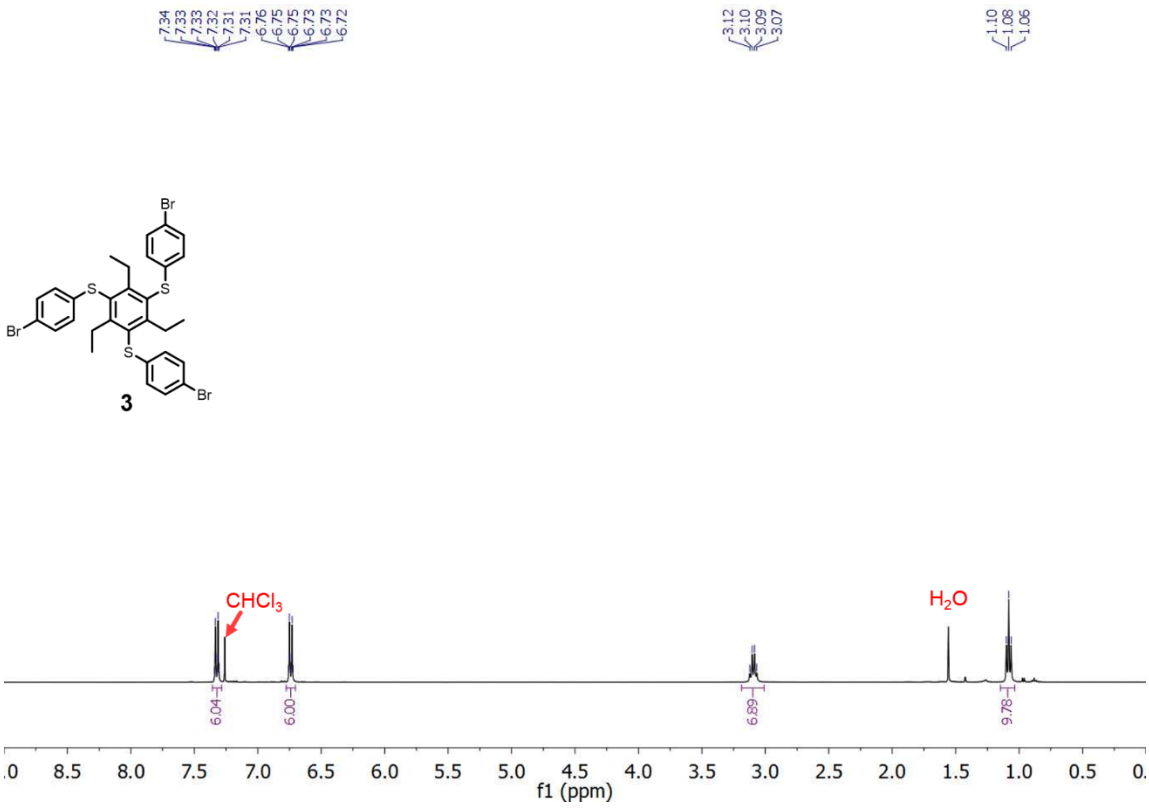

Figure 2.33: *^{1}H NMR of **3** (400 MHz, $CDCl_3$).*

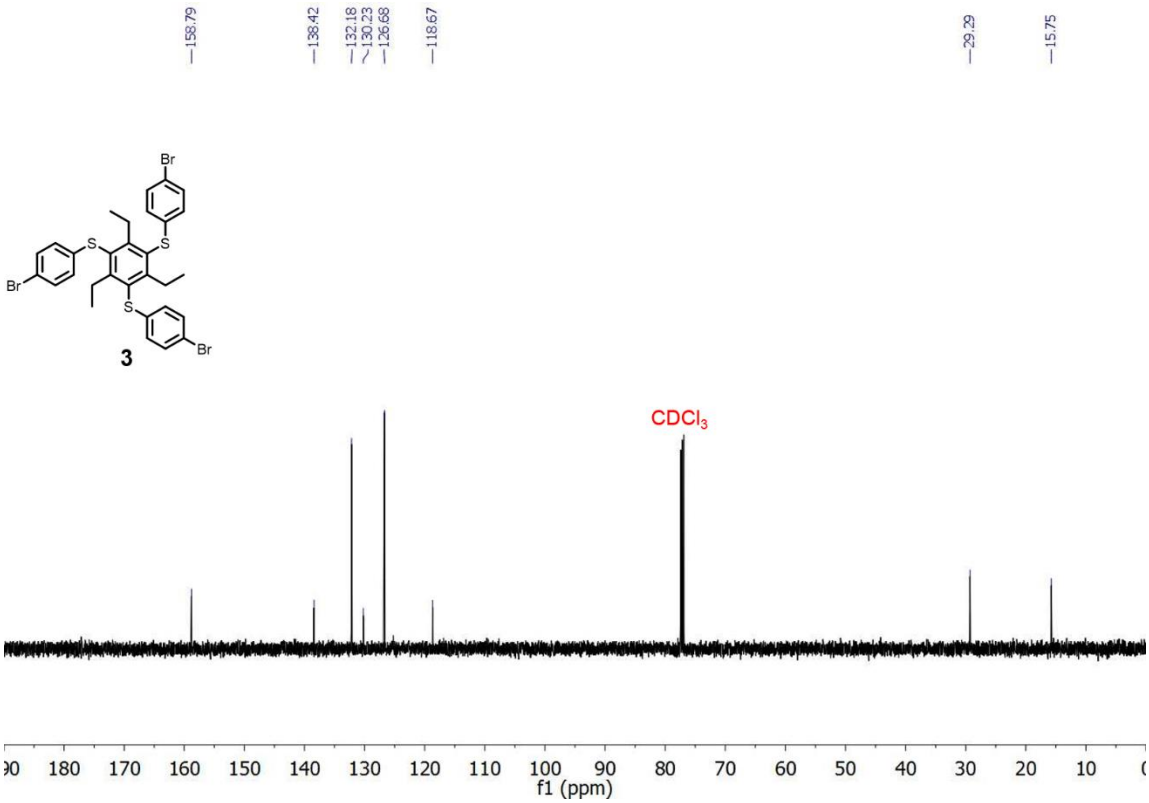

Figure 2.34: *^{13}C NMR of **3** (125 MHz, $CDCl_3$).*

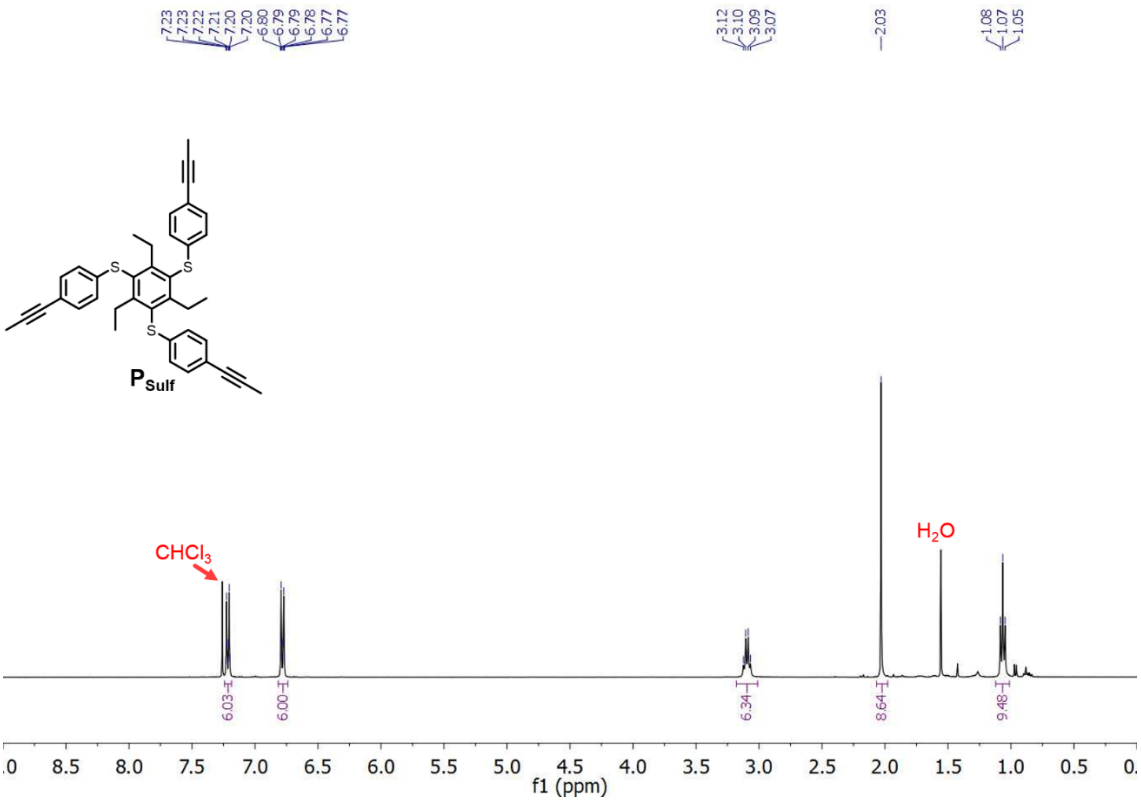

Figure 2.35: *^{1}H NMR of **P_{Sulf}** (400 MHz, $CDCl_3$).*

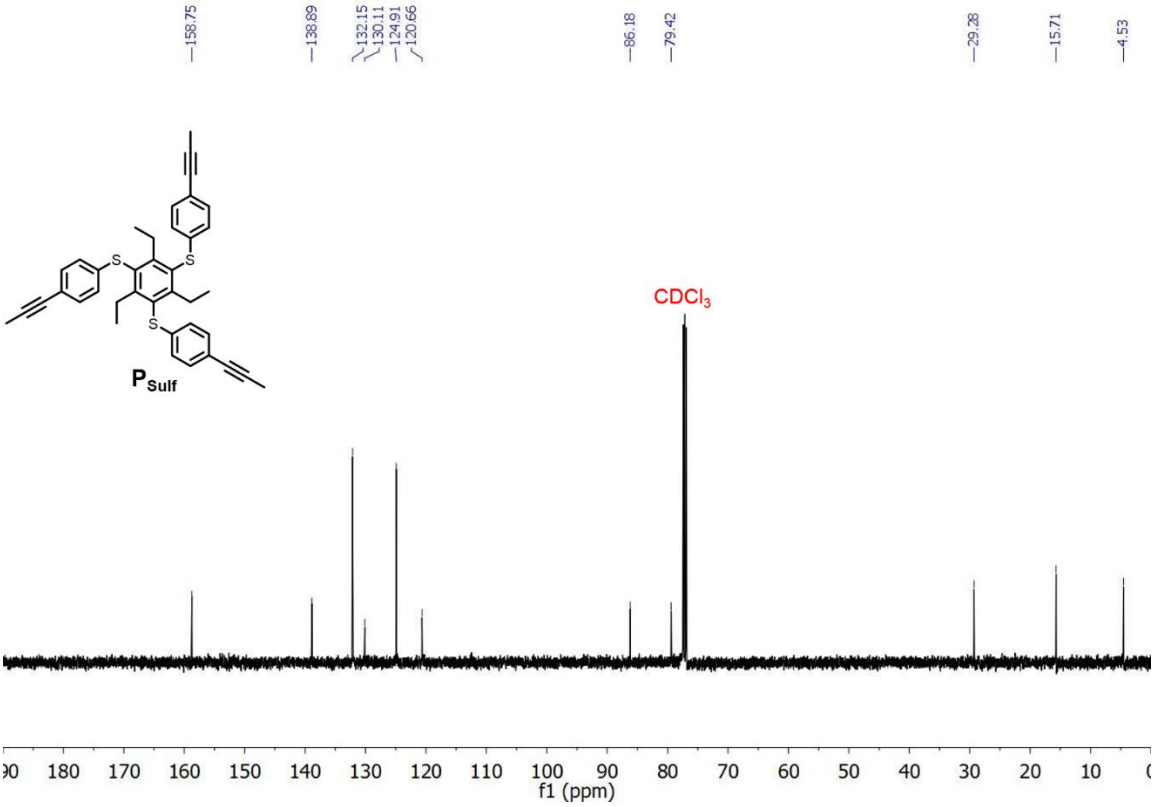

Figure 2.36: *^{13}C NMR of **P_{Sulf}** (125 MHz, $CDCl_3$).*

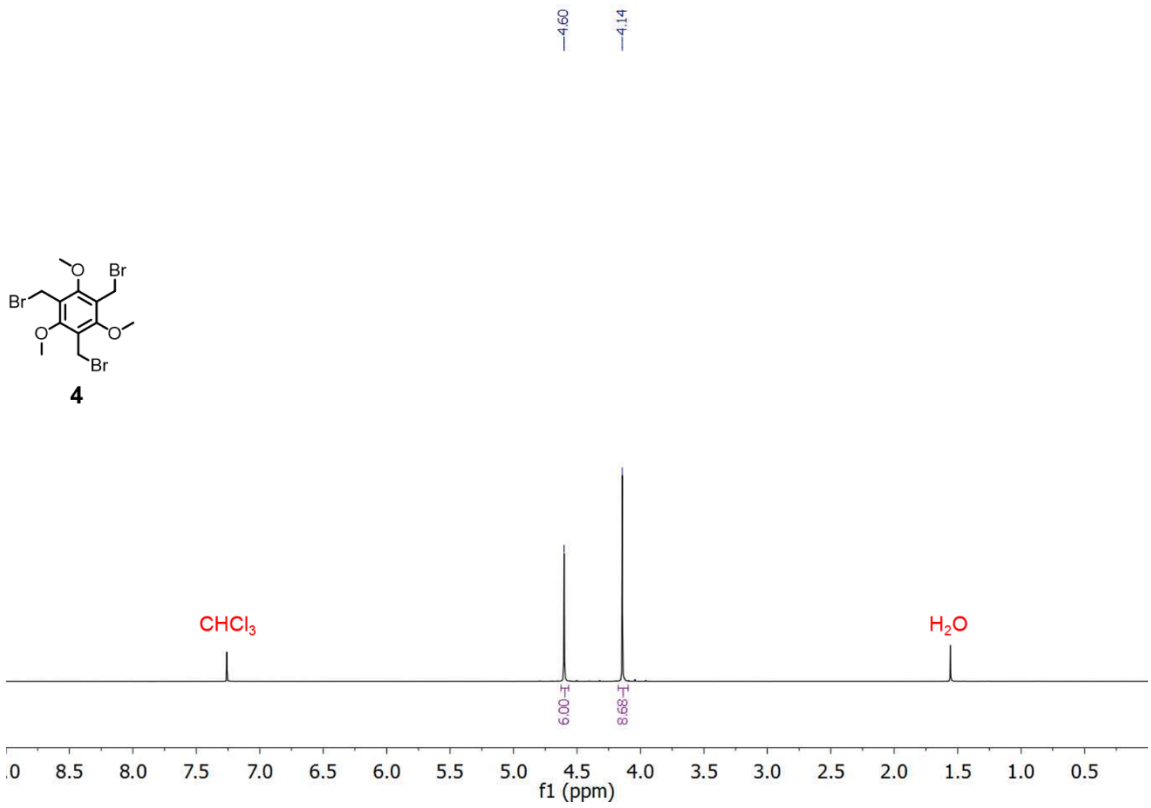

Figure 2.37: *^{1}H NMR of **4** (400 MHz, $CDCl_3$).*

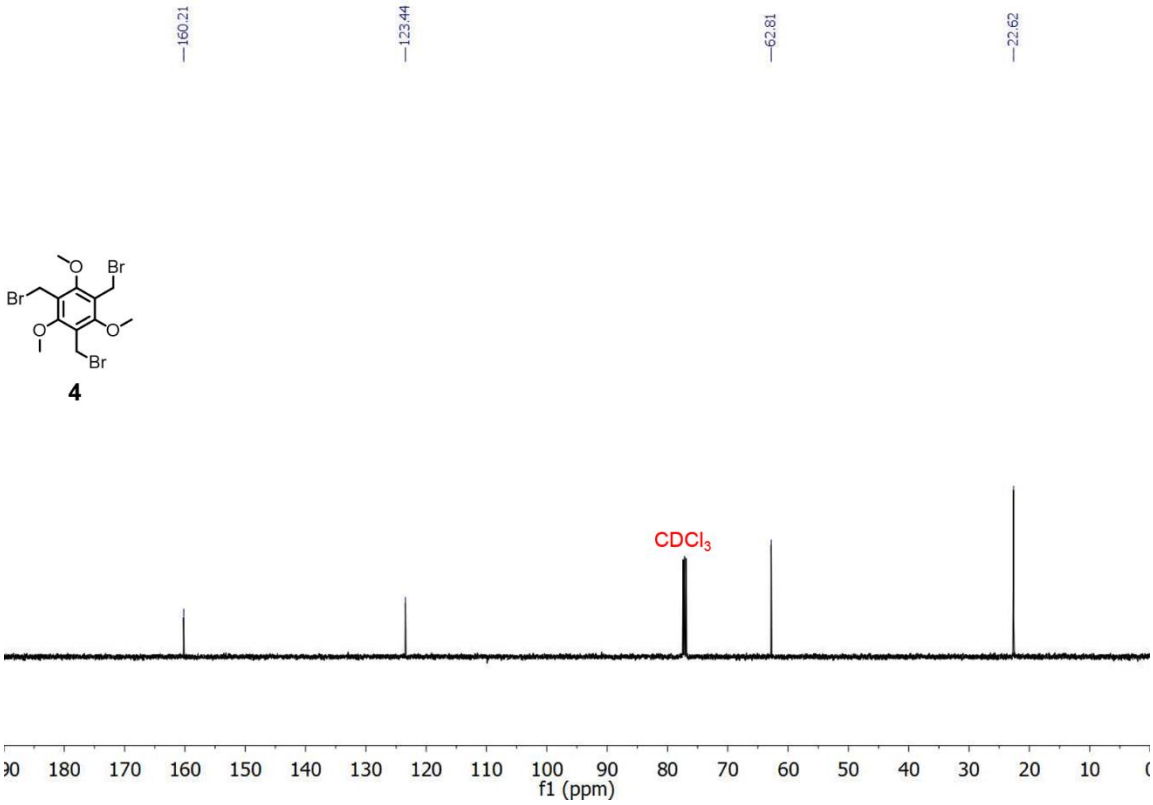

Figure 2.38: *^{13}C NMR of **4** (125 MHz, $CDCl_3$).*

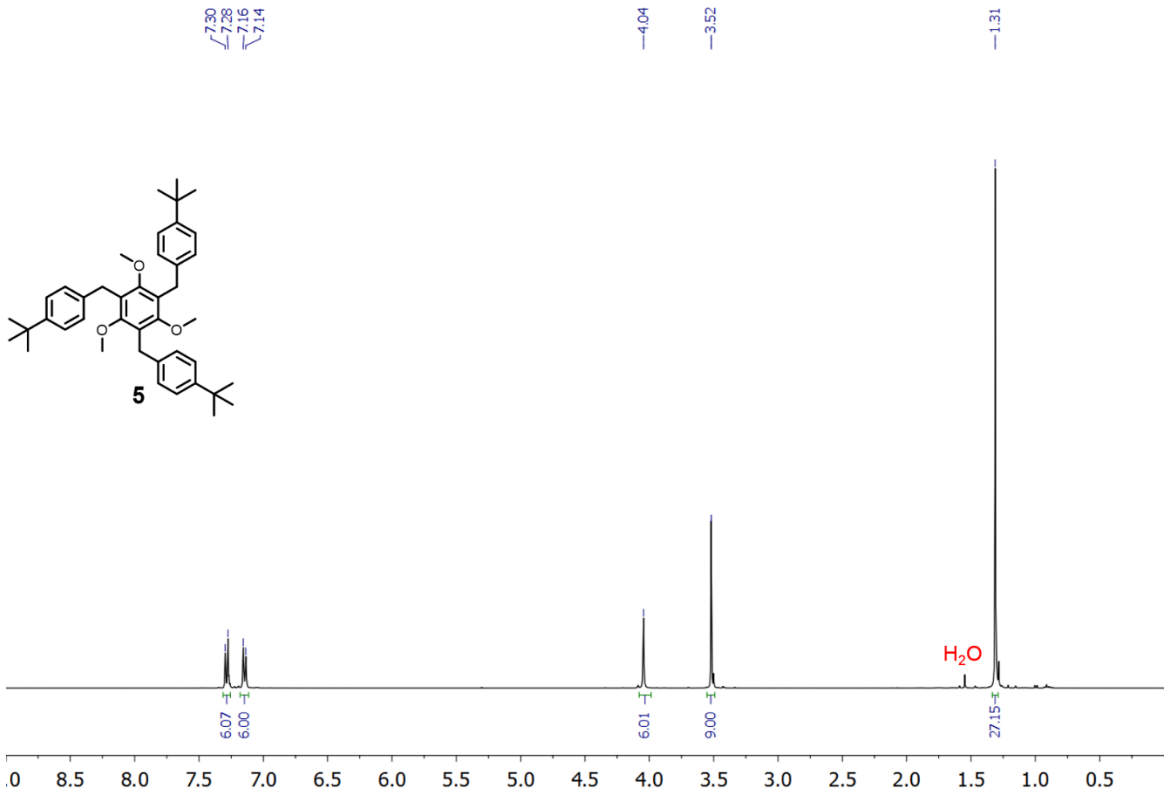

Figure 2.39: *^{1}H NMR of **5** (500 MHz, $CDCl_3$).*

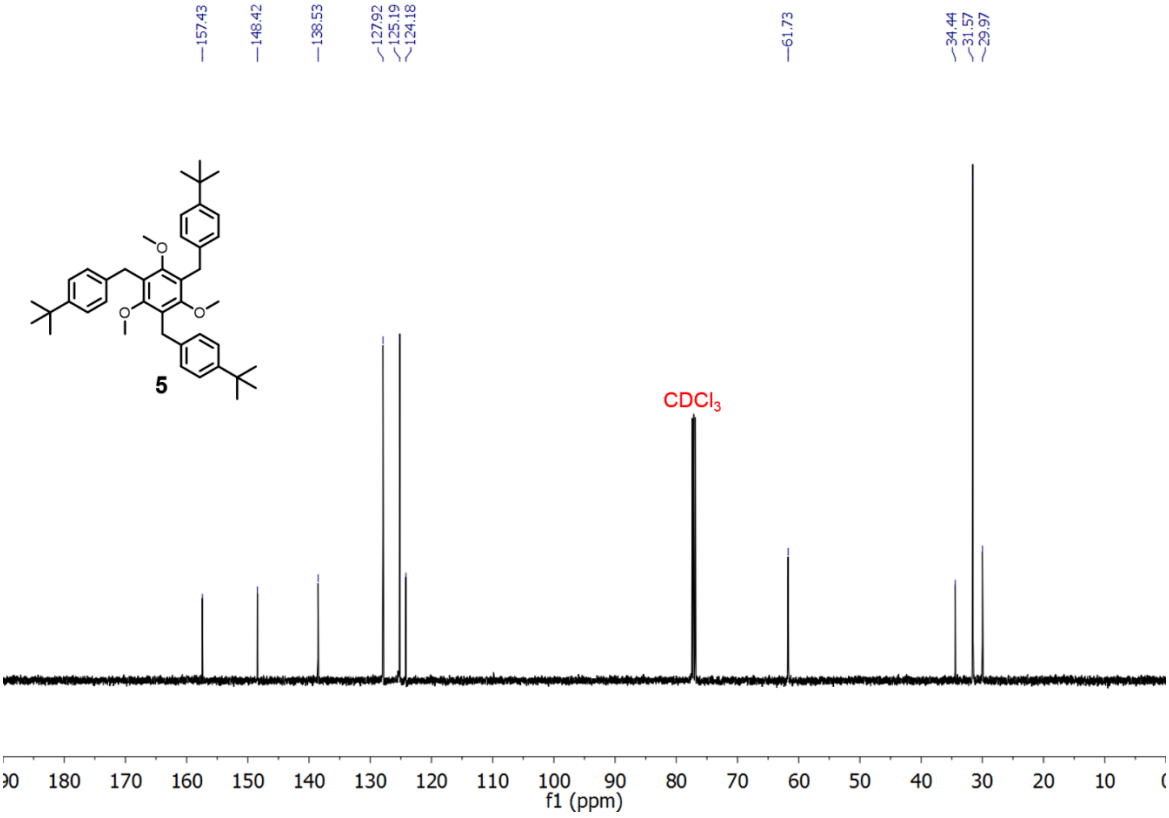

Figure 2.40: *^{13}C NMR of **5** (125 MHz, $CDCl_3$).*

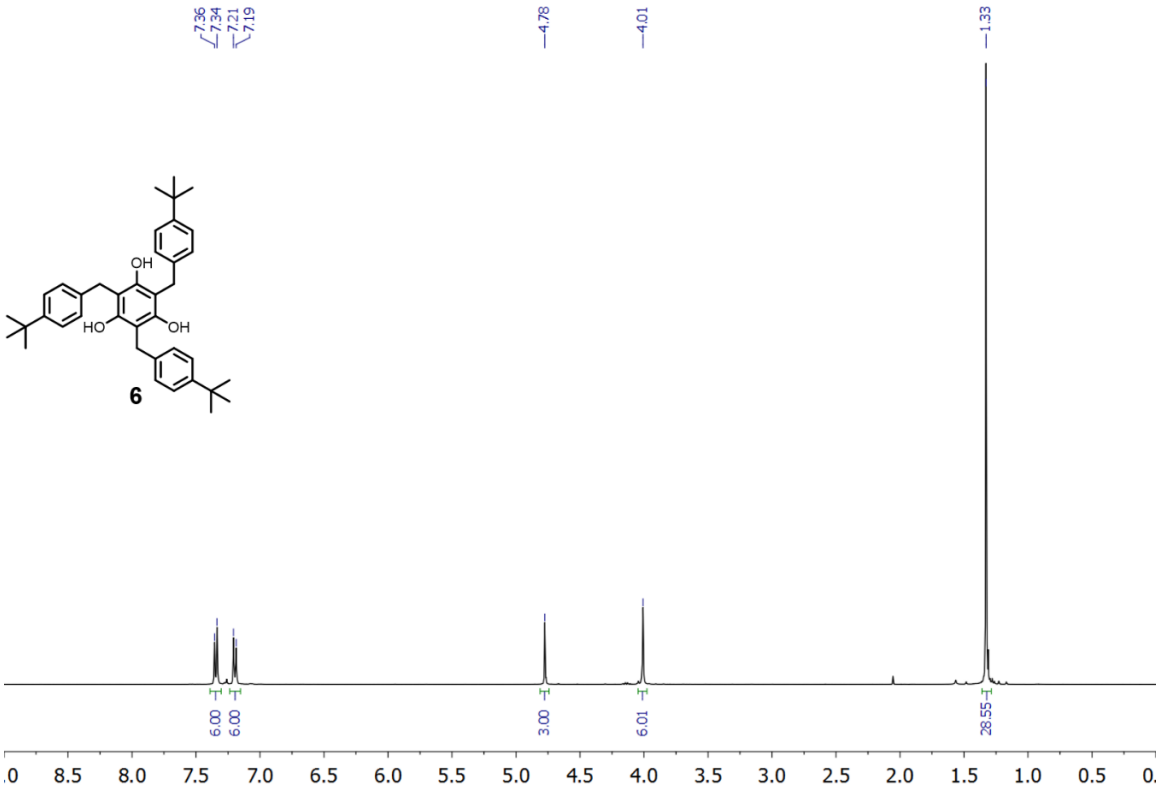

Figure 2.41: *^{1}H NMR of **6** (500 MHz, $CDCl_3$).*

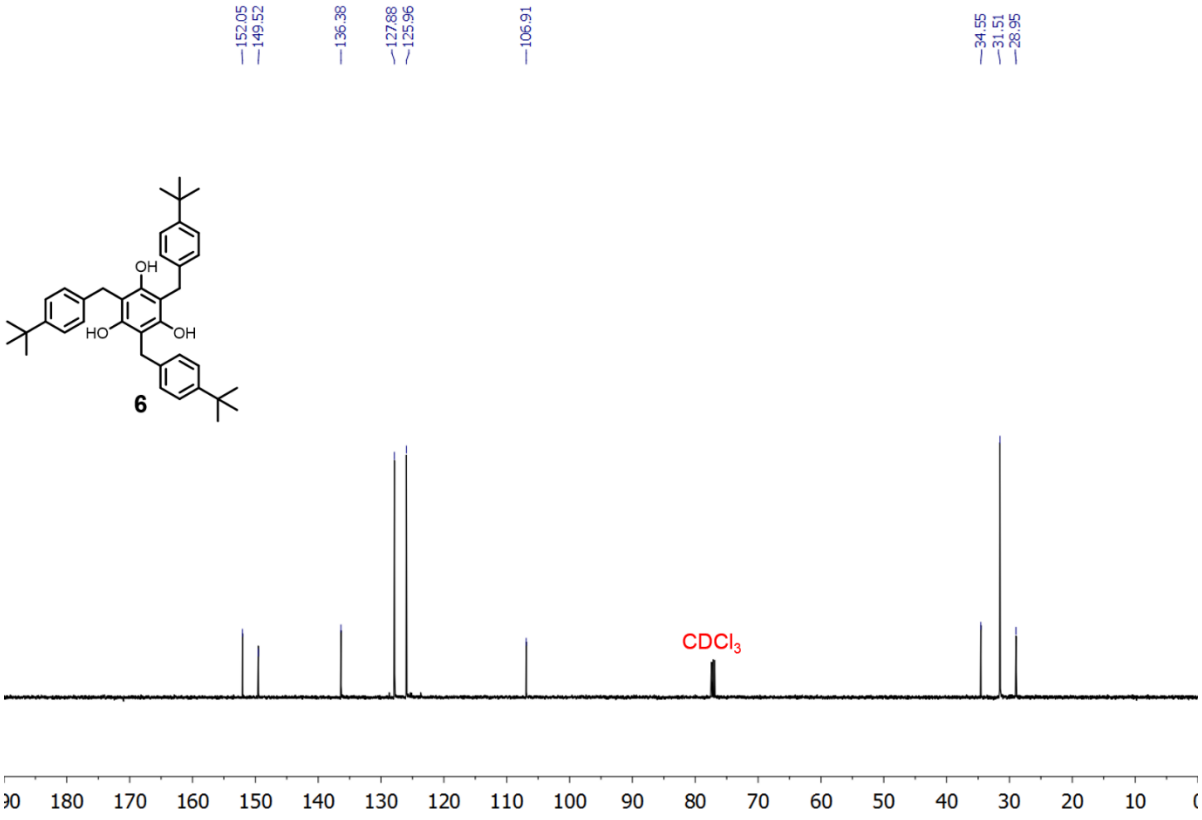

Figure 2.42: *^{13}C NMR of **6** (125 MHz, $CDCl_3$).*

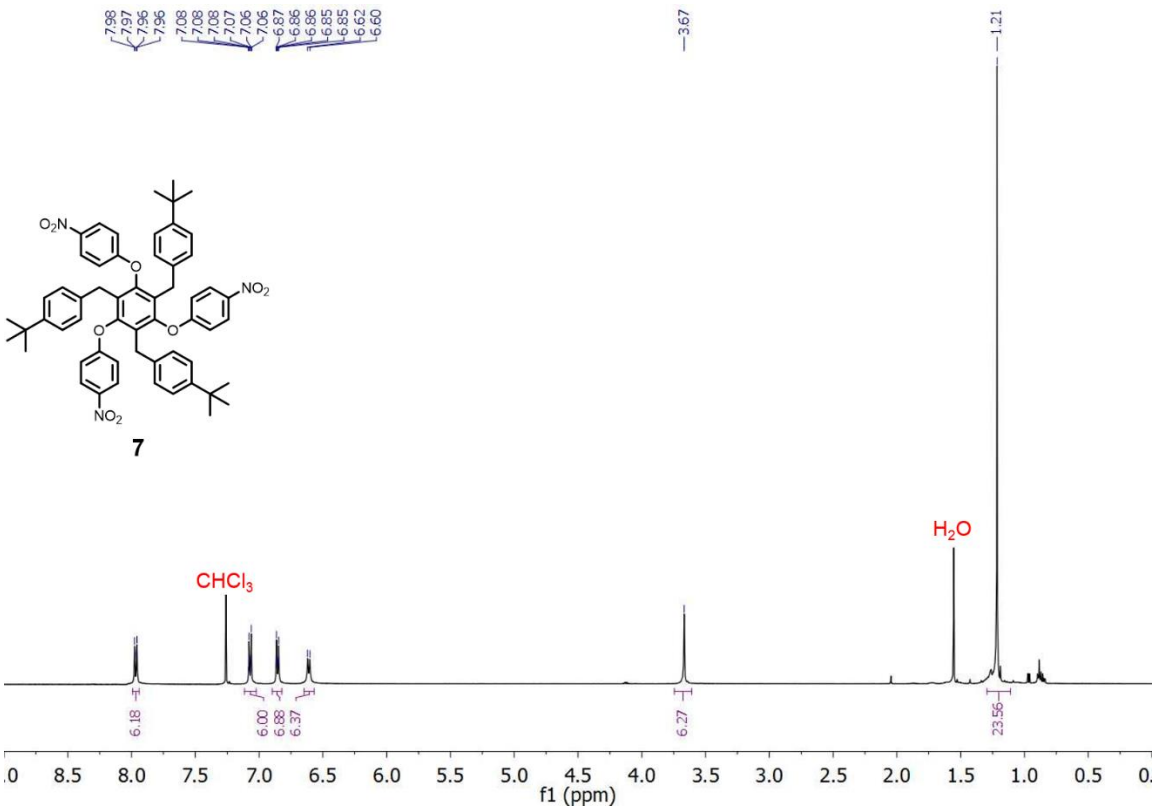

Figure 2.43: *^{1}H NMR of **7** (400 MHz, $CDCl_3$).*

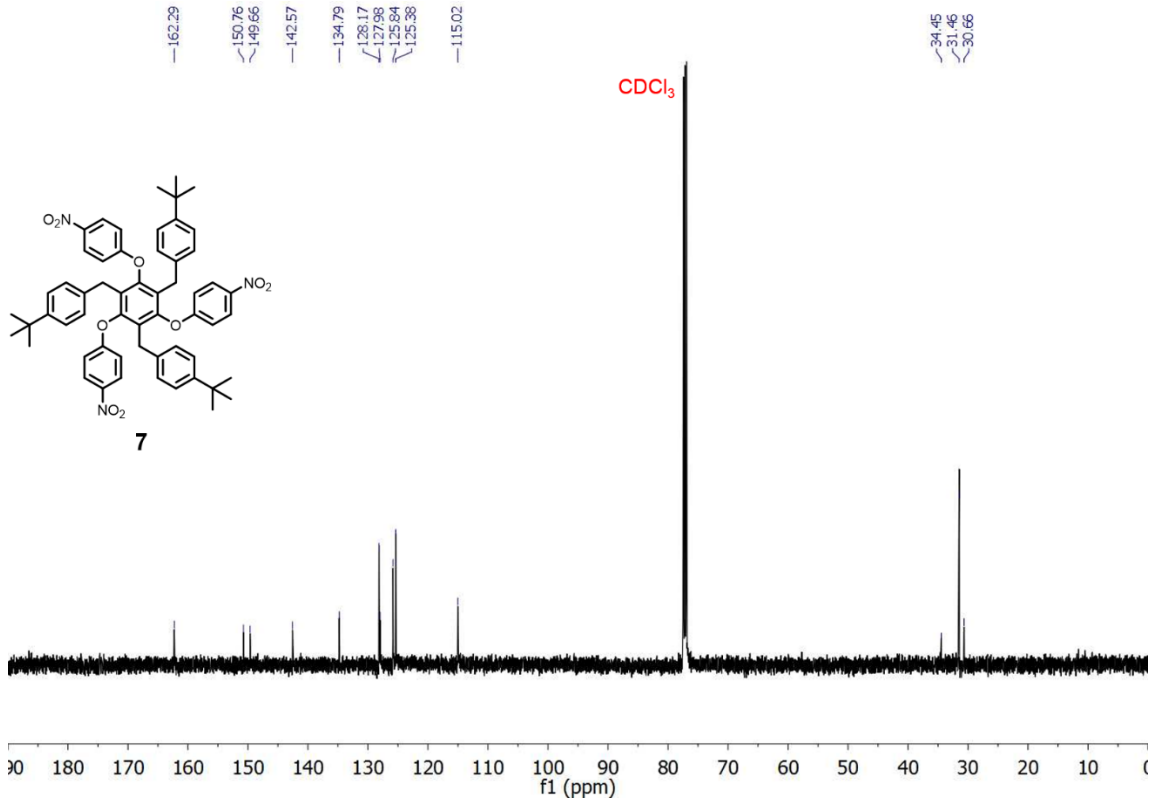

Figure 2.44: *^{13}C NMR of **7** (125 MHz, $CDCl_3$).*

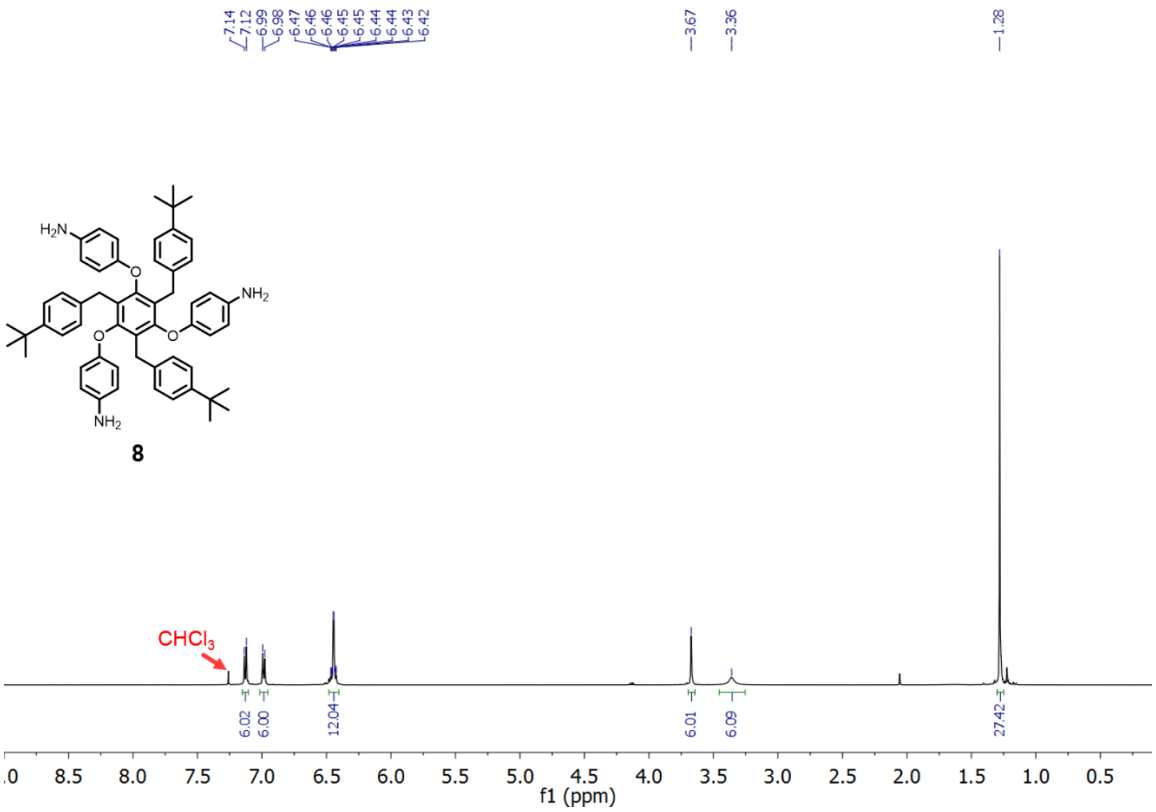

Figure 2.45: *^{1}H NMR of **8** (500 MHz, $CDCl_3$).*

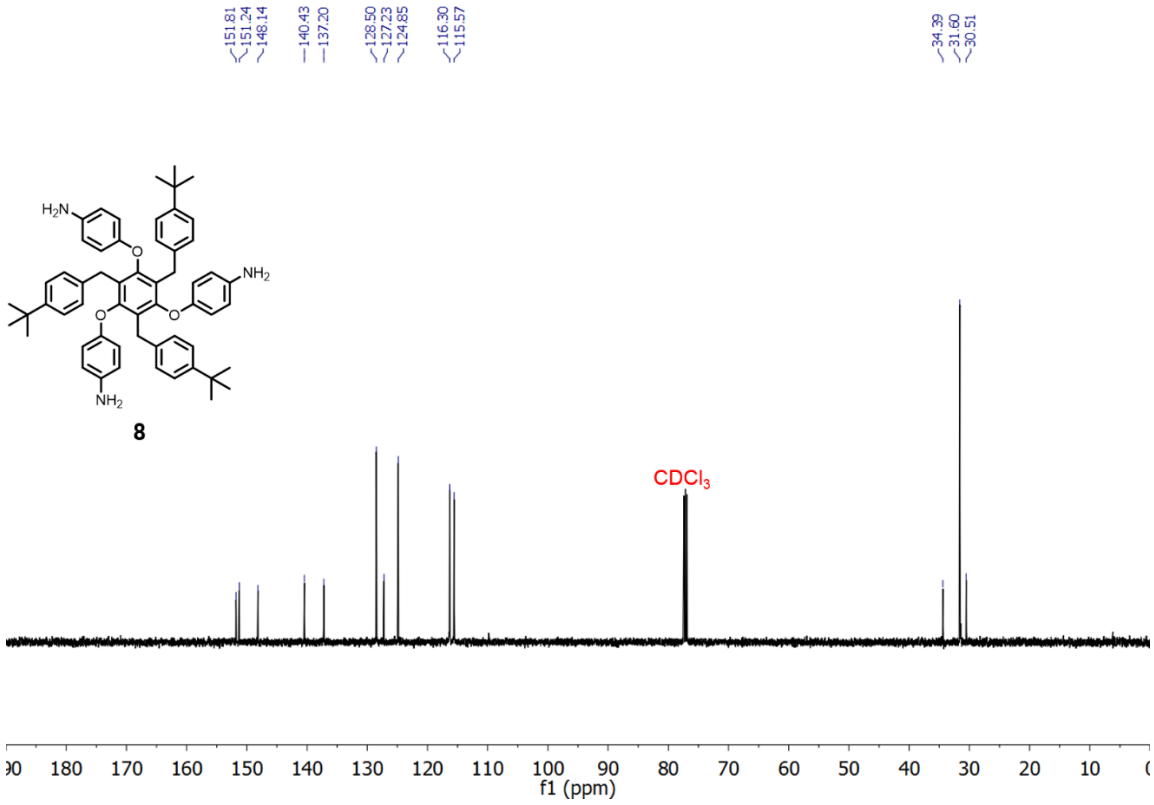

Figure 2.46: *^{13}C NMR of **8** (125 MHz, $CDCl_3$).*

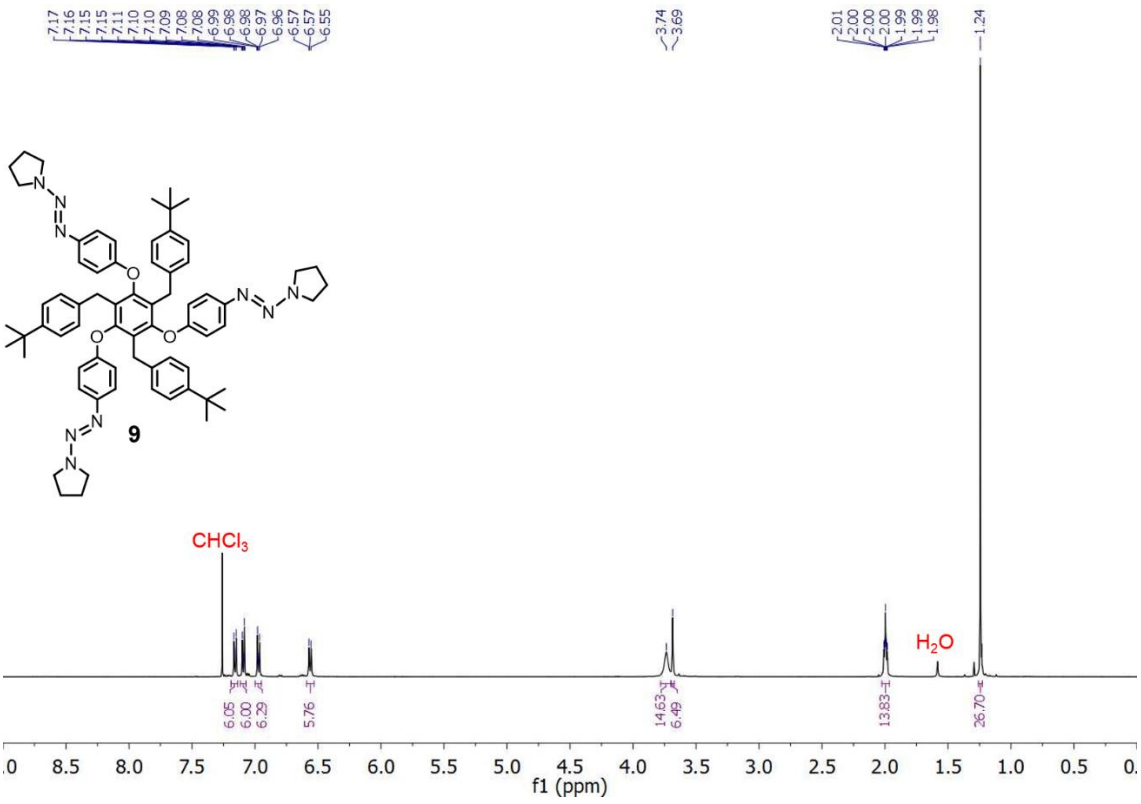

Figure 2.47: *^{1}H NMR of **9** (400 MHz, $CDCl_3$).*

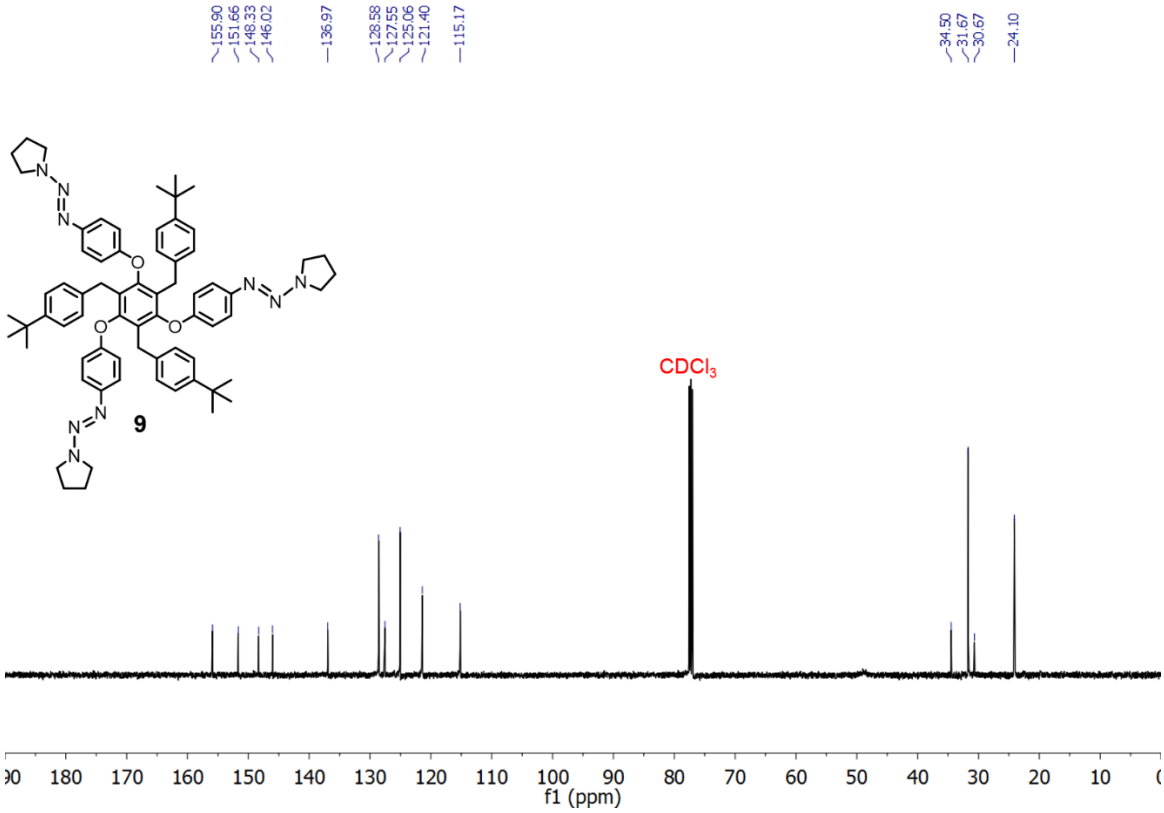

Figure 2.48: *^{13}C NMR of **9** (125 MHz, $CDCl_3$).*

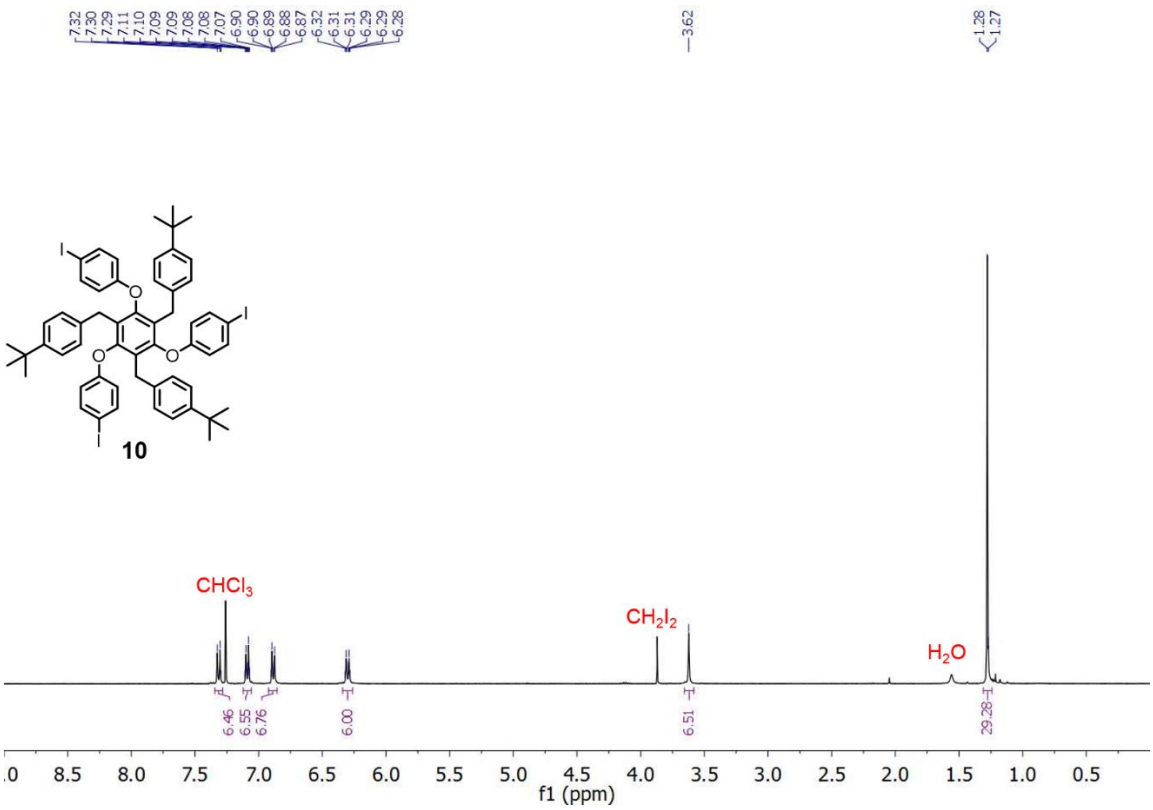

Figure 2.49: *^{1}H NMR of **10** (400 MHz, $CDCl_3$).*

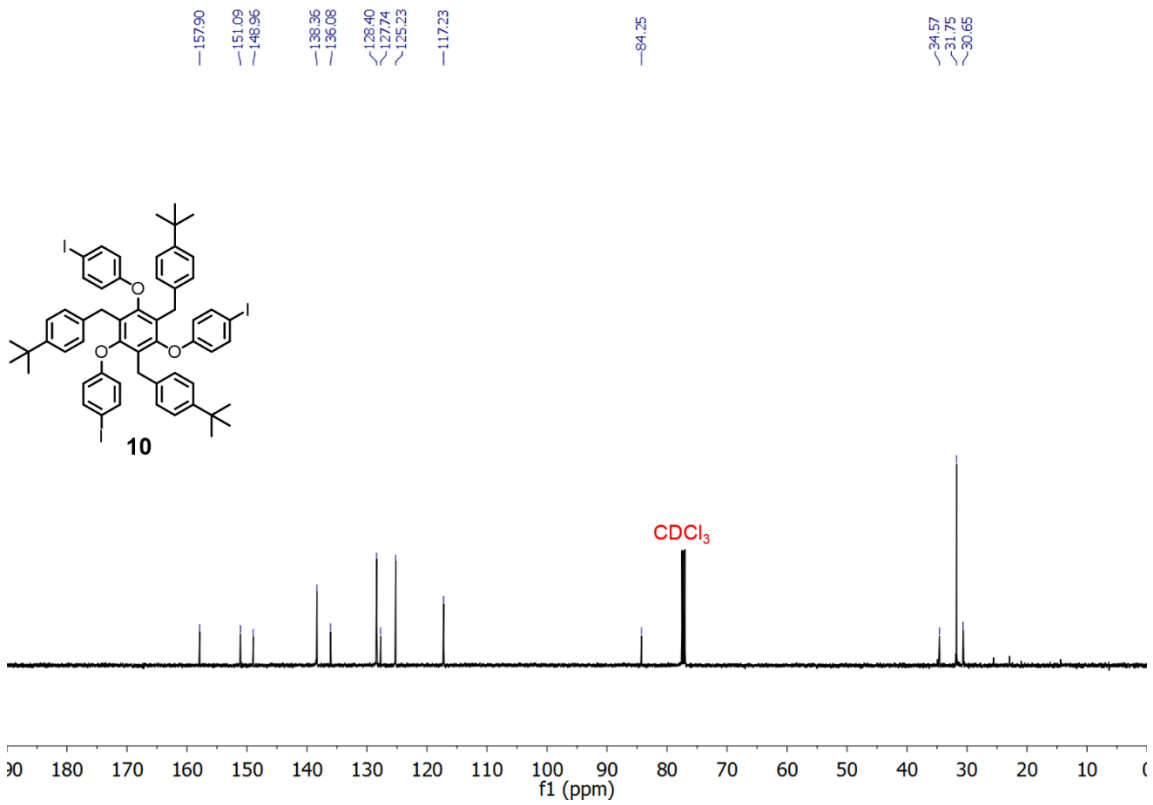

Figure 2.50: *^{13}C NMR of **10** (125 MHz, $CDCl_3$).*

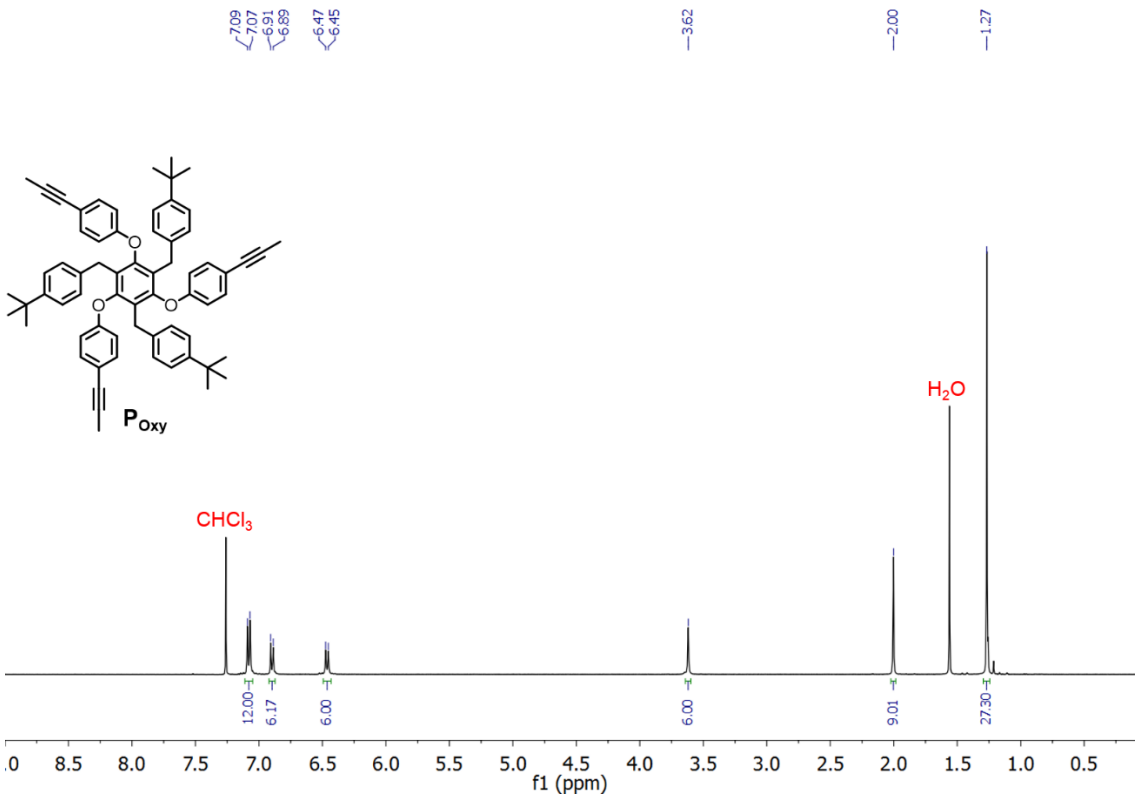

Figure 2.51: *^{1}H NMR of **P_{Oxy}** (500 MHz, $CDCl_3$).*

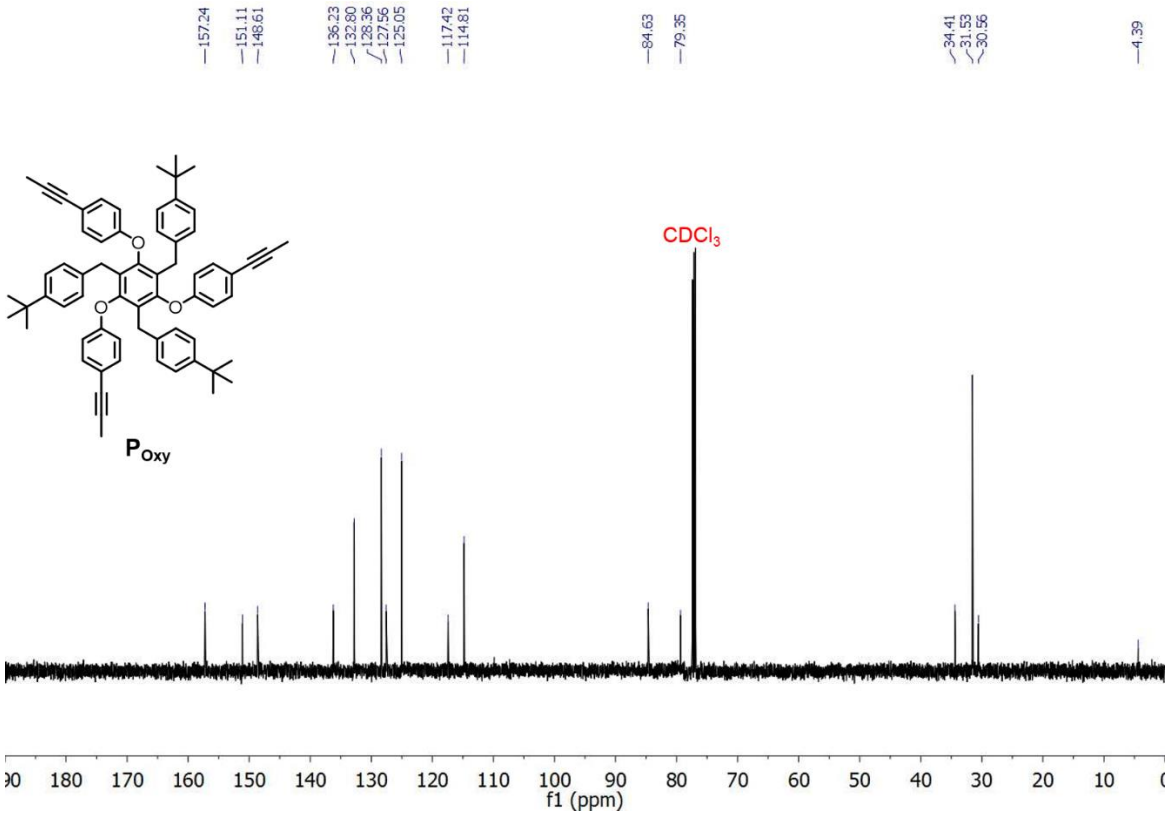

Figure 2.52: *^{13}C NMR of **P_{Oxy}** (125 MHz, $CDCl_3$).*

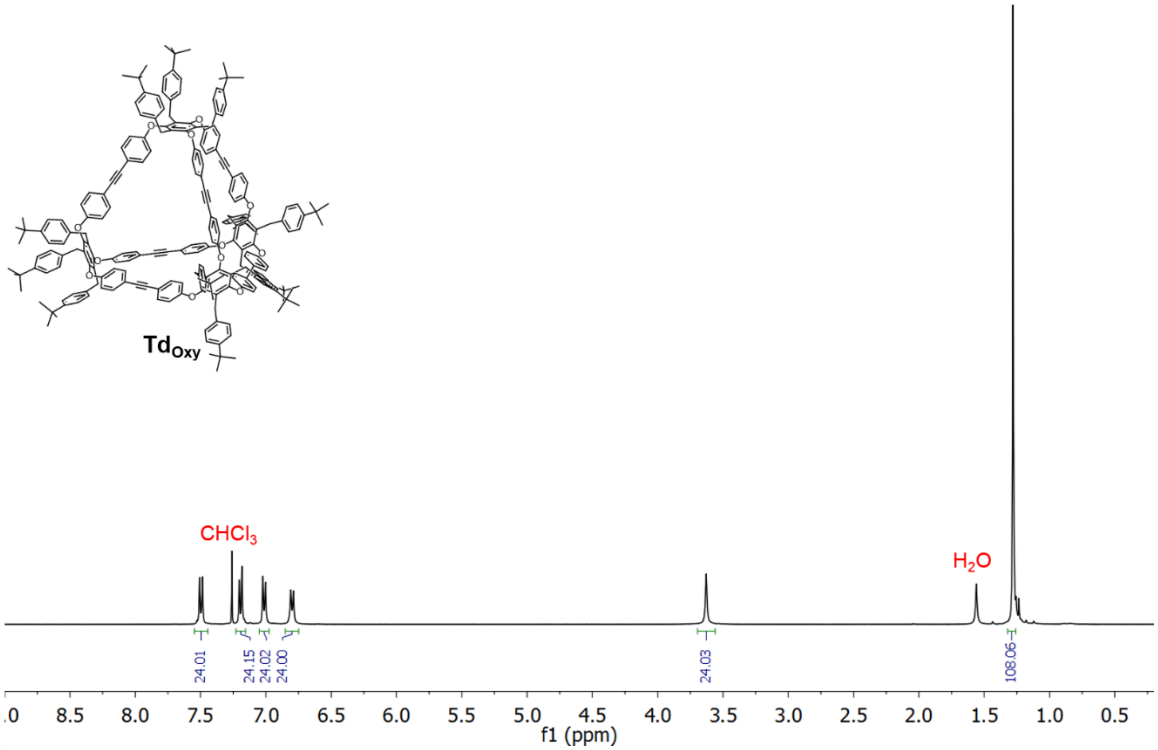

Figure 2.53: *^{1}H NMR of **Td$_{Oxy}$** (500 MHz, CDCl$_3$).*

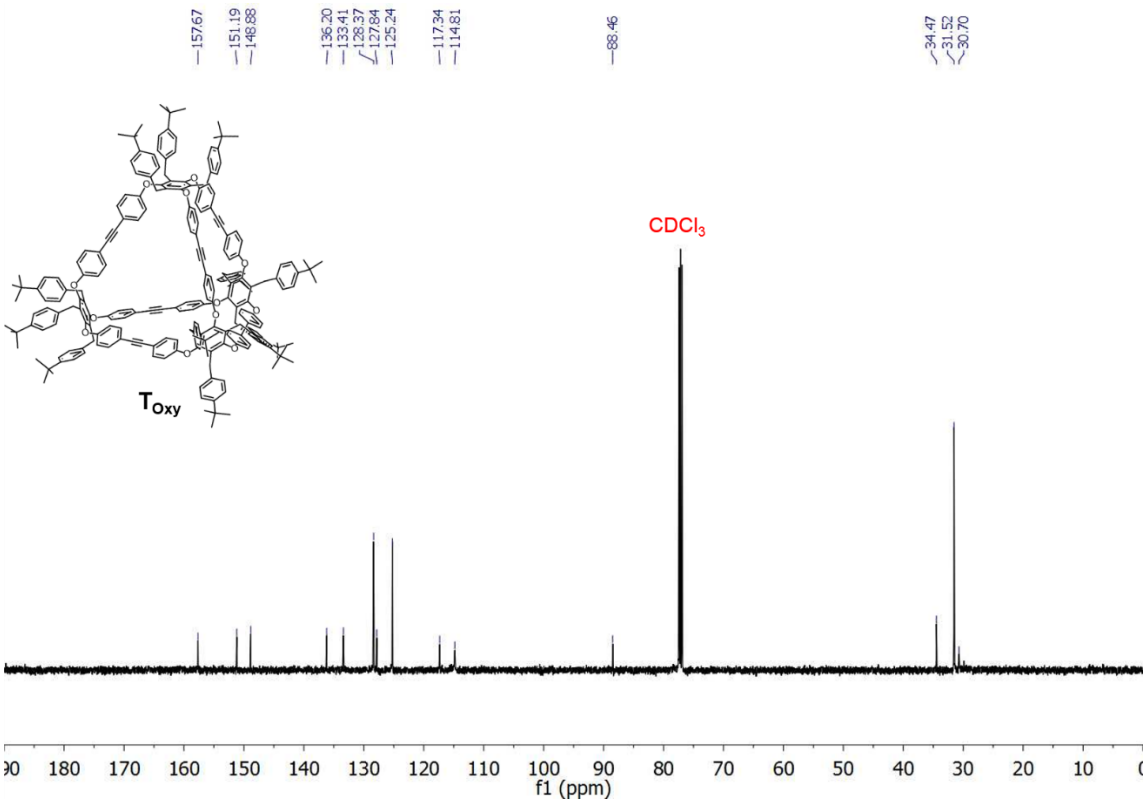

Figure 2.54: *^{13}C NMR of **Td$_{Oxy}$** (125 MHz, CDCl$_3$).*

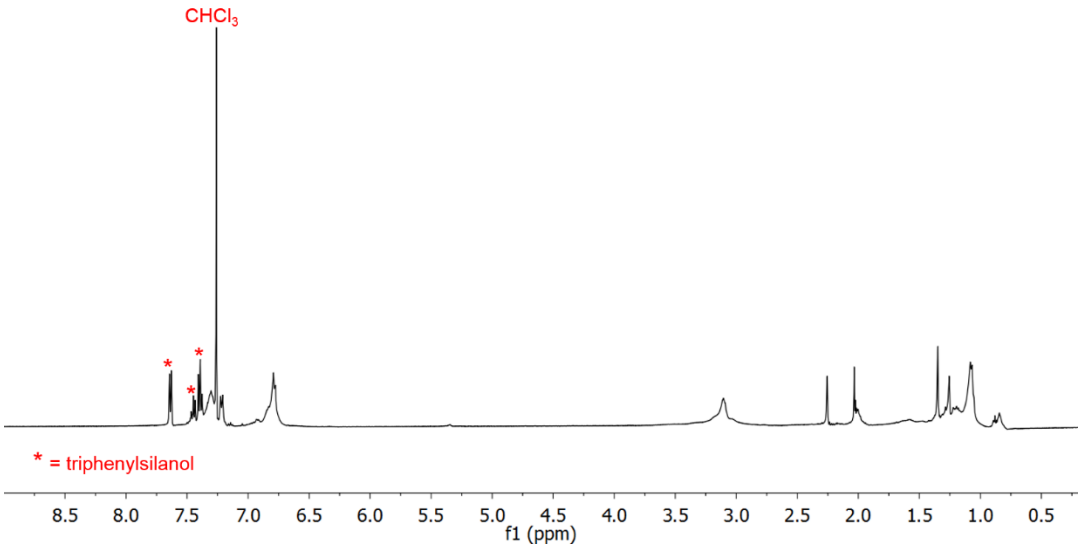

***Figure 2.55**: Crude ^{1}H NMR of the product distribution from metathesis of **P_{Sulf}** in chloroform at the 8 hour time point (500 MHz, $CDCl_3$).*

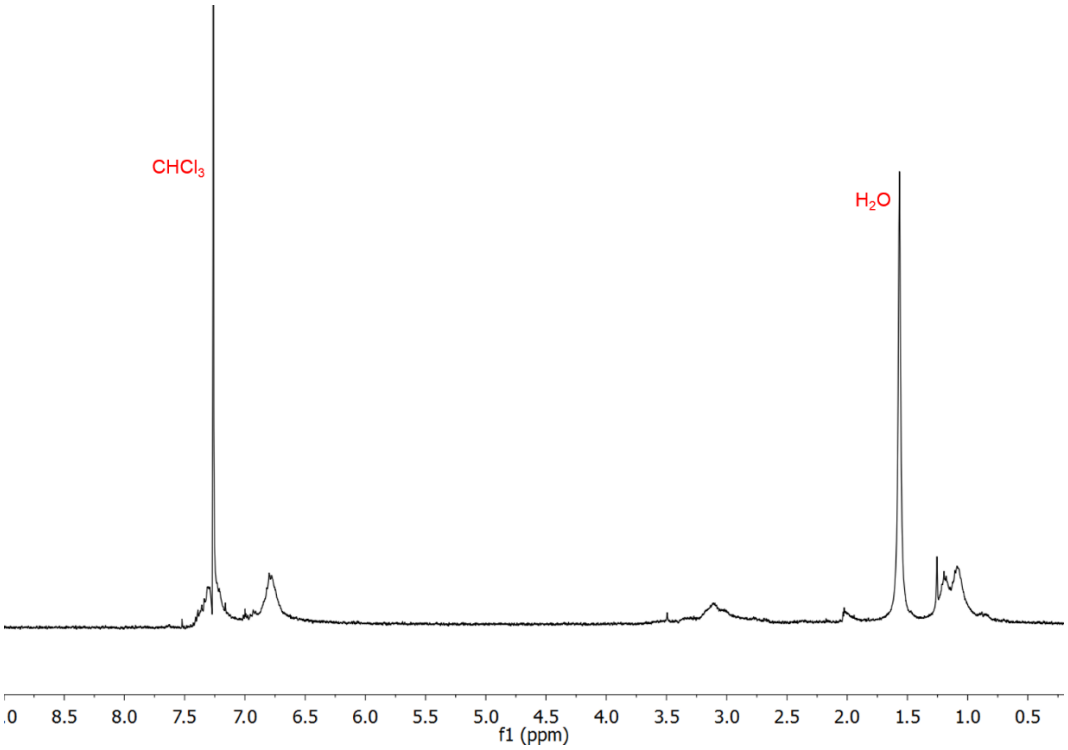

***Figure 2.56**: ^{1}H NMR of the product distribution from metathesis of **P_{Sulf}** in TCB after 12 hours (500 MHz, $CDCl_3$).*

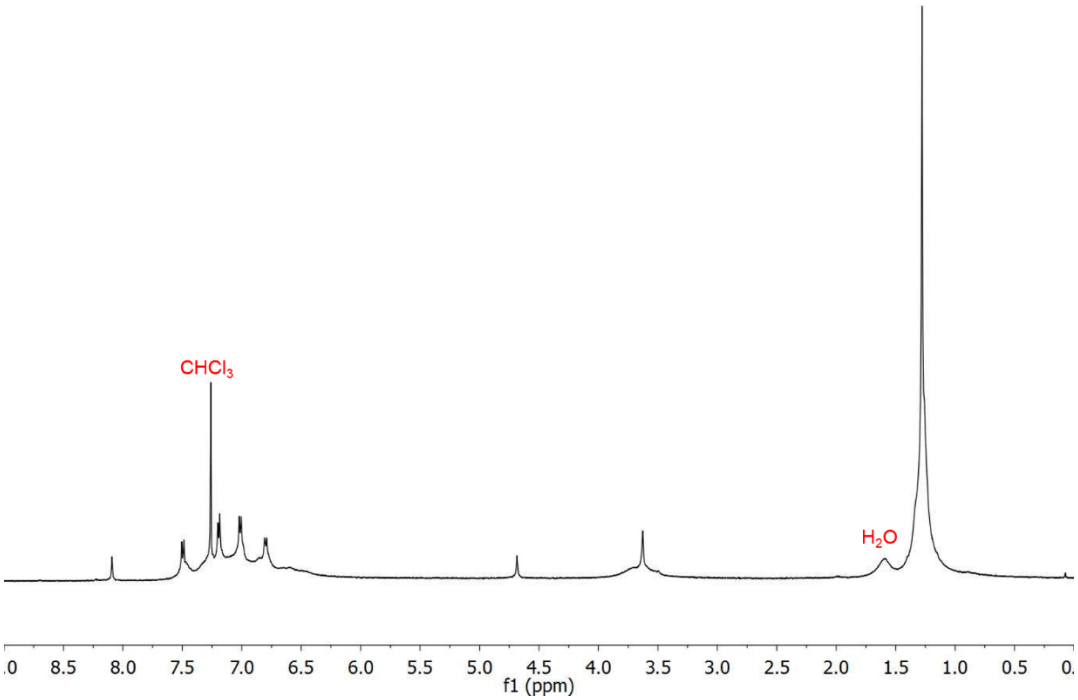

Figure 2.57: *^{1}H NMR of the product distribution from metathesis of* $\boldsymbol{P_{Oxy}}$ *at 70 ºC in TCB after 12 hrs (500 MHz, $CDCl_3$).*

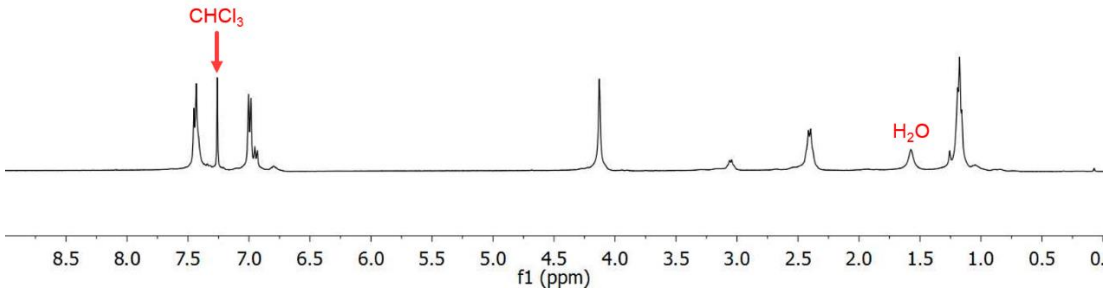

Figure 2.58: *^{1}H NMR of the product distribution from metathesis of the 1:3 mixture of* $\boldsymbol{P_{Sulf}}$***:***$\boldsymbol{P_{Carb}}$ *(500 MHz, $CDCl_3$).*

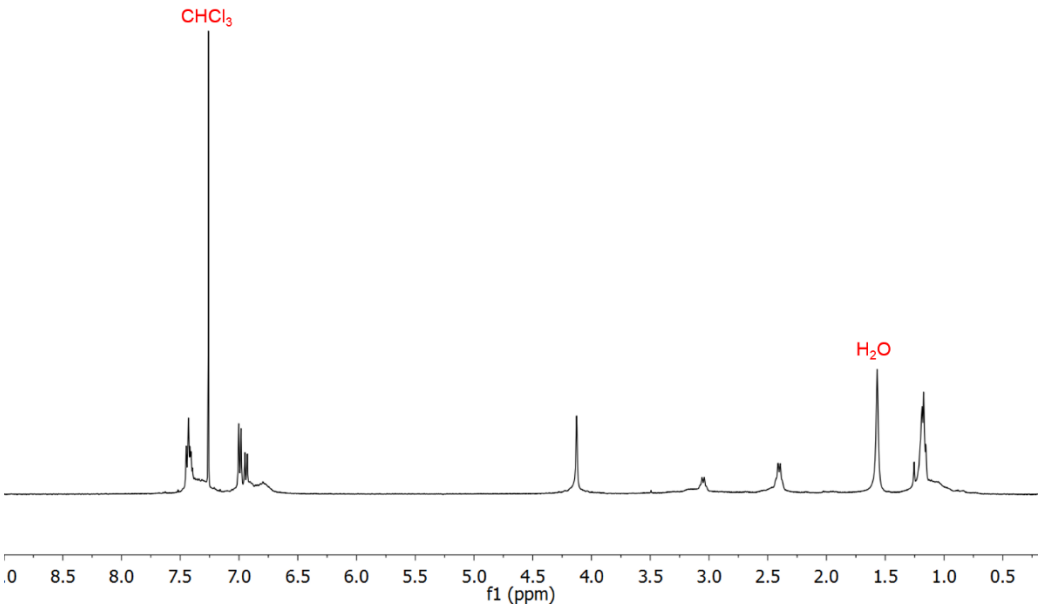

Figure 2.59: *^{1}H NMR of the product distribution from metathesis of the 1:1 mixture of* ***P_{Sulf}:P_{Carb}*** *(500 MHz, $CDCl_3$).*

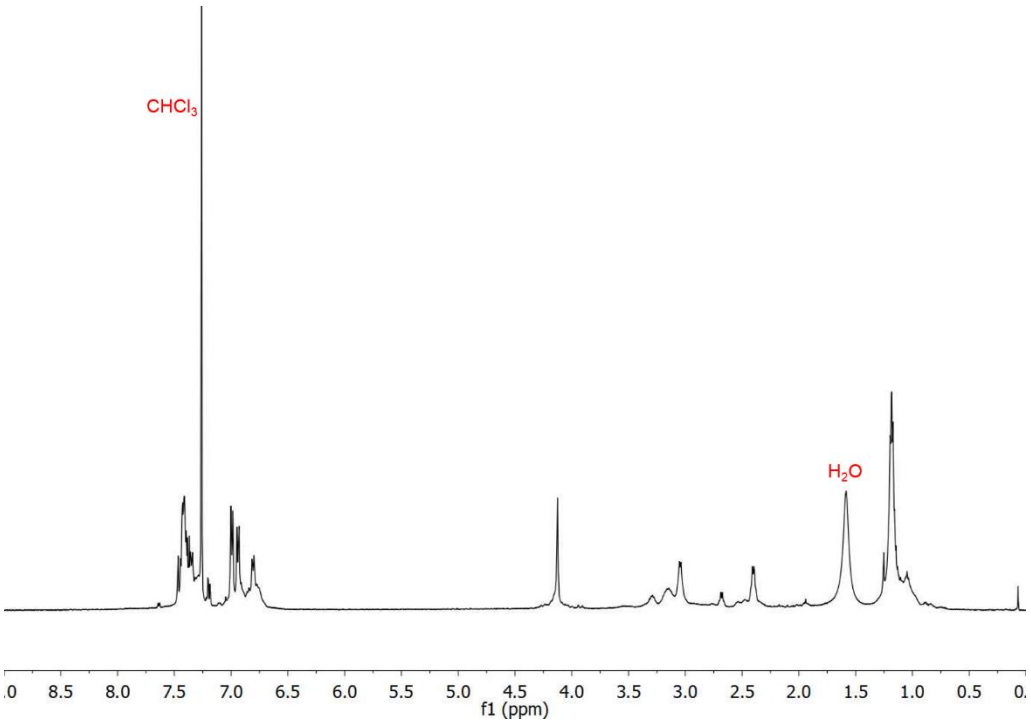

Figure 2.60: *^{1}H NMR of the product distribution from metathesis of the 3:1 mixture of* ***P_{Sulf}:P_{Carb}*** *(500 MHz, $CDCl_3$).*

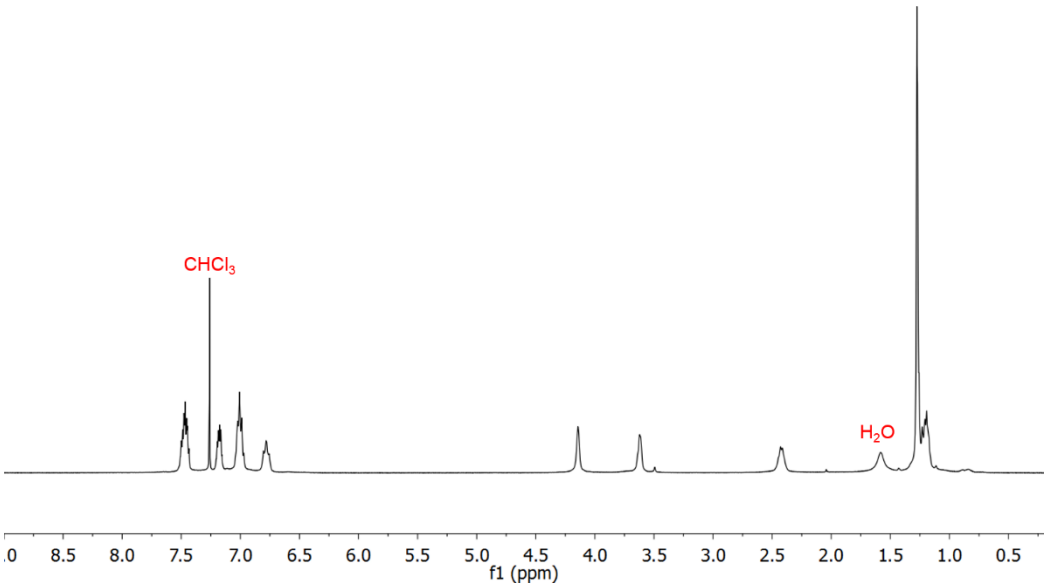

Figure 2.61: *^{1}H NMR of the product distribution from metathesis of the 1:1 mixture of* ***P_{Carb}:P_{Oxy}*** *(500 MHz, $CDCl_3$).*

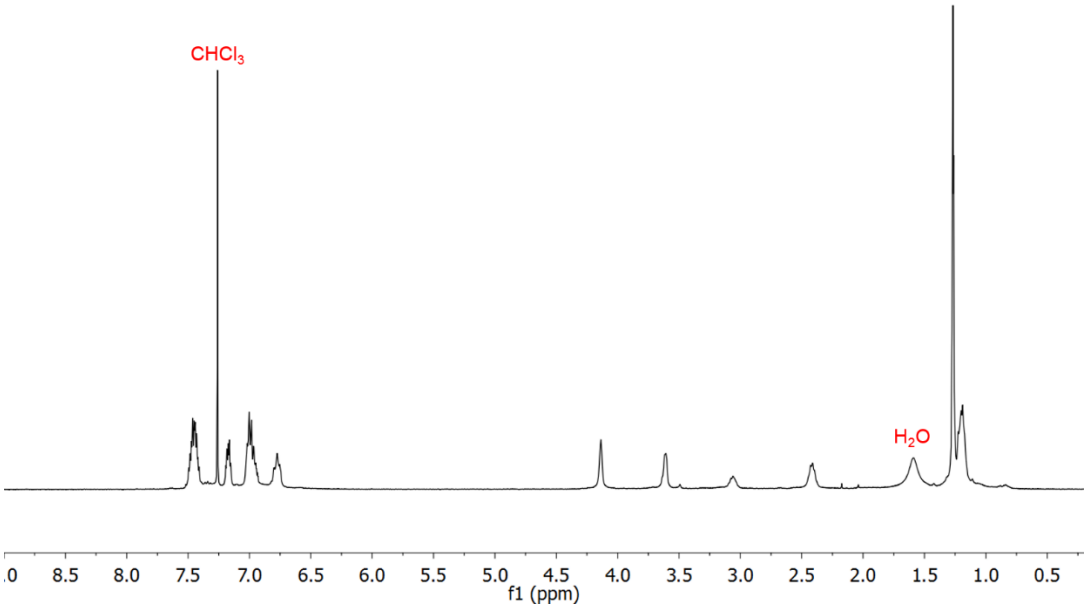

Figure 2.62: *^{1}H NMR of the product distribution from metathesis of the 1:1:1 mixture of* ***P_{Sulf}:P_{Carb}:P_{Oxy}*** *(500 MHz, $CDCl_3$).*

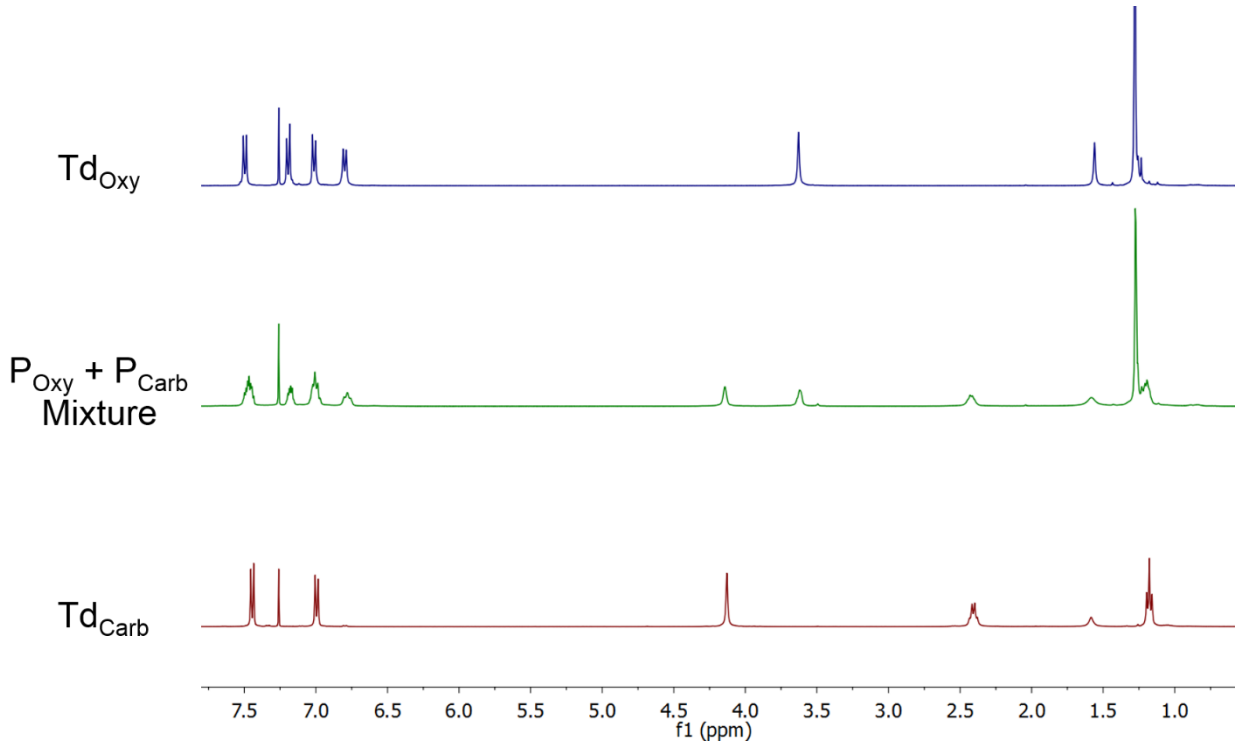

Figure 2.63: *^{1}H NMR comparison of* ***Td$_{Oxy}$***, ***Td$_{Carb}$***, *and the 1:1 metathesis mixing experiment of* ***P$_{Oxy}$*** *and* ***P$_{Carb}$*** *(400 MHz, $CDCl_3$).*

X-ray Diffraction Analysis

X-ray Crystallographic Analysis of P$_{Carb}$

Single crystals of **P$_{Carb}$** suitable for X-ray crystallography were grown by slow diffusion of CH_3OH into a solution of **P$_{Carb}$** in ethyl acetate. Intensity data were collected on a Bruker D8 Venture equipped with a four-circle kappa diffractometer and Photon 100 detector. An Iμs microfocus Mo (λ = 0.71073 Å) source with a multilayer mirror monochromator provided the incident beam. The sample was mounted on a 0.3mm loop with the minimal amount of Paratone-N oil. Data was collected as a series of φ and/ or ω scans. Data was collected at 100K in a cold stream of $N_{2(g)}$. Data was integrated and filtered for statistical outliers using SAINT within the APEX2 software package (1, 2) then corrected for absorption by the multi-scan method using SADABS v2014/5 (3). The structure was phased by intrinsic methods using SHELXT-2014-4 (4) and refined using SHELXL-2014-7 (5). The asymmetric unit contained one **P$_{Carb}$** molecule and one-half of an ethyl acetate molecule. CCDC: 1590140

Table 2.1: Crystal data and structure refinement for $\mathbf{P_{Carb}}$.

Identification code	d20d	
Empirical formula	C44H46O	
Formula weight	590.849	
Temperature	100(2) K	
Wavelength	0.71073 Å	
Crystal system	Monoclinic	
Space group	$P2_1/n$	
Unit cell dimensions	a = 16.549(3) Å	α = 90°
	b = 9.9129(17) Å	β = 104.799(7)°
	c = 22.008(5) Å	γ = 90°
Volume	3490.7(11) $Å^3$	
Z	4	
Density (calculated)	1.124 Mg/m^3	
Absorption coefficient	0.065 mm^{-1}	
F(000)	1272	
Crystal size	0.354 x 0.303 x 0.062 mm^3	
Theta range for data collection	2.26 to 25.35°.	
Index ranges	-19<=h<=19, -11<=k<=11, -26<=l<=26	
Reflections collected	56038	
Independent reflections	6407 [R(int) = 0.0310]	
Completeness to theta = 25.242°	99.9 %	
Absorption correction	Multi-scan	
Refinement method	Full-matrix least-squares on F^2	
Data / restraints / parameters	6407 / 33 / 441	
Goodness-of-fit on F^2	1.081	
Final R indices [I>2sigma(I)]	R1 = 0.0698, wR2 = 0.1275	
R indices (all data)	R1 = 0.0527, wR2 = 0.1188	
Extinction coefficient	none	
Largest diff. peak and hole	0.416 and -0.250 $e.Å^{-3}$	

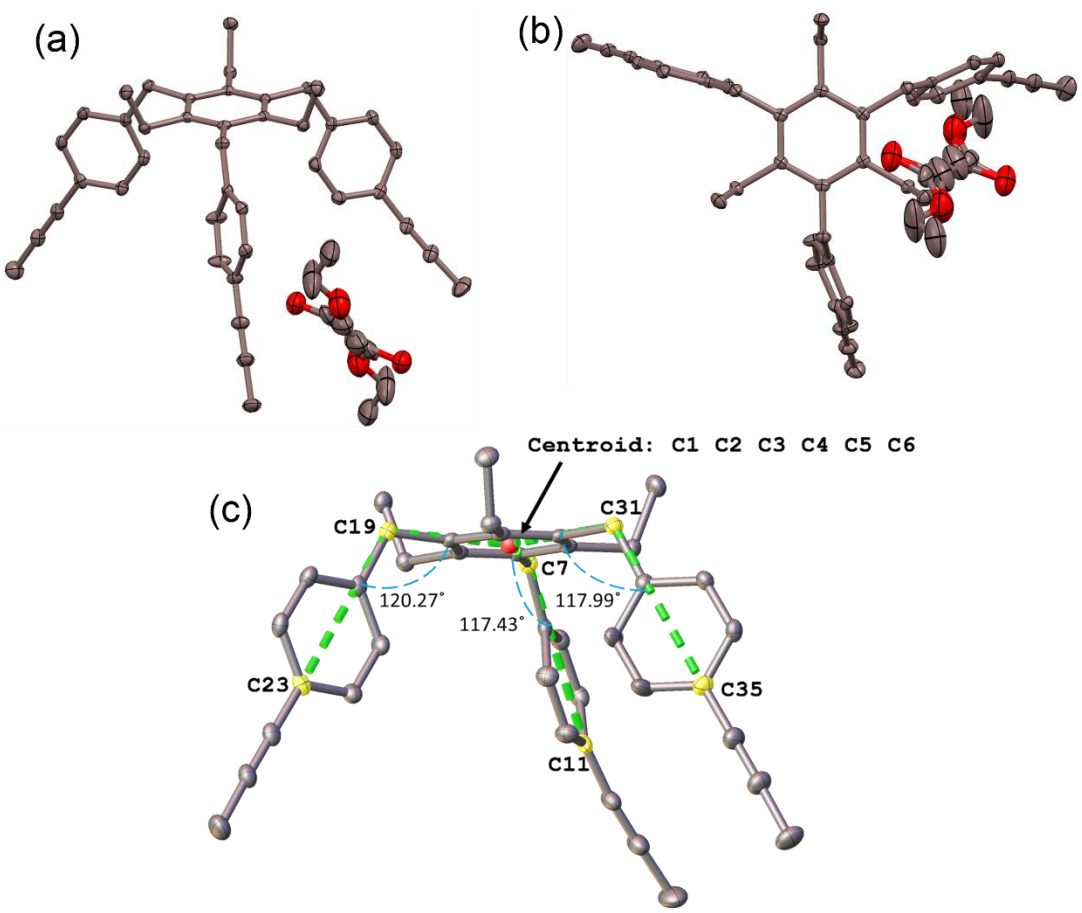

Figure 2.64: *X-ray crystal structure of* $\mathbf{P_{Carb}}$*, 50% probability ellipsoids with hydrogen atoms removed for clarity. (a) Side view (b) Top view. (c) Angles between the central benzene group and the three benzylic groups are shown, with labeled carbon atoms used to measure the angle (average 118.6°).*

X-ray Crystallographic Analysis of $\mathbf{P_{Sulf}}$

Single crystals of $\mathbf{P_{Sulf}}$ suitable for X-ray crystallography were grown from slow evaporation of $\mathbf{P_{Sulf}}$ in a 1:1 solution of dichloromethane and methanol. Intensity data were collected on a Bruker D8 Venture equipped with a four-circle kappa diffractometer and Photon 100 detector. An Iμs microfocus Mo (λ = 0.71073 Å) source with a multilayer mirror monochromator provided the incident beam. The sample was mounted on a 0.3mm loop with the minimal amount of Paratone-N oil. Data was collected as a series of φ and/ or ω scans. Data was collected at 100K in a cold stream of $N_{2(g)}$. Data was integrated and filtered for statistical outliers using SAINT within the

APEX2 software package (1, 2) then corrected for absorption by integration using SADABS v2014/5 (3). The structure was phased by direct methods using SHELXS-2014-7 (5) and refined using SHELXL-2014-7 (5). The asymmetric unit contained one **P_{Sulf}** molecule. CCDC: 1590139

Table 2.2: Crystal data and structure refinement for **P_{Sulf}**.

Identification code	d58a	
Empirical formula	C39H36S3	
Formula weight	600.86	
Temperature	100(2) K	
Wavelength	0.71073 Å	
Crystal system	Monoclinic	
Space group	$P2_1/n$	
Unit cell dimensions	a = 13.9615(6) Å	α = 90°.
	b = 14.7481(6) Å	β = 103.8694(15)°.
	c = 16.6133(7) Å	γ = 90°.
Volume	3321.0(2) $Å^3$	
Z	4	
Density (calculated)	1.202 Mg/m^3	
Absorption coefficient	0.249 mm^{-1}	
F(000)	1272	
Crystal size	0.483 x 0.421 x 0.28 mm^3	
Theta range for data collection	2.202 to 28.329°.	
Index ranges	-18<=h<=18, -19<=k<=19, -22<=l<=22	
Reflections collected	93160	
Independent reflections	8271 [R(int) = 0.0339]	
Completeness to theta = 25.242°	99.9 %	
Absorption correction	Integration	
Max. and min. transmission	0.94943 and 0.91564	
Refinement method	Full-matrix least-squares on F^2	
Data / restraints / parameters	8271 / 0 / 386	
Goodness-of-fit on F^2	1.049	
Final R indices [I>2sigma(I)]	R1 = 0.0346, wR2 = 0.0849	
R indices (all data)	R1 = 0.0400, wR2 = 0.0891	
Extinction coefficient	0.0232(7)	
Largest diff. peak and hole	0.325 and -0.296 $e.Å^{-3}$	

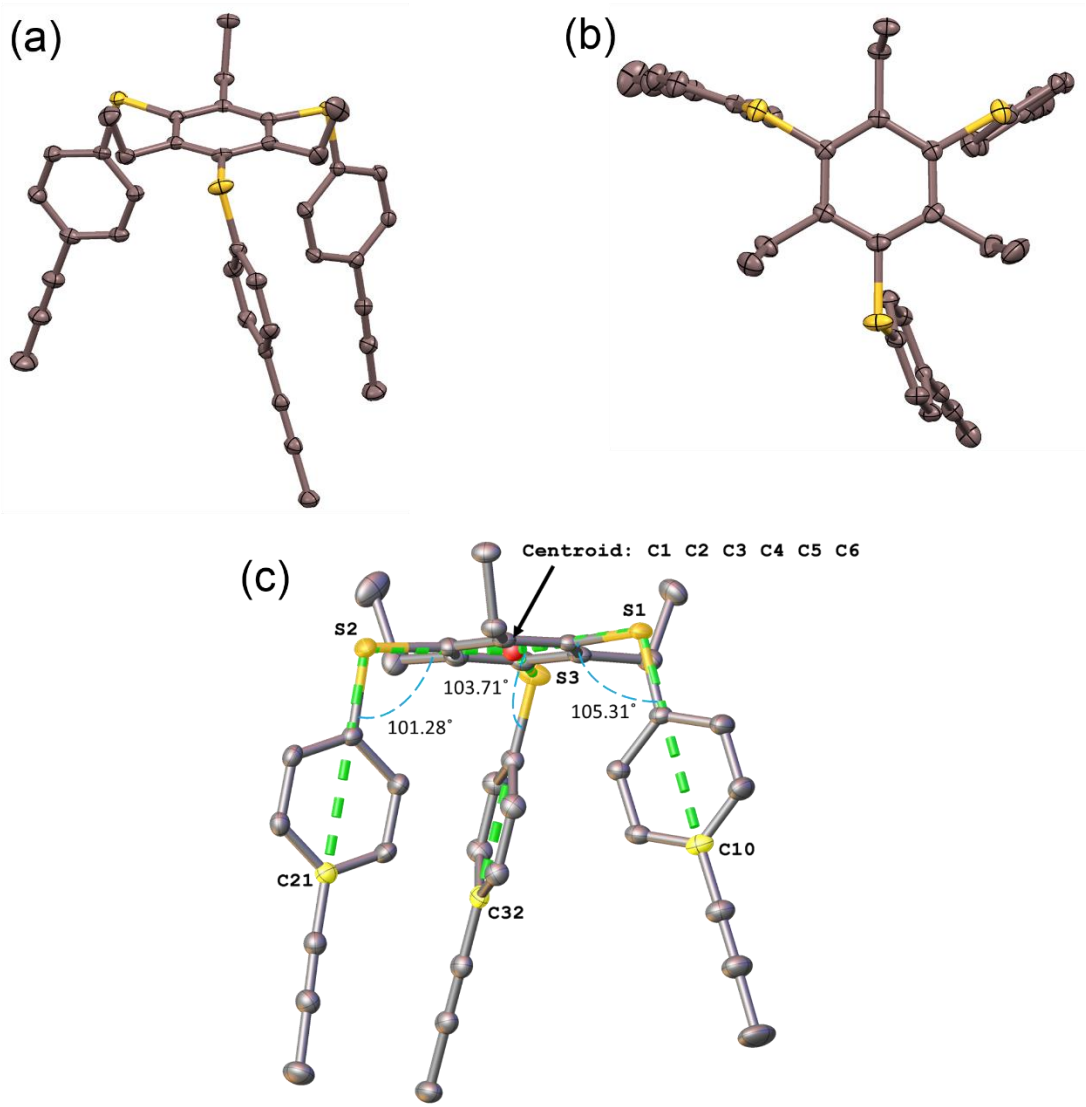

Figure 2.65: *X-ray crystal structure of* $\mathbf{P_{Sulf}}$*, 50% probability ellipsoids with hydrogen atoms removed for clarity. (a) Side view (b) Top view. (c) Angles between the central benzene group and the three benzylic groups are shown, with the labeled atoms that were used to measure the angle (average of 103.4º).*

X-ray Crystallographic Analysis of $\mathbf{P_{Oxy}}$

Single crystals of $\mathbf{P_{Oxy}}$ suitable for X-ray crystallography were grown from slow diffusion of methanol into a solution of $\mathbf{P_{Oxy}}$ in dichloromethane. Intensity data were collected on a Bruker D8 Venture equipped with a four-circle kappa diffractometer and Photon 100 detector. An Iμs microfocus Mo (λ = 0.71073 Å) source with a multilayer mirror monochromator provided the incident beam. The sample was mounted on a 0.3mm loop with the minimal amount of Paratone-

N oil. Data was collected as a series of φ and/ or ω scans. Data was collected at 100K in a cold stream of $N_{2(g)}$. Data was integrated and filtered for statistical outliers using SAINT within the APEX2 software package (1,2) then corrected for absorption by the multi-scan method using SADABS v2014/5 (3). The structure was phased by direct methods using SHELXS-2014-7 (5) and refined using SHELXL-2014-7 (5). The asymmetric unit contained one-third of a **P_{Sulf}** molecule and one disordered methanol solvent molecule. The position of the methanol solvent molecule could not be determined reliably so the electron density due to the disordered solvent was removed from the final refinement using the SQUEEZE routine in PLATON (6). CCDC: 1590138

Table 2.3: Crystal data and structure refinement for **P_{Oxy}**.

Identification code	d53a	
Empirical formula	C66H66O3	
Formula weight	907.18	
Temperature	100(2) K	
Wavelength	0.71073 Å	
Crystal system	Hexagonal	
Space group	P-3c1	
Unit cell dimensions	a = 15.284(10) Å	α = 90°.
	b = 15.284(10)Å	β = 90°.
	c = 27.213(19) Å	γ = 120°.
Volume	5505.3(8) $Å^3$	
Z	4	
Density (calculated)	1.095 Mg/m^3	
Absorption coefficient	0.249 mm^{-1}	
F(000)	1944	
Crystal size	0.483 x 0.421 x 0.28 mm^3	
Theta range for data collection	2.202 to 28.329°.	
Index ranges	-18<=h<=18, -19<=k<=19, -22<=l<=22	
Reflections collected	93160	
Independent reflections	8271 [R(int) = 0.0339]	
Completeness to theta = 25.242°	99.9 %	
Absorption correction	multi-scan	

***Table 2.3**: (cont.)*

Max. and min. transmission	0.94943 and 0.91564
Refinement method	Full-matrix least-squares on F^2
Data / restraints / parameters	8271 / 0 / 386
Goodness-of-fit on F^2	1.049
Final R indices [I>2sigma(I)]	R1 = 0.0346, wR2 = 0.0849
R indices (all data)	R1 = 0.0400, wR2 = 0.0891
Extinction coefficient	0.0232(7)
Largest diff. peak and hole	0.325 and -0.296 e.$Å^{-3}$

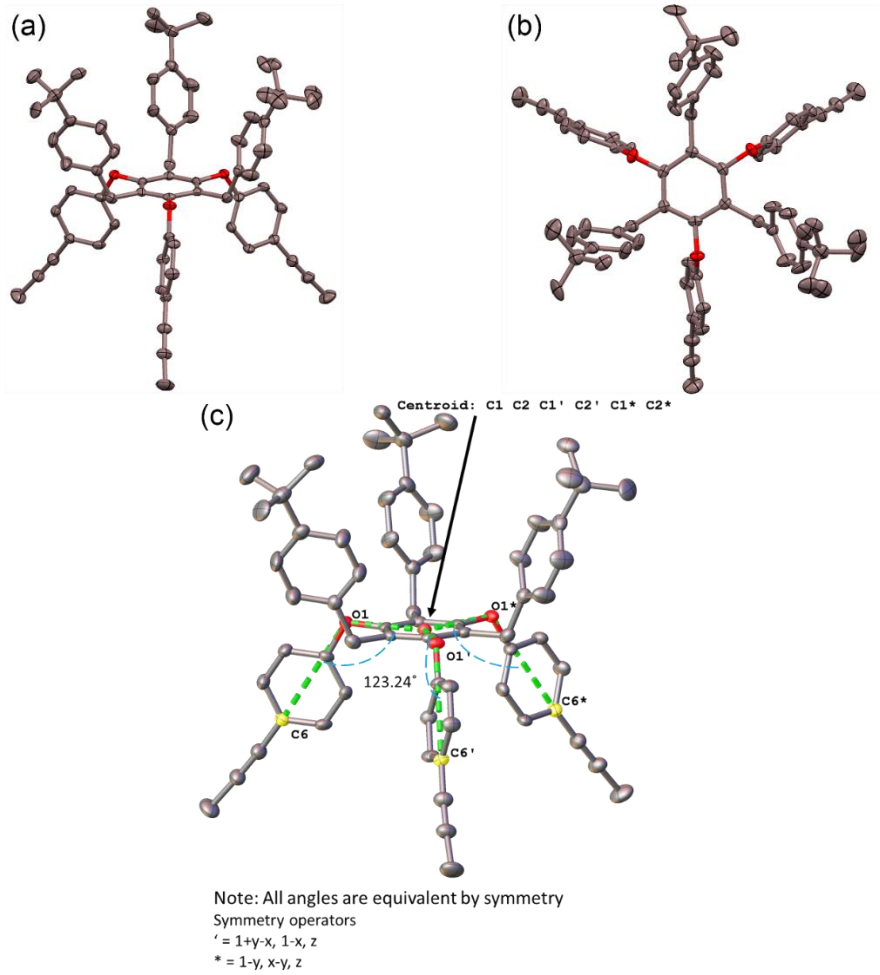

***Figure 2.66**: X-ray crystal structure of **P_{Oxy}**, 50% probability ellipsoids with hydrogen atoms removed for clarity. (a) Side view (b) Top view. (c) Angles between the central benzene group and the three benzylic groups are shown, with labeled carbon atoms used to measure the angle (average 123.24º).*

Bite Angle Calculation

Bite angles were calculated using coordinates from single crystal XRD structures. Two atoms on each precursor arm were selected (as indicated with red circles in Figure 2.67) and defined as points in three-dimensional Euclidean space. Vectors were defined from the coordinates of these points. The angle between vectors was calculated with the equation given in Figure 2.67. The final bite angle for each precursor was calculated as the average of three angles.

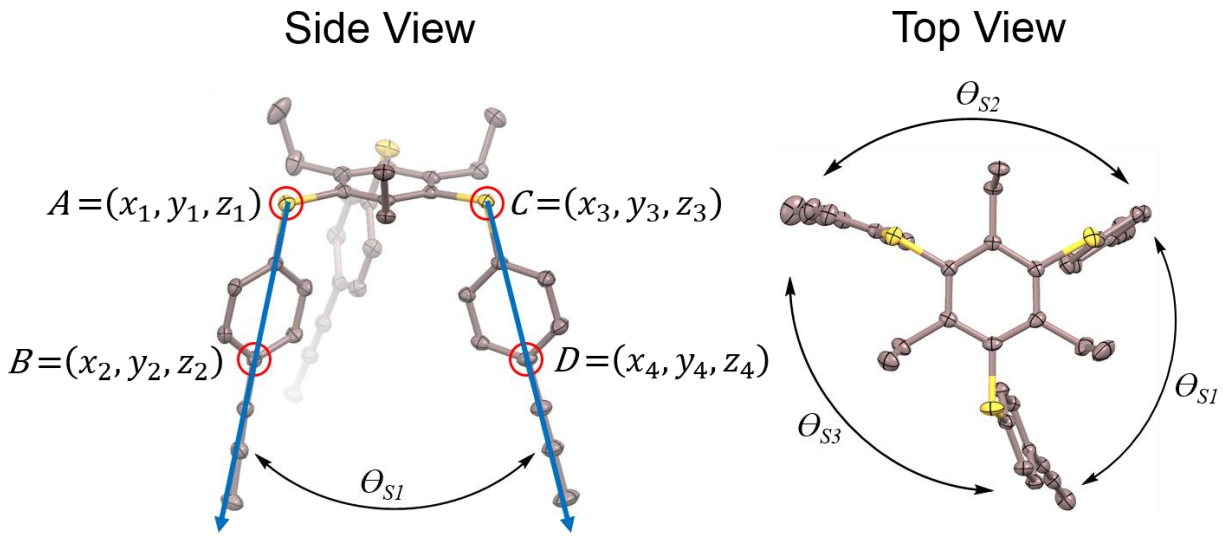

$$\overrightarrow{AB} = \vec{V}_1 = \langle x_2 - x_1, y_2 - y_1, z_2 - z_1 \rangle$$
$$\overrightarrow{CD} = \vec{V}_2 = \langle x_4 - x_3, y_4 - y_3, z_4 - z_3 \rangle$$

$$\theta_{S1} = arccosine \frac{\vec{V}_1 \cdot \vec{V}_2}{\|\vec{V}_1\| \cdot \|\vec{V}_2\|}$$

$$Bite\ Angle\ = \frac{1}{3}\sum_i \theta_i$$

***Figure 2.67**: Bite angle calculation for* $\mathbf{P_{Sulf}}$.

Cartesian Coordinates of Calculated Structures

Note: The structures for OT_{Oxy} and Td_{Oxy} were calculated with ethyl moieties (instead of *t*-butylbenzyl) on the precursors to simplify the calculation.

OT_{Sulf} (-41,456.164 kcal/mol)

box:	30.3914	30.3914	30.3914
C	13.59848	6.730788	13.79054
C	12.50458	6.430737	16.34669
C	12.2122	6.783297	13.99379
C	14.41826	6.480924	14.89559
C	13.88882	6.3237	16.18487
C	11.64765	6.685494	15.2675
C	14.18227	6.91616	12.43378
C	14.7673	6.014525	17.34521
C	10.18018	6.835196	15.46958
C	14.40123	5.600696	11.71462
C	14.8951	4.519133	17.56211
C	9.442519	5.516266	15.37462
C	11.07806	8.469296	12.11903
C	10.773	11.10767	11.23503
C	10.87322	8.7392	10.76691
C	11.14969	9.523566	13.02577
C	11.00153	10.82482	12.58749
C	10.71631	10.03548	10.33294
C	16.88655	7.666954	15.20419
C	18.24657	9.970847	16.04883
C	18.21729	7.590974	15.61194
C	16.2379	8.896924	15.22341
C	16.90887	10.02975	15.64167
C	18.88634	8.724243	16.02265
C	11.72324	7.668486	18.67421
C	11.61066	10.09369	20.07143
C	12.45398	8.766978	18.23027
C	10.91834	7.792385	19.80751
C	10.8669	8.981898	20.49629
C	12.39321	9.962279	18.91768
C	11.57998	11.28677	20.81088
C	10.58466	12.41655	10.75339
C	18.9408	11.11891	16.48514
C	9.33741	20.43823	8.909371
C	11.74932	21.37644	7.842896
C	9.988312	19.74629	7.87859
C	9.913921	21.62438	9.369337
C	11.13695	22.09574	8.872432
C	11.20314	20.18459	7.345746
C	8.058875	19.93843	9.484213
C	11.75806	23.33541	9.412929
C	11.88003	19.42063	6.262911
C	6.846934	20.49901	8.769147
C	11.3529	24.57137	8.636931
C	11.3993	19.83388	4.887106
C	9.537829	17.03533	8.127427
C	10.10716	14.70567	9.568443
C	8.656826	15.95511	8.094346
C	10.69099	16.95761	8.902885
C	10.96779	15.80866	9.616397
C	8.939693	14.8072	8.79786
C	9.62334	22.29365	12.0371
C	10.44068	21.80277	14.66927
C	9.415873	23.25262	13.02835
C	10.2597	21.09877	12.36064
C	10.6652	20.85974	13.65863
C	9.812311	23.00944	14.3216
C	14.49975	21.22285	7.69771
C	16.79989	19.9791	8.6975
C	14.49427	20.66349	8.972344
C	15.65547	21.15258	6.921083
C	16.78833	20.54731	7.41476
C	15.62799	20.04811	9.462069
C	17.96117	19.34802	9.171756
C	10.39077	13.50118	10.23825
C	10.80536	21.58806	16.00693
C	14.078	20.29759	23.78097
C	12.47646	18.14072	24.56675
C	14.63577	19.17699	24.41229
C	12.69569	20.31841	23.58227
C	11.87935	19.23535	23.93659
C	13.8585	18.08117	24.79523
C	14.92792	21.44149	23.35254
C	10.41618	19.25657	23.66569
C	14.47929	16.89823	25.45022
C	15.05265	22.50185	24.42697
C	9.619784	19.80132	24.83336
C	14.56793	17.06047	26.95424

C	17.19796	18.74941	23.479	C	22.61385	16.86212	10.41615
C	18.78043	17.90009	21.3346	C	20.19886	18.16517	9.851338
C	18.51948	19.17929	23.36717	C	21.43045	16.43237	11.01002
C	16.66192	17.91417	22.50305	C	22.58972	17.96081	9.556257
C	17.44358	17.49967	21.44343	C	21.40347	18.59714	9.274815
C	19.29995	18.75686	22.31587	C	20.24286	17.0789	10.73379
C	11.69074	21.60303	21.34745	C	18.9913	18.79971	9.518802
C	11.28114	21.49631	18.58016	C	20.40998	17.07343	19.45498
C	10.7242	22.41026	20.74787	C	17.11426	10.8837	12.06944
C	12.4368	20.72801	20.5633	C	15.92343	10.76012	11.87341
C	12.23081	20.674	19.19899	C	19.5667	12.08182	16.87575
C	10.52695	22.36201	19.38831	C	20.30621	13.21818	17.34964
C	11.5426	15.58446	24.111	C	14.5151	10.61968	11.62891
C	11.55009	13.40159	22.35874	H	15.15075	7.441903	12.54276
C	11.7988	15.77627	22.75642	H	13.51122	7.5614	11.83768
C	11.297	14.29843	24.58946	H	14.34029	6.483912	18.25059
C	11.29419	13.22576	23.72698	H	15.76475	6.456252	17.17555
C	11.80536	14.69853	21.89452	H	9.789254	7.529395	14.70199
C	11.56293	12.28946	21.50167	H	10.00597	7.289611	16.46214
C	19.61663	17.44976	20.29632	H	13.44461	5.068018	11.57988
C	11.06154	21.49668	17.19434	H	15.08237	4.955411	12.29552
C	23.7093	13.42165	14.31799	H	14.85115	5.757962	10.72082
C	23.8884	15.06577	12.06257	H	15.33569	4.034678	16.6743
C	24.16598	14.74331	14.42171	H	13.90365	4.072033	17.7494
C	23.38469	12.93383	13.04823	H	15.53696	4.294803	18.42954
C	23.47171	13.74098	11.90441	H	9.808151	4.813506	16.1424
C	24.21633	15.59676	13.31722	H	9.597136	5.062671	14.38092
C	23.5916	12.5538	15.52191	H	8.358881	5.652069	15.52253
C	23.16513	13.19752	10.55364	H	10.84802	7.909122	10.05077
C	24.6186	17.02215	13.46764	H	11.303	9.313347	14.09191
C	24.83159	11.7141	15.75138	H	11.03466	11.65316	13.30326
C	24.40956	12.6571	9.876228	H	10.5579	10.24858	9.270555
C	26.1107	17.22436	13.30853	H	18.72802	6.619625	15.61335
C	23.48046	15.75108	16.90299	H	15.19387	8.964478	14.89161
C	21.41294	16.62064	18.57744	H	16.39565	10.99752	15.64567
C	23.59385	15.62164	18.28619	H	19.93024	8.65827	16.34917
C	22.32199	16.29838	16.35755	H	13.09022	8.674153	17.34139
C	21.30213	16.72502	17.18519	H	10.32209	6.935867	20.14458
C	22.5804	16.05473	19.11019	H	10.23527	9.077803	21.38566
C	21.2813	11.20467	12.62646	H	12.97892	10.82198	18.57564
C	18.50681	10.99725	12.26612	H	8.021004	20.22487	10.55204
C	20.73766	10.11749	11.94409	H	8.049512	18.83483	9.429365
C	20.43379	12.18848	13.12492	H	12.85759	23.21938	9.369888
C	19.06847	12.08535	12.94436	H	11.46966	23.44657	10.47382
C	19.37413	10.0142	11.77095	H	11.6767	18.3439	6.414912

H	12.97131	19.57335	6.341945	H	11.98472	16.78901	22.37754
H	6.857636	20.20925	7.704944	H	11.12216	14.14597	25.66114
H	6.840783	21.60027	8.83451	H	11.11372	12.21418	24.10486
H	5.911291	20.12726	9.2176	H	11.99807	14.84894	20.82711
H	10.26002	24.7139	8.680252	H	22.71672	11.88896	15.385
H	11.65381	24.47388	7.579922	H	23.40026	13.18832	16.40663
H	11.83465	25.47486	9.044784	H	22.72901	14.00393	9.935629
H	11.60631	20.90273	4.710173	H	22.40962	12.39762	10.64512
H	10.31258	19.66629	4.796074	H	24.30684	17.37061	14.47028
H	11.89936	19.25075	4.096923	H	24.07764	17.62245	12.71337
H	7.732432	16.02965	7.509129	H	25.71354	12.35842	15.90691
H	11.38624	17.80615	8.928352	H	25.02156	11.06508	14.87937
H	11.88401	15.73926	10.21232	H	24.71799	11.06605	16.63579
H	8.247409	13.95906	8.773839	H	24.84982	11.83835	10.47017
H	8.942311	24.20654	12.76599	H	25.16408	13.45496	9.765784
H	10.4234	20.34355	11.58165	H	24.17989	12.26684	8.871426
H	11.15441	19.91421	13.91608	H	26.4402	16.89609	12.30822
H	9.654287	23.7639	15.09948	H	26.65834	16.64105	14.06817
H	13.58798	20.72458	9.587746	H	26.38618	18.28463	13.42922
H	15.64973	21.56983	5.906885	H	24.49468	15.16285	18.71099
H	17.6921	20.48175	6.800045	H	22.23378	16.4088	15.26928
H	15.628	19.61561	10.46812	H	20.40026	17.17671	16.7582
H	14.48058	21.88824	22.44458	H	22.6674	15.9512	20.19675
H	15.92983	21.06084	23.08338	H	21.40439	9.347468	11.53546
H	10.08863	18.22214	23.44887	H	20.85583	13.04016	13.67385
H	10.22831	19.86842	22.7649	H	18.40528	12.85816	13.34814
H	15.49555	16.7611	25.03514	H	18.95225	9.161391	11.22736
H	13.88864	15.99768	25.20366	H	21.44338	15.56796	11.6856
H	15.51406	22.0792	25.33538	H	23.52476	18.31783	9.107712
H	14.05697	22.89818	24.68939	H	21.38634	19.45911	8.599556
H	15.67449	23.34537	24.08556	H	19.31038	16.73139	11.19106
H	9.921308	20.83884	25.0557	H	20.73357	13.81372	16.52025
H	9.790165	19.18471	25.73234	H	21.15272	12.91651	17.99288
H	8.539059	19.79532	24.61746	H	19.67499	13.90362	17.9439
H	13.56194	17.18415	27.38935	H	14.31226	9.948409	10.77464
H	15.1724	17.94815	27.20752	H	14.03695	11.58937	11.40024
H	15.04112	16.18292	27.42386	H	13.98005	10.19575	12.49992
H	18.9299	19.86383	24.11905	S	24.86401	15.28066	15.9489
H	15.62274	17.57305	22.59121	S	24.15243	16.0693	10.63721
H	17.02876	16.82749	20.68472	S	23.01372	11.21905	12.86664
H	20.3372	19.09581	22.22549	S	16.32634	19.24542	24.9068
H	10.11624	23.07776	21.37041	S	11.44447	16.89252	25.26288
H	13.19779	20.09279	21.0335	S	11.93047	21.81709	23.06085
H	12.82606	19.9945	18.57971	S	9.149826	18.39917	7.11096
H	9.764939	22.99188	18.91742	S	13.13972	22.08242	7.020813

S	8.989213	22.65903	10.45464
S	11.14963	6.789532	12.58699
S	11.78667	6.095266	17.92183
S	16.13779	6.195341	14.62881

Td$_{Sulf}$ (-41,423.631 kcal/mol)

box:	30.1717	30.1717	30.1717
C	11.97075	5.779305	13.45851
C	11.43193	5.885669	16.2011
C	10.72248	6.205166	13.93214
C	12.92884	5.385218	14.39494
C	12.68987	5.455493	15.77406
C	10.4409	6.291534	15.29705
C	12.26188	5.724272	12.00087
C	13.73442	5.061043	16.75666
C	9.118287	6.777195	15.7733
C	11.93542	4.373824	11.3969
C	13.63988	3.599944	17.14519
C	8.099897	5.661611	15.88604
C	9.648375	8.06739	12.19604
C	9.79526	10.6723	11.18772
C	9.106676	8.36886	10.94742
C	10.28122	9.06592	12.92987
C	10.35568	10.35051	12.42905
C	9.173813	9.650785	10.45489
C	15.60538	5.842318	13.88234
C	17.68062	7.716706	13.81831
C	16.93222	5.424872	13.9766
C	15.31798	7.199537	13.77634
C	16.3436	8.123793	13.7482
C	17.95221	6.346204	13.93887
C	11.20529	7.329977	18.5459
C	11.52799	9.809709	19.79887
C	12.06795	8.278791	18.00555
C	10.48837	7.631026	19.70283
C	10.65144	8.847965	20.32184
C	12.22367	9.50365	18.62357
C	11.68617	11.02834	20.47816
C	9.81703	11.97276	10.65922
C	18.75358	8.620082	13.7567
C	9.226214	20.04145	8.757064
C	11.68807	20.86752	7.717879
C	9.858388	19.31653	7.737782
C	9.848695	21.20247	9.220221
C	11.09446	21.6203	8.733213
C	11.09993	19.69555	7.223083
C	7.918805	19.60361	9.3149
C	11.75669	22.84229	9.262893
C	11.76416	18.88997	6.163928
C	6.743921	20.22599	8.589184
C	11.3956	24.083	8.472462
C	11.33914	19.30504	4.770416
C	9.238664	16.63318	7.973913
C	9.603814	14.27553	9.434148
C	8.293908	15.61037	7.904231
C	10.35506	16.48289	8.790899
C	10.53204	15.31984	9.513851
C	8.477279	14.44911	8.617342
C	9.593168	21.91759	11.87712
C	10.41852	21.44914	14.50866
C	9.464367	22.91537	12.84202
C	10.15383	20.69289	12.22623
C	10.56349	20.46428	13.52498
C	9.864689	22.68257	14.13668
C	14.44027	20.64979	7.613869
C	16.72587	19.438	8.677907
C	14.41129	20.10705	8.894793
C	15.60845	20.56724	6.857509
C	16.73332	19.97675	7.38321
C	15.53958	19.50643	9.417277
C	17.90465	18.8685	9.185188
C	9.763854	13.06311	10.12383
C	10.78936	21.24611	15.84747
C	14.15563	20.10707	23.62445
C	12.66267	17.85325	24.34352
C	14.76477	19.00502	24.23979
C	12.77755	20.0574	23.40431
C	12.01453	18.92857	23.73218
C	14.04352	17.85932	24.58289
C	14.94644	21.3058	23.23685
C	10.55275	18.88305	23.46108
C	14.72027	16.69084	25.20663
C	14.9853	22.35196	24.33181
C	9.731694	19.37714	24.63421
C	14.7864	16.79962	26.71622
C	17.37233	18.76325	23.35775
C	19.06223	18.10069	21.22971
C	18.67294	19.26274	23.31191
C	16.91226	17.94914	22.32741

C	17.74666	17.6257	21.27592	C	21.3723	18.60536	9.251694
C	19.50535	18.93167	22.26872	C	20.51449	16.90266	10.71762
C	11.70346	21.29722	21.18015	C	18.97853	18.4194	9.536608
C	11.28207	21.17381	18.41693	C	20.8086	17.52165	19.36847
C	10.66444	22.0193	20.5946	C	19.75049	9.313192	13.69229
C	12.51804	20.49797	20.38389	H	13.33641	5.942062	11.85204
C	12.30651	20.4357	19.02071	H	11.68135	6.512858	11.48866
C	10.46156	21.96311	19.2357	H	13.61721	5.688836	17.66019
C	11.81314	15.2742	23.82858	H	14.73014	5.269539	16.3252
C	11.81065	13.13561	22.02524	H	8.74969	7.539136	15.06066
C	12.05932	15.49886	22.47762	H	9.247528	7.265811	16.75599
C	11.58577	13.97484	24.27964	H	10.86398	4.141797	11.51971
C	11.57885	12.9248	23.39208	H	12.52409	3.57908	11.8864
C	12.06113	14.44162	21.58951	H	12.17013	4.356187	10.32038
C	11.76677	12.03831	21.15023	H	13.7705	2.953322	16.26097
C	19.95433	17.76569	20.19881	H	12.65615	3.382915	17.59565
C	11.05583	21.16649	17.03121	H	14.41624	3.336755	17.8817
C	24.99271	14.4125	14.50373	H	8.439349	4.896773	16.60484
C	24.56095	15.74189	12.08048	H	7.946311	5.177883	14.90614
C	24.99928	15.81247	14.4378	H	7.1272	6.049135	16.22963
C	24.79057	13.70045	13.31973	H	8.637182	7.571837	10.35881
C	24.5457	14.34562	12.10004	H	10.7068	8.827863	13.91258
C	24.75945	16.49697	13.24427	H	10.83957	11.14009	13.01319
C	25.21841	13.70215	15.79075	H	8.752531	9.887893	9.472742
C	24.30051	13.5692	10.85543	H	17.15276	4.357128	14.0922
C	24.73907	17.98411	13.20943	H	14.27376	7.527486	13.70173
C	26.68061	13.38244	16.02515	H	16.11839	9.190599	13.64918
C	25.5756	13.29827	10.08371	H	18.99422	6.020086	14.01745
C	26.11479	18.57576	12.98162	H	12.63232	8.040664	17.09542
C	24.08511	16.86747	16.82291	H	9.785504	6.892979	20.10695
C	21.88277	17.27726	18.49833	H	10.08549	9.087465	21.22773
C	24.27117	17.08526	18.18743	H	12.91481	10.2441	18.20783
C	22.79522	16.83477	16.30227	H	7.882711	19.88923	10.38317
C	21.70905	17.03384	17.13132	H	7.853613	18.50215	9.255656
C	23.18856	17.29263	19.00943	H	12.85189	22.68935	9.225152
C	23.44551	11.28742	13.39295	H	11.46895	22.97643	10.32138
C	20.96686	10.00562	13.58517	H	11.50741	17.8256	6.323551
C	23.288	9.987272	12.91498	H	12.85939	18.99428	6.267017
C	22.35614	11.9519	13.94797	H	6.7504	19.94113	7.523565
C	21.13248	11.31899	14.0391	H	6.786413	21.32653	8.657816
C	22.07087	9.355537	13.0152	H	5.788958	19.89487	9.028285
C	22.88073	17.09956	10.357	H	10.30822	24.26467	8.509869
C	20.27225	17.97148	9.847236	H	11.69571	23.96927	7.416682
C	21.8012	16.46869	10.9676	H	11.90708	24.97113	8.877432
C	22.65501	18.18119	9.506819	H	11.59918	20.36049	4.582991

H	10.24901	19.18604	4.647502
H	11.83676	18.68684	4.005845
H	7.399246	15.74602	7.285133
H	11.09788	17.2883	8.84502
H	11.41818	15.19522	10.14468
H	7.733641	13.64735	8.567693
H	9.051751	23.88996	12.55566
H	10.25475	19.90781	11.46671
H	10.99005	19.49521	13.80353
H	9.768653	23.46734	14.89379
H	13.49177	20.1725	9.489503
H	15.61702	20.96726	5.836736
H	17.64981	19.90701	6.788506
H	15.5217	19.09372	10.43129
H	14.49226	21.7433	22.32774
H	15.97517	20.99093	22.98441
H	10.27336	17.83694	23.23312
H	10.3341	19.49519	22.56743
H	15.74663	16.62393	24.79886
H	14.18101	15.76928	24.92196
H	15.44911	21.9414	25.2447
H	13.96454	22.69021	24.57936
H	15.56806	23.23217	24.01565
H	9.981922	20.42527	24.86985
H	9.925872	18.76084	25.52876
H	8.653725	19.32233	24.41173
H	13.77224	16.85198	27.14704
H	15.34075	17.706	27.01438
H	15.3008	15.9279	27.15209
H	19.02108	19.92921	24.10991
H	15.88856	17.55666	22.36404
H	17.39009	16.97251	20.47281
H	20.52566	19.32609	22.22968
H	10.00457	22.62226	21.22956
H	13.33601	19.93025	20.84441
H	12.95736	19.81915	18.39217
H	9.642793	22.52583	18.77607
H	12.23783	16.52154	22.12313
H	11.42412	13.79783	25.34954
H	11.40536	11.90352	23.746
H	12.2394	14.62045	20.52417
H	24.63545	12.76181	15.77679
H	24.83543	14.32685	16.61793
H	23.60163	14.14373	10.21844
H	23.81271	12.6132	11.11865
H	24.33807	18.34936	14.17387
H	24.0525	18.31495	12.40916
H	27.28007	14.30786	16.05908
H	27.07078	12.74212	15.21551
H	26.81959	12.84747	16.97853
H	26.2823	12.7118	10.69486
H	26.06285	14.24613	9.797566
H	25.36551	12.73231	9.161812
H	26.52842	18.2372	12.01666
H	26.8054	18.26892	13.78578
H	26.07342	19.6769	12.9712
H	25.2873	17.0782	18.59914
H	22.6493	16.66341	15.22862
H	20.69491	17.02405	16.71886
H	23.33306	17.45918	20.08166
H	24.14052	9.47887	12.44933
H	22.48059	12.97494	14.32383
H	20.27919	11.83608	14.49005
H	21.94464	8.3364	12.63614
H	21.97949	15.61751	11.63632
H	23.51032	18.69554	9.052778
H	21.19402	19.45702	8.58751
H	19.66377	16.39624	11.18529
S	16.43632	19.15352	24.77597
S	11.69404	16.5446	25.01665
S	11.94221	21.52178	22.89253
S	25.52584	16.72177	15.85202
S	24.53421	16.57426	10.52812
S	25.05277	11.9582	13.31581
S	8.967997	18.01709	6.948545
S	13.1064	21.51277	6.896137
S	8.957456	22.27756	10.29416
S	9.41486	6.439617	12.77508
S	11.00685	5.721726	17.90278
S	14.39532	4.588337	13.83113

OT_{Carb} (-45,118.369 kcal/mol)

box:	30.3914	30.3914	30.3914
C	13.61557	6.849733	13.82968
C	12.49431	6.570664	16.37763
C	12.22858	6.934698	14.00063
C	14.43339	6.58021	14.92898
C	13.87419	6.441976	16.20455
C	11.66904	6.827486	15.27641
C	14.20748	7.002074	12.46511
C	15.91609	6.460976	14.76883
C	14.75218	6.106212	17.36634
C	11.89889	6.450796	17.74518
C	10.19073	6.939286	15.46626
C	11.35613	7.105354	12.7943
C	14.40178	5.665349	11.77253
C	14.86817	4.60341	17.55332
C	9.497305	5.592185	15.36793
C	11.19395	8.501169	12.27041
C	10.76828	11.0955	11.24184
C	10.979	8.710855	10.91062
C	11.20363	9.61287	13.10671
C	10.99182	10.88684	12.60827
C	10.76749	9.975199	10.40047
C	16.6893	7.66882	15.2084
C	18.1871	9.918162	15.99938
C	18.018	7.542003	15.60148
C	16.12086	8.936344	15.21481
C	16.85416	10.04523	15.59777
C	18.75848	8.640634	15.99034
C	11.79767	7.735322	18.51934
C	11.64298	10.09079	20.06758
C	12.52054	8.870306	18.16942
C	10.98657	7.802601	19.65083
C	10.90786	8.948528	20.4145
C	12.44684	10.02755	18.92368
C	11.58443	11.26143	20.85358
C	10.55395	12.38216	10.70179
C	18.92848	11.04082	16.42758
C	9.418294	20.37946	9.012037
C	11.83274	21.28651	7.927565
C	10.04192	19.65801	7.986912
C	9.995916	21.5623	9.479877
C	11.21528	22.00648	8.953633
C	11.25264	20.10433	7.450797
C	8.112193	19.90588	9.563942
C	9.302471	22.38268	10.524
C	11.82231	23.27428	9.46256
C	13.10695	21.77817	7.310033
C	11.90764	19.35562	6.335214
C	9.385938	18.41897	7.45855
C	6.92645	20.48633	8.812803
C	11.38246	24.4874	8.661818
C	11.40536	19.80638	4.974631
C	9.639496	17.15334	8.226274
C	10.1261	14.70582	9.545091
C	8.731687	16.09974	8.147807
C	10.78676	16.96819	8.989811
C	11.0301	15.76992	9.63841
C	8.964067	14.89901	8.786547
C	9.734713	22.17223	11.94674
C	10.4256	21.80246	14.65966
C	9.489468	23.16359	12.89477
C	10.33901	20.99621	12.37704
C	10.67948	20.80945	13.70573
C	9.820575	22.98938	14.22166
C	14.37046	21.13283	7.801869
C	16.78334	19.97528	8.699924
C	14.46983	20.58414	9.07584
C	15.50066	21.09932	6.987841
C	16.68506	20.53898	7.420562
C	15.65031	20.01759	9.521628
C	17.97871	19.35888	9.126878
C	10.36671	13.46835	10.1803
C	10.76038	21.64282	16.02115
C	14.07665	20.23807	23.65186
C	12.50573	18.0628	24.44337
C	14.67048	19.13395	24.27497
C	12.69576	20.25888	23.44277
C	11.91054	19.16166	23.81841
C	13.88881	18.04268	24.66266
C	14.91922	21.40885	23.25938
C	12.03767	21.46605	22.84857
C	10.43348	19.19596	23.58951
C	11.67441	16.90531	24.90781
C	14.51098	16.87497	25.35856
C	16.14464	19.14829	24.54139
C	15.0235	22.4414	24.36827
C	9.676789	19.7555	24.78165
C	14.57261	17.07336	26.86335
C	17.02986	18.72976	23.403

C	18.77573	17.87632	21.35606	C	19.08584	12.12535	13.00167
C	18.34789	19.17692	23.34728	C	19.50629	10.09003	11.80344
C	16.5947	17.86116	22.408	C	22.55569	16.77174	10.56544
C	17.44708	17.43905	21.40265	C	20.19028	18.13618	9.84705
C	19.20848	18.76188	22.35179	C	21.32355	16.3903	11.08478
C	11.77233	21.43469	21.37112	C	22.58607	17.85633	9.690717
C	11.28962	21.50339	18.59074	C	21.43456	18.52585	9.331783
C	10.80097	22.27374	20.82883	C	20.16199	17.057	10.73791
C	12.49301	20.6251	20.50027	C	19.00537	18.80274	9.468975
C	12.2607	20.65492	19.13592	C	20.462	17.0757	19.50167
C	10.56201	22.31587	19.47217	C	17.20147	10.85201	12.1009
C	11.65532	15.70274	24.00889	C	16.01229	10.72747	11.90039
C	11.56203	13.41803	22.35404	C	19.55557	12.00137	16.82046
C	11.86079	15.80456	22.63726	C	20.28195	13.14268	17.30233
C	11.39481	14.44043	24.53742	C	14.60308	10.60216	11.65389
C	11.34374	13.31918	23.73487	H	15.17376	7.539305	12.53229
C	11.81455	14.68846	21.82153	H	13.56051	7.653202	11.84824
C	11.55804	12.26591	21.53873	H	14.35976	6.574279	18.28781
C	19.66544	17.44323	20.34937	H	15.75521	6.547281	17.22194
C	11.02691	21.55681	17.20544	H	9.766756	7.633974	14.71739
C	23.5875	13.45721	14.3143	H	9.97531	7.403343	16.44629
C	23.75937	15.12995	12.07824	H	13.44087	5.130647	11.66724
C	24.02171	14.78049	14.4584	H	15.06387	5.005779	12.36127
C	23.2821	12.96291	13.04448	H	14.83968	5.77953	10.76686
C	23.36625	13.79874	11.92517	H	15.28529	4.124553	16.64954
C	24.07796	15.62676	13.3477	H	13.87611	4.146269	17.71947
C	23.49793	12.56904	15.51439	H	15.51393	4.339192	18.40711
C	22.83489	11.54713	12.86153	H	9.891222	4.88697	16.12168
C	23.08414	13.24666	10.5653	H	9.674782	5.12657	14.38187
C	23.82408	16.03133	10.88558	H	8.407467	5.675226	15.51522
C	24.52151	17.04567	13.50051	H	10.97891	7.846564	10.23362
C	24.4564	15.261	15.80944	H	11.38579	9.465848	14.17986
C	24.76174	11.75244	15.71765	H	10.98987	11.74888	13.28305
C	24.34649	12.70601	9.916131	H	10.59999	10.11992	9.32832
C	26.02257	17.19796	13.32741	H	18.47929	6.5465	15.60861
C	23.37401	15.70574	16.74772	H	15.06942	9.04787	14.91886
C	21.42173	16.62439	18.56982	H	16.3954	11.03867	15.59689
C	23.54725	15.56361	18.12213	H	19.79924	8.52475	16.30776
C	22.20168	16.30535	16.29867	H	13.16124	8.835488	17.2779
C	21.24287	16.76102	17.1877	H	10.39998	6.920615	19.93907
C	22.59919	16.01208	19.01894	H	10.26655	8.980454	21.30123
C	21.35712	11.38275	12.66379	H	13.02815	10.90968	18.63672
C	18.58802	11.01737	12.30938	H	8.041319	20.16698	10.63613
C	20.86257	10.27544	11.98113	H	8.072205	18.80155	9.53095
C	20.44728	12.30328	13.16851	H	12.92533	23.19435	9.445847

H	11.55768	23.41179	10.52705	H	12.84059	20.01317	18.46503
H	11.73611	18.27	6.458439	H	9.793363	22.9801	19.06462
H	13.00404	19.48429	6.391709	H	12.0744	16.79213	22.20703
H	6.960227	20.21451	7.742711	H	11.23593	14.33834	25.6188
H	6.929326	21.59016	8.854844	H	11.14859	12.33424	24.17075
H	5.965709	20.13263	9.222448	H	11.98058	14.78554	20.74418
H	10.28456	24.60596	8.688817	H	22.62247	11.89715	15.42031
H	11.65975	24.38433	7.597596	H	23.29575	13.1777	16.41536
H	11.83347	25.41862	9.043083	H	22.63232	14.02646	9.925
H	11.59207	20.88394	4.818979	H	22.32184	12.44926	10.63179
H	10.31356	19.66288	4.885409	H	24.21831	17.42966	14.49216
H	11.89011	19.25561	4.151591	H	23.99129	17.68255	12.76901
H	7.812071	16.23191	7.563327	H	25.64119	12.40859	15.84572
H	11.50446	17.79512	9.074604	H	24.96975	11.11838	14.83741
H	11.94283	15.63885	10.22846	H	24.69391	11.09745	16.60202
H	8.238668	14.08275	8.712106	H	24.79467	11.90523	10.53119
H	9.02289	24.10362	12.57303	H	25.11429	13.49504	9.82294
H	10.54869	20.20987	11.63952	H	24.15386	12.29555	8.91119
H	11.15113	19.87513	14.0266	H	26.34559	16.83916	12.3338
H	9.62177	23.78096	14.95113	H	26.57032	16.59237	14.07147
H	13.58536	20.59646	9.726849	H	26.34748	18.24636	13.43408
H	15.44098	21.5227	5.976767	H	24.46064	15.08249	18.49551
H	17.55909	20.51333	6.762063	H	22.04336	16.41198	15.21699
H	15.71089	19.58861	10.52679	H	20.33236	17.24182	16.816
H	14.50641	21.87855	22.34704	H	22.75397	15.89087	20.09591
H	15.92948	21.06123	22.9749	H	21.56907	9.543399	11.56994
H	10.06728	18.17848	23.35754	H	20.82564	13.18785	13.69784
H	10.21081	19.79662	22.6886	H	18.37913	12.85653	13.40614
H	15.52811	16.69834	24.96159	H	19.13157	9.221141	11.25381
H	13.945	15.95476	25.12462	H	21.28239	15.53985	11.77878
H	15.46116	22.00218	25.28239	H	23.55001	18.18048	9.277463
H	14.02683	22.82396	24.65176	H	21.47968	19.37347	8.640467
H	15.6475	23.30142	24.07318	H	19.20009	16.73774	11.15174
H	10.00483	20.78423	25.01425	H	12.0158	16.57778	25.90896
H	9.863298	19.15474	25.68966	H	10.62996	17.24027	25.06175
H	8.58878	19.77794	24.60472	H	16.45928	20.15831	24.86681
H	13.56342	17.22345	27.2865	H	16.36737	18.49216	25.40586
H	15.15775	17.97359	27.12325	H	10.89178	5.997161	17.68911
H	15.02975	16.21014	27.37491	H	12.49616	5.736104	18.34563
H	18.70582	19.87586	24.11434	H	16.28893	5.585174	15.33491
H	15.5535	17.51242	22.4287	H	16.1654	6.248097	13.71194
H	17.09002	16.74844	20.63202	H	11.74029	6.475169	11.96929
H	20.24082	19.12494	22.32508	H	10.34884	6.700107	13.01442
H	10.2146	22.9131	21.5013	H	23.35364	11.09446	11.99422
H	13.25482	19.95116	20.91466	H	23.14426	10.93812	13.73211

H	24.63867	16.77006	11.00438
H	24.10939	15.44019	9.992663
H	25.0376	14.46539	16.3141
H	25.17178	16.09759	15.68512
H	13.06383	21.65062	6.210978
H	13.19271	22.87172	7.464002
H	9.414703	23.45869	10.2891
H	8.211616	22.19669	10.46843
H	8.290997	18.56926	7.397529
H	9.705881	18.25276	6.411091
H	11.07628	21.65759	23.36327
H	12.65382	22.36118	23.06515
H	20.70947	13.74382	16.47651
H	21.12267	12.84345	17.95417
H	19.63289	13.81567	17.89229
H	14.39806	9.939592	10.79352
H	14.14306	11.58223	11.43061
H	14.06404	10.17989	12.52415

Td_{Carb} (-45,114.223 kcal/mol)

box:	30.1717	30.1717	30.1717
C	12.025	5.890932	13.47599
C	11.45936	6.015471	16.21272
C	10.7693	6.329226	13.91418
C	12.98987	5.503177	14.40978
C	12.71425	5.578587	15.78069
C	10.48957	6.406095	15.28098
C	12.30871	5.797745	12.00893
C	14.31751	4.973929	13.95831
C	13.7498	5.146917	16.77191
C	11.12438	6.044349	17.67348
C	9.144365	6.859634	15.75608
C	9.722945	6.684614	12.90156
C	11.96384	4.432817	11.4397
C	13.62658	3.676731	17.13176
C	8.154045	5.713599	15.86204
C	9.787797	8.066009	12.31655
C	9.778789	10.66387	11.20204
C	9.22083	8.31411	11.06813
C	10.3598	9.137788	12.99274
C	10.35713	10.41227	12.4526
C	9.209052	9.578876	10.51962
C	15.46308	5.944739	13.93945
C	17.67032	7.70478	13.80221
C	16.77004	5.47103	14.02869
C	15.27822	7.314498	13.79082
C	16.35612	8.181303	13.72173
C	17.85253	6.322902	13.95814
C	11.2586	7.36626	18.37285
C	11.54336	9.788245	19.80183
C	12.12837	8.35844	17.93414
C	10.52551	7.610785	19.53201
C	10.66146	8.787959	20.23692
C	12.27272	9.546077	18.631
C	11.66471	10.98974	20.53461
C	9.759443	11.95118	10.62067
C	18.79199	8.561072	13.73817
C	9.295304	19.99021	8.8487
C	11.7615	20.78564	7.794139
C	9.901636	19.23735	7.83544
C	9.919247	21.14756	9.3217
C	11.16049	21.54007	8.805264
C	11.14094	19.62399	7.317979
C	7.961394	19.57388	9.385698
C	9.256026	21.99875	10.36213
C	11.81197	22.79036	9.309101
C	13.06024	21.2235	7.18754
C	11.78785	18.83145	6.225265
C	9.191797	18.03302	7.294334
C	6.809574	20.21336	8.630789
C	11.42209	24.01212	8.49614
C	11.34197	19.28	4.844885
C	9.337485	16.7558	8.070133
C	9.605521	14.2826	9.412581
C	8.365945	15.76362	7.95607
C	10.43936	16.49451	8.876889
C	10.57652	15.28454	9.535225
C	8.491564	14.55305	8.604154
C	9.695035	21.79611	11.78363
C	10.40048	21.44822	14.49891
C	9.533818	22.82515	12.70913
C	10.22409	20.59315	12.23798
C	10.57004	20.41677	13.5667
C	9.871546	22.66203	14.0356
C	14.30637	20.57251	7.714383
C	16.71879	19.46111	8.680733
C	14.3879	20.0438	8.997741
C	15.44937	20.5257	6.91894
C	16.63091	19.98914	7.384267
C	15.56704	19.49956	9.476565

C	17.93634	18.9104	9.137604	C	25.13436	13.68619	15.79454
C	9.714918	13.03834	10.07274	C	24.71054	12.1898	13.32623
C	10.74537	21.3028	15.86061	C	24.21499	13.5885	10.86259
C	14.15684	20.05433	23.50913	C	24.24146	16.50484	10.81339
C	12.69192	17.78285	24.23311	C	24.65835	17.98235	13.2454
C	14.79918	18.96787	24.1158	C	25.16099	16.56027	15.74306
C	12.77917	20.00593	23.27956	C	26.60979	13.38852	15.99558
C	12.04636	18.86437	23.6279	C	25.51524	13.3327	10.12129
C	14.07225	17.82657	24.46507	C	26.05212	18.53651	13.00979
C	14.94333	21.27733	23.15269	C	24.00809	16.77404	16.68096
C	12.06424	21.18282	22.68768	C	21.89372	17.29151	18.48367
C	10.56815	18.82991	23.39157	C	24.25185	16.99639	18.03451
C	11.91395	16.57769	24.66828	C	22.68779	16.80413	16.24632
C	14.75028	16.66769	25.12735	C	21.6482	17.05787	17.12481
C	16.26632	19.0565	24.41111	C	23.22638	17.25347	18.9195
C	14.96417	22.29883	24.27627	C	23.39687	11.46621	13.39886
C	9.780733	19.33754	24.58653	C	20.98527	10.00603	13.60196
C	14.79277	16.81034	26.63862	C	23.29878	10.16348	12.91446
C	17.20449	18.7377	23.28262	C	22.2649	12.03	13.97693
C	19.0584	18.09101	21.24891	C	21.08144	11.31904	14.08002
C	18.49739	19.25725	23.29214	C	22.12741	9.443176	13.01347
C	16.85127	17.89775	22.23232	C	22.85949	17.01264	10.51983
C	17.75559	17.57645	21.23473	C	20.28304	17.95383	9.838423
C	19.40857	18.94372	22.30646	C	21.71754	16.41885	11.04637
C	11.79502	21.13844	21.21127	C	22.69012	18.09172	9.654627
C	11.29728	21.18802	18.42955	C	21.43745	18.55399	9.314125
C	10.74776	21.88716	20.6785	C	20.45347	16.8751	10.71534
C	12.58249	20.4061	20.32994	C	19.00898	18.4457	9.480139
C	12.34375	20.4275	18.96641	C	20.85731	17.55371	19.40687
C	10.50112	21.92013	19.32259	C	19.79328	9.253471	13.68979
C	11.91479	15.39888	23.73798	H	13.37403	6.024324	11.81988
C	11.79372	13.14941	22.0306	H	11.74396	6.579351	11.46913
C	12.10522	15.52945	22.36709	H	13.67184	5.763938	17.68583
C	11.67334	14.12248	24.24175	H	14.75916	5.34802	16.36968
C	11.60869	13.0209	23.41496	H	8.749447	7.634806	15.07399
C	12.0457	14.43134	21.52577	H	9.243338	7.358004	16.73743
C	11.72924	12.00718	21.20182	H	10.89469	4.199388	11.58845
C	20.00428	17.78443	20.24576	H	12.53641	3.635277	11.94543
C	11.02559	21.23098	17.04419	H	12.17613	4.368904	10.35944
C	24.86882	14.40446	14.50822	H	13.7351	3.038442	16.23705
C	24.42989	15.76326	12.1023	H	12.63389	3.454729	17.56173
C	24.87388	15.80461	14.48086	H	14.38997	3.364389	17.86382
C	24.65815	13.68806	13.32723	H	8.513682	4.942284	16.56595
C	24.42396	14.36598	12.1245	H	8.018205	5.214555	14.88626
C	24.64026	16.48579	13.28331	H	7.163775	6.05249	16.20961

H	8.776858	7.478459	10.51155	H	15.40839	21.87182	25.1929
H	10.82345	8.956526	13.97139	H	13.94133	22.62127	24.53982
H	10.80692	11.24254	13.00626	H	15.54386	23.19785	24.00772
H	8.759451	9.749815	9.53598	H	10.05623	20.37918	24.82918
H	16.93705	4.394228	14.16035	H	9.992569	18.7349	25.48731
H	14.25418	7.705714	13.73329	H	8.692855	19.30903	24.40803
H	16.18749	9.255577	13.59771	H	13.7742	16.88639	27.05861
H	18.87104	5.928309	14.03216	H	15.32823	17.72942	26.93563
H	12.70254	8.187578	17.0141	H	15.29438	15.95514	27.1215
H	9.822652	6.845914	19.88694	H	18.79141	19.93324	24.10576
H	10.07323	8.959302	21.14421	H	15.83183	17.49097	22.20233
H	12.96872	10.3109	18.27139	H	17.45857	16.90676	20.42116
H	7.894742	19.83054	10.45875	H	20.41894	19.36483	22.33408
H	7.868948	18.47357	9.342562	H	10.10603	22.46111	21.35964
H	12.91064	22.66843	9.299148	H	13.40317	19.79947	20.73483
H	11.54577	22.94837	10.36991	H	12.98053	19.84859	18.28989
H	11.56432	17.75741	6.360592	H	9.671494	22.51503	18.92655
H	12.88682	18.91305	6.306	H	12.3107	16.52624	21.95562
H	6.837801	19.94233	7.560484	H	11.53457	13.99618	25.3234
H	6.86403	21.31519	8.68069	H	11.41942	12.02683	23.83342
H	5.829788	19.9042	9.031481	H	12.19187	14.5587	20.4485
H	10.32975	24.17223	8.519862	H	24.55473	12.74528	15.82301
H	11.70189	23.88925	7.435016	H	24.75693	14.28645	16.64217
H	11.90574	24.93001	8.869815	H	23.50791	14.12661	10.20496
H	11.58522	20.34386	4.675367	H	23.72342	12.62637	11.09427
H	10.24798	19.18245	4.72957	H	24.24957	18.38478	14.19033
H	11.82077	18.69254	4.043582	H	23.97581	18.34389	12.45509
H	7.481015	15.95582	7.335511	H	27.20489	14.31879	16.00408
H	11.20733	17.27118	8.988506	H	27.00557	12.76623	15.17371
H	11.45677	15.0972	10.15862	H	26.79946	12.85804	16.94358
H	7.715158	13.7881	8.500595	H	26.2252	12.76608	10.74945
H	9.130175	23.7873	12.36773	H	26.01444	14.28118	9.855151
H	10.37046	19.77626	11.51905	H	25.35629	12.76117	9.191573
H	10.97846	19.45848	13.90385	H	26.46713	18.1731	12.05298
H	9.737684	23.4855	14.74468	H	26.74903	18.21065	13.80207
H	13.49206	20.05946	9.632583	H	26.06055	19.639	12.98383
H	15.40147	20.92508	5.897485	H	25.2863	16.96266	18.40008
H	17.51625	19.96143	6.74052	H	22.47719	16.61648	15.1852
H	15.61033	19.09472	10.49283	H	20.61639	17.08413	16.75983
H	14.52623	21.73606	22.23751	H	23.4415	17.42374	19.97939
H	15.97824	20.99238	22.89049	H	24.17762	9.705553	12.44198
H	10.2537	17.79907	23.14561	H	22.32144	13.06055	14.35147
H	10.3188	19.43146	22.49864	H	20.20424	11.77998	14.54525
H	15.77707	16.56095	24.73206	H	22.07278	8.421372	12.62393
H	14.2343	15.72872	24.85631	H	21.83366	15.57634	11.74081

H	23.58018	18.58278	9.239263
H	21.32853	19.4049	8.633418
H	19.56763	16.38845	11.1362
H	12.28205	16.23294	25.65419
H	10.86054	16.8696	24.85126
H	16.51127	20.07153	24.78016
H	16.50925	18.38596	25.25929
H	10.0886	5.683152	17.82536
H	11.75694	5.308008	18.20804
H	14.61039	4.114548	14.59236
H	14.2134	4.546118	12.94123
H	9.752546	5.959357	12.06511
H	8.719127	6.54957	13.35132
H	25.244	11.83631	12.4224
H	25.33855	11.84632	14.17233
H	24.93537	17.36719	10.77487
H	24.55532	15.8578	9.970062
H	25.96794	16.05212	16.30609
H	25.58307	17.55244	15.48681
H	13.03183	21.06636	6.091782
H	13.16882	22.3197	7.308602
H	9.395942	23.06847	10.11251
H	8.159746	21.84347	10.31602
H	8.110229	18.25068	7.197169
H	9.531703	17.84449	6.25646
H	11.09626	21.32983	23.20543
H	12.63833	22.10577	22.90433

OT$_{Oxy}$ (-42,261.795 kcal/mol)

box:	30.3914	30.3914	30.3914
C	13.64186	7.003292	13.84418
C	12.49757	6.792931	16.37091
C	12.26707	7.134686	14.02922
C	14.40544	6.736651	14.97314
C	13.86874	6.603217	16.25126
C	11.66269	7.017672	15.27745
C	14.2762	7.088184	12.50299
C	14.71003	6.209086	17.41238
C	10.18746	7.055612	15.43225
C	14.408	5.715575	11.86248
C	14.81169	4.693912	17.51626
C	9.583947	5.660741	15.34653
C	11.28269	8.592091	12.42461
C	10.76277	11.09824	11.26424
C	11.02637	8.697872	11.06209
C	11.28221	9.73595	13.21513
C	11.01603	10.96773	12.63678
C	10.7719	9.926285	10.49389
C	16.50202	7.711347	15.19875
C	18.1052	9.856855	15.96961
C	17.82727	7.493135	15.54216
C	15.96636	8.993305	15.23028
C	16.77079	10.05336	15.60557
C	18.61705	8.555469	15.92573
C	11.87753	7.866455	18.38013
C	11.68482	10.10594	20.06576
C	12.58858	9.023448	18.08168
C	11.07687	7.824678	19.51624
C	10.9836	8.923037	20.34235
C	12.48869	10.12261	18.91821
C	11.59724	11.24458	20.89676
C	10.52102	12.36038	10.66434
C	18.89583	10.94573	16.38878
C	9.499133	20.29323	9.170613
C	11.91232	21.14315	8.074105
C	10.14074	19.56562	8.169306
C	10.13283	21.44894	9.616743
C	11.32979	21.915	9.074407
C	11.33004	19.97761	7.575968
C	8.16208	19.89415	9.682623
C	11.92497	23.20924	9.499093
C	11.91178	19.25156	6.415844
C	7.037217	20.49329	8.850071
C	11.40528	24.37252	8.666206
C	11.38562	19.79145	5.092849
C	9.773367	17.2283	8.352382
C	10.16074	14.70593	9.532127
C	8.836164	16.21625	8.175154
C	10.905	16.98752	9.123187
C	11.09106	15.73995	9.697316
C	9.027253	14.98055	8.753771
C	9.861292	22.01954	11.91128
C	10.42493	21.78477	14.657
C	9.535825	23.04924	12.78775
C	10.46429	20.8665	12.40095
C	10.73488	20.75618	13.75584
C	9.812689	22.93281	14.13139
C	14.27452	21.02471	7.952728
C	16.75655	19.95778	8.720872
C	14.42882	20.46444	9.215412

C	15.35924	21.07575	7.084641	C	23.38633	12.5475	15.4884
C	16.576	20.55063	7.462925	C	23.00064	13.33325	10.56003
C	15.65669	19.94578	9.590182	C	24.42728	17.07706	13.56773
C	17.98265	19.36626	9.095139	C	24.69532	11.79024	15.64595
C	10.35564	13.4358	10.13211	C	24.29667	12.7749	9.989347
C	10.72218	21.68286	16.03258	C	25.93283	17.13769	13.35009
C	14.09286	20.18019	23.46204	C	23.22625	15.6994	16.61283
C	12.5732	17.98497	24.25001	C	21.41742	16.63801	18.54777
C	14.67933	19.06434	24.05729	C	23.50861	15.55961	17.96694
C	12.71749	20.13659	23.25507	C	22.03972	16.30645	16.21628
C	11.92354	19.06265	23.65637	C	21.15662	16.77525	17.17728
C	13.94652	17.96447	24.49321	C	22.62143	16.01948	18.91493
C	14.88858	21.39235	23.13401	C	21.39693	11.56145	12.71959
C	10.44349	19.09289	23.51669	C	18.68184	11.0616	12.33407
C	14.58727	16.85706	25.25096	C	20.99478	10.41292	12.05567
C	14.96598	22.35304	24.31252	C	20.45623	12.46402	13.20106
C	9.769125	19.69961	24.73892	C	19.11114	12.20442	13.0131
C	14.57223	17.1192	26.75125	C	19.65196	10.16972	11.86407
C	16.88563	18.6686	23.27795	C	22.43548	16.70184	10.71838
C	18.76396	17.84201	21.35646	C	20.16043	18.10267	9.847637
C	18.19688	19.12872	23.33134	C	21.17844	16.35134	11.19883
C	16.50487	17.79802	22.26296	C	22.55752	17.74325	9.805258
C	17.43781	17.39155	21.32279	C	21.44154	18.42874	9.37816
C	19.11673	18.72252	22.38911	C	20.06235	17.04676	10.76384
C	11.86684	21.25827	21.33615	C	19.00601	18.79696	9.424383
C	11.30668	21.49508	18.59054	C	20.50136	17.08783	19.53238
C	10.90611	22.15916	20.8889	C	17.30754	10.83877	12.11445
C	12.556	20.47622	20.4165	C	16.12053	10.71612	11.9072
C	12.27801	20.60162	19.06449	C	19.52282	11.90126	16.78876
C	10.63298	22.27339	19.54419	C	20.23625	13.04664	17.27489
C	11.76042	15.7962	23.8595	C	14.71207	10.60481	11.65978
C	11.58457	13.44063	22.33774	H	15.27396	7.551721	12.61471
C	11.95749	15.84188	22.48436	H	13.67805	7.751818	11.85564
C	11.45184	14.58594	24.47035	H	14.27176	6.624323	18.3359
C	11.36748	13.43113	23.72312	H	15.71782	6.648348	17.31302
C	11.8631	14.67816	21.74009	H	9.762615	7.698797	14.64269
C	11.55653	12.25439	21.57226	H	9.936114	7.510714	16.40513
C	19.70797	17.42866	20.3826	H	13.42233	5.22866	11.77471
C	11.00472	21.60618	17.21665	H	15.05746	5.065248	12.47226
C	23.43785	13.48826	14.33927	H	14.84125	5.764617	10.852
C	23.56237	15.19913	12.14967	H	15.24186	4.265526	16.59523
C	23.82264	14.81957	14.48256	H	13.81516	4.245481	17.66721
C	23.14572	13.05327	13.05315	H	15.44929	4.374938	18.3549
C	23.21628	13.87198	11.92933	H	10.00779	4.999248	16.121
C	23.91207	15.69532	13.40473	H	9.787053	5.206719	14.362

H	8.492149	5.672364	15.48713	H	14.06494	15.90971	25.03375
H	11.04646	7.7846	10.45727	H	15.4144	21.86542	25.19465
H	11.47448	9.658941	14.29311	H	13.9614	22.71144	24.59466
H	10.98793	11.86544	13.26037	H	15.57857	23.2386	24.08291
H	10.58556	9.990508	9.417554	H	10.12729	20.72689	24.92032
H	18.21088	6.46738	15.52466	H	9.978615	19.10046	25.64103
H	14.91663	9.160698	14.95743	H	8.67548	19.75068	24.62274
H	16.36757	11.07088	15.62543	H	13.54171	17.25261	27.12102
H	19.65502	8.378449	16.2184	H	15.14393	18.0303	26.99636
H	13.23595	9.059186	17.19704	H	15.017	16.28797	27.31991
H	10.52148	6.904788	19.72916	H	18.47228	19.82822	24.12804
H	10.33911	8.872906	21.22494	H	15.4726	17.42935	22.21581
H	13.05256	11.03107	18.69066	H	17.14409	16.69449	20.53399
H	8.068445	20.22525	10.73125	H	20.13894	19.10762	22.44126
H	8.081903	18.79379	9.676888	H	10.3682	22.76106	21.62934
H	13.02241	23.14263	9.402247	H	13.32242	19.7715	20.76314
H	11.69737	23.38347	10.56446	H	12.8288	19.99588	18.34023
H	11.66542	18.17965	6.50654	H	9.864592	22.97785	19.21231
H	13.0114	19.33725	6.440668	H	12.17984	16.79837	21.99454
H	7.117166	20.18495	7.793822	H	11.30015	14.57131	25.55511
H	7.064845	21.5954	8.886833	H	11.1468	12.48406	24.22445
H	6.045289	20.17632	9.207705	H	12.00758	14.71251	20.65733
H	10.30699	24.44887	8.733896	H	22.55514	11.83729	15.32421
H	11.67405	24.24599	7.604057	H	23.16016	13.10725	16.41184
H	11.82061	25.33593	8.999661	H	22.61413	14.13641	9.90974
H	11.6076	20.86675	4.985892	H	22.22891	12.54425	10.58426
H	10.29287	19.65943	5.021155	H	24.17904	17.43286	14.58227
H	11.83663	19.27862	4.229269	H	23.92039	17.7408	12.84752
H	7.942925	16.43088	7.578718	H	25.53847	12.48885	15.77806
H	11.65	17.78018	9.265326	H	24.89658	11.17666	14.75206
H	11.98833	15.54469	10.2899	H	24.68784	11.11712	16.5167
H	8.270759	14.20287	8.613029	H	24.6969	11.97394	10.63392
H	9.068165	23.95306	12.38227	H	25.06193	13.56603	9.913634
H	10.71398	20.0462	11.71644	H	24.16012	12.3486	8.983653
H	11.19748	19.84429	14.14269	H	26.20094	16.7726	12.34415
H	9.56197	23.7596	14.8024	H	26.45976	16.51284	14.09084
H	13.58074	20.44219	9.910866	H	26.32476	18.16252	13.44179
H	15.21788	21.52098	6.093763	H	24.44343	15.06583	18.25485
H	17.41325	20.57836	6.759408	H	21.8153	16.4286	15.14886
H	15.78322	19.51499	10.58675	H	20.23592	17.27676	16.86816
H	14.42523	21.8981	22.26937	H	22.85591	15.88902	19.97549
H	15.9062	21.09126	22.83295	H	21.76393	9.733194	11.67274
H	10.08218	18.0608	23.36649	H	20.7796	13.37229	13.72584
H	10.17332	19.67128	22.61718	H	18.35751	12.89987	13.39549
H	15.62835	16.74375	24.90244	H	19.33834	9.275259	11.31958

H	21.07124	15.52002	11.90598
H	23.55824	18.0045	9.443695
H	21.5611	19.25152	8.667488
H	19.07233	16.76818	11.13367
H	20.65446	13.65322	16.44863
H	21.08169	12.7607	17.9272
H	19.57858	13.71428	17.86222
H	14.49521	9.942135	10.80208
H	14.2606	11.58964	11.4384
H	14.17232	10.19133	12.53353
O	24.18053	15.2525	15.74565
O	23.59354	16.07181	11.07896
O	22.74188	11.74881	12.87547
O	16.04622	19.09449	24.26954
O	11.82473	16.89919	24.66709
O	12.08894	21.22748	22.68437
O	9.522814	18.41301	7.717594
O	13.09991	21.56711	7.506731
O	9.529236	22.21192	10.59928
O	11.48365	7.331102	12.90703
O	11.91785	6.729072	17.62343
O	15.7698	6.617737	14.82991

Td$_{Oxy}$ (-42,262.375 kcal/mol)

box:	30.1717	30.1717	30.1717
C	12.15621	6.148311	13.47955
C	11.54214	6.316356	16.18354
C	10.917	6.604998	13.91795
C	13.07804	5.7984	14.45643
C	12.79883	5.851932	15.81826
C	10.56972	6.683341	15.2596
C	12.4433	5.937994	12.03503
C	13.7557	5.333284	16.83203
C	9.187347	7.036553	15.68085
C	12.01214	4.554428	11.58171
C	13.55967	3.846005	17.06852
C	8.310569	5.80179	15.79246
C	9.959618	8.170917	12.42901
C	9.782987	10.67955	11.21816
C	9.316341	8.310909	11.20527
C	10.51489	9.27929	13.05722
C	10.42164	10.52019	12.45535
C	9.230371	9.546408	10.60815
C	15.36959	6.146972	13.99591
C	17.66303	7.725825	13.79392
C	16.62752	5.557973	14.03667
C	15.24694	7.523582	13.85074
C	16.3855	8.301343	13.74749
C	17.75743	6.335643	13.93865
C	11.3458	7.508662	18.21453
C	11.56334	9.79804	19.79567
C	12.19647	8.536265	17.8248
C	10.60918	7.618124	19.38772
C	10.71519	8.746545	20.16638
C	12.3039	9.66678	18.61319
C	11.64261	10.96789	20.57506
C	9.723517	11.93431	10.5905
C	18.81693	8.520184	13.72888
C	9.419637	19.85691	9.072384
C	11.87943	20.58354	8.00262
C	10.03563	19.09859	8.081448
C	10.10026	20.98377	9.514133
C	11.32357	21.38751	8.988992
C	11.25369	19.44216	7.511671
C	8.049747	19.54201	9.557459
C	11.95449	22.6757	9.382017
C	11.80675	18.68615	6.356026
C	6.990433	20.20197	8.692398
C	11.4502	23.82283	8.524133
C	11.32096	19.25895	5.03609
C	9.490445	16.80487	8.238387
C	9.631074	14.28042	9.421513
C	8.490504	15.8682	8.005075
C	10.56636	16.48795	9.058883
C	10.63383	15.23519	9.640126
C	8.558622	14.62547	8.58924
C	9.843122	21.62035	11.77512
C	10.40318	21.42456	14.50243
C	9.584554	22.69394	12.61912
C	10.37773	20.44383	12.28549
C	10.65047	20.34956	13.63746
C	9.861838	22.59784	13.96222
C	14.23516	20.43644	7.887121
C	16.71755	19.45715	8.703523
C	14.3762	19.89204	9.158023
C	15.32564	20.49724	7.028057
C	16.54862	20.01374	7.429333
C	15.60897	19.41096	9.55931
C	17.96153	18.93094	9.099043
C	9.681074	13.0222	10.04341

C	10.71665	21.34153	15.87086	C	25.9268	18.4034	13.06711
C	14.18254	19.96338	23.23461	C	23.82449	16.68852	16.57194
C	12.78706	17.67181	23.95641	C	21.87456	17.29725	18.47411
C	14.82304	18.8742	23.81746	C	24.19079	16.95346	17.88595
C	12.81735	19.84462	23.01423	C	22.48684	16.72861	16.19823
C	12.08322	18.72047	23.3799	C	21.52443	17.03371	17.14286
C	14.15429	17.72136	24.20748	C	23.23012	17.25175	18.82317
C	14.90174	21.23703	22.96348	C	23.23811	11.63416	13.42365
C	10.60094	18.68369	23.26316	C	20.96965	10.01746	13.61777
C	14.85078	16.64256	24.95819	C	23.27362	10.32386	12.96085
C	14.88926	22.15009	24.17669	C	22.07562	12.14368	13.989
C	9.934643	19.25764	24.50121	C	20.95559	11.33861	14.08617
C	14.78422	16.87862	26.457	C	22.15599	9.528326	13.05555
C	17.06773	18.66952	23.11086	C	22.73147	16.93466	10.69178
C	19.05	18.06989	21.23933	C	20.26955	17.93661	9.841141
C	18.34519	19.19721	23.2544	C	21.55567	16.38399	11.18719
C	16.77243	17.83828	22.03704	C	22.68176	17.97686	9.773714
C	17.75808	17.54116	21.11445	C	21.46924	18.47172	9.35553
C	19.32196	18.90261	22.33244	C	20.33843	16.88112	10.76043
C	11.89547	20.94562	21.13843	C	19.03045	18.46778	9.438081
C	11.31439	21.1791	18.41786	C	20.89138	17.57065	19.44179
C	10.86288	21.77279	20.71382	C	19.82127	9.215222	13.68066
C	12.64621	20.23402	20.21001	H	13.52652	6.070752	11.86771
C	12.35691	20.35541	18.86356	H	11.93063	6.716937	11.44315
C	10.57498	21.8867	19.37433	H	13.60673	5.889183	17.77434
C	12.02933	15.47049	23.55143	H	14.78884	5.539369	16.49964
C	11.78985	13.15718	22.00891	H	8.761334	7.738039	14.94233
C	12.21284	15.53862	22.17543	H	9.224462	7.573313	16.64545
C	11.72459	14.25743	24.15678	H	10.93659	4.389363	11.77119
C	11.60771	13.11748	23.3972	H	12.56904	3.773117	12.12805
C	12.08971	14.39063	21.41479	H	12.19039	4.40809	10.50283
C	11.7053	11.9814	21.23874	H	13.67267	3.274538	16.13015
C	20.04035	17.7986	20.27863	H	12.54782	3.64344	17.46144
C	10.99573	21.27066	17.05105	H	14.29127	3.451142	17.79395
C	24.58509	14.37285	14.55408	H	8.738048	5.072711	16.50404
C	24.13445	15.77748	12.19984	H	8.220434	5.297364	14.81406
C	24.56735	15.76334	14.52848	H	7.294769	6.055959	16.13948
C	24.34784	13.71956	13.35154	H	8.89633	7.421876	10.72954
C	24.13788	14.39065	12.1513	H	11.01121	9.161105	14.02696
C	24.36425	16.49791	13.36799	H	10.85211	11.3981	12.94549
C	24.9498	13.61991	15.78392	H	8.744395	9.64977	9.633487
C	24.03292	13.66105	10.85912	H	16.69507	4.475036	14.1603
C	24.49787	17.97915	13.35675	H	14.25084	7.978529	13.80788
C	26.4523	13.42674	15.89002	H	16.29777	9.384856	13.62746
C	25.40063	13.42818	10.24183	H	18.74663	5.871692	13.99529

H	12.78114	8.436532	16.90333	H	15.26724	16.06043	27.01788
H	9.941022	6.799785	19.66584	H	18.54796	19.85501	24.10263
H	10.11517	8.840965	21.07648	H	15.76569	17.41647	21.93815
H	12.9746	10.47794	18.31556	H	17.53464	16.88307	20.26969
H	7.956325	19.88909	10.60136	H	20.31987	19.33931	22.43441
H	7.910003	18.44646	9.571266	H	10.28367	22.31453	21.46481
H	13.0495	22.57889	9.278335	H	13.46545	19.59201	20.55245
H	11.75062	22.87207	10.4497	H	12.94588	19.80189	18.12651
H	11.49941	17.6296	6.445682	H	9.745634	22.5198	19.04517
H	12.91001	18.70379	6.402791	H	12.44222	16.50158	21.70534
H	7.087554	19.89153	7.636992	H	11.59438	14.23093	25.24085
H	7.08804	21.30145	8.725434	H	11.39144	12.15932	23.87879
H	5.972731	19.94068	9.028043	H	12.22789	14.43647	20.33069
H	10.35147	23.91606	8.589052	H	24.44326	12.63888	15.76206
H	11.70734	23.65946	7.462683	H	24.56548	14.15765	16.66907
H	11.88895	24.78581	8.836568	H	23.40268	14.25102	10.17067
H	11.59071	20.32564	4.940871	H	23.51341	12.69997	11.02316
H	10.22171	19.18643	4.959344	H	24.17878	18.37057	14.33865
H	11.75814	18.72309	4.176693	H	23.80819	18.40281	12.60519
H	7.651856	16.14702	7.363402	H	26.98085	14.39648	15.88239
H	11.35634	17.22842	9.228627	H	26.83139	12.8352	15.03816
H	11.48013	14.97662	10.28293	H	26.72854	12.90008	16.81936
H	7.757343	13.89893	8.423913	H	26.05749	12.86566	10.92871
H	9.172125	23.60976	12.1901	H	25.89738	14.38903	10.01887
H	10.56766	19.59814	11.6146	H	25.32816	12.85666	9.301211
H	11.06643	19.42486	14.04783	H	26.27595	17.99546	12.10202
H	9.679474	23.45269	14.62056	H	26.61051	18.03328	13.85115
H	13.51464	19.86075	9.833772	H	26.02252	19.50168	13.02305
H	15.18471	20.92369	6.03274	H	25.24826	16.90719	18.1547
H	17.39976	20.04094	6.742318	H	22.20806	16.52991	15.15731
H	15.73007	18.98574	10.55977	H	20.46999	17.07281	16.85499
H	14.41912	21.73925	22.10652	H	23.51876	17.43665	19.86218
H	15.93986	21.01272	22.65898	H	24.19729	9.950868	12.51374
H	10.28457	17.63666	23.11399	H	22.06006	13.17384	14.36244
H	10.29066	19.24261	22.36288	H	20.03838	11.73174	14.53409
H	15.9036	16.60552	24.62761	H	22.17941	8.505272	12.66848
H	14.40052	15.66785	24.69946	H	21.60308	15.55418	11.90153
H	15.33935	21.65298	25.05425	H	23.6211	18.39671	9.407307
H	13.85495	22.42799	24.44634	H	21.433	19.30852	8.651479
H	15.45335	23.07969	23.99023	H	19.40785	16.45046	11.14179
H	10.26439	20.2955	24.68702	O	16.16968	18.98791	24.09241
H	10.19165	18.66249	25.39555	O	12.09317	16.55782	24.37962
H	8.836045	19.26583	24.40275	O	12.13084	20.91768	22.48567
H	13.73774	16.95231	26.80254	O	24.84797	16.43411	15.70025
H	15.29086	17.82179	26.72729	O	23.97949	16.48557	11.02648

O	24.40407	12.34221	13.3178	O	9.96903	6.9124	12.96464
O	9.356709	18.00281	7.591299	O	11.2031	6.338649	17.51983
O	13.06671	20.97045	7.417305	O	14.30164	5.294159	14.06894
O	9.506297	21.793	10.4602				

2.9 References

Notes: †This chapter is adapted from Moneypenny, II, T. P.; Yang, A.; Walter, N. P.; Woods, T. J.; Gray, D. L.; Zhang, Y.; Moore, J. S. *J. Am. Chem. Soc.* **2018**, *140*, **17**, 5825-5833. The materials are reproduced/adapted with permission. Copyright © 2018 American Chemical Society. This chapter is a collaborative work with Anna Yang, Nathan Walter, Toby Wood, and Danielle Gray. T. P. M. II conceived experiments, designed, synthesized, and characterized all precursors, grew precursor single crystals, performed single metathesis experiments, performed precursor mixing experiments, and authored all text. A. Y. performed single precursor time-dependent metathesis experiments. T. W. and D. G. performed single crystal XRD experiments and solved the structures of each precursor. N.W. performed the DFT calculations.

(1) Rowan, S. J.; Cantrill, S. J.; Cousins, G. R. L.; Sanders, J. K. M.; Stoddart, J. F. *Angew. Chem. Int. Ed.* **2002**, *41*, 898.

(2) Jin, Y.; Yu, C.; Denman, R. J.; Zhang, W. *Chem. Soc. Rev.* **2013**, *42*, 6634.

(3) Zhang, W.; Moore, J. S. *J. Am. Chem. Soc.* **2005**, *127*, 11863.

(4) Sisco, S. W.; Larson, B. M.; Moore, J. S. *Macromolecules* **2014**, *47*, 3829.

(5) Gallant, A. J.; MacLachlan, M. J. *Angew. Chem. Int. Ed.* **2003**, *42*, 5307.

(6) Yu, C.; Jin, Y.; Zhang, W. *Chem. Rec.* **2015**, *15*, 97.

(7) Klotzbach, S.; Beuerle, F. *Angew. Chem. Int. Ed.* **2015**, *54*, 10356.

(8) Mastalerz, M. *Angew. Chem. Int. Ed.* **2010**, *49*, 5042.

(9) Tozawa, T.; Jones, J. T. A.; Swamy, S. I.; Jiang, S.; Adams, D. J.; Shakespeare, S.; Clowes, R.; Bradshaw, D.; Hasell, T.; Chong, S. Y.; Tang, C.; Thompson, S.; Parker, J.; Trewin, A.; Bacsa, J.; Slawin, A. M. Z.; Steiner, A.; Cooper, A. I. *Nat. Mater.* **2009**, *8*, 973.

(10) Xu, D.; Warmuth, R. *J. Am. Chem. Soc.* **2008**, *130*, 7520.

(11) Mastalerz, M. *Chem.Commun.* **2008**, 4756.

(12) Ding, S.-Y.; Wang, W. *Chem. Soc. Rev.* **2013**, *42*, 548.

(13) Colson, J. W.; Woll, A. R.; Mukherjee, A.; Levendorf, M. P.; Spitler, E. L.; Shields, V. B.; Spencer, M. G.; Park, J.; Dichtel, W. R. *Science* **2011**, *332*, 228.

(14) Côté, A. P.; Benin, A. I.; Ockwig, N. W.; O'Keeffe, M.; Matzger, A. J.; Yaghi, O. M. *Science* **2005**, *310*, 1166.

(15) Xie, T.-Z.; Endres, K. J.; Guo, Z.; Ludlow, J. M.; Moorefield, C. N.; Saunders, M. J.; Wesdemiotis, C.; Newkome, G. R. *J. Am. Chem. Soc.* **2016**, *138*, 12344.

(16) Lu, X.; Li, X.; Guo, K.; Xie, T.-Z.; Moorefield, C. N.; Wesdemiotis, C.; Newkome, G. R. *J. Am. Chem. Soc.* **2014**, *136*, 18149.

(17) Slater, A. G.; Little, M. A.; PulidoA; Chong, S. Y.; HoldenD; ChenL; MorganC; WuX; ChengG; ClowesR; Briggs, M. E.; HasellT; Jelfs, K. E.; Day, G. M.; Cooper, A. I. *Nat. Chem.* **2017**, *9*, 17.

(18) Stefankiewicz, A. R.; Sanders, J. K. M. *Chem.Commun.* **2013**, *49*, 5820.

(19) Ponnuswamy, N.; Cougnon, F. B. L.; Clough, J. M.; Pantoş, G. D.; Sanders, J. K. M. *Science* **2012**, *338*, 783.

(20) Cougnon, F. B. L.; Ponnuswamy, N.; Jenkins, N. A.; Pantoş, G. D.; Sanders, J. K. M. *J. Am. Chem. Soc.* **2012**, *134*, 19129.

(21) Schneider, M. W.; Oppel, I. M.; Mastalerz, M. *Chem. Eur. J.* **2012**, *18*, 4156.

(22) Sun, J.; Warmuth, R. *Chem. Commun.* **2011**, *47*, 9351.

(23) Cook, T. R.; Stang, P. J. *Chem. Rev.* **2015**, *115*, 7001.

(24) Bunzen, J.; Iwasa, J.; Bonakdarzadeh, P.; Numata, E.; Rissanen, K.; Sato, S.; Fujita, M. *Angew. Chem. Int. Ed.* **2012**, *51*, 3161.

(25) Seidel, S. R.; Stang, P. J. *Acc. Chem. Res.* **2002**, *35*, 972.

(26) Dill, K. A.; Chan, H. S. *Nat. Struct. Mol. Biol.* **1997**, *4*, 10.

(27) Hasell, T.; Cooper, A. I. *Nat. Rev. Mater.* **2016**, *1*, 16053.

(28) Liu, X.; Warmuth, R. *J. Am. Chem. Soc.* **2006**, *128*, 14120.

(29) Jelfs, K. E.; Eden, E. G. B.; Culshaw, J. L.; Shakespeare, S.; Pyzer-Knapp, E. O.; Thompson, H. P. G.; Bacsa, J.; Day, G. M.; Adams, D. J.; Cooper, A. I. *J. Am. Chem. Soc.* **2013**, *135*, 9307.

(30) Wang, Q.; Yu, C.; Zhang, C.; Long, H.; Azarnoush, S.; Jin, Y.; Zhang, W. *Chem. Sci.* **2016**, *7*, 3370.

(31) Lee, S.; Yang, A.; Moneypenny, T. P.; Moore, J. S. *J. Am. Chem. Soc.* **2016**, *138*, 2182.

(32) Yoneya, M.; Tsuzuki, S.; Yamaguchi, T.; Sato, S.; Fujita, M. *ACS Nano* **2014**, *8*, 1290.

(33) Sun, Q.-F.; Iwasa, J.; Ogawa, D.; Ishido, Y.; Sato, S.; Ozeki, T.; Sei, Y.; Yamaguchi, K.; Fujita, M. *Science* **2010**, *328*, 1144.

(34) Hennrich, G.; Lynch, V. M.; Anslyn, E. V. *Chem. Eur. J.* **2002**, *8*, 2274.

(35) Gilmore, C. J.; MacNicol, D. D.; Murphy, A.; Russell, M. A. *Tetrahedron Lett.* **1983**, *24*, 3269.

(36) Schaubach, S.; Gebauer, K.; Ungeheuer, F.; Hoffmeister, L.; Ilg, M. K.; Wirtz, C.; Fürstner, A. *Chem. Eur. J.* **2016**, *22*, 8494.

(37) Nielsen, B. E.; Gotfredsen, H.; Rasmussen, B.; Tortzen, C. G.; Pittelkow, M. *Synlett* **2013**, *24*, 2437.

(38) Wu, Z.; Moore, J. S. *Tetrahedron Lett.***1994**, *35*, 5539.

(39) Zhang, W.; Lu, Y.; Moore, J. S. In *Organic Syntheses*; John Wiley & Sons, Inc.: 2003.

(40) Zhang, W.; Kraft, S.; Moore, J. S. *J. Am. Chem. Soc.* **2004**, *126*, 329.

Chapter 3

Impact of Shape Persistence on the Porosity of Molecular Cages†

3.1 Introduction

Materials with permanent microporosity have fundamentally improved our ability to perform better separations and size-selective catalysis with increasingly smaller volumes.[1] Such materials have revolutionized important technologies including adsorption, catalysis, and molecular separations. Extensive interest in open pore structures has led to the development of various synthetic functional porous materials, each with unique characteristics and physical properties including zeolites,[2,3] metal-organic frameworks (MOFs),[4-8] covalent organic frameworks (COFs),[9-12] and polymers with intrinsic microporosity (PIMs),[13-15] all of which contribute to the wealth of literature on this topic. While the structural stability and chemical robustness of extended frameworks contributes to their overall utility, these features also engender difficulty with handling, modification, and solution processing methods post-synthetically. Recently, a new class of materials which exhibit permanent porosity in the solid state, yet are soluble in common organic solvents have proven to be extremely useful. Materials which retain open pores in the solid state but can be dissolved with proper solvent provide the significant advantage of solution processing. Consequently, film-deposition, co-crystallization of multiple constituents, and guest recognition may be pursued.

Porous organic cages (POCs) have emerged as a class of porous materials which can exhibit unique pore topologies in the solid state that are otherwise inaccessible with nonporous discrete molecules.[1,16-21] Additionally, unlike network solids, POCs are soluble in common organic solvents.[18] Although the field of POCs has seen many recent advances, fundamental studies relating molecular structure to macroscopic properties are needed to accelerate rational design. For example, current research efforts in the field of MOFs involve constructing frameworks with flexible building units that expand or "breathe" when exposed to adsorbates.[22-24] The flexibility in some MOFs provides an avenue towards functional materials that respond to specific stimuli. On the other hand, introducing flexibility in the structural design of POCs tends to induce adverse effects to their physical properties. Since most molecular cages possess accessible windows resembling the size of small gas molecules (< 2 nm), and the crystal lattice energy is dominated by weak van der Waals interactions, structural motion (and thus cage flexibility) greatly affects the porosity of these materials.[25,26] For example, researchers have shown that flexibility of cage structure permits cooperative diffusion mechanisms, whereby transient molecular reorganizations induced by the adsorbate elicit the formation of diffusion-accessible pathways within the solid.[25,26] However, if the cage architecture becomes too flexible, removal of enclatherated solvent molecules from the solvate is often accompanied by a collapse of the cage structure, thus significantly reducing the adsorption capacity or eliminating it completely. For example, Zhang and coworkers reported flexible [2+3] amine cages that collapsed after desolvation to yield a material with very low porosity.[27] Mastalerz and coworkers synthesized [4+6] salicylbisimine cages that collapsed after hydrogenation to the corresponding amines.[28] Cooper and coworkers reported a [4+6] imine cage that collapsed after reduction to amines, then re-achieved shape persistence and porosity after post-synthetic tying with formaldehyde.[29]

Although these experiments hint at the undesirable effects of excess molecular flexibility, they describe all-or-nothing scenarios where added structural flexibility results in complete cage collapse and reduced adsorption capacity. To date, there have not been any studies investigating the effects of gradual alterations in flexibility on the porosity of molecular cages. Herein, we test the hypothesis that cage shape-persistence dominates adsorption capacity in molecular cage solids. We describe a system that specifically modifies the edges of a POC previously synthesized by our group, **Td$_A$** (Scheme 3.1),[30] to achieve controlled, stepwise adjustments in flexibility. Utilizing alkyne metathesis (AM) and post-synthetic modifications (PSMs), we synthesized organic cages

of varying structural shape-persistence: **Td$_A$**, **Td$_{Br}$**, and **Td$_H$** (Scheme 3.1). X-ray crystal structures confirmed their tetrahedral geometry and transformations at all six edges. Nitrogen adsorption experiments of both rapidly-crystallized and slowly-crystallized samples exhibited a trend in surface area: **Td$_A$** > **Td$_{Br}$** > **Td$_H$**. Short-time *ab initio* molecular dynamics (AIMD) and long-time classical molecular dynamics (MD) modeling of cage motions corroborated the trend in our experimental data and emphasized that shape-persistence governs the microporosity of these materials.

3.2 Synthesis and Characterization of Molecular Cages

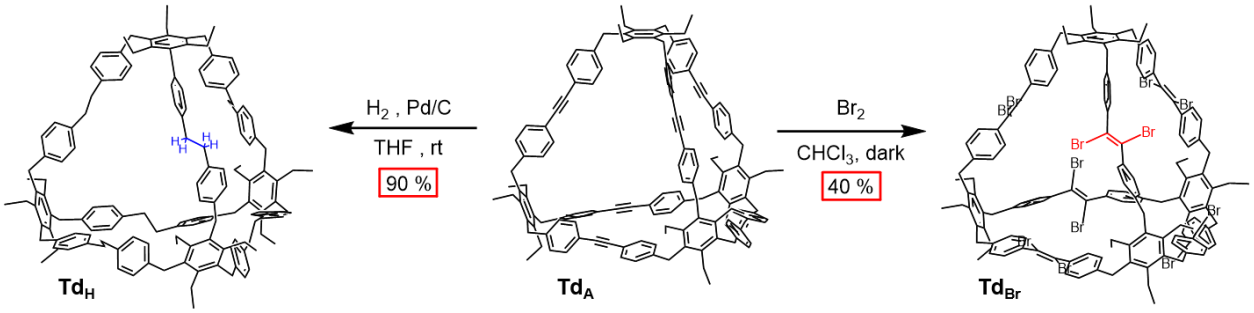

***Scheme 3.1**: Synthesis of synthetically modified cages, **Td$_H$** and **Td$_{Br}$**, from **Td$_A$**.*

Synthesis of the molecular cages was performed using alkyne metathesis and a post-synthetic transformation strategy which allowed precise modifications of the molecular architecture and resulting shape persistence. Three molecular cages were synthesized, **Td$_A$**, **Td$_{Br}$**, and **Td$_H$** (Scheme 3.1), each with various degrees of molecular shape-persistence. Cage **Td$_A$** was synthesized via alkyne metathesis following a previously reported procedure in nearly quantitative yields.[30] The two modified cages, **Td$_{Br}$** and **Td$_H$**, were synthesized from **Td$_A$** using post-synthetic modifications in good yields. Specifically, **Td$_{Br}$** was synthesized using a procedure adapted from a previous report[31] in 40 % yield in one step by bromination with excess bromine in chloroform ($CHCl_3$). Cage **Td$_H$** was synthesized in 90 % in one step by hydrogenation using Pd/C and hydrogen gas in tetrahydrofuran (THF).

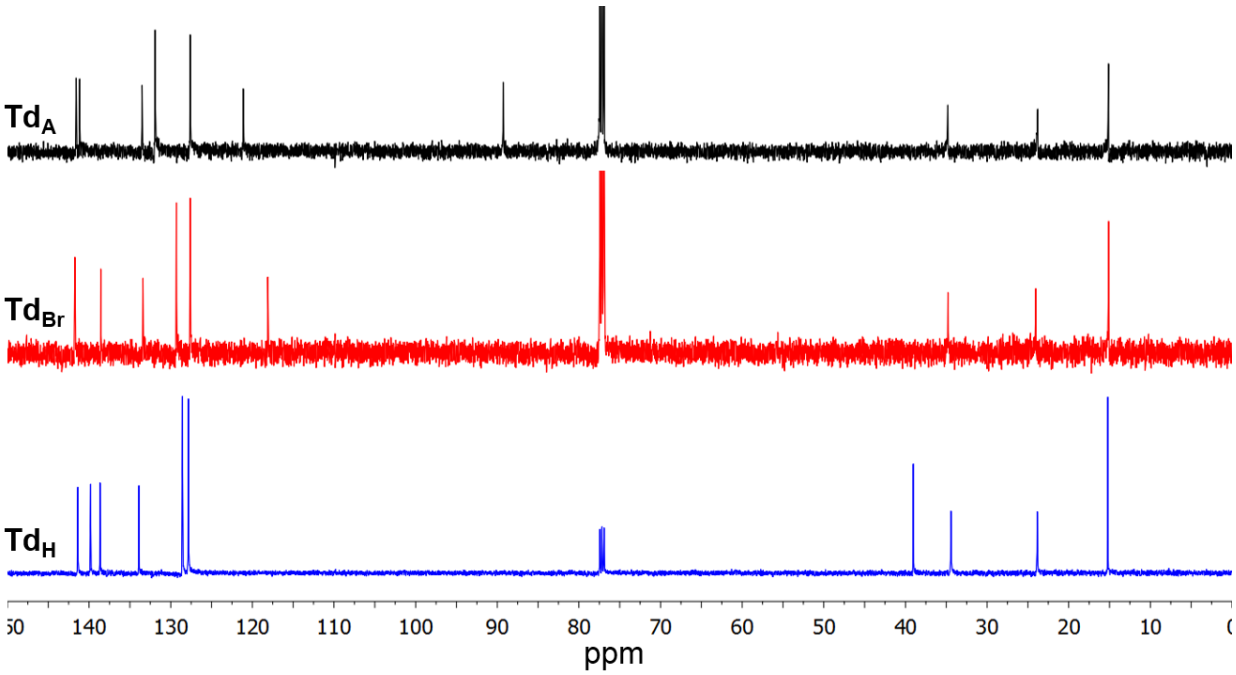

***Figure 3.1**: [13]C NMR of each cage.*

All cages were characterized by nuclear magnetic resonance (NMR). The spectra, shown in Figure 3.1 and in Figures 3.10-3.15, demonstrate their high symmetry such that only one-sixth of the structure is visible by NMR. The ^{1}H NMR of **Td$_{A}$** exhibits two sets of aromatic doublets at 7.44 ppm and 6.99 ppm, respectively, as well as a benzylic singlet at 4.14 ppm, and ethyl resonances at 2.41 ppm and 1.17 ppm. The ^{13}C NMR of **Td$_{A}$** exhibits a peak at 89.28 ppm corresponding to the alkynyl carbon atoms. The ^{1}H NMR of **Td$_{Br}$** reveals only two sets of aromatic doublets at 7.44 and 7.11 ppm, indicating that only one geometrical isomer formed. The ^{13}C NMR confirms only one geometrical isomer with the single peak at 118.11 ppm corresponding to a single dibromoalkenyl carbon. The ^{1}H NMR of **Td$_{H}$** indicates the presence of a new resonance corresponding to benzylic protons. The ^{13}C NMR exhibits a significant upfield shift of the previous alkynyl carbon to 39.03 ppm corresponding to the new benzylic carbon.

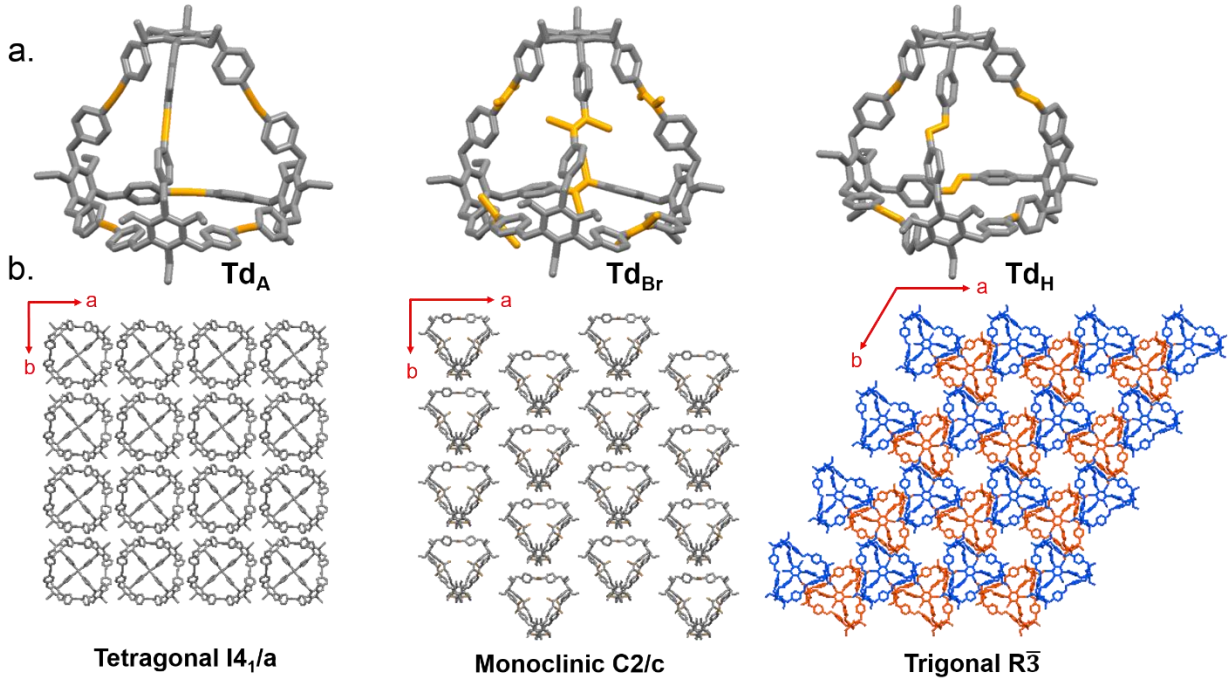

***Figure 3.2**: (a) XRD structures of each cage. (b) Crystal packing of each cage viewed along the c-axis. In each crystal structure, solvent was removed for clarity.*

To compare their solid-state packing and confirm successful transformations on all six alkynyl edges, single crystal X-ray diffraction analysis was performed (Figure 3.2). Cage **Td_A** crystallized from slow diffusion of a 1:1 (*v/v*) layered mixture of $CHCl_3$ and toluene in the tetragonal space group I41/a. Intensity data were collected at 200K on a D8 goniostat equipped with a Bruker PHOTON100 CMOS detector at Beamline 11.3.1 at the Advanced Light Source (Lawrence Berkeley National Laboratory) using synchrotron radiation tuned to λ=1.2399 Å. For data collection frames were measured for a duration of 1s at 0.5° intervals of ω with a maximum 2 θ value of ~100°.The cages pack in an edge-to-edge fashion exhibiting mainly CH···π (alkyne) interactions.

Cage **Td_{Br}** crystallized from slow diffusion of a 1:1 (*v/v*) mixture of $CHCl_3$ and toluene in the monoclinic space group C2/c. Single crystals were mounted on a 0.3 mm loop with the minimal amount of Paratone-N oil and flash cooled to 100 K. Single crystal X-ray data were collected on a Bruker D8 Venture equipped with a four-circle kappa diffractometer and Photon 100 detector. A Iμs microfocus Mo (λ = 0.71073 Å) source supplied the multi-mirror monochromated incident beam. The crystal structure showed that the tetrahedral structure remained intact, and all six alkynyl linkages were transformed exclusively to the corresponding trans-dibromoalkene (Figure

3.2). We hypothesize that rigidity enforced by cage vertices restricts edge motion, prompting solely the trans geometric isomer to form. A similar result was observed with post-synthetic bromination of a MOF.[31] The **Td$_{Br}$** cages align primarily in edge-to-edge motifs through CH···Br interactions.

Cage **Td$_{H}$** crystallized from slow diffusion of a 1:1 (*v/v*) layered mixture of $CHCl_3$ and methanol in the trigonal $R\bar{3}$ space group. Single crystals were mounted on a 0.3 mm loop with the minimal amount of Paratone-N oil and flash cooled to 100 K. Single crystal X-ray data were collected on a Bruker D8 Venture equipped with a four-circle kappa diffractometer and Photon 100 detector. A Iμs microfocus Cu (λ = 1.54178 Å) source supplied the multi-mirror monochromated incident beam. The single crystal structure showed that the tetrahedral structure remained intact and all six alkynyl linkages transformed to the corresponding alkyl carbon atoms. The resulting crystal is a racemate of two atropisomers (*M* and *P*, depicted as blue and orange respectively in Figure 3.2) that pack in both window-to-window and edge-to-edge packing motifs through T-shaped CH···π (aryl) interactions.

3.3 Preparation and Characterization of Molecular Solids

As reported in the literature, the preparative conditions of POC solids greatly influence the resulting porosity of the material.[18,32,33] The most obvious example of this phenomenon is shown in a report by Cooper et al. which demonstrates drastic changes in the adsorption capacity of three different molecular cages due to changes in crystallization conditions. In the case of the ethanediamine-derived cage, CC1, when crystallized from ethyl acetate in the space group C2/*c*, the solid is essentially non-porous; however, when crystallized with 1,4-dioxane, the BET surface area becomes 333 $m^2\ g^{-1}$.[20] Furthermore, they showed that even when crystallized from the same solvent mixture, the rate at which the solids are crystallized has a huge effect on the porosity of the resulting solid. A solid of CC2β exhibits a surface area of 330 $m^2\ g^{-1}$ when crystallized slowly, but is much more porous (720 $m^2\ g^{-1}$) when crystallized rapidly.[20] Rapid crystallization engenders crystal defects, which may increase the surface area of the material, while slow crystallization reduces the amount of defects in the solid.

In light of these findings, we prepared molecular solids of each cage using two separate procedures: rapid and slow crystallization. Rapidly crystallized powders were prepared by precipitation from a $CHCl_3$ solution with the rapid addition of an excess amount of methanol. The

resulting mixtures were stirred for 30 min before being filtered, collected and dried under high vacuum for 12 h. Slowly crystallized samples of each cage were prepared by slow evaporation of a $CHCl_3$ solution over the course of 5-7 days. The solids were desolvated by leaving the samples open to air for 12 h, then dried under high vacuum for 1 h.

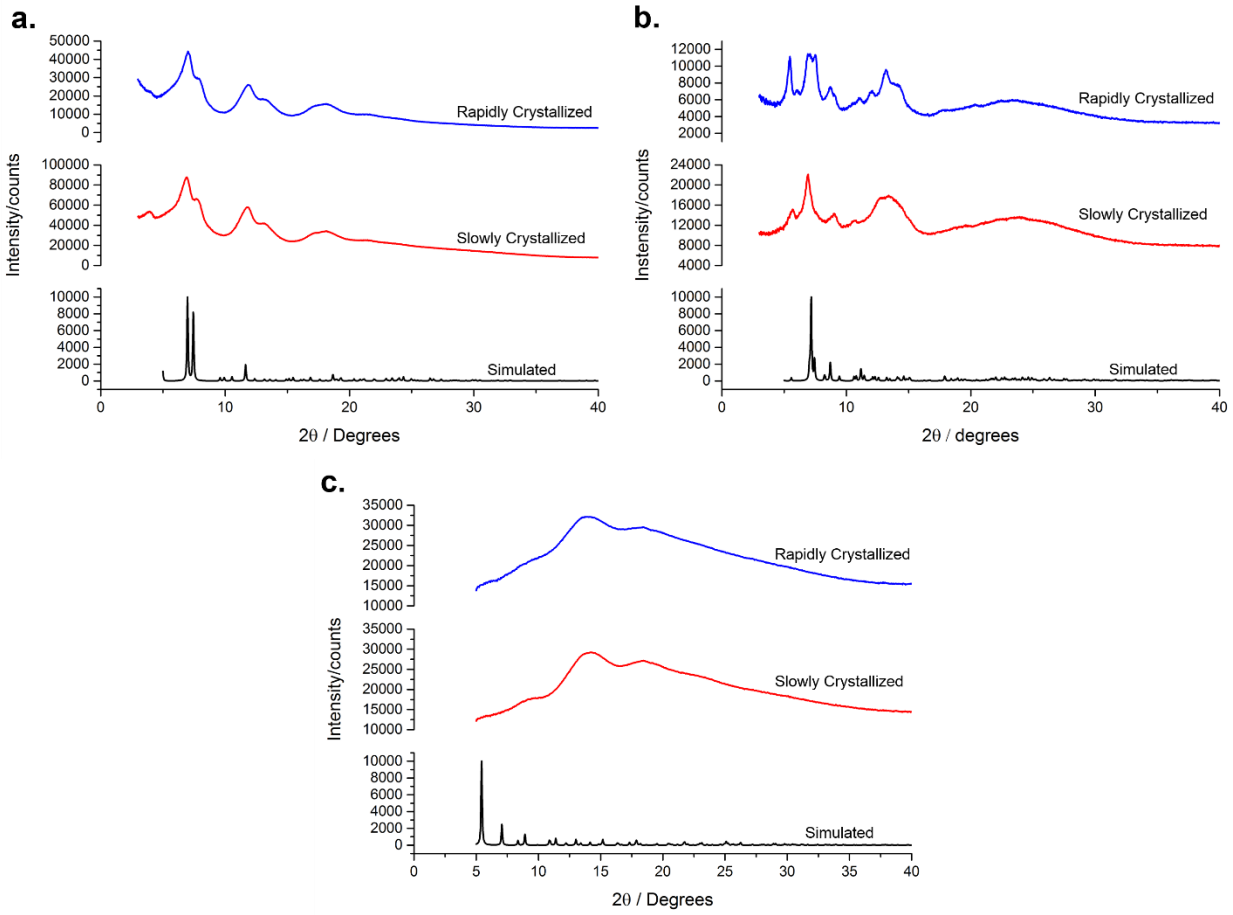

***Figure 3.3**: Powder XRD diffraction data for (a) **Td**$_A$, (b) **Td**$_{Br}$, and (c) **Td**$_H$.*

The molecular solids were characterized by powder X-ray diffraction (PXRD) to probe crystallite size and molecular packing (Figure 3.3). PXRD of the rapidly precipitated powders of **Td**$_A$ and **Td**$_B$ exhibited broad peaks indicative of small crystallite size as a result of the preparative conditions. The PXRD of the slowly crystallized samples of **Td**$_A$ and **Td**$_B$ were also quite similar to those of the rapidly crystallized powders, indicating that the difference between the two types of samples were difficult to distinguish via PXRD. Both samples of **Td**$_H$ proved to be amorphous by diffraction methods, indicating that this cage undergoes a phase change to an amorphous solid upon desolvation.[29] This phenomenon is indicative of cage collapse after removing enclatherated solvent.

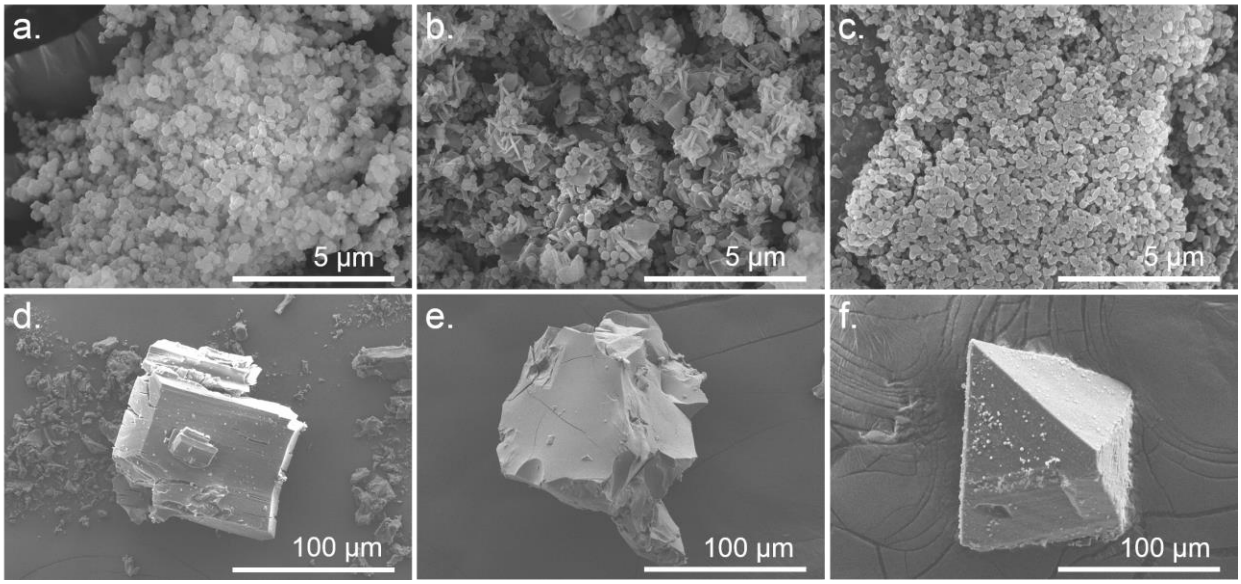

***Figure 3.4**: Scanning electron miscroscopy images of molecular cage solids. (a) Rapidly crystallized* $\mathbf{Td_A}$ *solid. (b) Rapidly crystallized* $\mathbf{Td_{Br}}$ *solid. (d) Rapidly crystallized* $\mathbf{Td_H}$ *solid. (d) Slowly crystallized* $\mathbf{Td_A}$ *solid. (e) Slowly crystallized* $\mathbf{Td_{Br}}$ *solid. (f) Slowly crystallized* $\mathbf{Td_H}$ *solid.*

To further characterize these materials and probe how the morphology of each molecular solid differs due to the preparatory conditions, scanning electron microscopy (SEM) was used. As seen in Figure 3.4, the preparatory conditions severely altered the morphology of each molecular solid on the micron scale. Rapid precipitation results in very small crystallize size domanins (on the order of nanometers) for each cage as shown in Figure 3.4a-c. Slowly crystallized samples tend to have crystallite sizes that are much larger (ca. 100 µm) as shown in Figure 3.4d-f. The crystallites of $\mathbf{Td_A}$ and $\mathbf{Td_{Br}}$ exhibit cracking and breaking, a phenomenon most likely associated with the loss of solvent during the vacuum treatment.[20]

3.4 Nitrogen Adsorption Isotherms and BET Analysis

To test the hypothesis that shape persistence governs the porosity of molecular cages, all samples were tested for their nitrogen adsorption capacity using BET analysis. Samples were first heated to 70 ºC under high vacuum for 12 h to remove any adsorbates. Nitrogen isotherms were measured at 77 K. As shown in Figure 3.5, each sample exhibited a type I isotherm, typical of microporous materials (pore size < 2 nm).[34] The results of these experiments are summarized in

Table 3.1. Overall, **Td_A** was the most porous molecular cage, followed by **Td_{Br}**, and then by **Td_H**, which was observed to be non-porous in both preparative conditions.

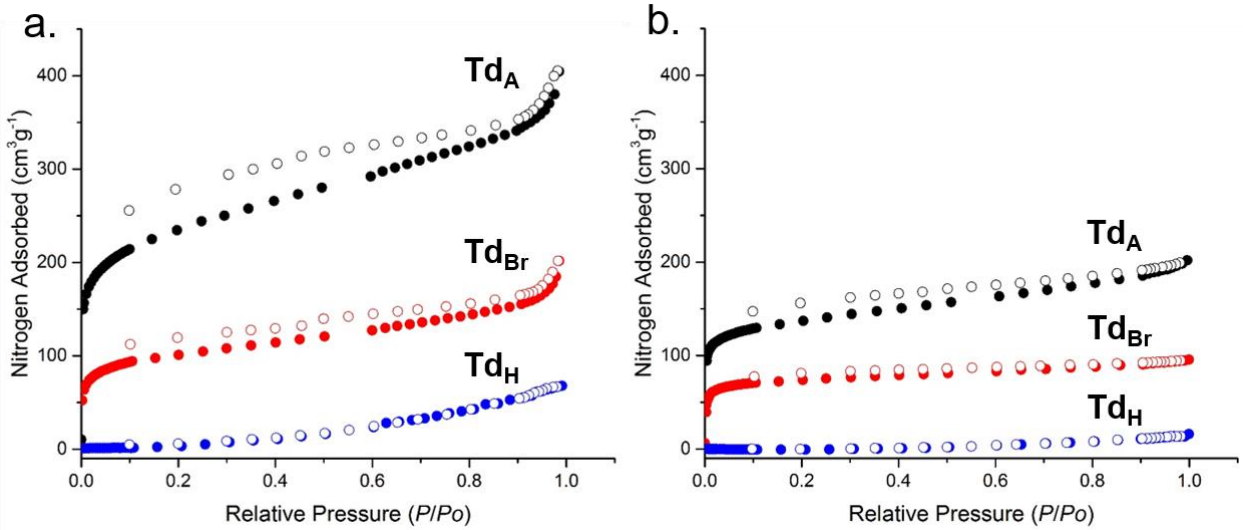

***Figure 3.5**: Nitrogen BET isotherms of each cage prepared from (a) rapid precipitation and (b) slow crystallization. Solid circles represent adsorption while empty circles represent desorption.*

***Table 3.1**: Specific surface area data of all samples obtained from nitrogen adsorption experiments.*

Powder	SA_{BET} $[m^2g^{-1}]$	$SA_{Langmuir}$ $[m^2g^{-1}]$	**Crystal**	SA_{BET} $[m^2g^{-1}]$	$SA_{Langmuir}$ $[m^2g^{-1}]$
Td_A	823	941	Td_A	509	586
Td_{Br}	378	436	Td_{Br}	279	319
Td_H	5	6	Td_H	0	0

The resulting nitrogen isotherm data supports our hypothesis and also corroborates many observations made with other cage systems. Three main observations are extrapolated from this data. Namely, 1) rapidly crystallized samples tend to be more porous than their slowly crystallized counterparts, 2) a trend in surface area exists in both sets of data: **Td_A** > **Td_{Br}** > **Td_H**, and 3) **Td_H** is non-porous regardless of preparation. For the first observation, it has been shown in multiple investigations that rapidly crystallized molecular solids tend to be more porous as a result of crystal defects.[20,33] Cooper et al. calculated that an absence of one cage in eight in the crystal packing results in the increase of surface area by 78 %.[20] In the case of **Td_A** solids, for example, we observed that rapidly crystallization results in a 61.7 % increase in surface area as compared to the slowly

crystallized sample, whereas **Td$_{Br}$** solids exhibited a 35.4 % increase in surface area. The observation that **Td$_{H}$** is non-porous in both preparatory conditions (and amorphous) allows us to conclude that the cage collapses upon desolvation. This phenomenon has been observed in other studies with different cage systems.[27,29] Finally, it is interesting to note that the isotherms for **Td$_{A}$** and **Td$_{Br}$** exhibit adsorption hysteresis. Usually, such hysteresis occurs in systems which are mesoporous. In the case of these cage systems, however, this phenomenon cannot be justified by the crystal structures alone, since there should not exist any instances of pores larger than 2 nm. It is likely, however, that the cracking and breaking of the crystallites as a result of the vacuum treatment can induce mesoporous character during desorption and thus give rise to hysteresis. This observation has been previously reported in a different cage system.[20]

3.5 Molecular Dynamics Simulations

To better understand cage shape-persistence and the observed trend in the nitrogen adsorption experiments, we performed theoretical computations. Our approach focused on modeling the molecular motion of individual cages on the picosecond timescale via *ab initio* molecular dynamics (AIMD) and classical molecular dynamics (MD). AIMD and classical MD were performed to capture the short-time and long-time properties of the molecular cages, respectively, with initial configurations generated from X-ray coordinates.

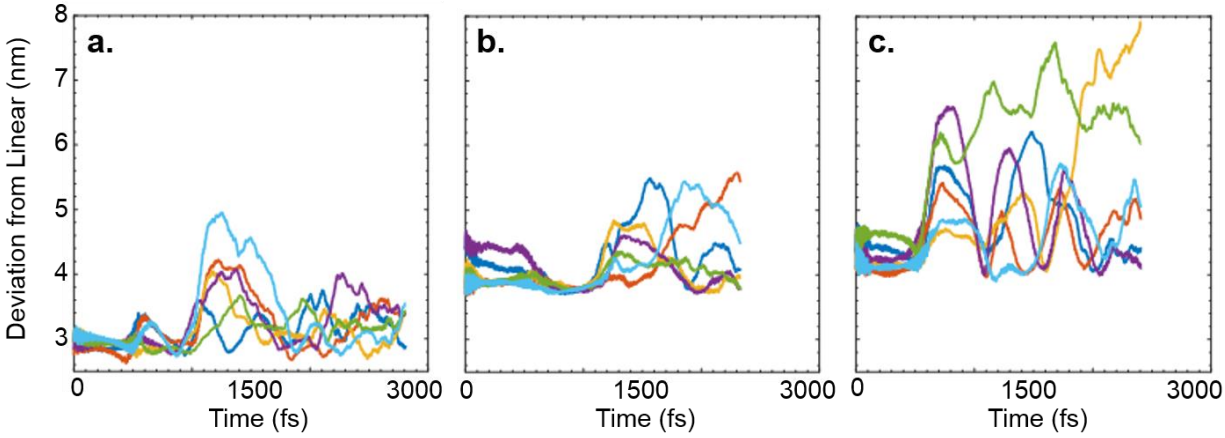

***Figure 3.6**: Deviation from linear plotted as a function of time for (a) **Td$_{A}$**, (b) **Td$_{Br}$**, and (c) **Td$_{H}$** calculated from the AIMD simulation. Each colored line corresponds to one edge, with a total of six edges per cage.*

To quantify the short-time shape-persistence of the molecular cages, we performed AIMD simulations at 300 K in an NVT ensemble with a time step of 1 fs. The bending flexibility of the edges can be visually observed from simulation movies (*Movies S1-S6* provided in the published article). Cage **Td$_A$** shows the smallest amplitude of edge motion, while **Td$_H$** shows the largest. To be more precise, we computed an average linear deviation of each edge from its initial structural configuration, $\langle \delta l \rangle$, and used this term to quantify the short-time flexibility. Figure 3.6 shows the deviation from linear as a function of time for all three cages. We then averaged the data obtained from the simulation by edge and over the entire simulation time. Over an elapsed time period of 3 ps, the time-averaged edge deviations of **Td$_A$**, **Td$_{Br}$**, and **Td$_H$** were 3.2 nm, 4.2 nm, and 5.0 nm, respectively. When compared to the experimentally measured specific surface area SA_{BET} values for both the powders and desolvated crystals, these values correlate well (Figure 3.7).

The long-time shape-persistence and volume/porosity of the molecular cages were modeled by classical MD simulations using the universal force field[35] with time steps of 0.05 fs for **Td$_A$** and 1.0 fs for **Td$_{Br}$** and **Td$_H$.** Production runs were performed for 300 ps in an NVT ensemble at 300 K. From these simulations, the time-averaged root mean squared deviation, ⟨RMSD⟩, was computed from the molecular cages relative to their initial configurations and was used to indicate the long-time flexibility of the entire molecule. Again, **Td$_A$** proved to be the most rigid structure with a ⟨RMSD⟩ of 0.05 nm, while **Td$_{Br}$** and **Td$_H$** had ⟨RMSD⟩ values of 0.1 nm and 0.3 nm, respectively. These values also correlate well with the experimentally measured specific area, SA_{BET}, values for both the powders and desolvated crystals (Figure 3.7).

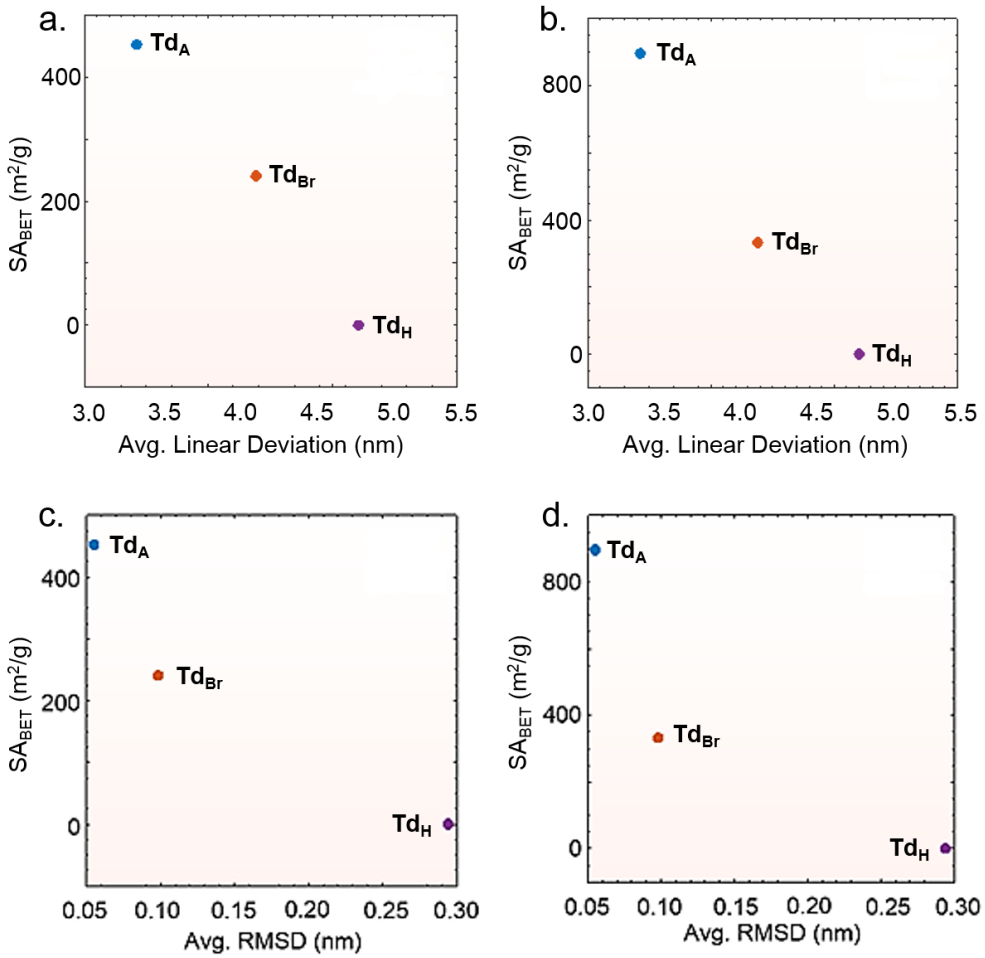

***Figure 3.7**: Experimental measures of porosity plotted against measures of flexibility. (a) Specific surface areas of slowly crystallized samples vs. average linear deviation. (b) Specific surface areas of rapidly crystallized samples vs. average linear deviation. (c) Specific surface areas of slowly crystallized samples vs. average RMSD. (d) Specific surface areas of rapidly crystallized samples vs. average RMSD.*

Lastly, the time-dependent internal volume of molecular cages, ⟨V⟩, obtained from the classical MD simulations, served as a theoretical measure of the cage porosity. The time-averaged ⟨V⟩ was computed as the summation of volumes of many small internal tetrahedrons, which were constructed by connecting representative atoms on cage edges from the initial starting configuration of **Td$_A$** as shown in Figure 3.8. The ⟨V⟩ correlates well with ⟨δl⟩ obtained from the AIMD simulation and with ⟨RMSD⟩ obtained from the classical MD simulation (Figure 3.9). Interestingly, the classical MD simulation captured the partial collapse of **Td$_H$** during the simulation time window (Figure 3.9), while **Td$_A$** and **Td$_{Br}$** retained their structure during the entire

simulation. These results provide a molecular-scale understanding of the non-porous nature of desolvated **Td$_H$** solid, as well as its structural change to an amorphous solid after desolvation.

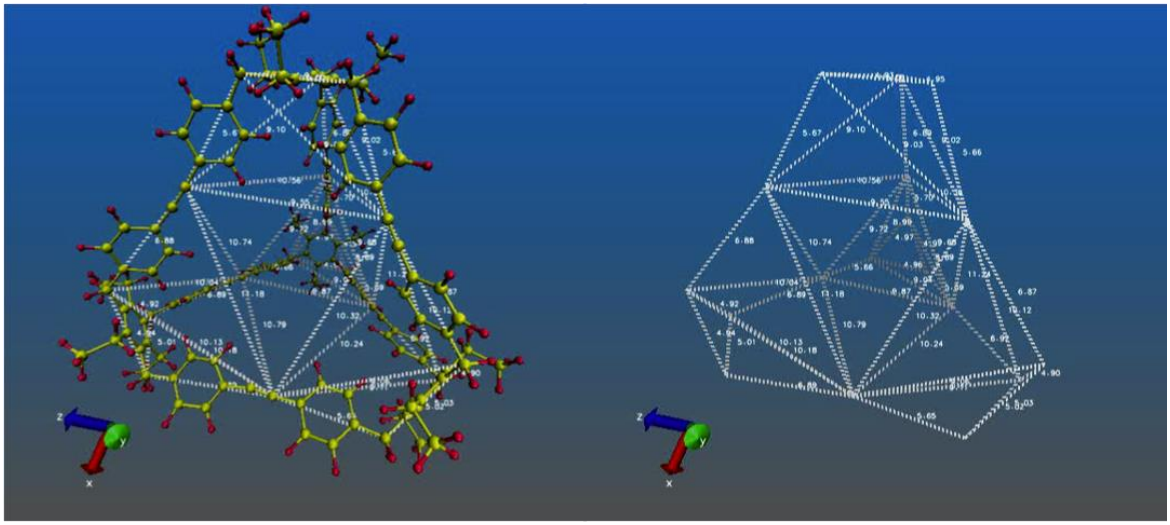

***Figure 3.8**: Tessellation of **Td$_A$** with critical atoms shown used for the ⟨V⟩ calculation.*

These simulations suggest that shape-persistence of the molecular cages governs their porosity. Close inspection of cage motion in the simulation movies reveals key structural features responsible for this phenomenon. In the simulations for **Td$_A$**, the alkynyl edges restrict bending and/or rotation about the C_{arene}-$C_{alkynyl}$-$C_{alkynyl}$-C_{arene} torsional angle. This restricted movement fortifies the vertices and prevents partial window closure and cage collapse after desolvation. In the simulations for **Td$_{Br}$**, the alkenyl edges provide limited bending and rotation about the C_{arene}-$C_{alkenyl}$-$C_{alkenyl}$-C_{arene} torsional angle. This added flexibility allows the edges to bend in and out, which leads to partial blockage of cage windows in the process. However, the edges are still rigid enough to prevent the vertices from collapse. Finally, the simulations for **Td$_H$** indicate that the alkyl edges have essentially unrestricted bending and/or rotation about the C_{arene}-C_{alkyl}-C_{alkyl}-C_{arene} torsion angle, which provides enough flexibility to allow at least two edges to collapse inward. Thus, the edges in **Td$_H$** are not rigid enough to maintain cage shape-persistence after desolvation.

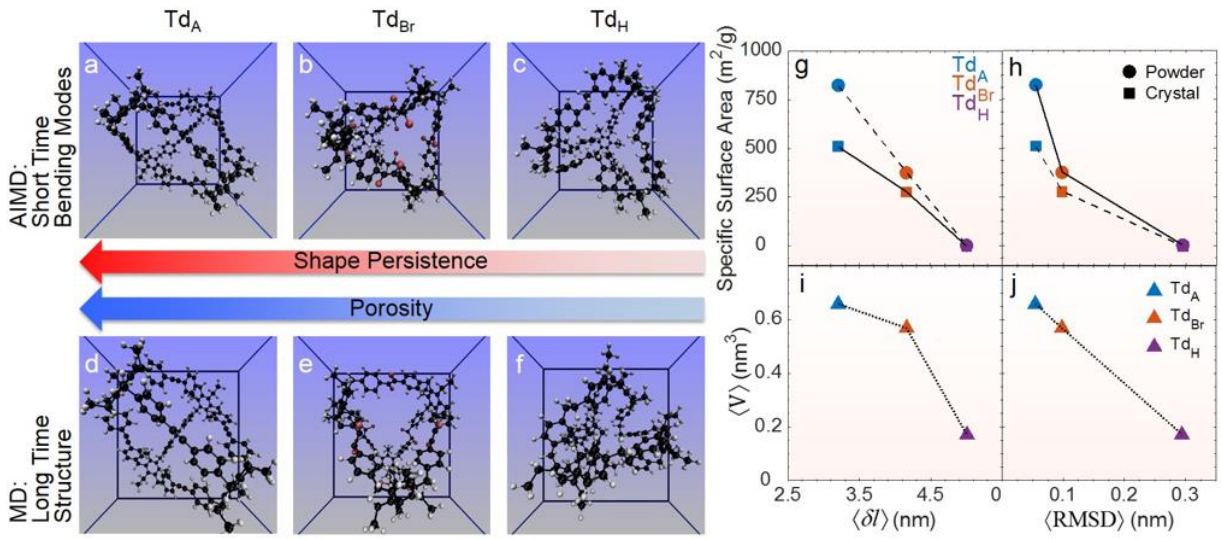

***Figure 3.9**: (a-c) Molecular configurations of cages at their maximum concave bending from AIMD simulations. (d-f) Long-time configurations from classical MD simulations. (g-j) Measures of porosity and volume plotted against measures of flexibility. All lines are included for guidance only. Figure reprinted (adapted) with permission from (J. Am. Chem. Soc. 2017, 139, 3259-3264). Copyright (2017) American Chemical Society.*

Overall, although both **Td$_A$** and **Td$_{Br}$** retain their shape throughout the simulation (i.e. they maintain at least 95% of their initial volume), **Td$_H$** collapses, preserving only 10% of its initial volume after tens of picoseconds. This loss in shape-persistence afforded non-porous molecular solids of **Td$_H$** in both preparative conditions. In terms of the flexibility, our simulations indicate that even a minor increase in $\langle \delta l \rangle$ of 1.0 nm (from **Td$_A$** to **Td$_{Br}$**) leads to a decrease in surface area of ca. 45 % in desolvated crystals and ca. 54% in powders. Furthermore, an increase by 1.8 nm (from **Td$_{Br}$** to **Td$_H$**) leads to cage collapse and loss of porosity. The method presented here constitutes a qualitative analysis of the relationship between shape persistence and porosity. Certainly, other factors such as guest-host interactions may also contribute significantly to molecular flexibility and porosity, as previously reported.[36] However, the advantage of our method is that it requires significantly less computational power and provides a "fingerprint" of a given molecule independent of a specific guest.

3.6 Conclusions

In conclusion, we performed a systematic study of the effects of molecular shape-persistence on the porosity of molecular cage solids. Utilizing the significant advantage of cage solubility allowed us to modify **Td$_A$** in high yields using PSMs with common organic reagents to afford **Td$_{Br}$** and **Td$_H$**. These modifications characteristically affected their gas adsorption capacity and revealed a relationship between shape-persistence and porosity in both rapidly and slowly crystallized samples. AIMD and classical MD provided molecular-scale understanding of how bond flexibility affects porosity of the molecular cages and supported our experimental data.

This integrated synthetic and computational approach exemplifies how minor changes in molecular design greatly affect the physical properties of the bulk materials. In particular, we showed that the microporosity of this class of molecular cage solids can be fine-tuned at both the atomic level by synthetic modifications and the micro-scale by modular molecular packing. Our high-throughput computational methodology, accompanied with powerful *in silico* materials design strategies,[37] may provide a route to screen potential candidate POCs before they are synthesized, minimizing and eventually eliminating trial-and-error practices. The ability to control and predict micro- and meso-porosity through modular assembly of rationally constructed building blocks unlocks the potential of designing porous materials with specific physical properties *a priori*. In effect, these results provide the basis to streamline the process of designing novel molecular architectures for targeted materials applications.

3.7 Experimental

General. All air or moisture-sensitive manipulations were performed under an atmosphere of nitrogen using standard Schlenk techniques or in an argon-filled glove box. Analytical TLC was performed on Kieselgel F-254 precoated silica gel plates and visualization was performed with UV light (254 nm) or a CAM stain. All metathesis reactions were set up in an argon-filled glove box and run under an inert atmosphere. Reaction vessels were 20 mL I-CHEM vials fitted with PTFE/Silicone septa purchased from VWR International unless specified otherwise.

Materials. Unless otherwise stated, all starting materials and reagents were purchased from Sigma Aldrich and used without further purification. The following compounds were prepared according to literature procedure: 1,3,5-Tris(4-propynylbenzyl)-2,4,6-triethylbenzene[30] (**Precursor A**),

molybdenum(IV) propylidyne precatalyst **[Mo]**.[38,39] Tetrahydrofuran (THF) was obtained from a Solvent Delivery System (SDS) equipped with activated neutral alumina columns under argon.

NMR. ^{1}H and ^{13}C NMR spectra were recorded on Varian Unity 400 MHz, Varian Unity 500 MHz, and Varian VXR 500 MHz at room temperature (298 K). All spectra were recorded in $CDCl_3$ unless specified otherwise. Chemical shifts are reported in δ (ppm) referenced on tetramethylsilane (TMS) or residual solvent peaks ($CDCl_3$: 7.26 for ^{1}H, 77.16 for ^{13}C). Coupling constants (J) are expressed in Hertz (Hz). Splitting patterns are designated as: s (singlet), d (doublet), t (triplet), m (multiplet).

Mass-Spec. Low-resolution EI and ESI mass spectra were recorded on a Micromass 70-VSE spectrometer and Waters Quattro II spectrometer, respectively. High resolution EI and ESI mass spectra were recorded on a Micromass 70-VSE spectrometer and Micromass Q-TOF Ultima spectrometer. MALDI mass spectra were recorded on a Bruker Daltonics UltrafleXtreme MALDI TOF spectrometer using a DHB matrix.

PXRD. Powder XRD data were collected on either a Rigaku Miniflex 600 with samples contained on a glass slide holder or a Bruker D8 Venture equipped with a four-circle kappa diffractometer and Photon 100 detector with samples contained in 1.0 mm glass capillaries. For the Rigaku, data were measured using Cu Kα radiation (1.54178 Å) with Kβ filtered out using Ni foil. Data were collected stepwise over the range 3-40º in 0.02º steps at 1s per step. Using the Bruker, an Iμs microfocus Cu Kα (1.54178 Å) source supplied the multi-mirror monochromated incident beam. The samples were exposed for 180s for each of several frames. The 2D frames were merged and integrated from 5 to 45 degrees 2θ in 0.02 degree steps. In the final spectrum data was normalized to facilitate pattern matching.

Thermogravimetric Analysis. TGA was performed on a TA Instruments Q50 analyzer. Samples were heated to 600 ºC in a platinum crucible at a rate of 10 ºC/min under a nitrogen atmosphere.

Gas Sorption Analysis. Surface areas were measured by nitrogen sorption at 77.3 K. All samples were degassed offline at 70 ºC for 12 h under dynamic vacuum before analysis, followed by degassing on the analysis port under vacuum at the same temperature. Isotherms were measured using a Quantachrome Nova 2200 Multi-station AnyGas Sorption Analyzer standard model Version 11.02.

SEM Imaging. Characterization of materials was carried out in the Center for Microanalysis of Materials, University of Illinois at Urbana-Champaign. Prior to imaging, the samples were

prepared by mounting on a stub using carbon tape and sputter coated with gold-palladium using a deposition current of 20 mA and a deposition duration of 30 s. The samples were imaged using a Hitachi S4800 operating at 10.0 kV at a working distance of 5.5 mm, accelerating voltage of 10.0 kV, extracting voltage of 5.1 kV, emission current of 10 μA, probe current set to high, and ultra-high resolution mode.

Synthesis

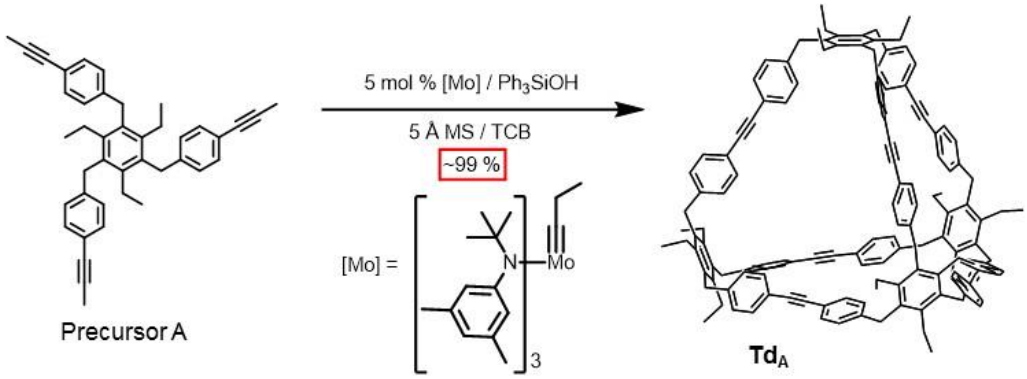

Scheme 3.2: *Synthesis of tetrahedral cage* ***Td$_A$***.

Td$_A$: The synthesis for **Td$_A$** follows a previously reported method with a few changes.[1] 1,3,5-tris(4-propynylbenzyl)-2,4,5-triethylbenzene (**Precursor A**, 2.00 g, 3.66 mmol, 1 equiv), 5 Å molecular sieves powder (9 g), and 1,2,4-trichlorobenzene (60 mL) were added to a round bottom flask in an argon-charged glovebox. A solution of molybdenum (VI) alkylidyne precatalyst (49 mg, 0.073 mmol, 0.02 equiv) and Ph_3SiOH (121 mg, 0.44 mmol, 0.12 equiv) in 1,2,4-trichlorobenzene (60 mL) was stirred in a separate flask for 10 min then added to the reaction mixture containing 1,3,5-tris(4-propynylbenzyl)-2,4,5-triethylbenzene. The reaction mixture was stirred at 70 ^oC for 12 hrs in an argon-filled glovebox. The reaction was cooled to rt and removed from the glovebox. It was then filtered through a pad of Celite and washed with $CHCl_3$. The filtrate was collected and $CHCl_3$ was removed under vacuum. MeOH was added to the solution and the precipitates were collected using the membrane filter and washed extensively with MeOH. The resulting powder was dried under vacuum to give a light beige solid. Yield (1.71 g, >99 %); ^1H NMR (500 MHz, CDCl3): δ = 7.44 (d, *J* = 8.1 Hz, 24H), 6.99 (d, *J* = 8.1 Hz, 24H), 4.13 (s, 24H), 2.40 (q, *J* = 8.0 Hz, 24H). 1.17 (t, *J* = 7.4 Hz, 36H) ppm. ^{13}C NMR (125 Hz, CDCl3): δ = 141.58, 141.16, 133.52, 131.90, 127.61, 121.12, 89.28, 34.82, 23.83, 15.14 ppm. MS-MALDI-TOF: [M]+ calcd 1862.04, found 1862.08.

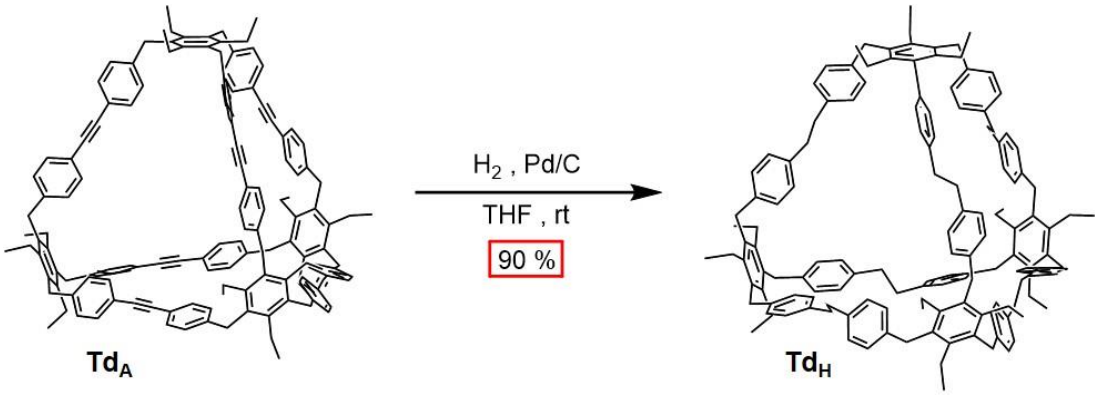

Scheme 3.3: *Synthesis of tetrahedral cage* ***Td$_H$***.

Td$_H$: A 20 mL vial equipped with a septum was charged with 20 mg (.0107 mmol) of **Td$_A$**, 5 mg of 10% Pd on activated carbon, and a stir bar. The vial was evacuated and purged with H_2 three times. Then, 15 mL of dry THF was added and the mixture was sonicated for 15 minutes. The reaction was stirred rigorously under an atmosphere of hydrogen (balloons) for 48 h at rt before the mixture was filtered through a pad of silica. The silica pad was washed with dichloromethane and the volatiles were evaporated. The solid was taken up in minimum chloroform and precipitated with 50 mL of methanol. This precipitate was filtered off, washed with methanol, and dried under high vacuum to yield 18 mg of a white powder. Yield (90 %); ^{1}H NMR ($CDCl_3$, 500 MHz): δ = 7.28 (d, *J* = 7.8 Hz, 24 H, Ar-H), 7.08 (d, *J* = 7.7 Hz, 24 H, Ar-H), 4.19 (s, 24 H, Ar-CH-Ar), 2.87 (s, 24 H, Ar-CH), 2.52 (q, *J* = 7.6 Hz, 24 H, Ar-CH), 1.28 (t, *J* = 7.4 Hz, 36 H, -CCH) ppm. ^{13}C NMR (125 Hz, CDCl3): δ = 141.38, 139.81, 138.66, 133.89, 128.56, 127.83, 39.03, 34.43, 23.86, 15.21 ppm. MS-MALDI-TOF: [M]+Na^+ calcd 1909.82, found 1909.70.

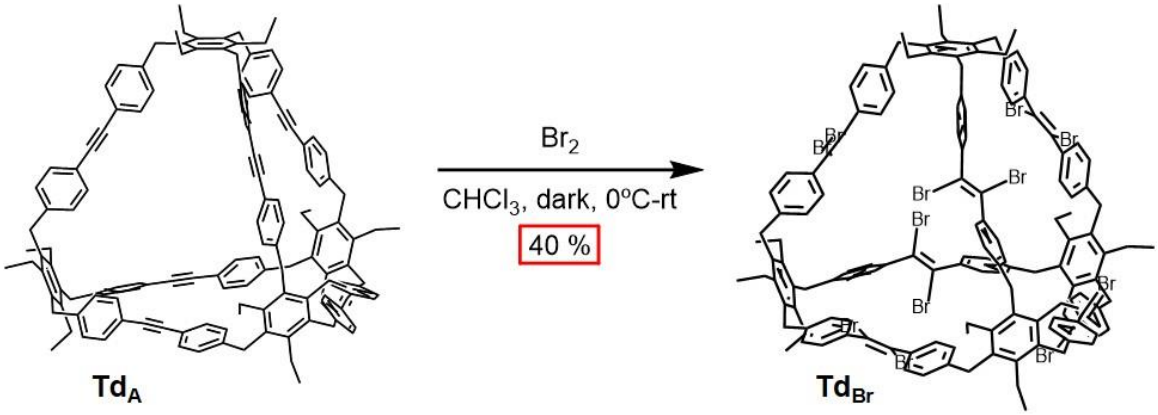

Scheme 3.4: *Synthesis of tetrahedral cage* ***Td$_{Br}$***.

Td_{Br}: The synthesis followed a procedure similar to that reported by Forgan and coworkers for bromination of a MOF[31] with adjustments. A 50 mL round bottom flask equipped with a septum was charged with 100 mg of **Td_A** (1 equiv, 0.053 mmol) and a stir bar. The vial was evacuated and purged with N_2 three times before 25 mL of dry chloroform was added. The contents were sonicated for 5 minutes to completely dissolve **Td_A**. The vial was then wrapped in aluminum foil and cooled to 0 ºC before a solution of bromine (0.254 g, 1.59 mmol, 30 equiv) in 5 ml of chloroform was added dropwise via syringe. The reaction stirred in the dark for 12 hours and was allowed to slowly reach room temperature. The mixture was quenched with 15% wt. sodium bisulfite solution and extracted with chloroform (3 x 10 mL). The organic layers were collected and washed with DI water (3 x 20 mL) and saturated brine solution (1 x 20 mL). The organic layer was then dried over $MgSO_4$, filtered, and the volatiles were removed using a rotary evaporator. The off-white powder was then taken up in minimum chloroform (~15 mL) and precipitated with the addition of methanol. The precipitate was filtered off, washed with methanol and dried over high vacuum. The crude product was dissolved in a 1:5 (v/v) solution of toluene:CHCl3 and the product recrystallized from slow evaporation of this solution to yield 61 mg of colorless crystals. Yield (40 %). ^{1}H NMR ($CDCl_3$, 500 MHz): δ = 7.44 (d, *J* = 8.2 Hz, 24 H, Ar-H), 7.11 (d, *J* = 7.90 Hz, 24 H, Ar-H), 4.17 (s, 24 H, Ar-CH), 2.47 (q, *J* = 7.5 Hz, 24 H, Ar-CH), 1.22 (t, *J* = 7.4 Hz, 36 H) ppm. ^{13}C NMR (125 Hz, CDCl3): δ = 141.76, 141.74, 138.57, 133.40, 129.31, 127.62, 118.11, 34.79, 24.05, 15.12 ppm. MS-MALDI-TOF: [M]-6Br calcd 2342.09, found 2341.50.

^{1}H and ^{13}C NMR Spectra

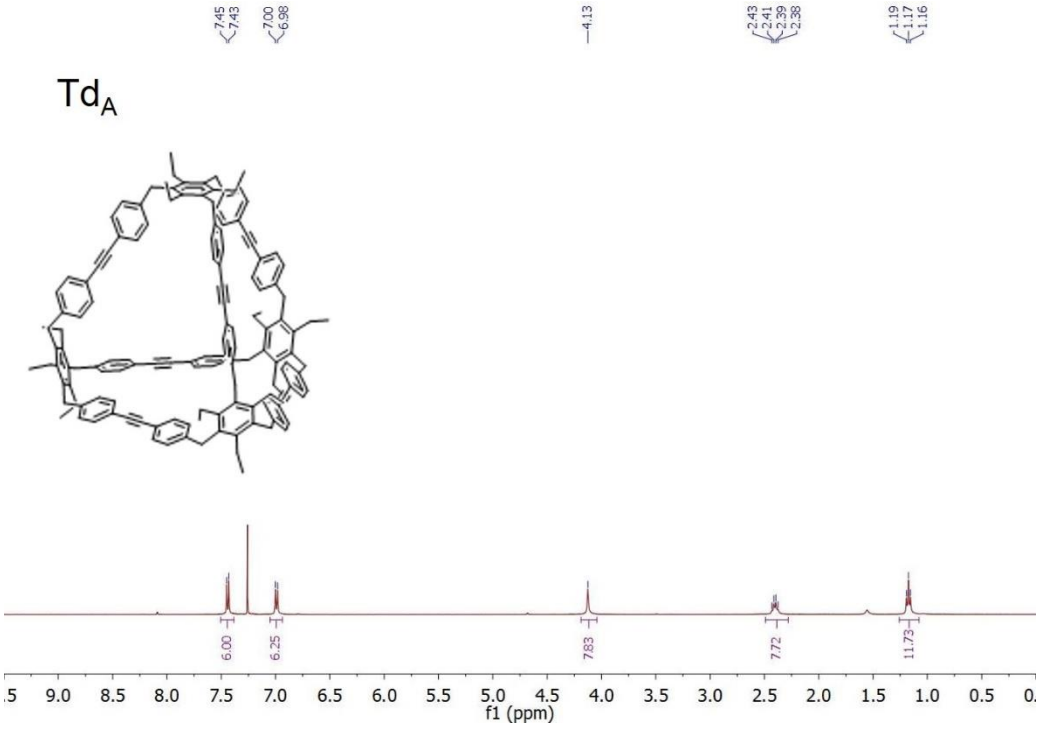

***Figure 3.10**: ^{1}H NMR spectrum of **Td$_A$** (400 MHz, $CDCl_3$).*

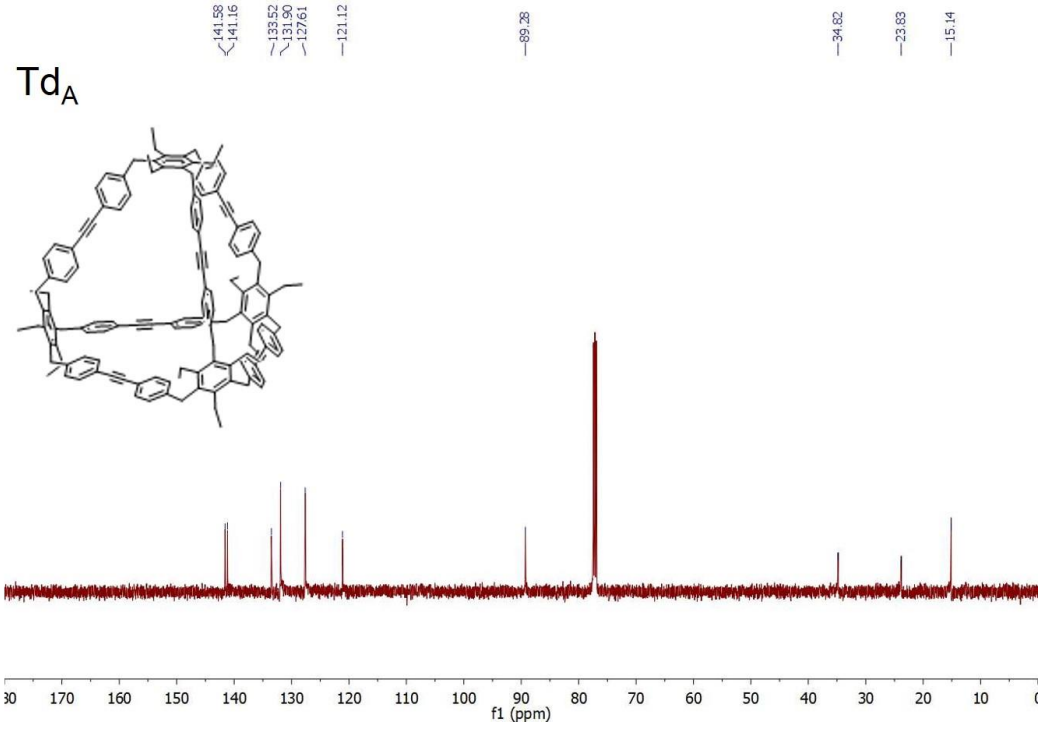

***Figure 3.11**: ^{13}C NMR spectrum of **Td$_A$** (125 MHz, $CDCl_3$).*

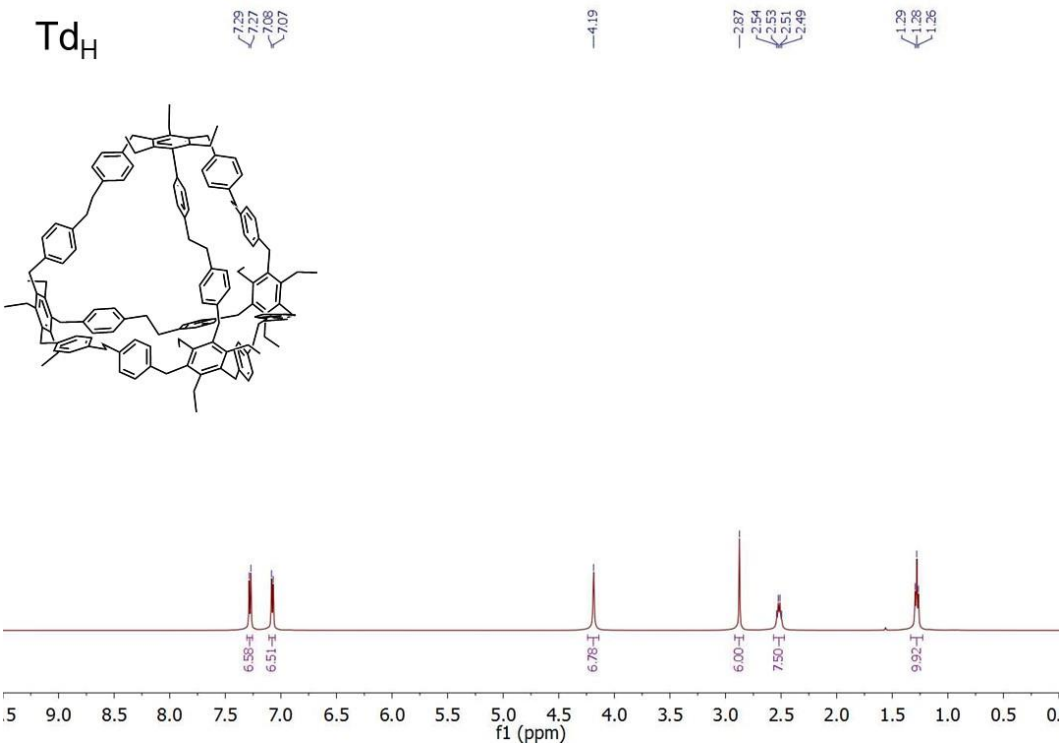

Figure 3.12: *^{1}H NMR spectrum of* ***Td_H*** *(500 MHz, $CDCl_3$).*

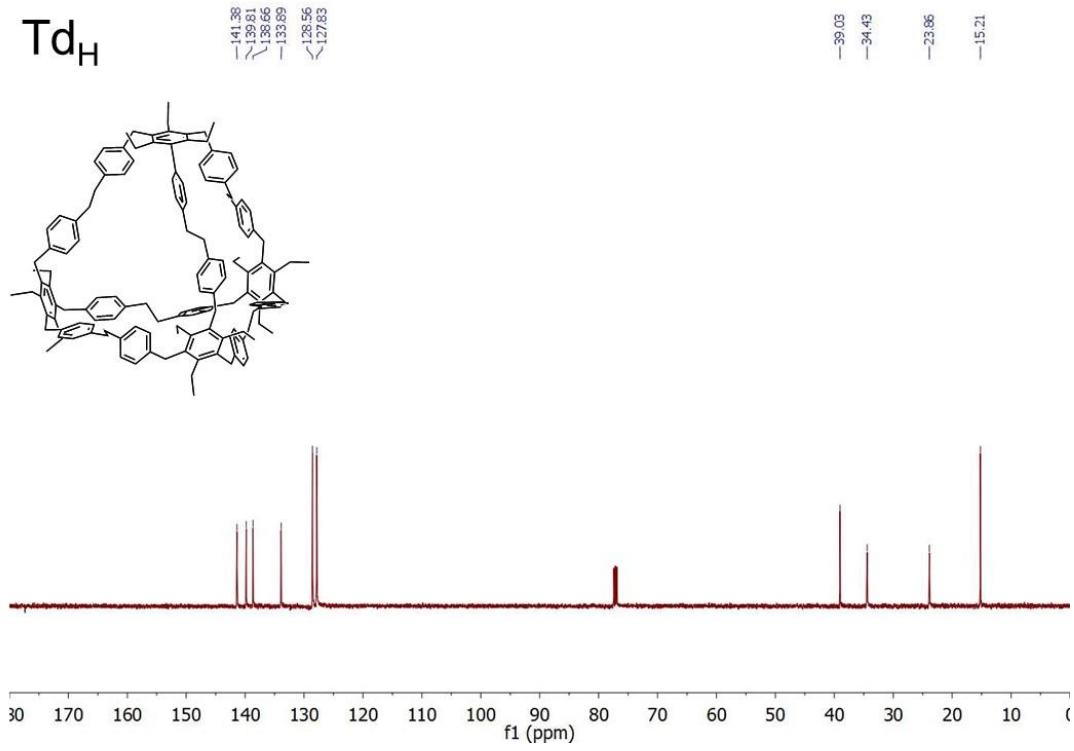

Figure 3.13: *^{13}C NMR spectrum of* ***Td_H*** *(125 MHz, $CDCl_3$).*

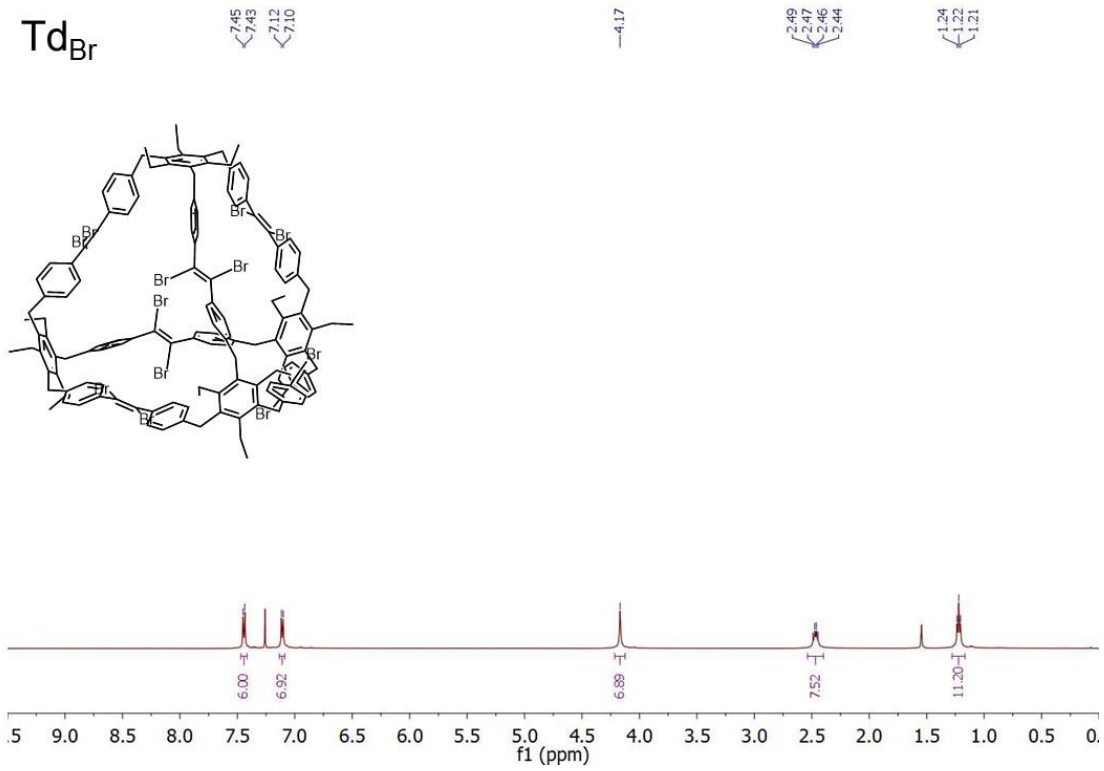

Figure 3.14: *^{1}H NMR spectrum of* ***Td$_{Br}$*** *(500 MHz, $CDCl_3$).*

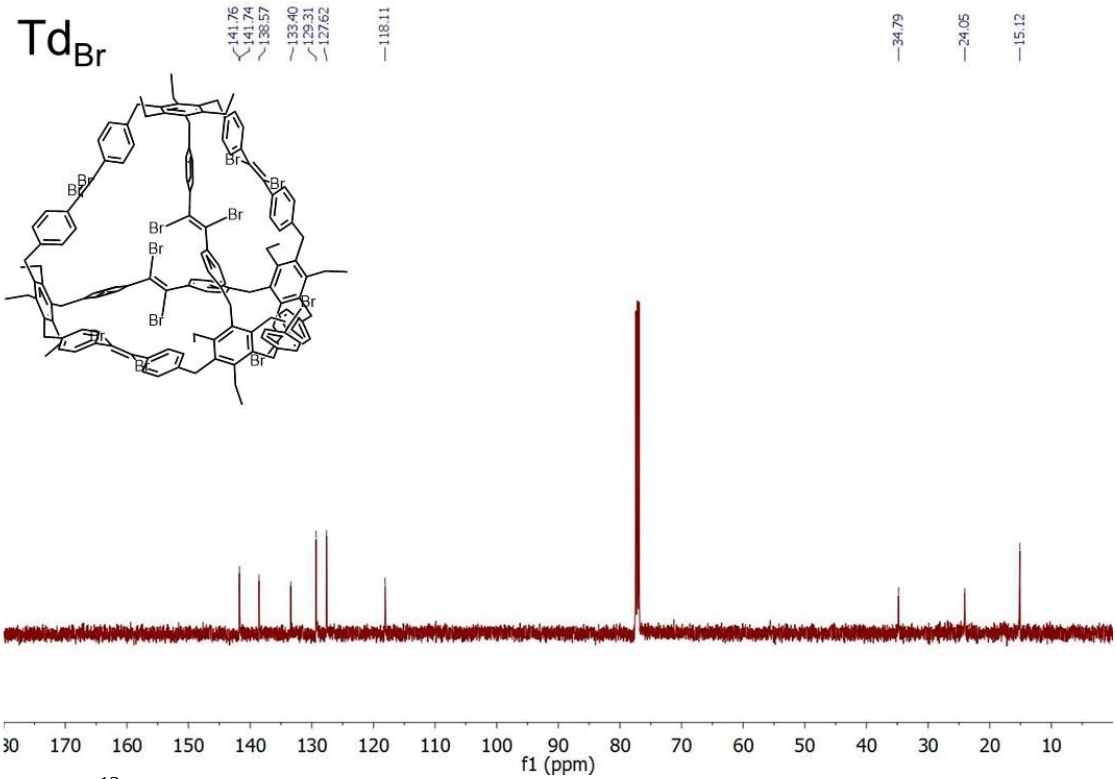

Figure 3.15: *^{13}C NMR spectrum of* ***Td$_{Br}$*** *(125 MHz, $CDCl_3$).*

Mass-spec. Data

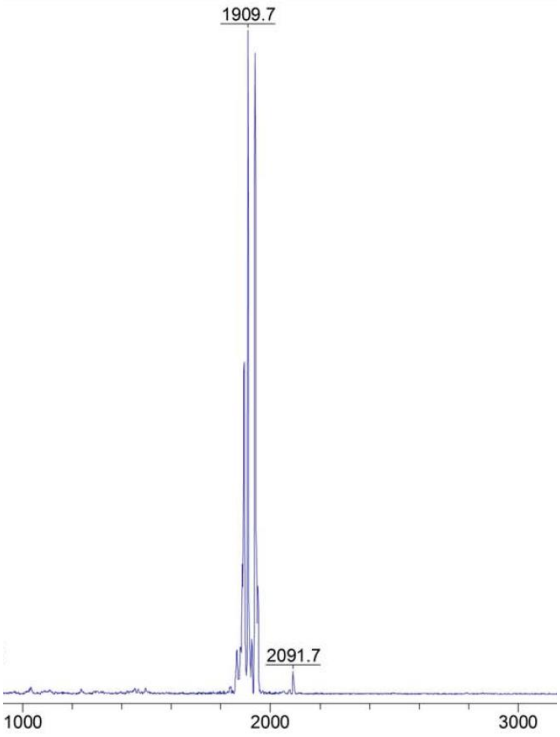

Figure 3.16: *MS-MALDI-TOF spectrum of* $\boldsymbol{Td_H}$.

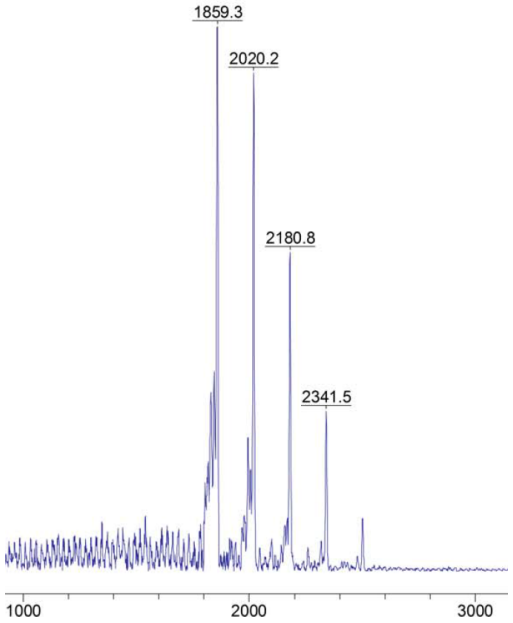

Figure 3.17: *MS-MALDI-TOF spectrum of* $\boldsymbol{Td_{Br}}$.

Single Crystal X-ray Crystallography Analyses

Note: Crystal structures of each cage exhibited disorder in at least one edge.

Single Crystal X-ray Data of Td_A. This data was reported in a previous communication. The figures are reproduced from this crystal structure.[30] Crystallographic data have been deposited at the Cambridge Crystallographic Data Centre under deposition number CCDC 1452245.

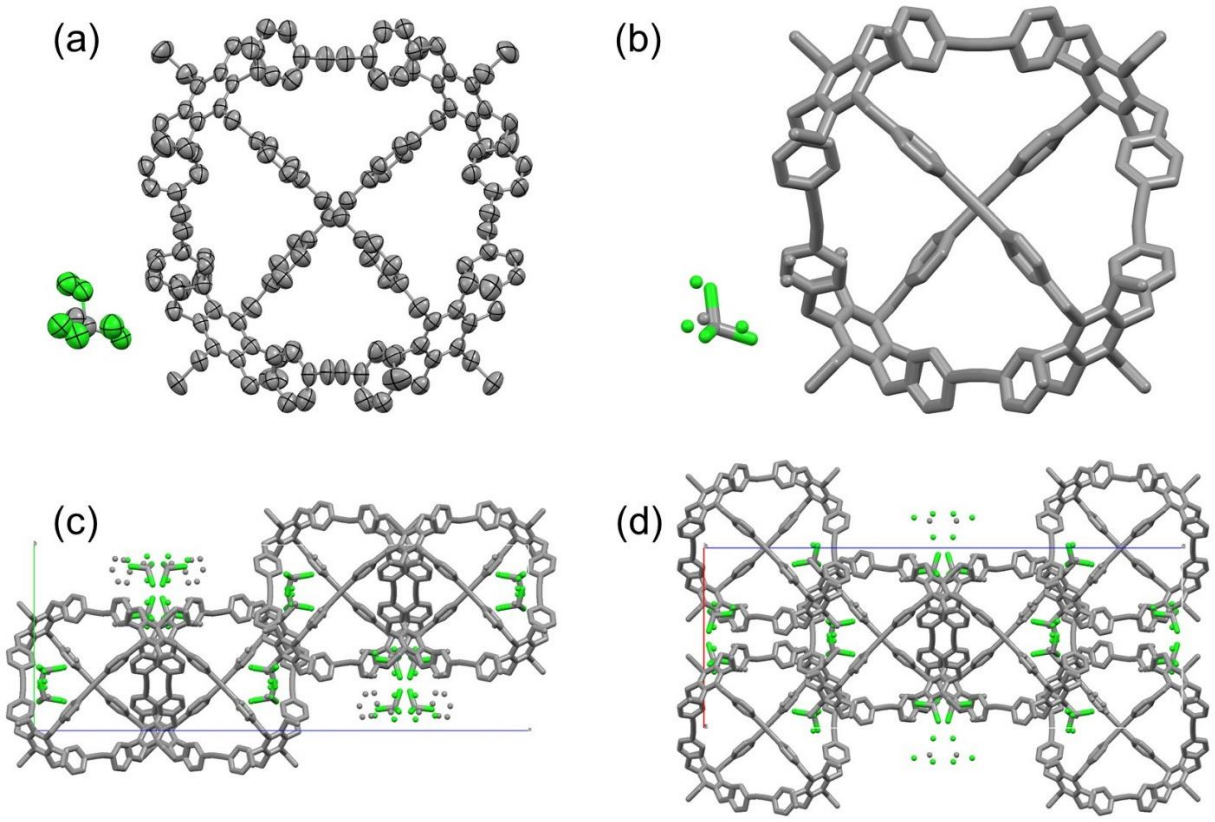

Figure 3.18: *Selected images of* ***Td_A*** *with hydrogens omitted for clarity. (a) Single molecule ellipsoid view of* ***Td_A*** *at the 50% probability level viewed along the a-axis (b) single molecule viewed along the a-axis (c) unit cell viewed along the a-axis (d) unit cell viewed along the b-axis.*

Single Crystal X-ray Crystallographic Analysis of Td_{Br}

Single Crystal Data of Td_{Br}. Single crystals were grown from slow diffusion of a layered 1:1 (v/v) mixture of chloroform and toluene. Single crystals were mounted on a 0.3 mm loop with the minimal amount of Paratone-N oil and flash cooled to 100 K. Single crystal X-ray data were collected on a Bruker D8 Venture equipped with a four-circle kappa diffractometer and Photon 100 detector. A Iμs microfocus Mo (λ = 0.71073 Å) source supplied the multi-mirror monochromated incident beam. Data were collected as a series of φ and ω scans and was integrated and filtered for statistical outliers using SAINT then corrected for absorption by integration SADABS v2014/5. The structure was phased by direct methods using the SHELX software package SHELX-2014-4. Severely disordered solvent molecules within the cavity were removed using the bypass method in Platon SQUEEZE.[40] Crystallographic data have been deposited at the Cambridge Crystallographic Data Centre under deposition number CCDC 1504099.

Table 3.2: Crystal data and structure refinement for **Td_{Br}**.

Identification code	**Td_{Br}**	
Empirical formula	C144 H132 Br12	
Formula weight	2821.41	
Temperature	100(2) K	
Wavelength	0.71073 Å	
Crystal system	Monoclinic	
Space group	C2/c	
Unit cell dimensions	a = 43.8914 (19) Å	α = 90°.
	b = 20.3623 (8) Å	β = 121.4860 (10)°.
	c = 25.1357 (10) Å	γ = 90°.
Volume	19157.1 (14) $Å^3$	
Z	4	
Density (calculated)	0.978 Mg/m^3	
Absorption coefficient	2.542 mm^{-1}	
F(000)	5664	
Crystal size	0.342 x 0.247 x 0.142 mm^3	
Theta range for data collection	2.176 to 25.408°.	
Index ranges	-52<=h<=52, -24<=k<=24, -30<=l<=30	
Reflections collected	17594	
Independent reflections	17594 [R(int) = 0.0655]	
Completeness to theta = 25.242°	99.9 %	
Absorption correction	Semi-empirical from equivalents	
Max. and min. transmission	0.7452 and 0.5553	
Refinement method	Full-matrix least-squares on F^2	

Table 3.2: *(cont.).*

Data / restraints / parameters	17594 / 1295 / 880
Goodness-of-fit on F^2	1.094
Final R indices [I>2sigma(I)]	R1 = 0.0651, wR2 = 0.1922
R indices (all data)	R1 = 0.0905, wR2 = 0.2150
Extinction coefficient	n/a
Largest diff. peak and hole	1.614 and -0.818 e.$Å^{-3}$

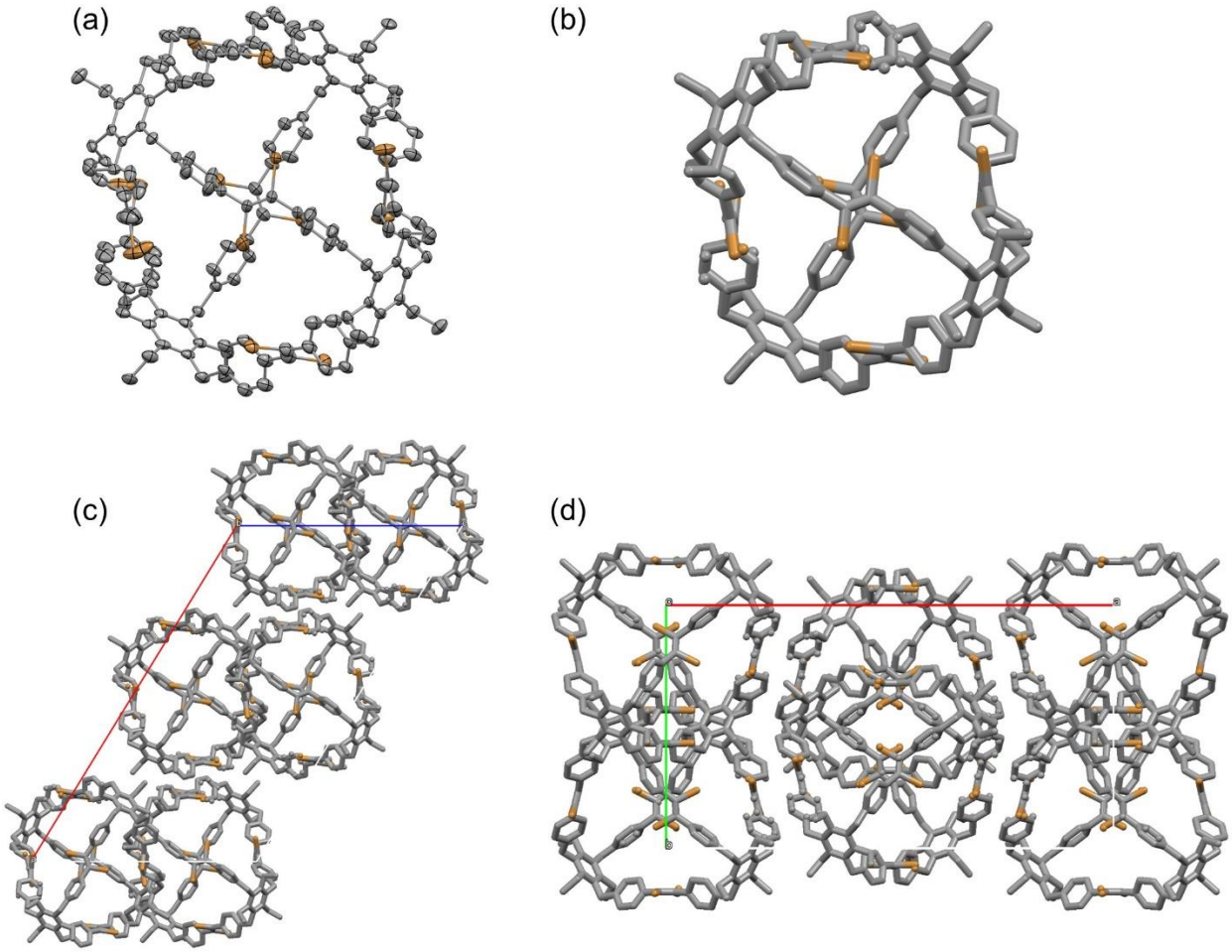

Figure 3.19: *Selected images of* ***Td$_{Br}$*** *with hydrogens omitted for clarity. (a) Single molecule ellipsoid view of* ***Td$_{Br}$*** *at the 50% probability level viewed along the b-axis (b) single molecule viewed along the b-axis (c) unit cell viewed along the b-axis (d) unit cell viewed along the c-axis.*

Single Crystal X-ray Crystallographic Analysis of Td_H

Single Crystal Data Td_H. Single crystals were grown from slow diffusion of a 1:1 (v/v) layered mixture of chloroform and methanol. Single crystals were mounted on a 0.3 mm loop with the minimal amount of Paratone-N oil and flash cooled to 100 K. Single crystal X-ray data were collected on a Bruker D8 Venture equipped with a four-circle kappa diffractometer and Photon 100 detector. A Iμs microfocus Cu (λ = 1.54178 Å) source supplied the multi-mirror monochromated incident beam. Data were collected as a series of φ and ω scans and was integrated and filtered for statistical outliers using SAINT then corrected for absorption by integration SADABS v2014/5. The structure was phased by direct methods using the SHELX software package SHELX-2014-4. Severely disordered solvent molecules within the cavity were removed using the bypass method in Platon SQUEEZE.[40] Crystallographic data have been deposited at the Cambridge Crystallographic Data Centre under deposition number CCDC 1504097.

Table 3.3: Crystal data and structure refinement for **Td_H**.

Identification code	**Td_H**	
Empirical formula	C148 H160 Cl2	
Formula weight	2364.15	
Temperature	101(2) K	
Wavelength	1.54178 Å	
Crystal system	Trigonal	
Space group	R-3	
Unit cell dimensions	a = 25.0005(10) Å	α = 90°.
	b = 25.0005(10) Å	β = 90°.
	c = 48.793(2) Å	γ = 120°.
Volume	26411(2) $Å^3$	
Z	6	
Density (calculated)	0.892 Mg/m^3	
Absorption coefficient	2.006 mm^{-1}	
F(000)	7512	
Crystal size	0.562 x 0.477 x 0.32 mm^3	
Theta range for data collection	2.232 to 77.922°.	
Index ranges	-30<=h<=31, -31<=k<=31, -61<=l<=58	
Reflections collected	92907	
Independent reflections	12361 [R(int) = 0.0639]	
Completeness to theta = 67.679°	100.0 %	
Absorption correction	Semi-empirical from equivalents	
Max. and min. transmission	0.7541 and 0.4870	

Table 3.3: *(cont.).*

Refinement method	Full-matrix least-squares on F^2
Data / restraints / parameters	12361 / 258 / 536
Goodness-of-fit on F^2	1.131
Final R indices [I>2sigma(I)]	R1 = 0.0698, wR2 = 0.1925
R indices (all data)	R1 = 0.0744, wR2 = 0.1956
Extinction coefficient	0.000153(9)
Largest diff. peak and hole	0.897 and -0.505 e.$Å^{-3}$

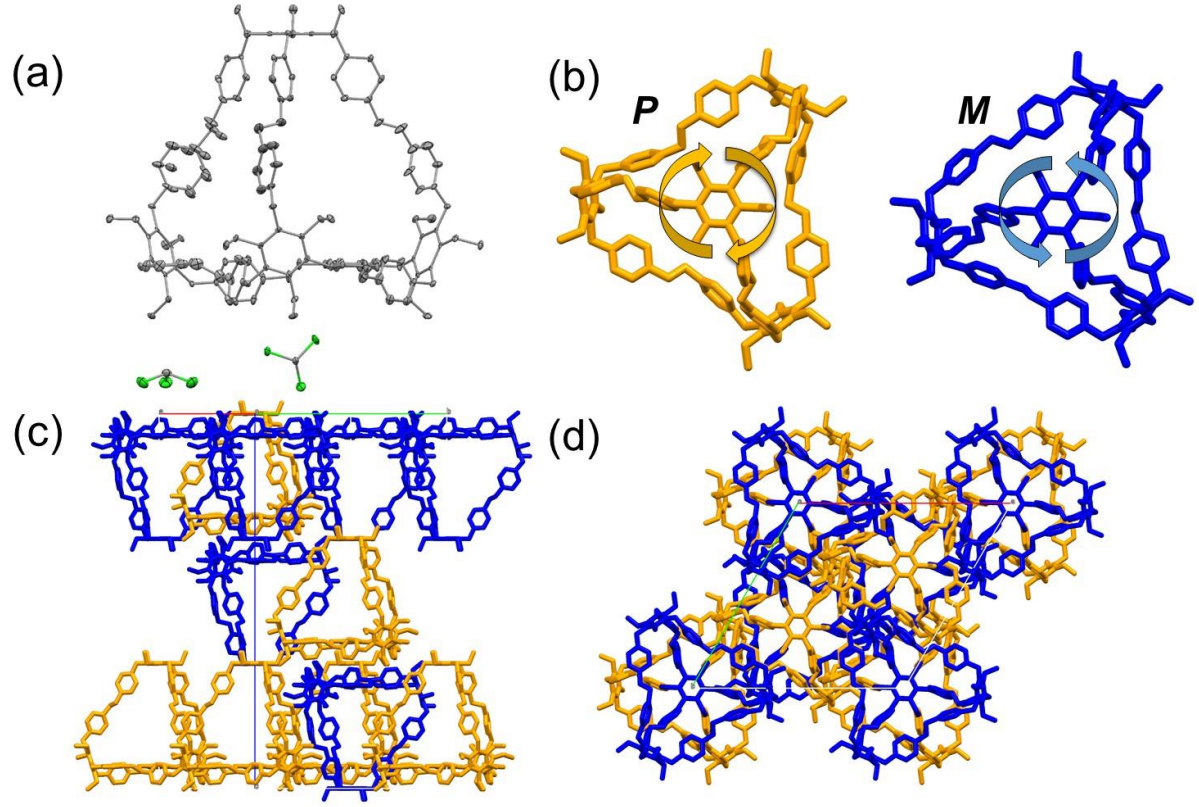

Figure 3.20: *Selected images of* $\boldsymbol{Td_H}$ *with hydrogens omitted for clarity. (a) Single molecule ellipsoid view of* $\boldsymbol{Td_H}$ *at the 50% probability level viewed along the a-axis (b) single molecule ball and stick views of* $\boldsymbol{Td_H}$ *atropisomers, P and M, illustrated as orange and blue, respectively (c) unit cell viewed along the a'-axis (d) unit cell viewed along the c-axis.*

Scanning Electron Microscopy Images

Rapidly Crystallized Samples

Note: Powder samples were prepared by rapid precipitation from addition of MeOH into a solution of $CHCl_3$.

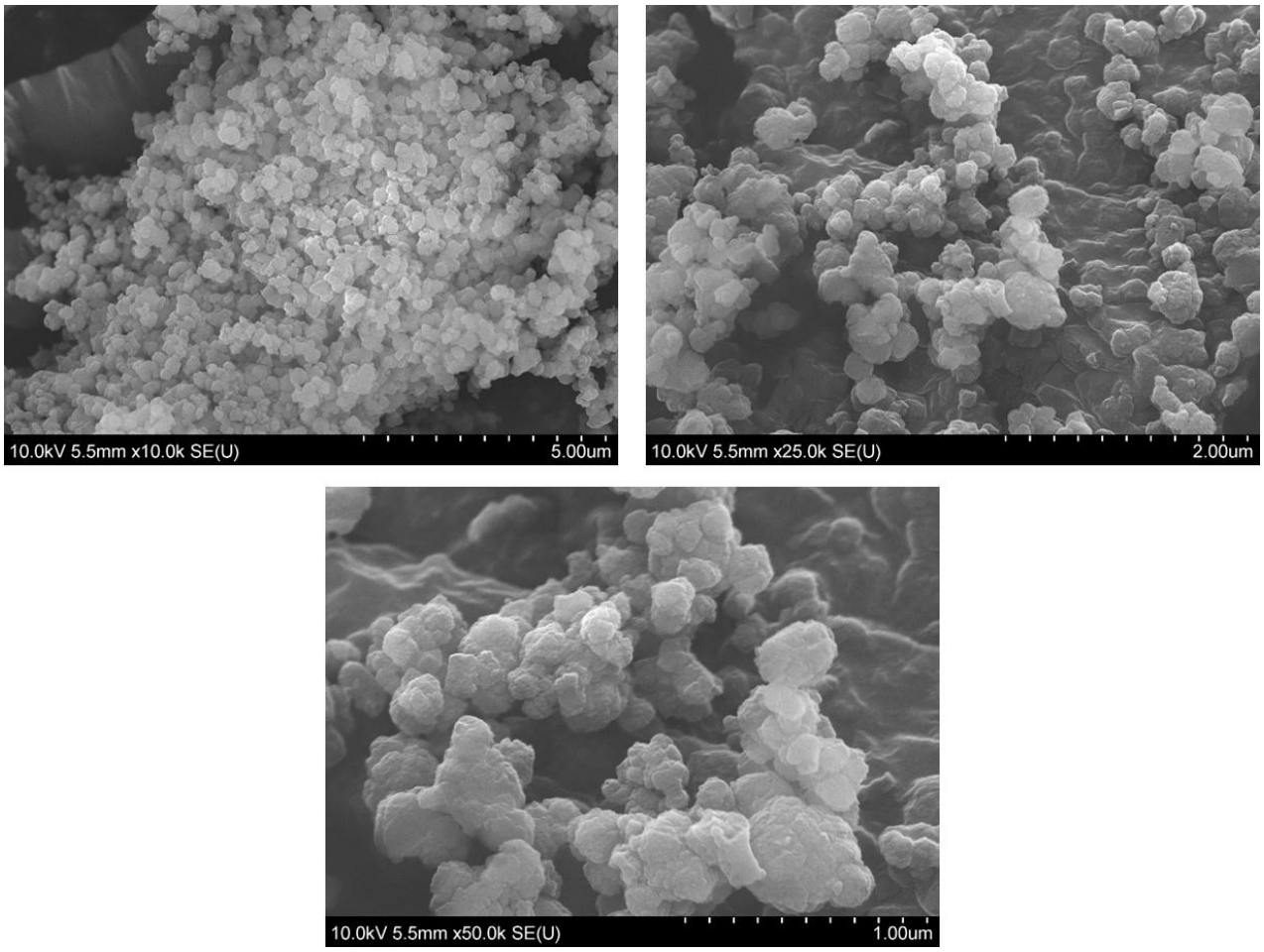

Figure 3.21: *SEM images of* ***Td_A*** *powder at 10,000x, 25,000x, and 50,000x magnification.*

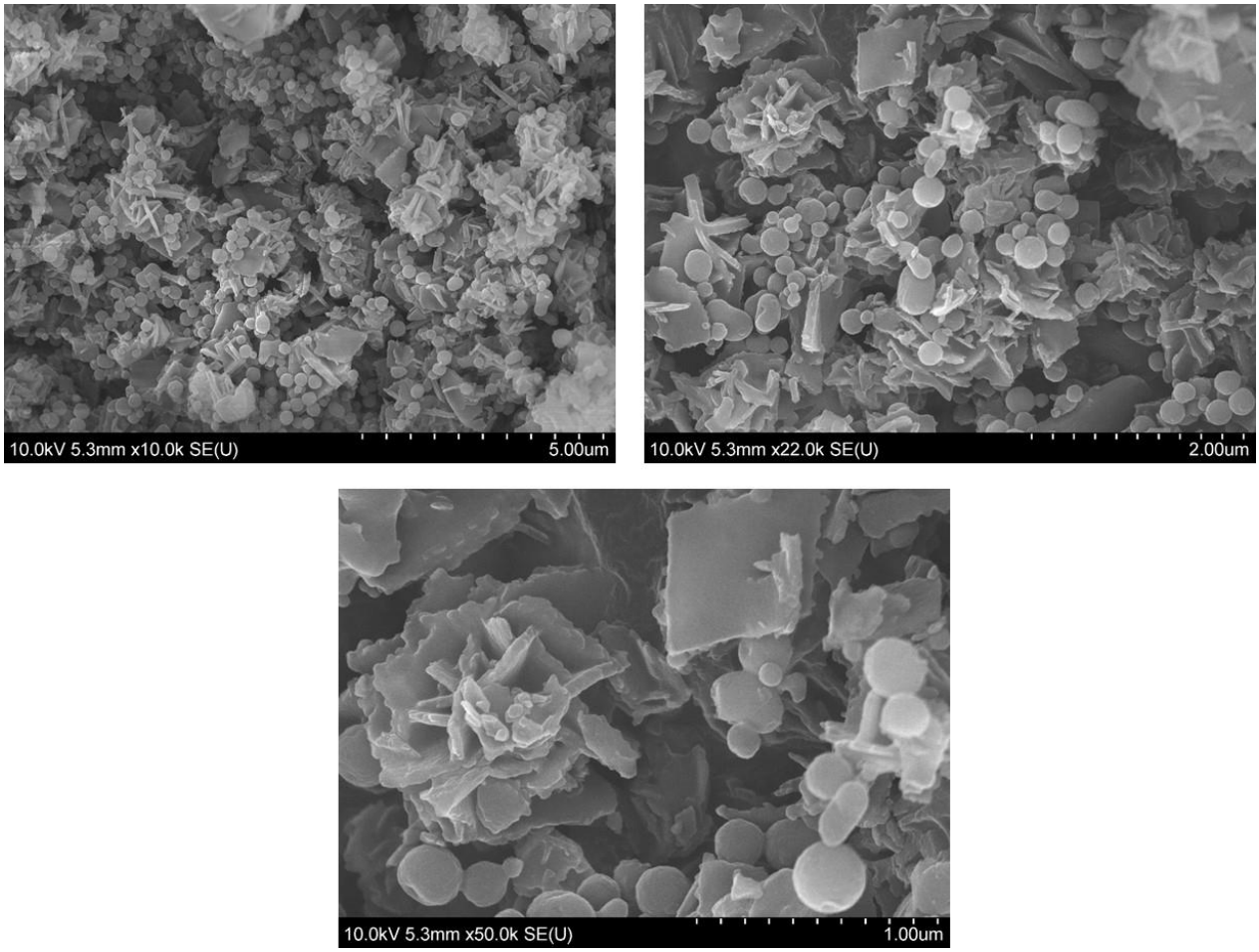

Figure 3.22: *SEM images of* $\boldsymbol{Td_{Br}}$ *powder at 10,000x, 22,000x, and 50,000x magnification.*

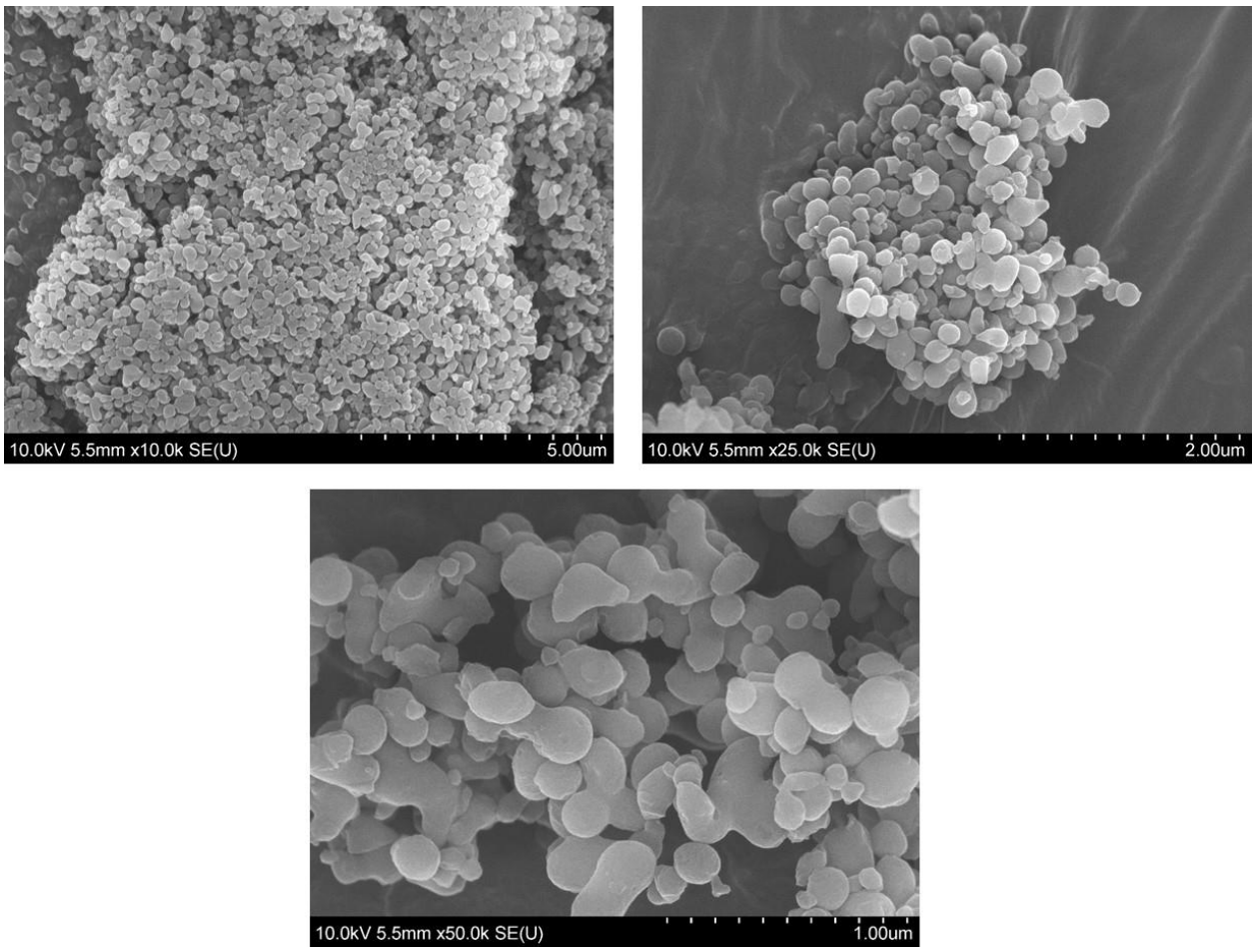

Figure 3.23: *SEM images of* $\boldsymbol{Td_H}$ *powder at 10,000x, 25,000x, and 50,000x magnification.*

Slowly Crystallized Samples-

Note: Samples were prepared by slow evaporation of a chloroform solution in a 40 ml screwcap vial with the cap loosened, typically over the course of 5-7 days.

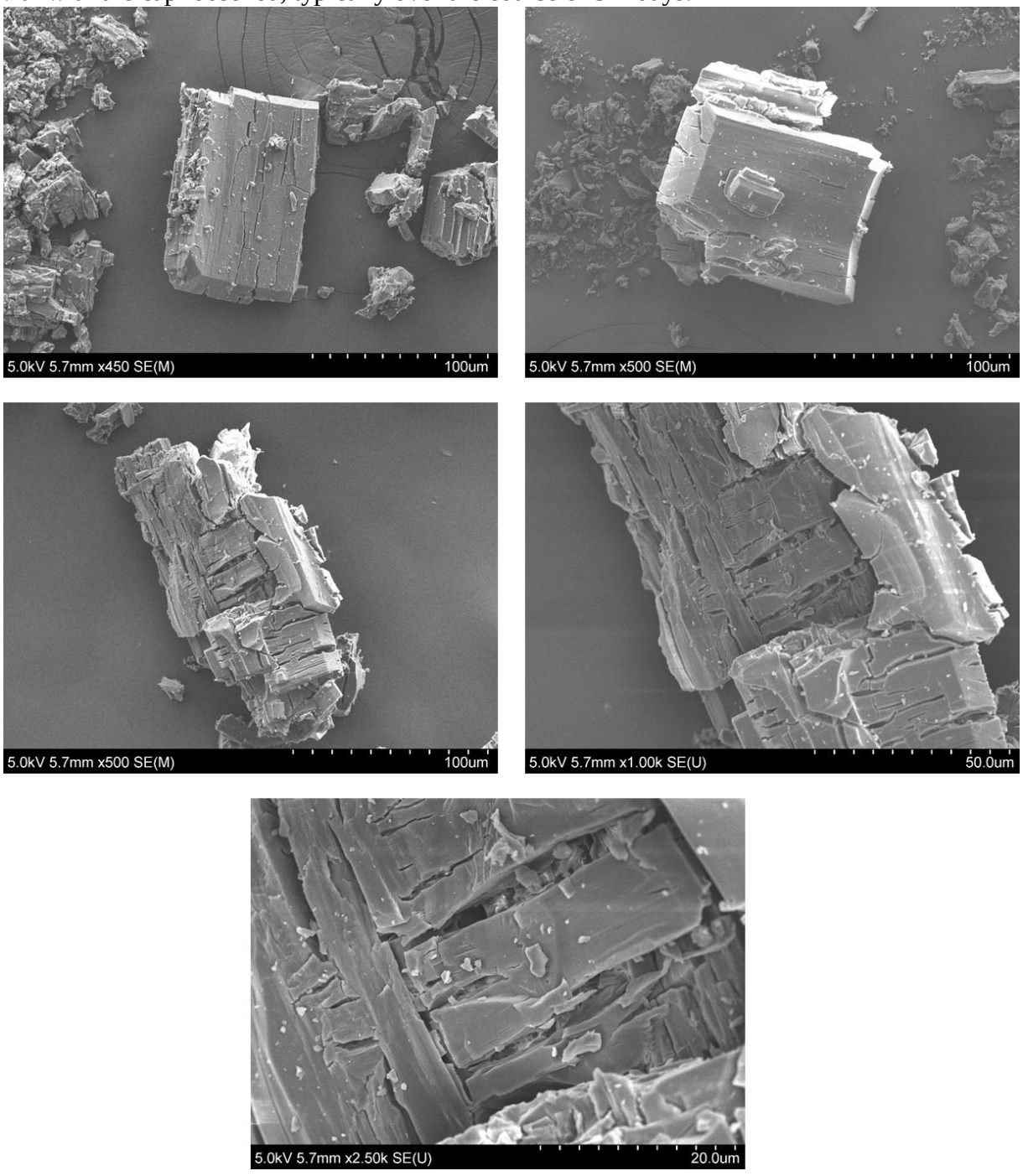

Figure 3.24: *SEM images of slowly crystallized* ***Td_A*** *samples after adsorption experiments at 500x, 1,000x, and 2,500x magnification.*

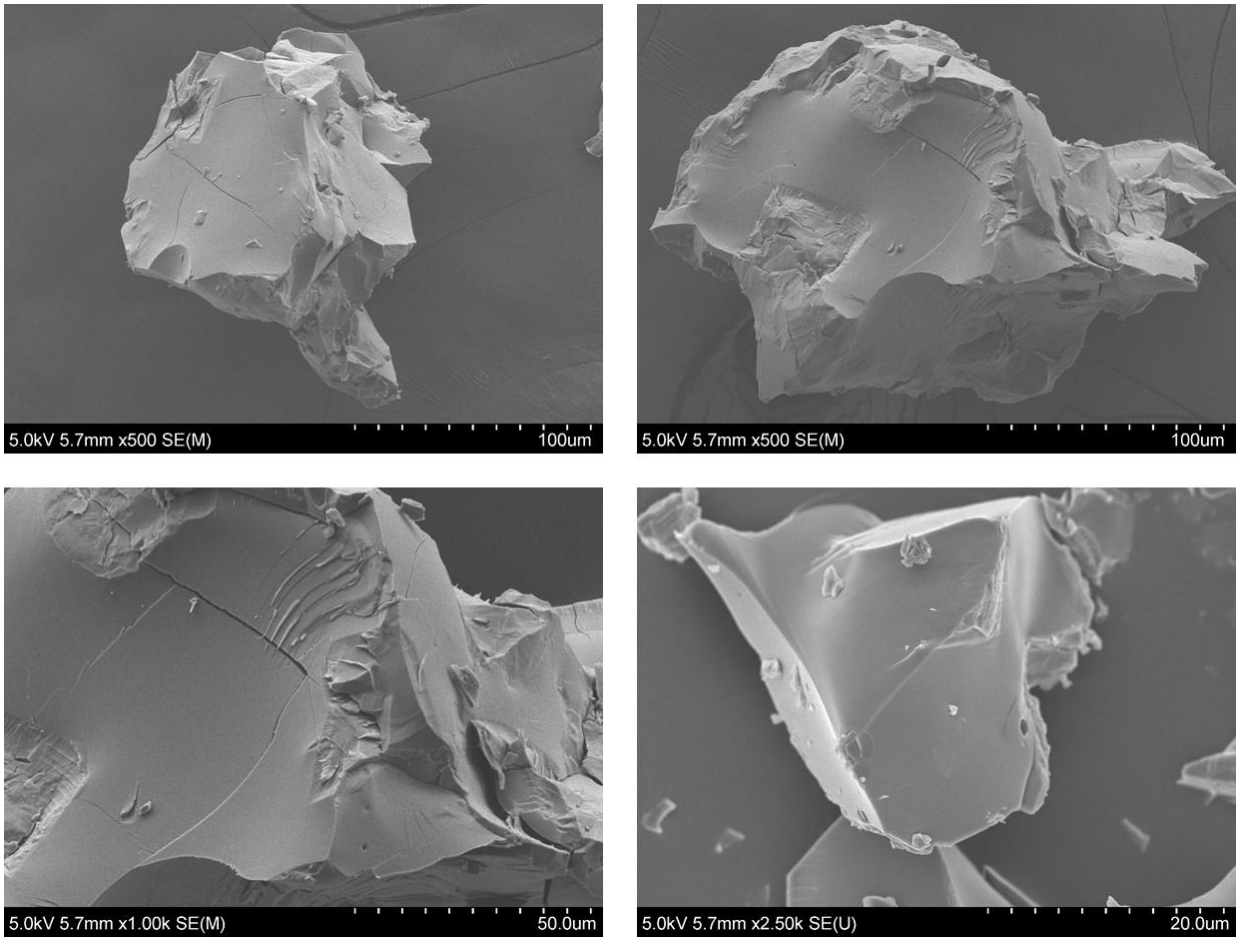

Figure 3.25: *SEM images of slowly crystallized* $\mathbf{Td_{Br}}$ *samples after adsorption experiments at 500x, 1,000x, and 2,500x magnification.*

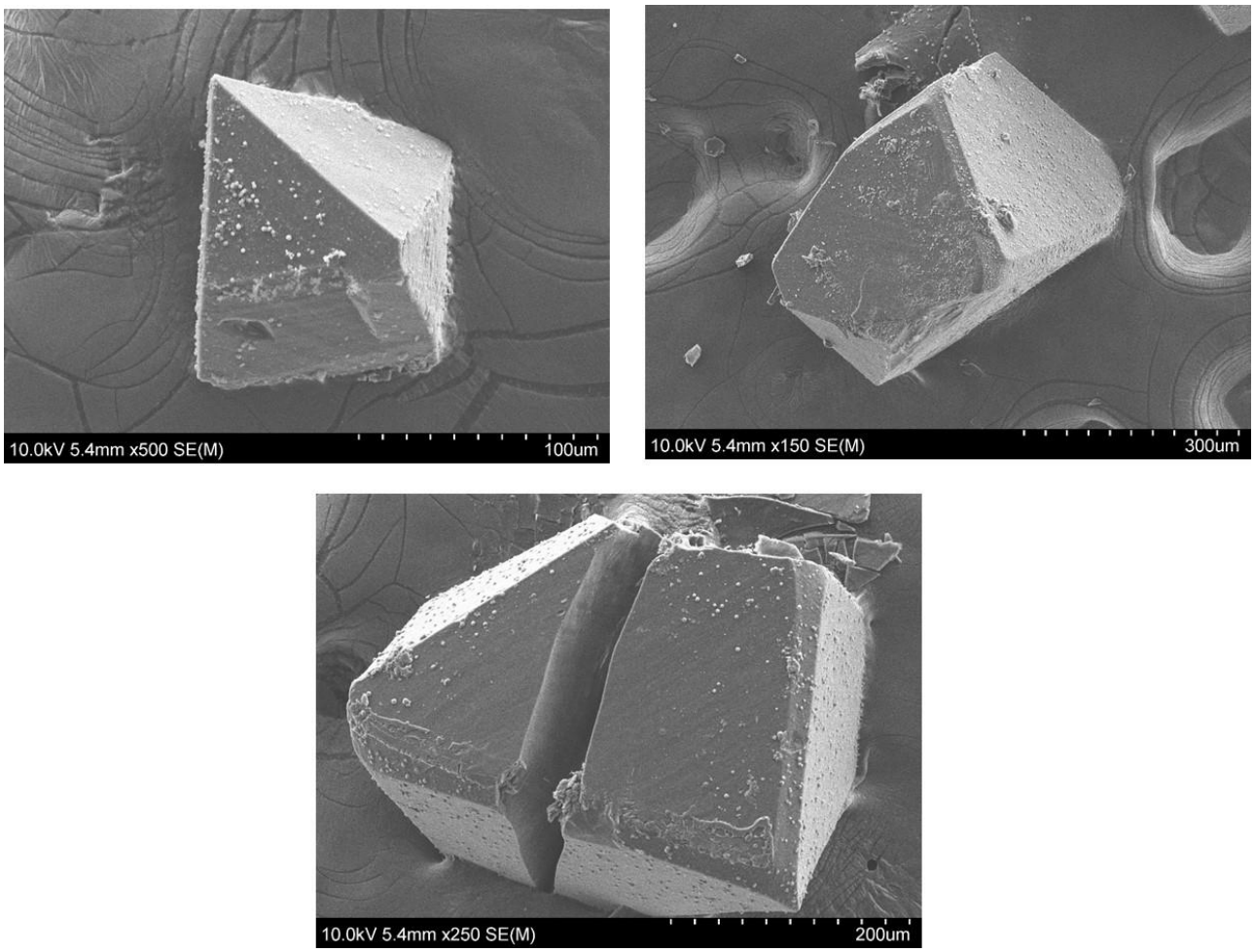

Figure 3.26: *SEM image of slowly crystallized* $\boldsymbol{Td_H}$ *samples after adsorption experiments at 500x, 150x, and 250x magnification.*

Thermogravimetric Analysis

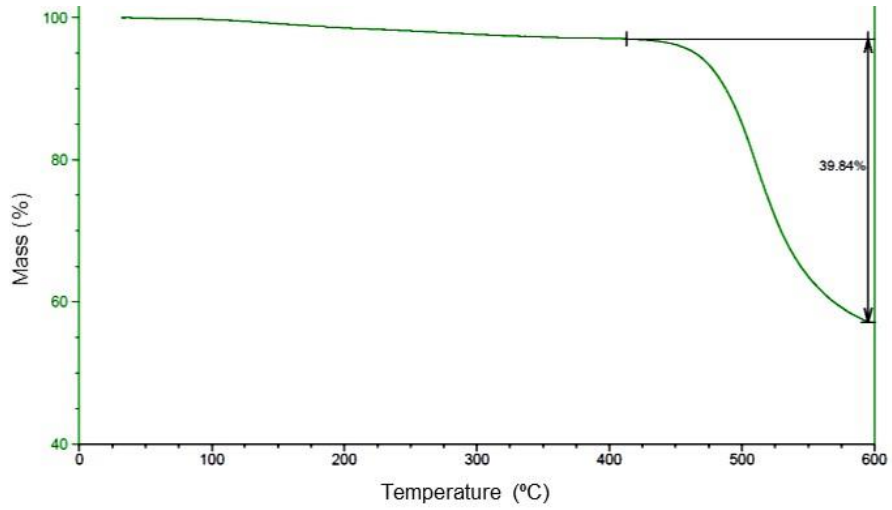

Figure 3.27: *TGA of* $\boldsymbol{Td_A}$.

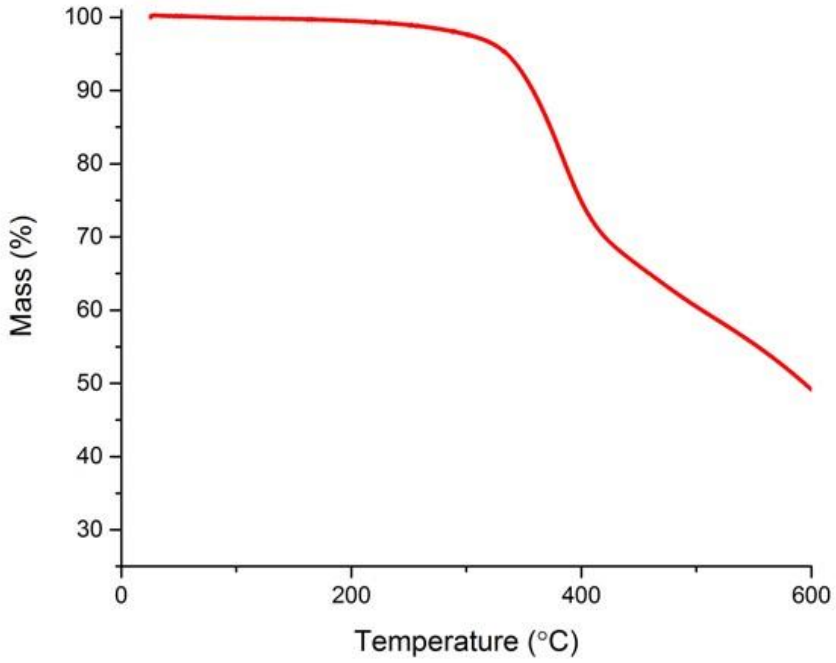

Figure 3.28: *TGA of* $\boldsymbol{Td_{Br}}$.

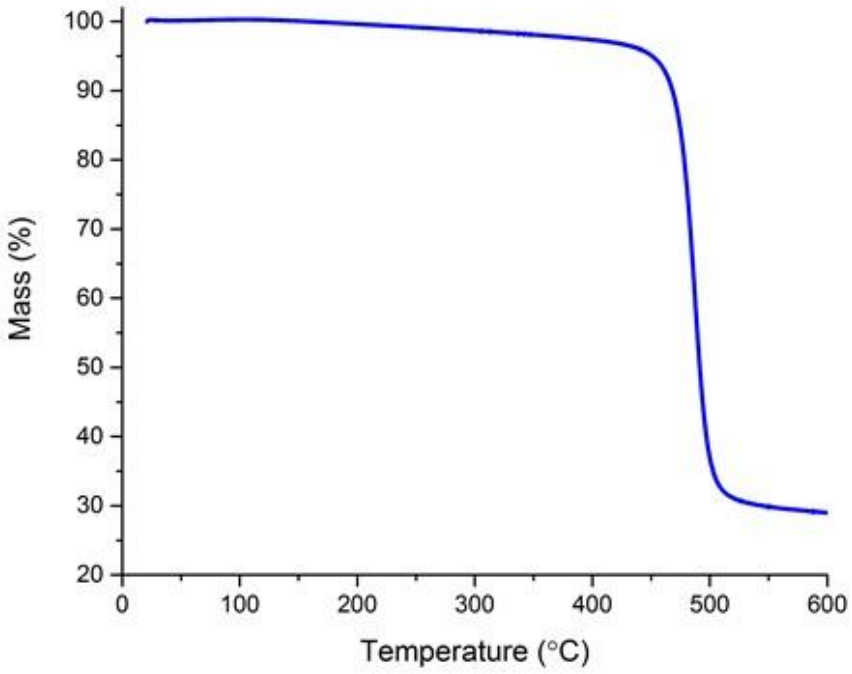

Figure 3.29: *TGA of* $\boldsymbol{Td_H}$.

Gas Adsorption Experiments

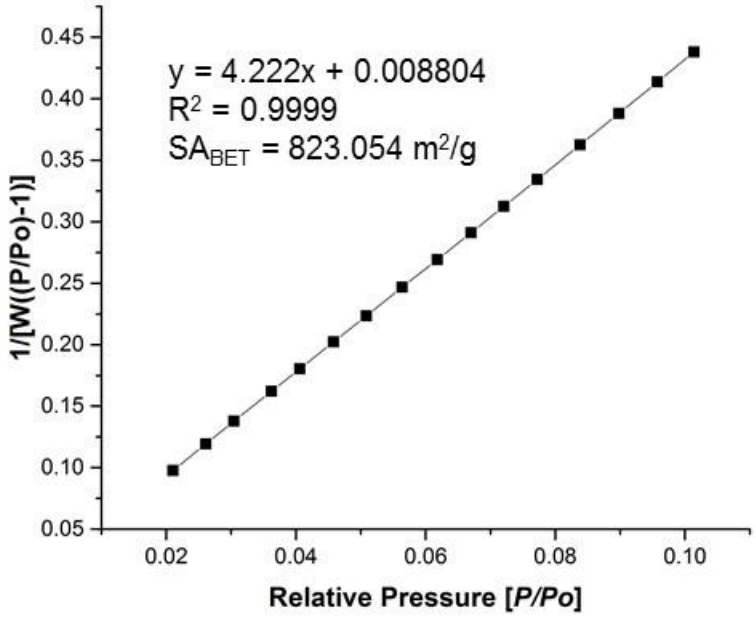

Figure 3.30: *BET-plot of* ***Td$_A$*** *powder.*

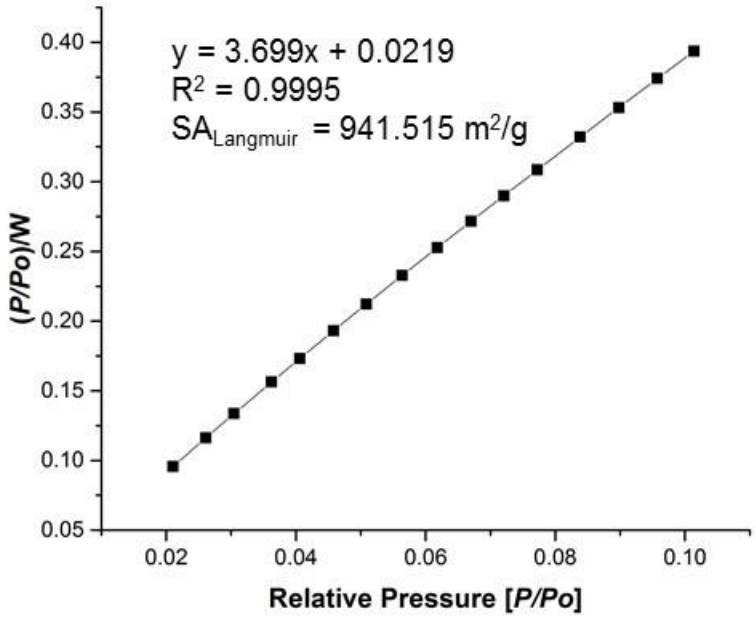

Figure 3.31: *Langmuir-plot of* ***Td$_A$*** *powder.*

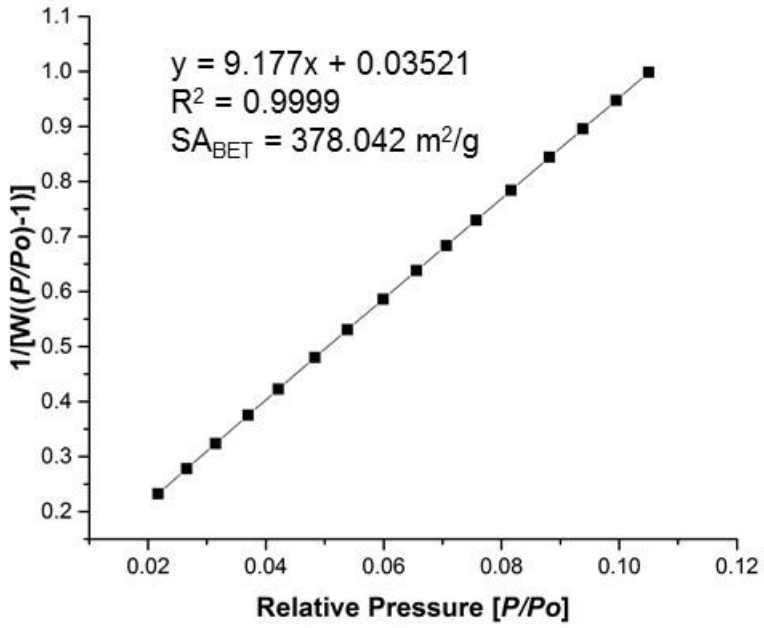

Figure 3.32: *BET-plot of* $\boldsymbol{Td_{Br}}$ *powder.*

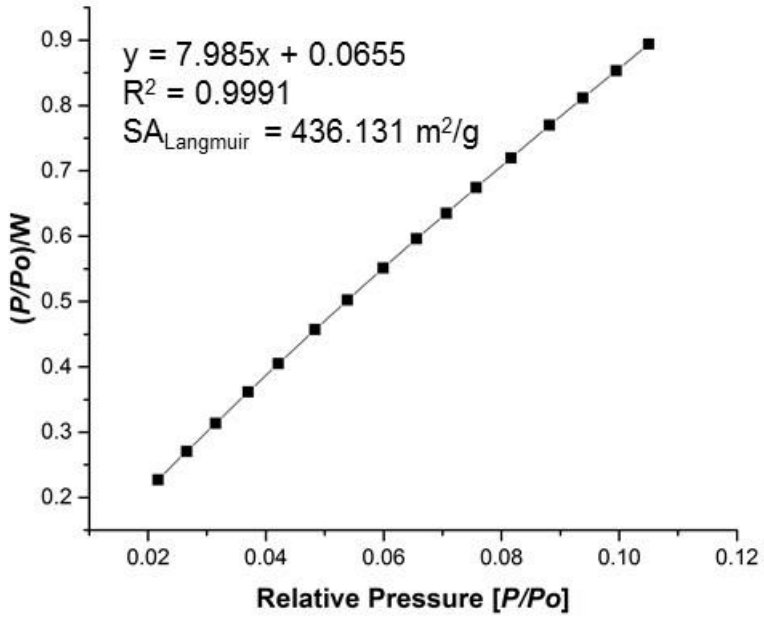

Figure 3.33: *Langmuir-plot of* $\boldsymbol{Td_{Br}}$ *powder.*

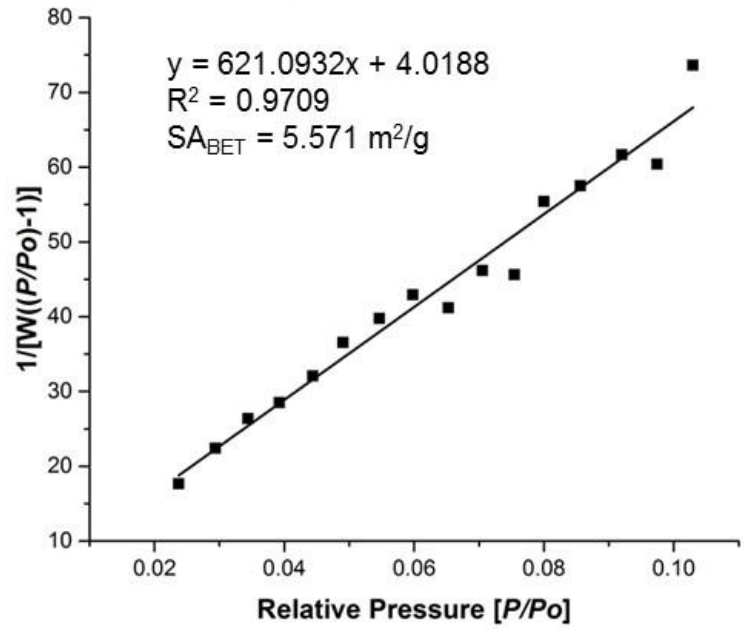

Figure 3.34: *BET-plot of* $\boldsymbol{Td_H}$ *powder.*

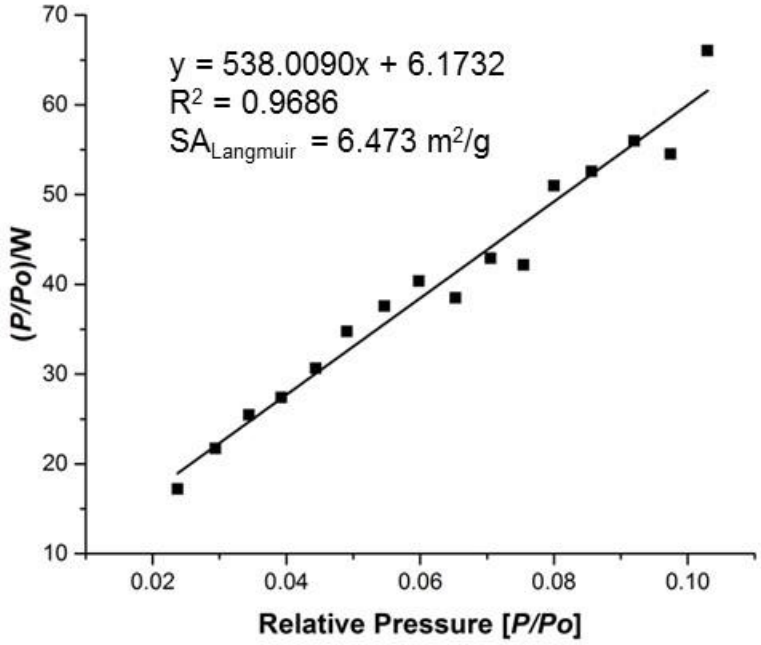

Figure 3.35: *Langmuir-plot of* $\boldsymbol{Td_H}$ *powder.*

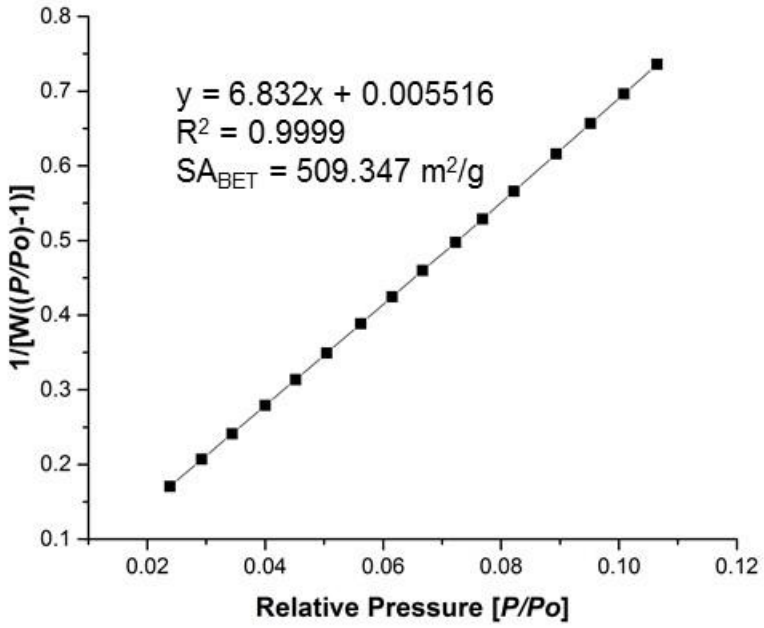

Figure 3.36: *BET-plot of* ***Td$_A$*** *desolvated crystals.*

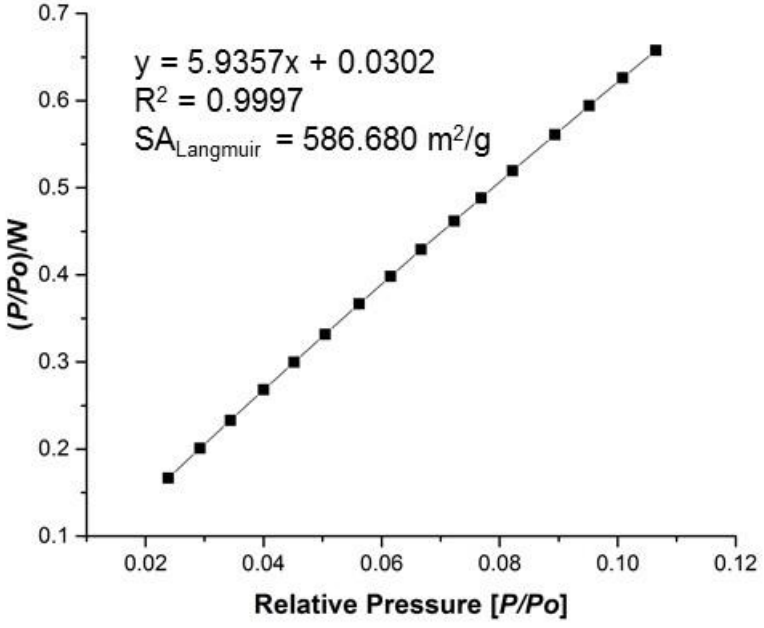

Figure 3.37: *Langmuir-plot of* ***Td$_A$*** *desolvated crystals.*

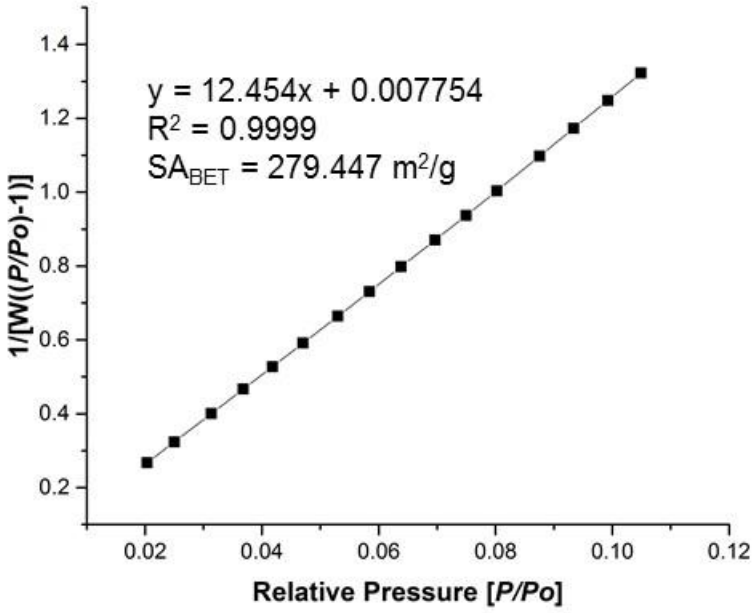

Figure 3.38: *BET-plot of* ***Td_{Br}*** *desolvated crystal.*

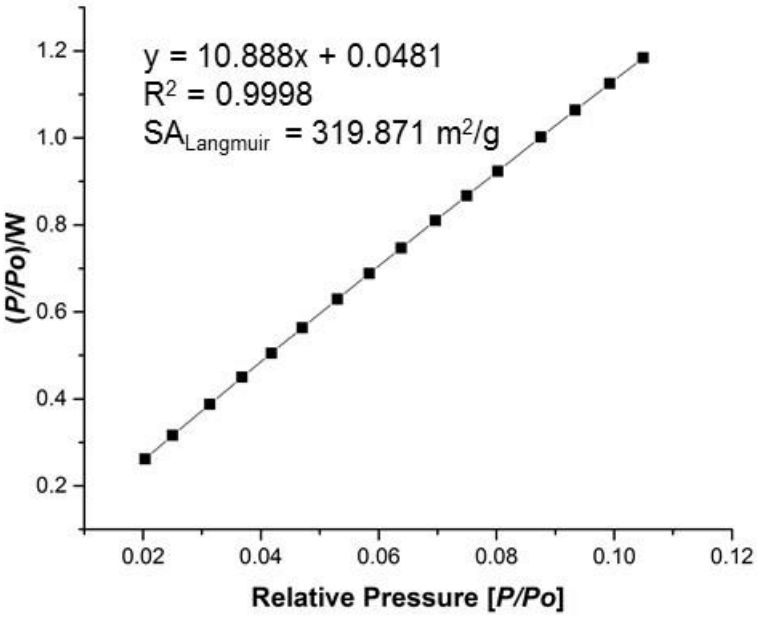

Figure 3.39: *Langmuir-plot of* ***Td_{Br}*** *desolvated crystal.*

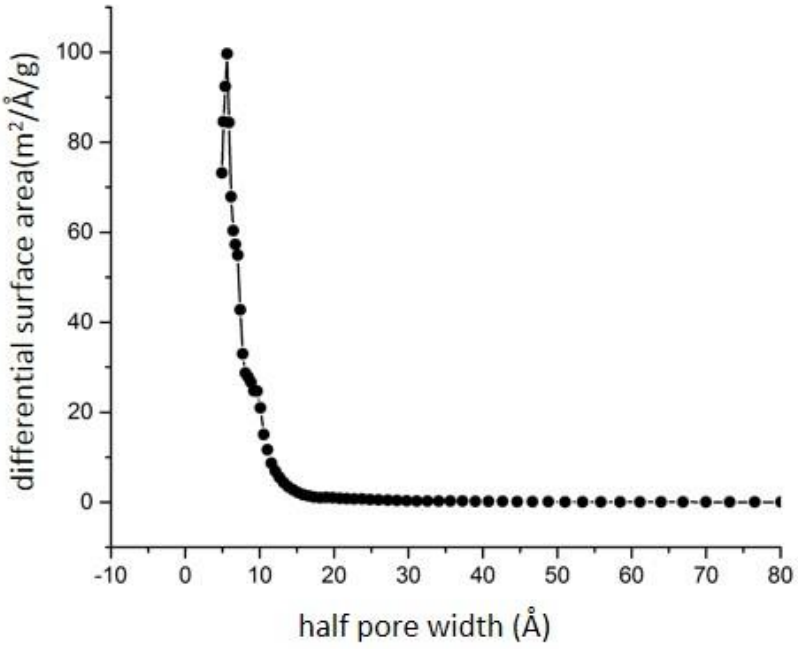

Figure 3.40: *NLDFT calculated pore size distribution (slit pore model) of* ***Td$_A$*** *desolvated crystal.*

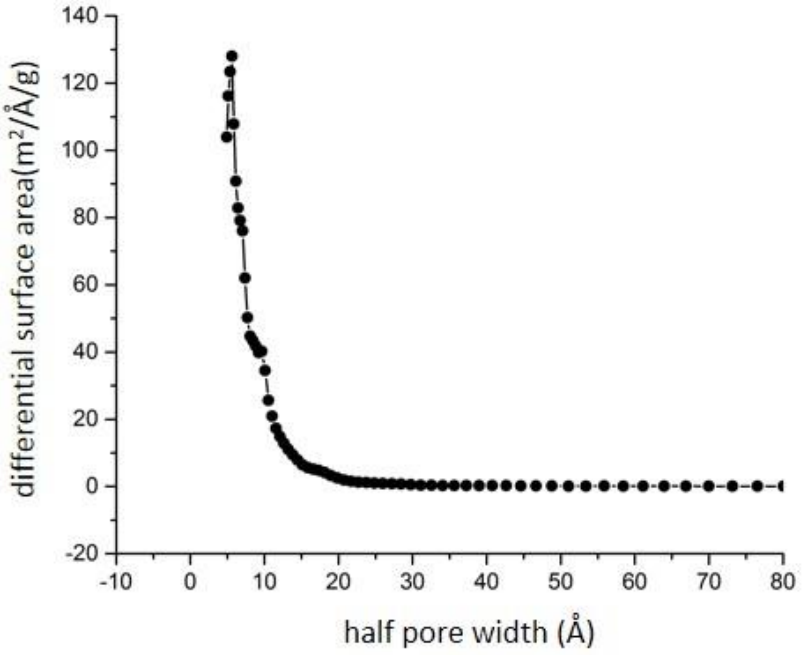

Figure 3.41: *NLDFT calculated pore size distribution (slit pore model) of* ***Td$_A$*** *powder.*

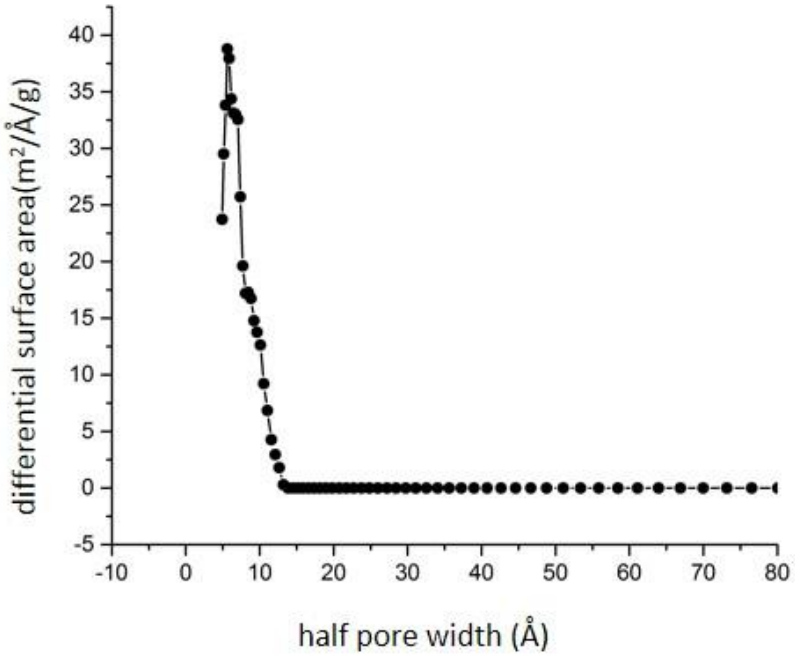

Figure 3.42: *NLDFT calculated pore size distribution (slit pore model) of* $\boldsymbol{Td_{Br}}$ *desolvated crystal.*

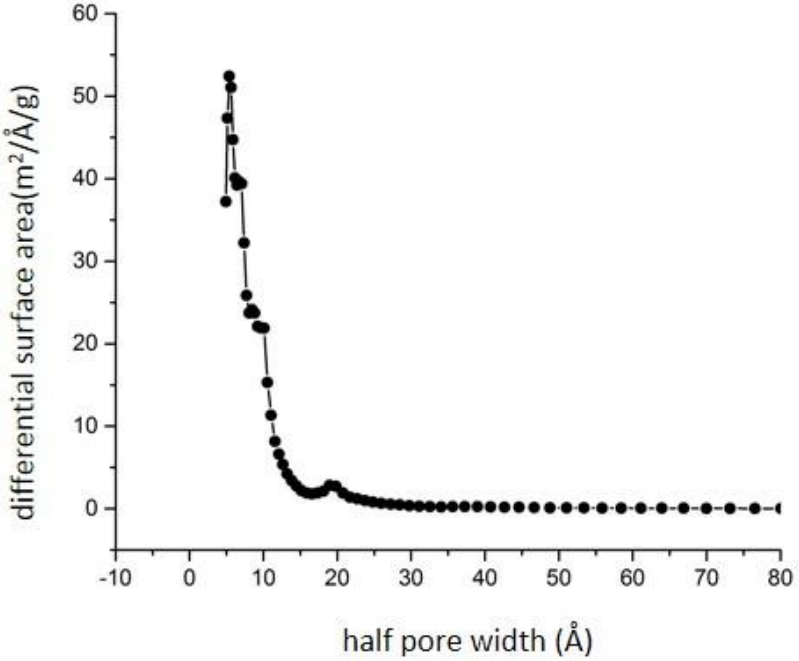

Figure 3.43: *NLDFT calculated pore size distribution (slit pore model) of* $\boldsymbol{Td_{Br}}$ *powder.*

Simulation Protocols

Molecular Dynamics (MD) simulations

MD simulations were performed on all three organic cages, **Td$_A$**, **Td$_{Br}$**, and **Td$_H$**, in GROMACS[41] using the Universal Force Field (UFF).[35] The initial configurations were generated from the X-ray crystal structures. OBGMX[42] was used to generate the required molecular topology files compatible with UFF. The sizes of the cubic simulation boxes were 35.2847 Å, 35.3296 Å, and 35.0079 Å, for **Td$_A$**, **Td$_{Br}$**, and **Td$_H$** respectively. For **Td$_{Br}$** and **Td$_H$**, the time step of the simulation was set to 1 fs. For **Td$_A$**, a smaller time step of 0.05 fs was required in order to maintain the co-linearity of the four nearest atoms that connect to each carbon-carbon triple bond. The three systems were thermally equilibrated at 300 K for 100 ps with NVT simulations. Position restraints were applied during this stage to avoid significant deformation of the initial cage conformations. After the thermal equilibration, the production MD runs were performed for 300 ps in the NVT ensemble for each system. A distance of 1 nm was used for all neighbor searching. With the UFF, no electrostatic interactions are present in the simulation. The reference temperature was set to 300 K with a time constant of 0.1 ps. Periodic boundary conditions are enforced for all simulations.

***Ab Initio* Molecular Dynamics (AIMD) simulations**

AIMD, or more precisely Born-Oppenheimer Molecular Dynamics (BOMD), was performed using VASP.[43] The Projector Augmented Wave (PAW) method was used. The Local-Density Approximation (LDA) was used for the exchange-correlation functional within the Hohenberg-Kohn–Sham framework of Density Functional Theory (DFT). Despite the known simplicity of the LDA functional, it is still sufficiently accurate to capture the bond-persistence in the simulated timescale. The simulations had one k-point vector (gamma-point mode). The box length for **Td$_A$**, **Td$_{Br}$**, and **Td$_H$** were respectively 21.9935 Å, 25.0000 Å, and 25.0005 Å. They are set to smaller values than the MD simulations in order to reduce memory usage of the AIMD simulations. The size of the simulation box does not affect the results of the simulation as long as it is larger than that of the molecule. The simulations were performed at 300K in NVT ensembles with a time step of 1 fs. The production runs last for 2.81 ps, 2.33 ps, 2.40 ps for **Td$_A$**, **Td$_{Br}$**, and **Td$_H$**, respectively. The simulations were performed on 96 processors for 72 hours. The total trajectory lengths are based on the number of steps which could be performed within the 72 allotted hours.

Averaged deviation of the edges of the molecular cage from its initial linear configuration, $\langle \delta l \rangle$

To quantify the shape-persistence of the molecular cages, the atomic displacement of the edges of the molecular cages from their initial linear configuration, $\langle \delta l \rangle$, was computed. For each edge, two atoms near the vertices of the cage were chosen as the straight base line:

$$x_1 + (x_2 - x_1)s$$

where x_1 and x_2 are the coordinates of the two atoms, s is the parameter of the parametric representation of the straight line. We then calculated the orthonormal distance, d_i^2, of each atom i with coordinate x_i, of the respective edge from the straight line connecting x_1 and x_2:

$$d_i^2 = |(x_1 - x_i) + (x_2 - x_i)s|^2$$

where s is minimized by taking $\frac{d(d_i^2)}{ds} = 0$, resulting in

$$s = -\frac{(x_1 - x_i) \cdot (x_2 - x_1)}{|x_2 - x_1|^2}$$

We then calculated the atomic displacement of each edge as

$$\delta l = \sum_{i=1}^{N} d_i$$

where N is the number of atoms in the edge. The averaged deviation $\langle \delta l \rangle$ was taken as the average of δl of all six edges of the molecular cages and over the simulation time:

$$\langle \delta l \rangle = \frac{1}{6}\frac{1}{T}\sum_{t,edge} \delta l$$

When we weighted the atomic displacement by d_i by the mass scaling factor m_i/M, where m is the mass of each atom and M is the total mass in the system, the resulting $\langle \delta l \rangle$ is nearly identical. Similarly, while yielding supplemental information as the atomic displacement, the bending angle of each edge was calculated as:

$$\theta = \cos^{-1}\frac{(x_1 - x_m) \cdot (x_2 - x_m)}{|x_1 - x_m||x_2 - x_m|}$$

where $\boldsymbol{x_m}$ is the coordinate of the furthest atom from the initial linear configuration.

Root Mean Squared Deviation (RMSD)

As a measure of the long-time shape-persistence of the molecular cages, the RMSD was computed. RMSD measures the atomic deviation from a reference structure, in this case, the initial structure of the cage after proper thermal equilibration. The RMSD is calculated as

$$\mathbf{RMSD}(\boldsymbol{t}) = \left[\frac{\mathbf{1}}{\boldsymbol{M}}\sum_{\boldsymbol{i=1}}^{\boldsymbol{N}} \boldsymbol{m_i}|\boldsymbol{r_i}(\boldsymbol{t}) - \boldsymbol{r_i}(\mathbf{0})|^{\mathbf{2}}\right]^{\frac{\mathbf{1}}{\mathbf{2}}}$$

where m_i is the mass of atom i, and M is the total mass of the structure. Both time-dependent and time-averaged RMSD were computed.

Volume

The internal volume of the molecular cage was approximated by tetrahedral tessellation. By choosing atoms near the vertices of the cage and the center of the edges of the cage, the entire molecular cage volume can be discretized into many small tetrahedrons. Each cage is approximated as 16 tetrahedrons, comprising 4 internal tetrahedrons formed only by the midpoints of the edges and 12 corner tetrahedrons, as shown in Figure 3.8. The volume of each tetrahedron is calculated as

$$\boldsymbol{V_{tetrahedron}} = \frac{|(\boldsymbol{x_1} - \boldsymbol{x_o}) \cdot [(\boldsymbol{x_2} - \boldsymbol{x_o}) \times (\boldsymbol{x_3} - \boldsymbol{x_o})]|}{\mathbf{6}}$$

where $\boldsymbol{x_i}$ are the coordinates of the each vertex of the small tetrahedrons. Both time-dependent and time-averaged internal volume of the molecular cages were computed.

3.8 References

Notes: †This chapter is adapted from Moneypenny, II, T. P.; Walter, N. P.; Cai, Z.; Miao, Y.; Gray, D. L.; Hinman, J. J.; Lee, S.; Zhang, Y.; Moore, J. S. *J. Am. Chem. Soc.* **2017**, *139*, **8**, 3259-3264. The materials are reproduced/adapted with permission. Copyright © 2017 American Chemical Society. This chapter is a collaborative work with Nathan Walter, Zhikun Cai, Yu-Run Miao, Danielle Gray, Jordan Hinman, Semin Lee, and Yang Zhang. T. P. M. II conceived experiments, performed cage syntheses, grew single crystals, prepared and characterized molecular solids, and authored text. N.W. performed the ab initio molecular dynamics, Z. C. performed the classical molecular dynamics, and Y. Z. authored related text. Y. M. performed nitrogen adsorption experiments. D. G. performed single crystal XRD experiments and solved the crystal structures of Td_{Br} and Td_{H}. J. H. performed SEM imaging. S. L. synthesized additional Td_{A}.

(1) Slater, A. G.; Cooper, A. I. *Science* **2015**, *348*.

(2) Cundy, C. S.; Cox, P. A. *Chem. Rev.* **2003**, *103*, 663.

(3) Cheetham, A. K.; Férey, G.; Loiseau, T. *Angew. Chem. Int. Ed.* **1999**, *38*, 3268.

(4) Furukawa, H.; Cordova, K. E.; O'Keeffe, M.; Yaghi, O. M. *Science* **2013**, *341*, 1230444.

(5) Furukawa, H.; Ko, N.; Go, Y. B.; Aratani, N.; Choi, S. B.; Choi, E.; Yazaydin, A. O.; Snurr, R. Q.; O'Keeffe, M.; Kim, J.; Yaghi, O. M. *Science* **2010**, *329*, 424.

(6) Deng, H.; Olson, M. A.; Stoddart, J. F.; Yaghi, O. M. *Nat. Chem.* **2010**, *2*, 439.

(7) Kitagawa, S.; Kitaura, R.; Noro, S.-i. *Angew. Chem. Int. Ed.* **2004**, *43*, 2334.

(8) Eddaoudi, M.; Kim, J.; Rosi, N.; Vodak, D.; Wachter, J.; O'Keeffe, M.; Yaghi, O. M. *Science* **2002**, *295*, 469.

(9) Segura, J. L.; Mancheno, M. J.; Zamora, F. *Chem. Soc. Rev.* **2016**.

(10) Ding, S.-Y.; Wang, W. *Chem. Soc. Rev.* **2013**, *42*, 548.

(11) Côté, A. P.; El-Kaderi, H. M.; Furukawa, H.; Hunt, J. R.; Yaghi, O. M. *J. Am. Chem. Soc.* **2007**, *129*, 12914.

(12) Côté, A. P.; Benin, A. I.; Ockwig, N. W.; O'Keeffe, M.; Matzger, A. J.; Yaghi, O. M. *Science* **2005**, *310*, 1166.

(13) Vilela, F.; Zhang, K.; Antonietti, M. *Energy Environ. Sci.* **2012**, *5*, 7819.

(14) McKeown, N. B.; Budd, P. M. *Macromolecules* **2010**, *43*, 5163.

(15) Jiang, J.-X.; Su, F.; Trewin, A.; Wood, C. D.; Campbell, N. L.; Niu, H.; Dickinson, C.; Ganin, A. Y.; Rosseinsky, M. J.; Khimyak, Y. Z.; Cooper, A. I. *Angew. Chem. Int. Ed.* **2007**, *46*, 8574.

(16) Mastalerz, M. *Chem. Eur. J.* **2012**, *18*, 10082.

(17) Holst, J. R.; Trewin, A.; Cooper, A. I. *Nat. Chem.* **2010**, *2*, 915.

(18) Tozawa, T.; Jones, J. T. A.; Swamy, S. I.; Jiang, S.; Adams, D. J.; Shakespeare, S.; Clowes, R.; Bradshaw, D.; Hasell, T.; Chong, S. Y.; Tang, C.; Thompson, S.; Parker, J.; Trewin, A.; Bacsa, J.; Slawin, A. M. Z.; Steiner, A.; Cooper, A. I. *Nat. Mater.* **2009**, *8*, 973.

(19) Zhang, G.; Presly, O.; White, F.; Oppel, I. M.; Mastalerz, M. *Angew. Chem. Int. Ed.* **2014**, *53*, 5126.

(20) Hasell, T.; Culshaw, J. L.; Chong, S. Y.; Schmidtmann, M.; Little, M. A.; Jelfs, K. E.; Pyzer-Knapp, E. O.; Shepherd, H.; Adams, D. J.; Day, G. M.; Cooper, A. I. *J. Am. Chem. Soc.* **2014**, *136*, 1438.

(21) Jones, J. T. A.; Holden, D.; Mitra, T.; Hasell, T.; Adams, D. J.; Jelfs, K. E.; Trewin, A.; Willock, D. J.; Day, G. M.; Bacsa, J.; Steiner, A.; Cooper, A. I. *Angew. Chem. Int. Ed.* **2011**, *50*, 749.

(22) Linder-Patton, O. M.; Bloch, W. M.; Coghlan, C. J.; Sumida, K.; Kitagawa, S.; Furukawa, S.; Doonan, C. J.; Sumby, C. J. *CrystEngComm* **2016**, *18*, 4172.

(23) Li, L.; Krishna, R.; Wang, Y.; Yang, J.; Wang, X.; Li, J. *J. Mater. Chem. A* **2016**, *4*, 751.

(24) Hyun, S.-m.; Lee, J. H.; Jung, G. Y.; Kim, Y. K.; Kim, T. K.; Jeoung, S.; Kwak, S. K.; Moon, D.; Moon, H. R. *Inorg. Chem.* **2016**, *55*, 1920.

(25) Holden, D.; Jelfs, K. E.; Trewin, A.; Willock, D. J.; Haranczyk, M.; Cooper, A. I. *J. Phys. Chem. C* **2014**, *118*, 12734.

(26) Jiang, S.; Jelfs, K. E.; Holden, D.; Hasell, T.; Chong, S. Y.; Haranczyk, M.; Trewin, A.; Cooper, A. I. *J. Am. Chem. Soc.* **2013**, *135*, 17818.

(27) Jin, Y.; Voss, B. A.; Jin, A.; Long, H.; Noble, R. D.; Zhang, W. *J. Am. Chem. Soc.* **2011**, *133*, 6650.

(28) Mastalerz, M.; Schneider, M. W.; Oppel, I. M.; Presly, O. *Angew. Chem. Int. Ed.* **2011**, *50*, 1046.

(29) Liu, M.; Little, M. A.; Jelfs, K. E.; Jones, J. T. A.; Schmidtmann, M.; Chong, S. Y.; Hasell, T.; Cooper, A. I. *J. Am. Chem. Soc.* **2014**, *136*, 7583.

(30) Lee, S.; Yang, A.; Moneypenny, T. P.; Moore, J. S. *J. Am. Chem. Soc.* **2016**, *138*, 2182.

(31) Marshall, R. J.; Griffin, S. L.; Wilson, C.; Forgan, R. S. *J. Am. Chem. Soc.* **2015**, *137*, 9527.

(32) Jiang, S.; Jones, J. T. A.; Hasell, T.; Blythe, C. E.; Adams, D. J.; Trewin, A.; Cooper, A. I. *Nat. Commun.* **2011**, *2*, 207.

(33) Burgun, A.; Valente, P.; Evans, J. D.; Huang, D. M.; Sumby, C. J.; Doonan, C. J. *Chem. Commun.* **2016**, *52*, 8850.

(34) Sing, K. S. W.; Everett, D. H.; Haul, R. A. W.; Moscou, L.; Pierotti, R. A.; Rouquerol, J.; Siemieniewska, T. *Pure Appl. Chem.* **1985**, *57*, 603.

(35) Rappe, A. K.; Casewit, C. J.; Colwell, K. S.; Goddard, W. A.; Skiff, W. M. *J. Am. Chem. Soc.* **1992**, *114*, 10024.

(36) Manurung, R.; Holden, D.; Miklitz, M.; Chen, L.; Hasell, T.; Chong, S. Y.; Haranczyk, M.; Cooper, A. I.; Jelfs, K. E. *J. Phys. Chem. C* **2015**, *119*, 22577.

(37) Jones, J. T. A.; Hasell, T.; Wu, X. F.; Bacsa, J.; Jelfs, K. E.; Schmidtmann, M.; Chong, S. Y.; Adams, D. J.; Trewin, A.; Schiffman, F.; Cora, F.; Slater, B.; Steiner, A.; Day, G. M.; Cooper, A. I. *Nature* **2011**, *474*, 367.

(38) Zhang, W.; Kraft, S.; Moore, J. S. *Chem. Commun.* **2003**, 832.

(39) Zhang, W.; Lu, Y.; Moore, J. S. In *Organic Syntheses, Vol 84*; Miller, M. J., Ed. 2007, p 163.

(40) van der Sluis, P.; Spek, A. L. *Acta Crystallographica Section A* **1990**, *46*, 194.

(41) Lindahl, E.; Hess, B.; van der Spoel, D. *Molecular modeling annual* **2001**, *7*, 306.

(42) Garberoglio, G. *J. Comput. Chem.* **2012**, *33*, 2204.

(43) Kresse, G.; Hafner, J. *Phys. Rev. B* **1993**, *47*, 558.

Chapter 4

Solid Lithium Electrolytes Derived from Molecular Cages†

4.1 Introduction

The development of Li ion batteries (LIBs) represents one of the most significant technological advancements for energy storage in recent history due to their high energy density and operating voltage.[1,2] Their rechargeable ability and high energy density offer unique advantages over antiquated nickel cadmium (NiCd) counterparts including longer battery life, reduced charging times, higher temperature stability, and no memory effect.[1,2] Hence, it is not surprising that LIBs are widely prevalent in modern portable devices such as cell phones, computers, and digital cameras. Furthermore, the global LIB market is only expected to rise in the foreseeable future, from $29.68 billion in 2015 to $77.42 billion in 2024.

While LIBs are promising and highly-utilized devices, they suffer from substantial practical limitations that restrict their capacity to power much larger machinery and equipment.[2-4] In reality, the long-standing challenge for LIBs resides in eliminating or reducing the substantial safety concerns related to the use of conventional organic liquid electrolyte systems that are used as charge carriers.[4-6] Liquid electrolytes provide high conductivity and fast ion mobility, but are typically unstable at both the anode and cathode, a phenomenon that inevitably leads to short-circuiting and prevents the use of Li metal at the anode.[7] Consequently, a major research thrust in the field of LIBs involves fabricating solid-state electrolytes that transport Li ions, yet eliminate the issues involved with using liquid systems.

Toward this end, researchers have investigated a variety of solid-state materials that enable ion conduction. Materials comprise of Li salts dissolved in organic polymers such as poly(ethylene oxide) were among the first solid-state electrolyte materials studied.[8] Despite extensive research efforts for this class of materials, performance remains low, with Li ion conductivities typically less than 1×10^{-4} S cm^{-1} at room temperature. Other inorganic ceramic materials, such as LISICON-like (lithium super ionic conductor) ceramics which exhibit ionic conductivities on the order of 1×10^{-2} S cm^{-1} have demonstrated exceptional performance, yet are often unstable at both the anode and cathode with few exceptions.[5,9-11] These complications severely limit application of solid-state electrolytes, as it is expected that they retain high conductivities while also remaining stable at both electrodes.

Recently, researchers have demonstrated the use of porous materials as charge carriers for solid-state electrolytes. Notable examples include the use of metal-organic frameworks (MOFs),[12] covalent-organic frameworks (COFs),[13,14] polymer networks,[15] and molecular solids.[16] For example, Long and coworkers discovered that by soaking a Mg_2(dobdc) (dobdc = 1,4-dioxido-2,5-benzenedicarboxylate) MOF with an electrolyte solution and the addition of lithium isopropoxide leads to a solid lithium electrolyte system of Mg_2(dobdc)•0.35LiO^{i}Pr•0.25LiBF$_4$•EC•DEC (EC = ethylene carbonate; DEC = diethyl carbonate).[12] They determined that this electrolyte exhibited a conductivity of 3.1×10^{-4} S cm^{-1} at 300 K and revealed an activation energy of 0.15 eV. Although this material is promising, no voltammetry was performed to investigate electrochemical stability.

Uribe-Romo and coworkers have discovered a Li ion conducting COF system. By immersing COF-5 with a 1 M lithium perchlorate/tetrahydrofuran solution, they were able to impregnate lithium salt into the COF material.[13] A COF-5 solid electrolyte system comprised of

3.77 mol % lithium exhibited an ionic conductivity of 2.6×10^{-4} S cm^{-1} at room temperature as well as an energy of activation of 0.037 eV. They determined that this material is electrochemically stable at potentials between -1.0 and 10 V vs. Li^+/Li up to 100 cycles. Finally, ^{7}Li magic-angle spinning nuclear magnetic resonance (MAS NMR) spectroscopy experiments indicate that lithium perchlorate is located within the pores, and this phenomenon enables high ionic mobility within the material.

Kim and workers have extended this concept into porous molecular solids.[16] They prepared a novel solid lithium-ion conducting electrolyte prepared by impregnating Li salt into molecular porous solids of cucurbit[6]uril (CB[6]). Solids of CB[6] pack in a honeycomb-like structure with one-dimensional channels along the *c*-axis with an average pore diameter of 7.5 Å and a pore aperture of 6 Å. To introduce Li ions into CB[6], the solid was immersed in a 1 M $LiPF_6$ solution of dimethylcarbonate (DMC) and allowed to soak for 12 hours followed by washing and drying. This procedure afforded a free-flowing, dry powder comprised of a molar ratio of 1:1.1:2.2 (CB[6]:$LiPF_6$:DMC). This electrolyte system exhibited high ionic conductivity (1×10^{-4} S cm^{-1}), and an energy of activation of 0.34 eV. Although they did not communicate any voltammetry experiments to test electrochemical stability, their results set the groundwork for ionically conductive porous molecular materials.

Given the previous reports of porous materials enabling Li ion conduction, we hypothesized that nanocomposites formulated from porous molecular cages[17-21] and an electrolyte solution are efficient Li ion electrolytes at room temperature. While only one report has shown proton conductance within porous molecular cage solids,[22] there have been no reports investigating lithium electrolyte activity. Herein, we test this hypothesis by formulating and characterizing solid lithium electrolyte nanocomposites (SLENs) derived from porous organic cage (POC) Td_A.[18] Our experiments demonstrate that this class of materials is promising, with high ionic conductivity (1×10^{-3} S cm^{-1}), low energy of activation (0.16 eV), and high oxidative stability (up to 4.7 V vs Li/Li^+). It is anticipated that results from this study will lead to a search for novel organic ion conducting composites with tunable microenvironments that are precise in molecular design.

4.2 Electrolyte Formulation

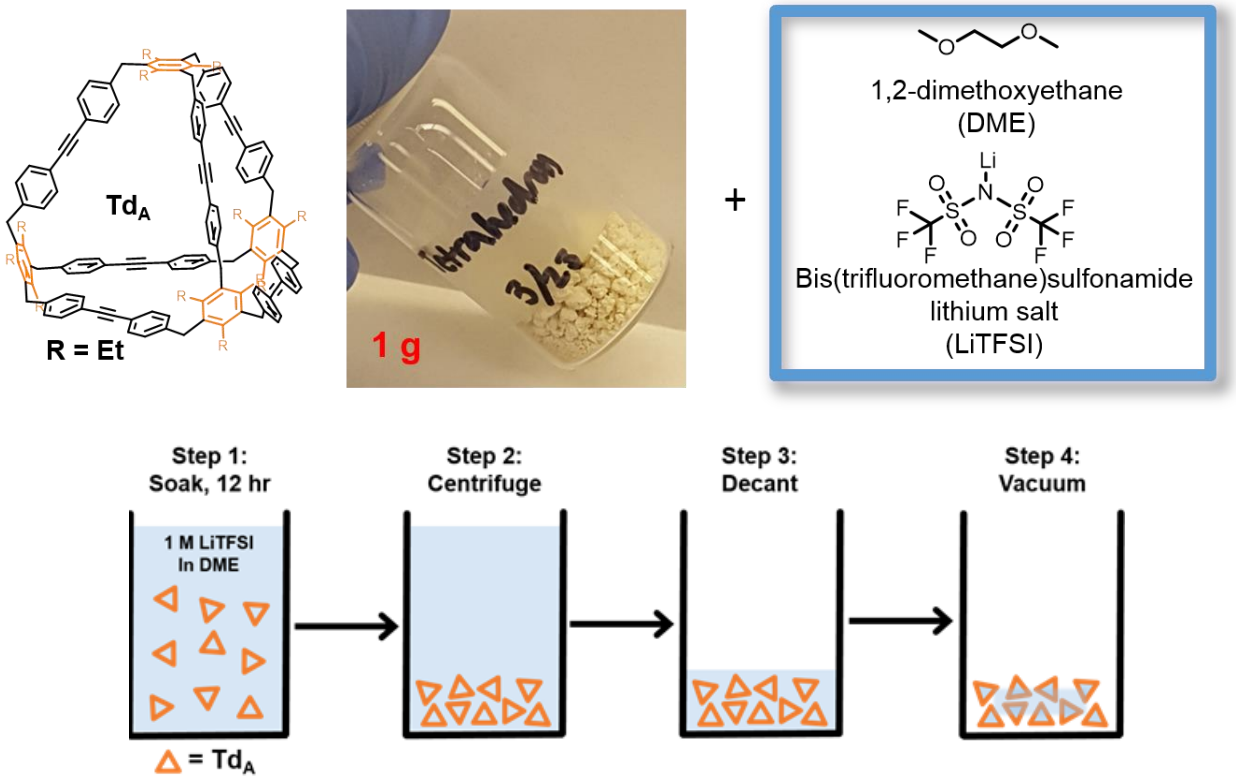

***Figure 4.1**: Chemical structures of SLEN components and preparation of the material.*

Preparation of the SLEN followed a procedure similar to the report by Kim et al.[16] but was formulated from a porous organic cage (Td_A), bis(trifluoromethane)sulfonamide lithium salt (LiTFSI) as the salt, and 1,2-dimethoxyethane (DME) as the solvent. Initial attempts used a 1:1 (v/v) mixture of DME/dioxolane, but the resulting composite did not yield reproducible electrochemical measurements as the dioxolane rapidly evaporated from the sample. The composite referred to throughout the rest of this chapter was formulated with only three components: Td_A, LiTFSI, and DME. Briefly, the rapidly precipitated powder of Td_A, prepared from precipitation from a solution of chloroform with the addition of methanol,[17] was added to a 1 M LiTFSI solution of DME and this suspension stirred overnight in a nitrogen filled glove box (Figure 4.1). The suspension was centrifuged, the supernatant was removed, and the collected solid was dried under vacuum at 60 ºC for 24 hours. This treatment resulted in the formation of a white, free-flowing powder.

4.3 Materials Characterization

To probe the composition of the SLEN, a variety of materials characterization experiments were performed including Fourier transform infrared spectroscopy (FTIR), thermal gravimetric analysis (TGA), NMR, scanning electron microscopy (SEM), energy dispersive X-ray spectroscopy (EDS), elemental analysis (EA), solid-state MAS ^{7}Li NMR (SSMAS NMR), and solid-state ^{13}C NMR. It was hypothesized that this characterization would provide information on the molar ratios of each component. Furthermore, it was hypothesized that this characterization would shed light on the coordinative environment within the material.

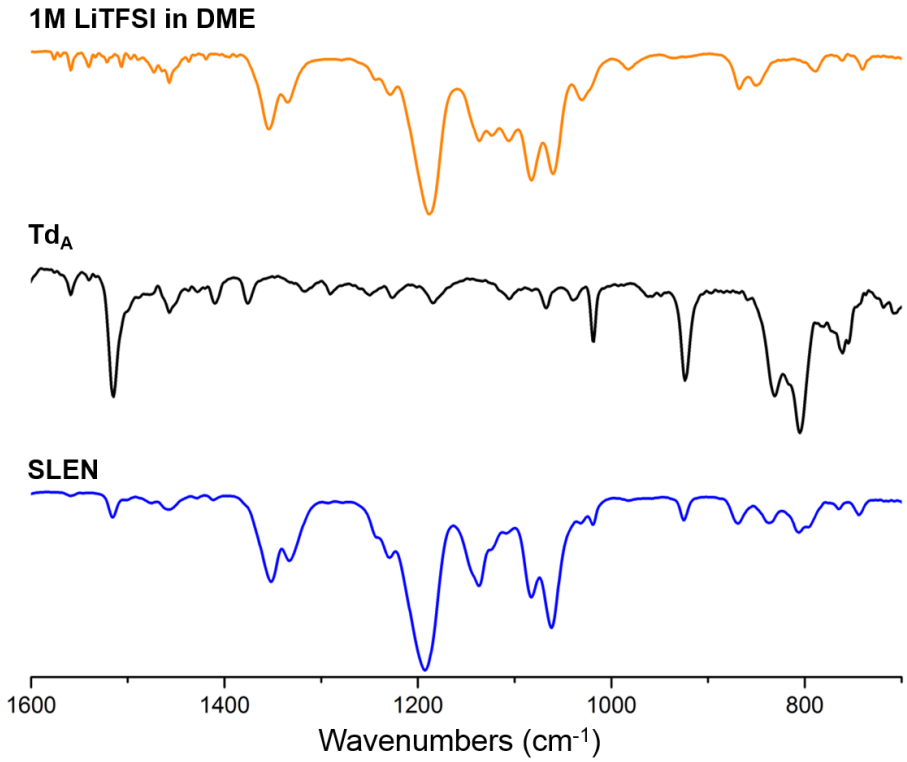

***Figure 4.2**: The fingerprint region of the FTIR of a 1 M LiTFSI solution in DME (orange), Td$_A$ (black), and the SLEN (blue).*

Figure 4.2 shows the fingerprint region of the FTIR spectra for samples of a 1 M LiTFSI in DME solution, Td$_A$, and the SLEN. The spectra show that the SLEN has a high molar concentration of LiTFSI solution. Characteristic peaks can be seen at ca. 1350 cm^{-1}, 1195 cm^{-1}, 1130 cm^{-1}, and 1080 cm^{-1} that correspond to the LiTFSI/DME solution. These peaks indicate a large relative concentration of the salt solution used in the preparation of the material, as well as a coordinative environment that resembles such a solution. Peaks corresponding to Td$_A$ can be seen

at ca. 1520 cm^{-1}, 1020 cm^{-1}, and 920 cm^{-1} indicating a relatively small molar amount of Td_A present in the SLEN.

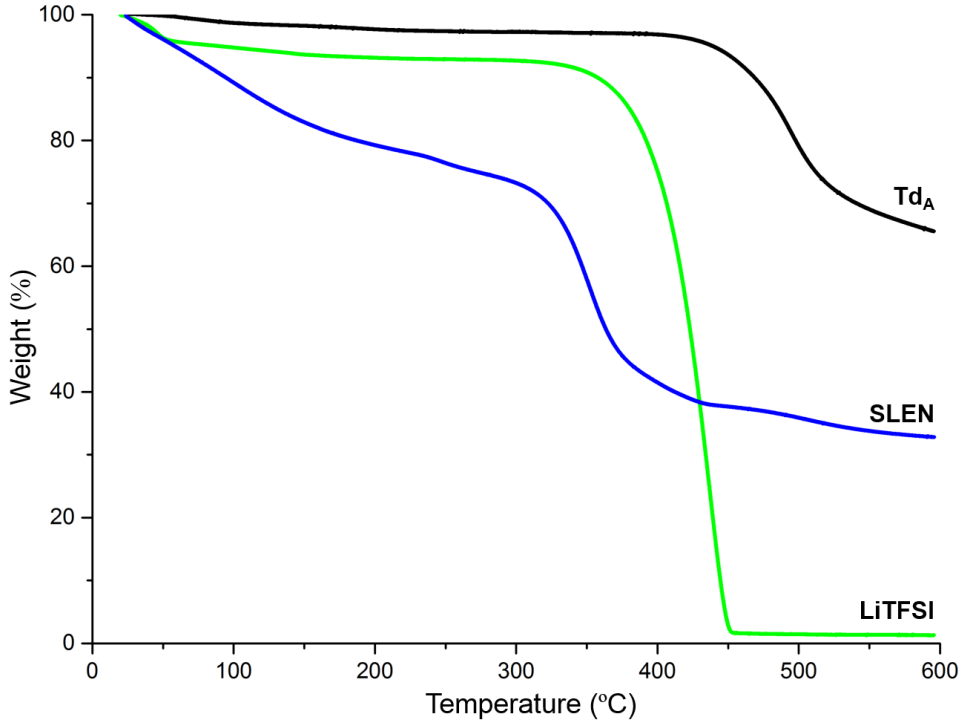

***Figure 4.3**: TGA experiments for Td_A (black), SLEN (blue), and LiTFSI (green).*

The thermal stability of the SLEN was investigated using TGA. The analyses were run under a stream of nitrogen with a temperature ramp of 10 ºC/min (Figure 4.3). The TGA curve of Td_A shows that this material is stable up to ca. 430 ºC before decomposition occurs. The SLEN material, however, exhibits a gradual decrease of mass even at lower temperatures, which we associate with the loss of DME. A similar observation was made upon thermal decomposition of a MOF-derived lithium electrolyte,[12] which exhibited a ca. 30 % loss in weight after heating to 100 ºC. The sharp decrease in mass in the SLEN (ca. 40 %) at 350 ºC is attributed to decomposition of LiTFSI in the composite, which corresponds well the TGA of LiTFSI (green). This data implies that the SLEN is not thermally stable for temperatures above 40 ºC. The thermal instability of this composite will most likely hinder practical applications, as solid state electrolytes are required to function at higher temperatures. Future studies will seek to eliminate the solvent component in this composite by covalently attaching coordination sites on the cage framework. Such a strategy is poised to significantly reduce the thermal instabilities of this material while retaining promising electrochemical properties.

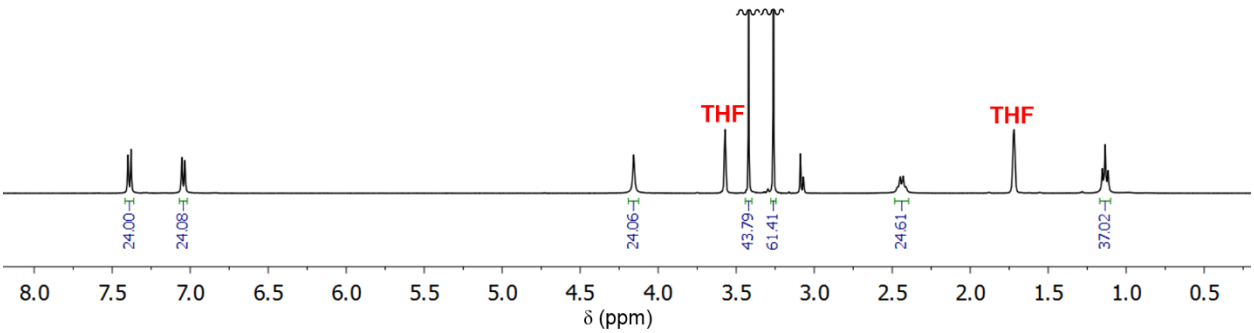

***Figure 4.4**: [1]H NMR of the SLEN in THF-d_8.*

The [1]H NMR spectrum of the SLEN (Figure 4.4) provides information on the molar amounts of DME and Td_A in the composite. The peaks at δ 7.49, 7.04, 4.16, 2.44, and 1.13 ppm correspond to Td_A, while those at δ 3.47 and 3.25 ppm correspond to DME. The peak at δ 3.08 ppm is attributed to hydration of the sample. From the ratio given by integration, the molar ratio of Td_A:DME in the composite is determined to be approximately 1:11. Furthermore, characterization of the SLEN using elemental analysis provides data on the amount of LiTFSI present in the sample (Table 4.1). It was determined from these analyses that the amount of lithium present in the material is approximately 1.01 % by weight. With these data, it was calculated that the overall molar ratio of each component in the material is 1:11:8 (Td_A:DME:LiTFSI).

***Table 4.1**: Weight percentage of each element within in the SLEN.*

Element	Wt. %
H	4.83
Li	1.01
C	43.95
N	2.3
F	17.59

The ratio of 11:8 DME to LiTFSI is notable. This molar ratio is analogous in composition to a 7 M solution which contains 2.75 DME coordination sites per Li ion. To investigate the composition of matter of the SLEN and the coordinative environment therein, we compared it with a saturated solution of LiTFSI in DME using solid state NMR experiments. As an initial experiment, SSMAS [7]Li NMR was performed on the SLEN and compared to LiTFSI. As shown in Figure 4.5a, the SLEN spectrum exhibits a narrower linewidth than that of the salt, indicative

of a more liquid-like chemical environment of Li ions, which allows freedom of motion and a larger degree of dynamic averaging.[23] The larger line width in the LiTFSI salt sample is the result of solid-state dipole-dipole and quadrupolar couplings between ^{7}Li sites. More mobile ^{7}Li species give rise to a reduced effect of solid-state couplings, ultimately affording more narrow signals, as seen in the signal of the SLEN. Two additional side peaks are also present in the spectrum of the SLEN, one side peak at δ -1.9 and one at -2.1 ppm. These two side peaks are attributed to additional chemical environments made possible by association with Td_A.

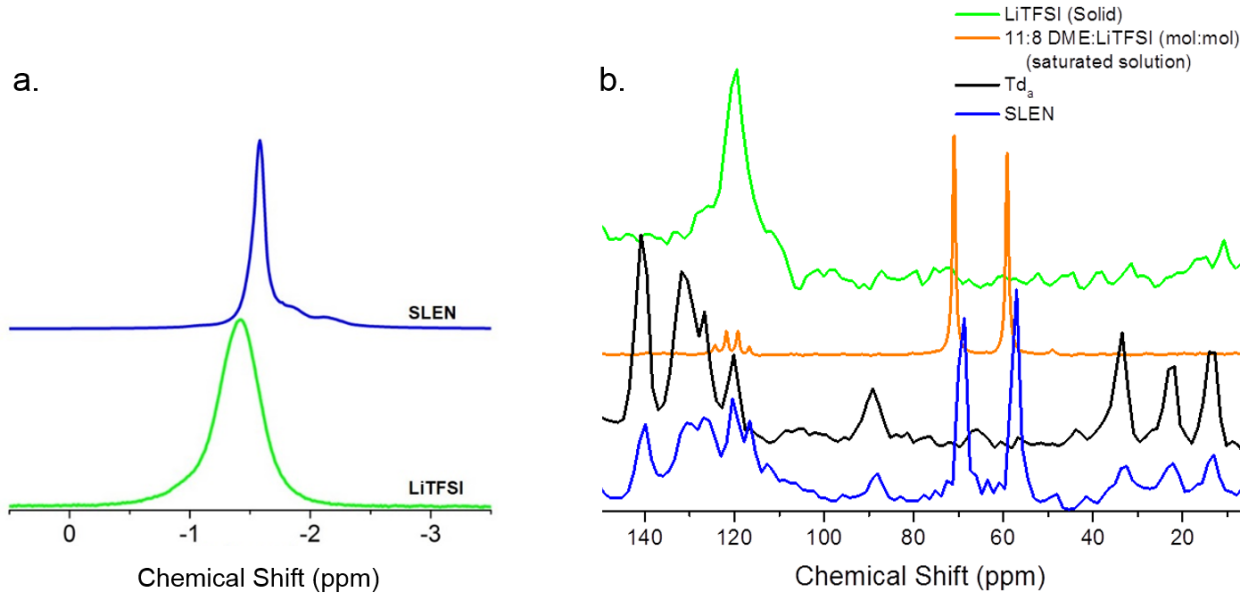

***Figure 4.5**: a) SSMAS ^{7}Li NMR of the SLEN (blue) and solid LiTFSI (green). b) solid state ^{13}C NMR of solid LiTFSI (green), saturated solution of LiTFSI in DME (orange), Td_A (black), and the SLEN (blue).*

Figure 4.5b displays the solid state ^{13}C NMR experiments of the SLEN and three reference systems. A solid state ^{13}C NMR DPMAS spectrum of LiTFSI salt taken on a 300 MHz spectrometer (green) exhibits a broad peak at δ 119.8 ppm. A solution ^{13}C spectrum of 11:8 molar solution of DME:LiTFSI (orange) exhibits two peaks (59.1 ppm and 71.0 ppm) which correspond to DME and a quartet centered at 120.5 ppm with a $^{1}J_{C\text{-}F}$ = 321 Hz corresponding to LiTFSI.[24] A ^{13}C NMR CPMAS solid state spectrum of Td_A (black) taken on a 300 MHz is in good agreement with those reported for a solution spectrum[17] although resolution of all the aromatic peaks is obscured by the large line width, which is expected in solid-state experiments. A ^{13}C NMR DPMAS solid state spectrum of the SLEN taken on a 300 MHz spectrometer is displayed in blue. By comparison to the spectrum for Td_A, we assign the peaks at δ 13.3, 22.4, 32.9, 88.3, 120.3,

126.5, 130.2, and 140.1 ppm to Td_A. We assign the peaks at δ 57.2 and 69.0 ppm to DME, albeit with a significant upfield shift as compared to the solution spectrum. Two additional peaks are present in the SLEN spectra: one at δ 112.6 and one at 116.7 ppm. Two possible assignments for these peaks were considered. First, the two peaks could be part of a quartet with the remaining signals obscured by the signal for Td_A. This possibility is discounted based on the separation of the two signals which, if coupled, would have J=307 Hz which is significantly different than that observed for LiTFSI. Based on chemical shift, these two peaks are assigned instead as two singlets from different chemical environments of LiTFSI. We note both peaks are upfield to the peak observed in the solid LiTFSI sample. In the SLEN, the peaks for LiTFSI and DME both appear more upfield than the corresponding peaks in the 11:8 DME:LiTFSI sample or the solid LiTFSI sample. We attribute this chemical shift difference to interaction between each component and Td_A.

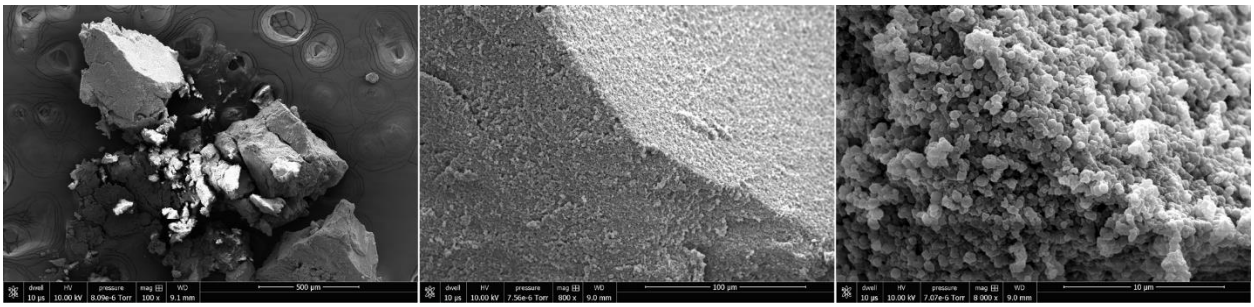

Figure 4.6*: Scanning electron microscopy images of the SLEN.*

To characterize the morphology of the SLEN material, SEM experiments were performed (Figure 4.6). Characterization of materials was carried out in the Microscopy Suite at the Beckman Institute for Advanced Science and Technology at the University of Illinois at Urbana-Champaign. Prior to imaging, the samples were prepared by mounting on a stub using carbon tape and sputter coated with gold-palladium using a deposition current of 20 mA and a deposition duration of 70 s. The samples were imaged using a FEI Quanta FEG 450 ESEM operating at 10.0 kV at a working distance of 10 mm, accelerating voltage of 10.0 kV, extracting voltage of 5.1 kV, emission current of 10 μA, probe current set to high, and ultrahigh resolution mode. The surface of SLEN particles appear rough, resembling the rapidly precipitated solid of Td_A as shown previously.[17] These observations indicate that the salt solution has penetrated the surface of the molecular solid and impregnated the solid.

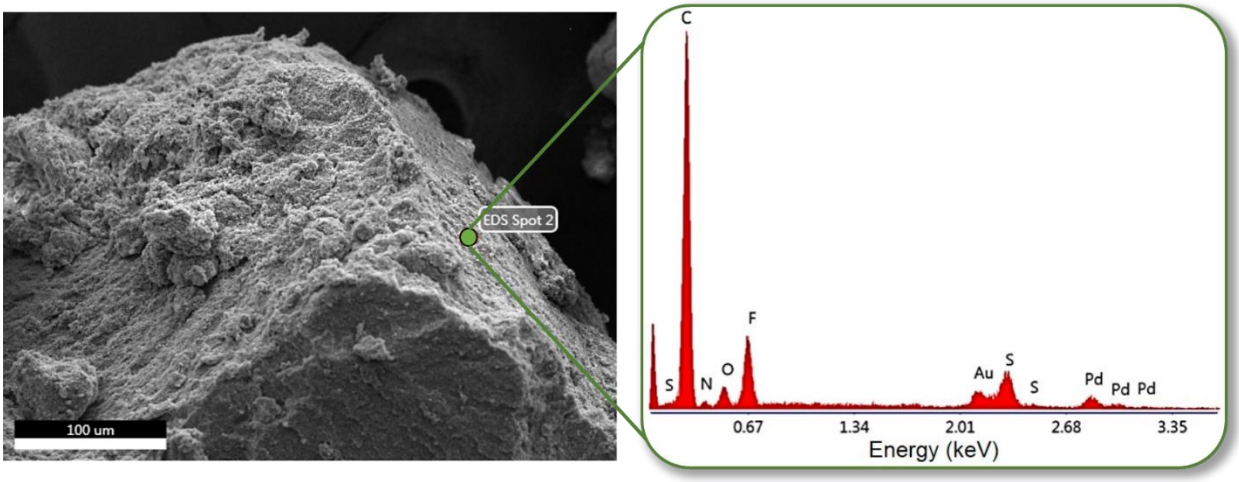

***Figure 4.7**: EDS characterization of the SLEN.*

Characterization by EDS and EDS elemental mapping further support this hypothesis. As shown in Figure 4.7, EDS experiments show that the material is comprised of nitrogen, carbon, fluorine, oxygen, and sulfur, all of which correspond to Td_A, LiTFSI, and DME. The Au and Pd present in the sample is a result of the sputtercoating treatment. Elemental mapping of this material (Figure 4.8) indicates that the material is not phase separated on length-scales greater than the instrument's resolution and that atoms are evenly distributed throughout the material.

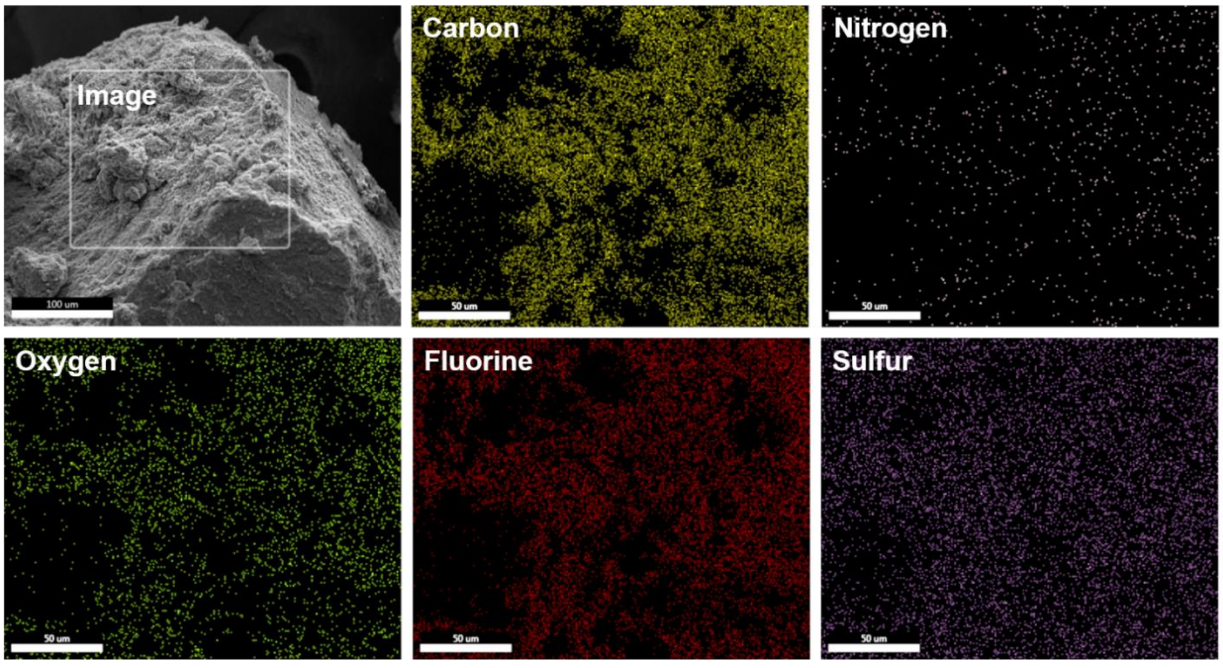

***Figure 4.8**: EDS elemental mapping of the SLEN.*

4.4 Electrochemical Characterization

To investigate the utility of the SLEN as a lithium electrolyte system, electrochemical impedance spectroscopy (EIS) was performed. Figure 4.9a displays the EIS data of the SLEN at various temperatures. In EIS experiments of typical ionically conducting solids, the complex impedance plot exhibits a half circle followed by a sloped line, with the diameter of the half circle corresponding to bulk resistance[25,26]. In the frequency range used in these experiments, only a sloped line is observed except at lower temperatures (black). This phenomenon has been observed in gel-polymer electrolytes, and is attributed to the liquid-like environment of the charge carriers, which allows fast dielectric relaxation and prevents dielectric capacitance throughout the material.[27-30] The resistance is calculated from the intercept of the line with the real axis (Z'). At room temperature, the measured conductivity was $1.0 \pm 0.1 \times 10^{-3}$ S cm^{-1} for the SLEN material. To our knowledge, this conductivity exceeds that of known MOF (3.1×10^{-4} S cm^{-1}),[12] COF (2.6×10^{-4} S cm^{-1}),[13] and porous organic (1.0×10^{-4} S cm^{-1})[16] based electrolytes. The lithium transference number of the SLEN was determined to be 0.56, indicating that ionic conduction in this material is not solution-based, as liquid electrolytes exhibit typical values between 0.2 and 0.4 and this number decreases with increasing salt concentration.

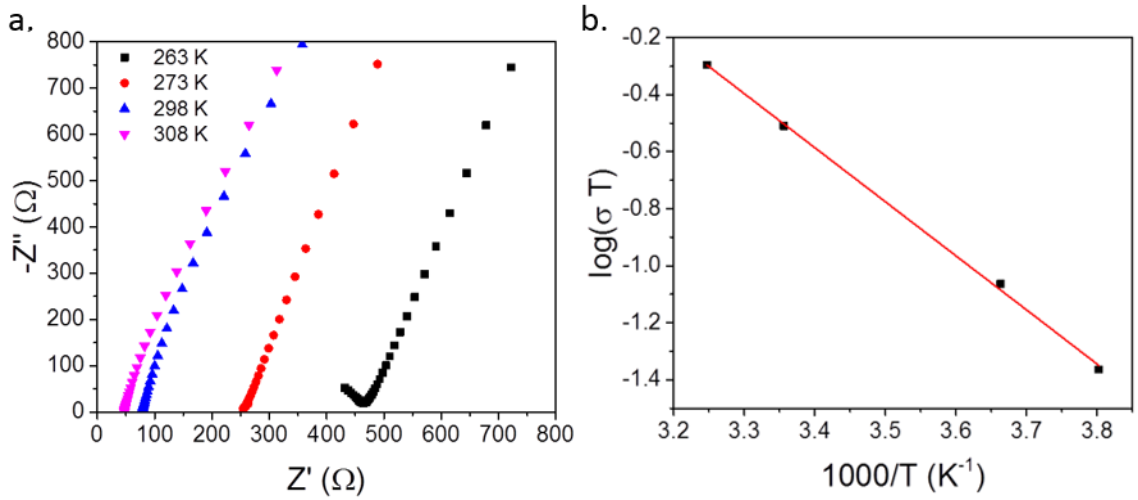

***Figure 4.9**: Electrochemical impedance spectroscopy (EIS) experiments. Measurements were taken in a Swagelock cell using stainless steel blocking electrodes. a) EIS experiments performed at various temperatures. b) Arrhenius plot of the temperature-dependent conductivity of the SLEN.*

Figure 4.9b displays the Arrhenius plot of the temperature-dependent conductivity of the SLEN. The material exhibits linear Arrhenius-like behavior over the temperature range of -10 to

35 ºC. From the slope of the plot, the activation energy of conduction was determined to be 16 kJ mol^{-1} (0.16 eV). This exceptionally low barrier is consistent with the SLEN being a superionic conductor.[31] It is important to note that at temperatures greater than 40 ºC reliable impedance data could not be obtained. As evident from the TGA, above 40 ºC, the material experiences thermal instability. As such, DME is lost and the conductivity subsequently decreases. These results emphasize the importance of eliminating the solvent in future research endeavors, as temperature stability is a necessity for solid-state electrolytes.

Figure 4.10a displays the linear sweep voltammogram of a Pt/SLEN/Li cell. The voltammogram exhibits no significant oxidative current until 4.7 V vs Li/Li^+. As such, it demonstrates that the material is stable up to about 4.7 V vs. Li/Li^+. Such high oxidative stability is attributed to the ratio of DME to LiTFSI (11:8), as a high salt concentration can prevent oxidative decomposition as previously shown in a different system.[32-34]

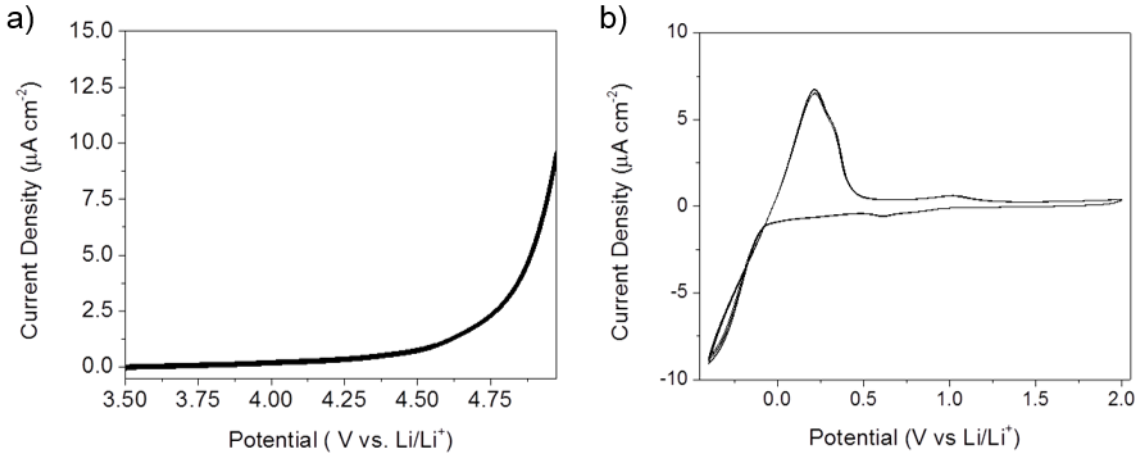

Figure 4.10*: a) linear sweep voltammetry of the SLEN run on a Pt/SLEN/Li cell. b) cycles 28-33 of the cyclic voltammetry experiment of the SLEN run on a Cu/SLEN/Li cell.*

Figure 4.10b shows cycles 28-33 of the cyclic voltammetry experiments run on a Cu/SLEN/Li cell. These cycles are the point at which the experiment stabilizes. Cyclic voltammograms for the anode reaction were conducted between -0.4 V and 2.0 V vs. Li/Li^+ at a scan rate of 0.25 mV s^{-1} with Cu foil as the working electrode for the evaluation of the Li plating and stripping reactions. The system exhibits two sets of redox pairs. A first set is seen with a reductive wave at 0.6 V and an oxidative wave at 1.0 V and is assigned to the underpotential deposition and stripping of lithium on copper.[35] The second redox couple at more negative potentials is assigned as the bulk deposition and stripping of lithium on the substrate.

In initial cycles of the cell, the bulk deposition and stripping exhibit poor coulombic efficiency, and the deposition peak gradually shifts from normal linear behavior to the diffusive regime exhibited in Figure 4.13 (Experimental section). Coulombic efficiencies increase with cycling before stabilizing at >98% at cycle 23. Current densities are variable between cycles but stabilize at cycle 28. We note that the current densities for the plating and stripping reactions are lower than those seen for ceramic solid electrolytes including β-Li_3PS_4, which has an ionic conductivity lower than the SLEN (ca. 10^{-4} S cm^{-2}).[36] Literature reports often utilize faster sweep rates than the one used in this experiment (250 μV s^{-1}), which will result in larger current densities.[31,36,37] The SLEN does not reversibly deposit Li^+ at higher scan rates, a phenomenon we attribute to its low concentration of Li^+. Additionally, we believe the low Li^+ concentration plays a role in the diffusive behavior observed in later cycles as poor stripping efficiencies can create depletion layers in the low Li^+ concentration material.

4.5 Conclusions

In conclusion, a novel solid state lithium electrolyte system was formulated from a porous molecular cage and LiTFSI/DME electrolyte solution. The SLEN exhibits exceptional room temperature conductivity of 1×10^{-3} S cm^{-1} with a low activation energy of 16 kJ mol^{-1}, both of which rival other solid electrolyte systems comprised of inorganic ceramic materials. Cyclic voltammetry demonstrates that this material exhibits excellent oxidative stability up to 4.7 V vs. Li/Li^+, as well as anodic stability upon cycling. Materials characterization indicates that the material presents as a solid, and enables a highly coordinated environment of DME and LiTFSI, which contributes to its excellent stability. The exceptional electrolyte properties of this material combined with the novel application of porous cages as functional materials makes future studies of this system of great interest.

4.6 Experimental

General. All air or moisture-sensitive manipulations were performed under an atmosphere of nitrogen using standard Schlenk techniques or in an argon-filled glove box. All metathesis reactions were set up in an argon-filled glove box and run under an inert atmosphere. Reaction

vessels were 20 mL I-CHEM vials fitted with PTFE/Silicone septa purchased from VWR International unless specified otherwise.

Materials. Unless otherwise stated, all starting materials and reagents were purchased from Sigma Aldrich and used without further purification. The following compounds were prepared according to literature procedure: 1,3,5-Tris(4-propynylbenzyl)-2,4,6-triethylbenzene (P_{Carb}), Td_A, molybdenum(IV) propylidyne precatalyst [Mo].

Solution NMR Spectroscopy. ^{1}H and ^{13}C NMR spectra were recorded on a Varian Unity 400 MHz (298 K). All spectra were recorded in chloroform-*d* or tetrahydrofuran-*d8* unless specified otherwise. Chemical shifts are reported in δ (ppm) referenced on tetramethylsilane (TMS) or residual solvent peaks (CDCl3: 7.26 for ^{1}H, 77.16 for ^{13}C; THF-*d8*: 1.72 and 3.58 for ^{1}H). Coupling constants (J) are expressed in Hertz (Hz). Splitting patterns are designated as: s (singlet), d (doublet), t (triplet), or m (multiplet).

Solid State ^{7}Li MAS NMR Spectroscopy. ^{7}Li SS NMR spectra were obtained in the SCS NMR facility using a Varian VNMRS 750 MHz NMR spectrometer (17.6 T) operating at a resonance frequency of ν_0 (^{7}Li) = 291.2 MHz at room temperature. A Varian 4 mm triple-resonance HXY T3 narrow-bore (NB) MAS probe was used for all experiments at a spinning rate of 15 kHz and two pulse phase modulation (TPPM) ^{1}H decoupling. Samples were packed into 4 mm zirconia rotors in a glove box to avoid exposure to moisture.

Experimental lithium chemical shift referencing, pulse calibration and setup were performed using 1M lithium chloride, which has a chemical shift of 0.00 ppm. Specific ^{7}Li pulse widths of 6.0 μs and recycle delays of 2 s were used, and 168 scans were acquired for the SLEN sample and 40 scans for the LiTFSI sample.

^{13}C solid-state NMR spectra were obtained in the SCS NMR facility using a Varian Unity Inova 300 NMR spectrometer (7.05 T) operating at a resonance frequency of ν_0 (^{13}C) = 75.47 MHz and ν_0 (^{7}Li) = 116.6 MHz at room temperature. A Varian/Chemagnetics 4 mm double-resonance APEX HX magic-angle spinning (MAS) probe was used for all experiments at a spinning rate of 10 kHz and two pulse phase modulation ^{1}H decoupling. Samples were packed into 4 mm zirconia rotors.

Experimental carbon chemical shift referencing, pulse calibration and cross-polarization condition were performed using powdered hexamethylbenzene (HMB), which has a chemical shift of 17.3 ppm (for the methyl peak) relative to the primary standard, trimethylsilane (TMS), at 0

ppm. For LiTFSI sample 668 scans were used, for SLEN sample 1932 scans were used, and for the Td_A sample 2584 scans were used.

Thermogravimetric Analysis. TGA was performed on a TA Instruments Q50 analyzer. Samples were heated to 600 ºC in a platinum crucible at a rate of 10 ºC/min under a nitrogen atmosphere.

SEM and EDS. Characterization of materials was carried out in the Microscopy Suite at the Beckman Institute for Advanced Science and Technology at the University of Illinois at Urbana-Champaign. Prior to imaging, the samples were prepared by mounting on a stub using carbon tape and sputter coated with gold-palladium using a deposition current of 20 mA and a deposition duration of 70 s. The samples were imaged using a FEI Quanta FEG 450 ESEM operating at 10.0 kV at a working distance of 10 mm, accelerating voltage of 10.0 kV, extracting voltage of 5.1 kV, emission current of 10 μA, probe current set to high, and ultrahigh resolution mode.

Fourier transform infrared spectroscopy (FTIR). Spectra were recorded on a Nicolet Nexus 670 spectrometer with a DRIFTS attachment.

Elemental Analysis. C, H, N, Li, and F elemental analyses were carried out in the University of Illinois School of Chemical Sciences Micro-analysis Laboratory.

Preparation of SLEN. In an Ar-filled glovebox, 35 mg of Td_A cage is added to 0.6 mL of a 1M solution of LiTFSI in DME. The resulting mixture is stirred overnight in the glovebox. After stirring, the mixture is transferred to a centrifuge tube with 0.3 mL of DME as a wash. The centrifuge tube is capped and wrapped in Parafilm before being transferred outside of the glovebox and centrifuged at 3300 RPM for 2 minutes. The tube is then transferred back into an Ar-filled glovebox and the supernatant is removed. The centrifuge tube is then capped with a septum and transferred outside the glovebox. The septum is pierced with a needle and quickly transferred into a vacuum oven where it is dried under vacuum at 60 ºC for 24 hrs. (Note: we have observed under higher temperature and pressure we can remove all of the solvent from the composite at the cost of decreased ionic conductivity.) The material is then transferred back into a glovebox where it is pressed by hand (typical pressure between 0.5-0.7 MPa) between 2 stainless steel (SS) disks in a 0.5 in diameter pellet die. We note that high pressured pelletization (>7 MPa) results in decreased conductivity. In experiments where electrodes rather than the stainless steel disks are desired, the pressing is done with Al foils rather than steel disks as they are easier to remove. Additionally while the pellets can be made and manipulated as described, doubling the preparation produces a large and more mechanically robust pellet.

Potentiostatic Electrochemical Impedance Spectroscopy. The resulting SS/SLEN/SS pellet is placed in a cell made of a modified Swagelok tube fitting[38]. Potentiostatic EIS (PEIS) was conducting using a Biologic (Seyssinet-Pariset France) SP150 potentiostat/galvanostat. PEIS was run between a frequency of 1 MHz and 1Hz at 0 V vs. the working electrode and with a perturbation amplitude of 20 mV. Temperature was controlled by protecting the cell and electrochemical leads in a thin plastic layer before submerging in a bath of the appropriate temperature and thermally equilibrating for 1 hr. The same procedures are used on the synthetic precursor to Td_A (P_{carb}) as a control and the results of the conductivity measurement are shown in Figure 4.14. Its characterization of the resulting composite is listed below.

Potentiostatic Evaluation of Anode Reaction. The samples were prepared as described above, but Cu or Pt foil was used in place of stainless steel discs. One piece of foil is peeled off the SLEN pellet with a razor blade and replaced with a piece of Li foil. Potentiostatic experiments were performed in a cell made of a modified Swagelok tube fitting inside a glove box. The experiments were conducted by using a CH Instruments (Austin, TX) electrochemical workstation. Cyclic voltammograms for the anode reaction were conducted between -0.4 V and 2.0 V vs. Li/Li^+ at a scan rate of 0.25 mV s^{-1} with Cu foil as the working for the evaluation of the Li plating and stripping reactions. For oxidative stability, a Pt working was used and linear sweep voltammetry was run from 2.0 V to 5.0 V vs Li/Li^+ at a scan rate of 0.5 mV s^{-1}.

Nuclear Magnetic Resonance Spectroscopy (NMR)

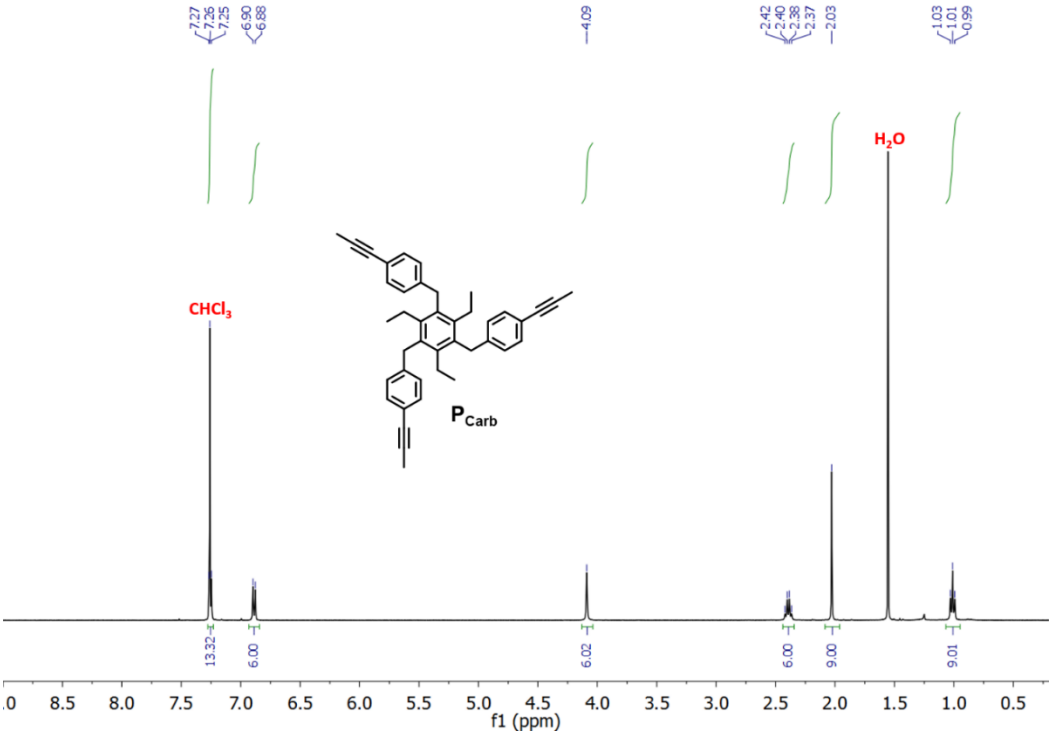

***Figure 4.11**: ^{1}H NMR of P_{Carb} (400 MHz, $CDCl_3$).*

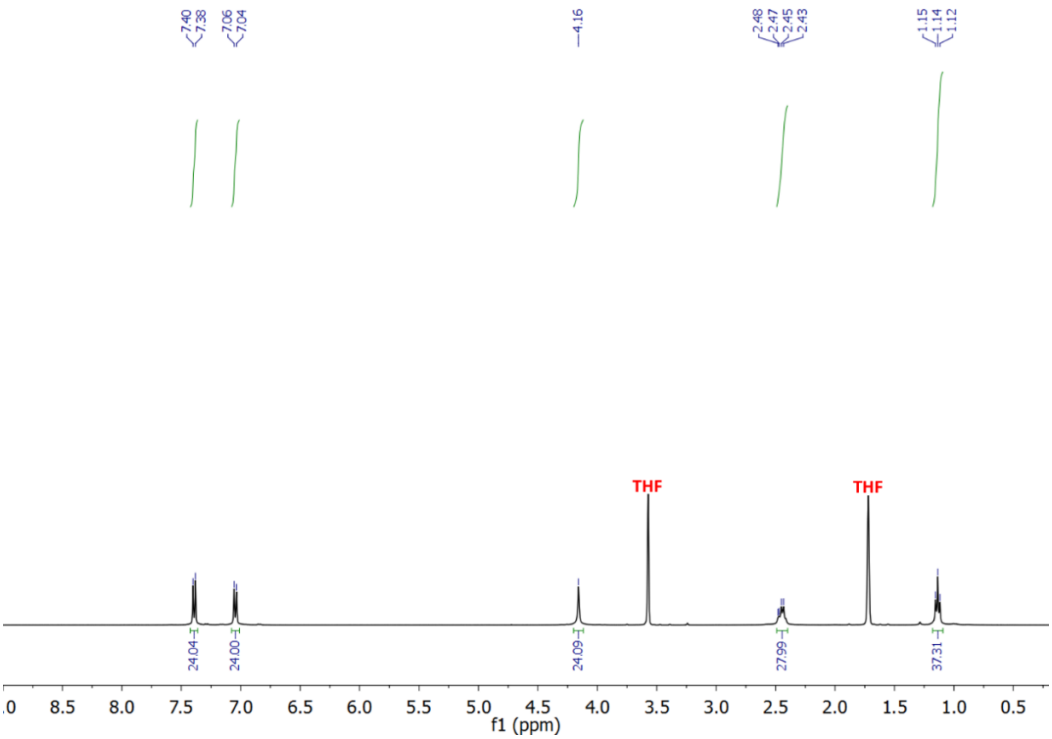

***Figure 4.12**: ^{1}H NMR of Td_A (400 MHz, THF-d_8).*

Voltammetry of Al/SLEN/Li Cell

Table 4.2*: Coulombic efficiencies of SLEN cell cycling.*

Cycle	Coulombic Efficiency	Cycle	Coulombic Efficiency
2	66 %	18	79 %
3	81 %	19	91 %
4	84 %	20	91 %
5	95 %	21	90 %
6	88 %	22	95 %
7	85 %	23	99 %
8	81 %	24	98 %
9	76 %	25	98 %
10	83 %	26	94 %
11	90 %	27	97 %
12	89 %	28	99 %
13	86 %	29	98 %
14	82 %	30	99 %
15	92 %	31	98 %
16	84 %	32	99 %
17	85 %	33	98 %

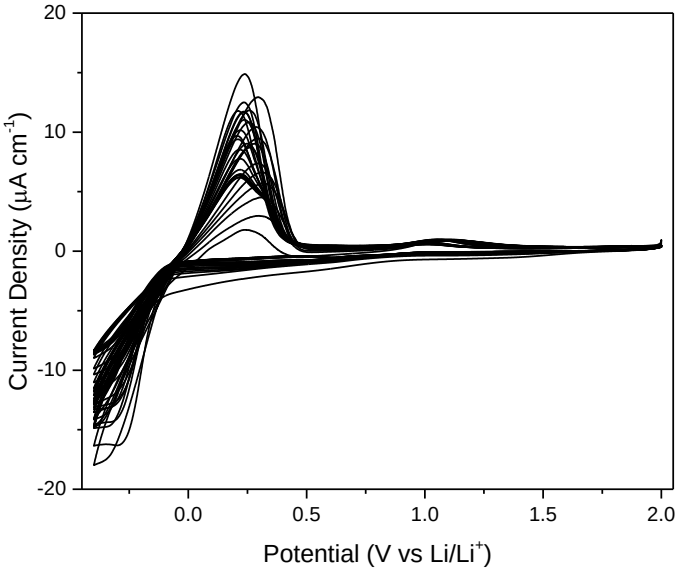

***Figure 4.13**: Cyclic voltammogram of a Cu/SLEN/Li cell cycled between -0.4 V and 2.0 V vs. Li/Li^+ at 250 $\mu V\ s^{-1}$ (cycles 2-33).*

Electrochemical Impedance Spectroscopy and characterization of P_{carb} Composite

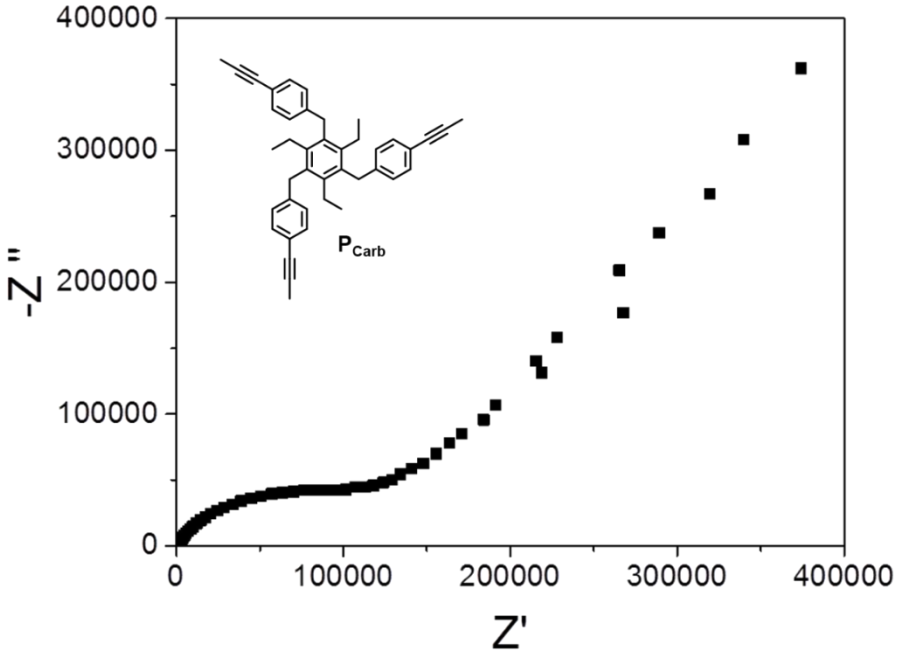

***Figure 4.14**: Complex impedance spectra of a composite fabricated from P_{Carb} subjected to the same preparatory conditions as the SLEN.*

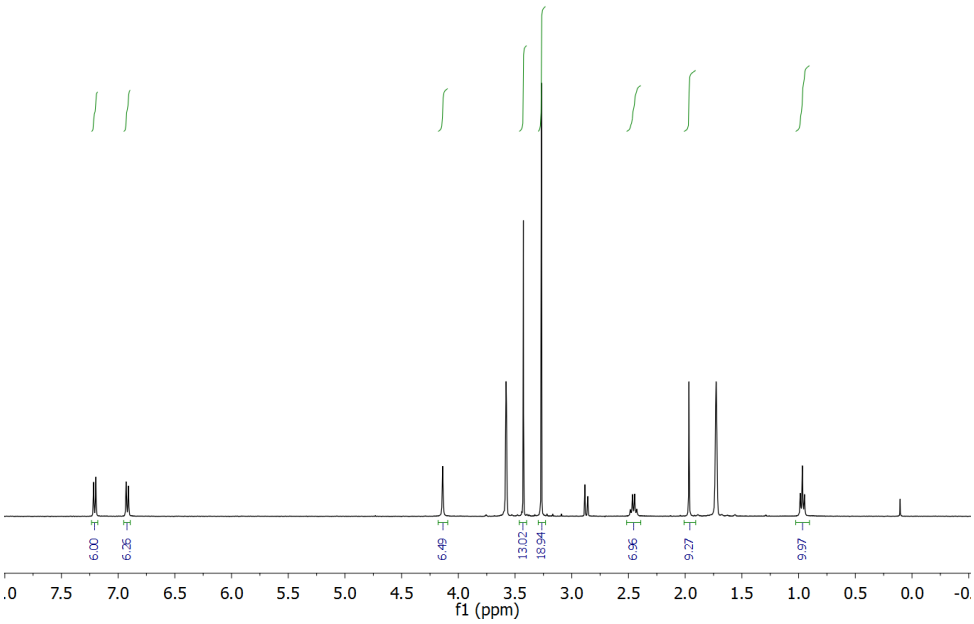

***Figure 4.15**: ^{1}H NMR of P_{Carb} composite (400 MHz, THF-d_8).*

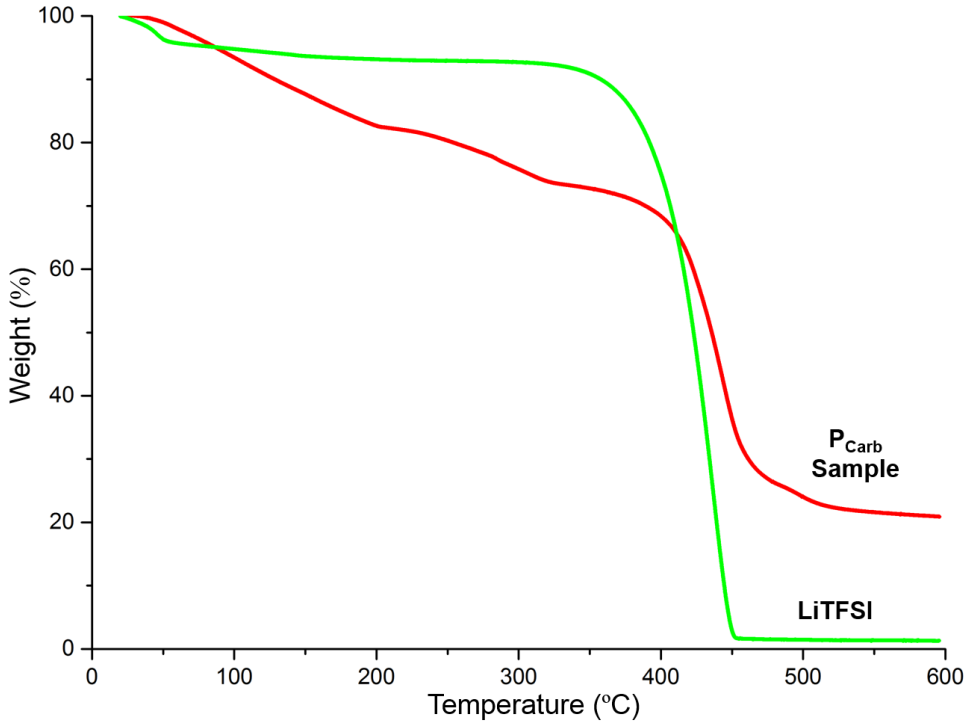

***Figure 4.16**: TGA of LiTFSI and the P_{carb} composite.*

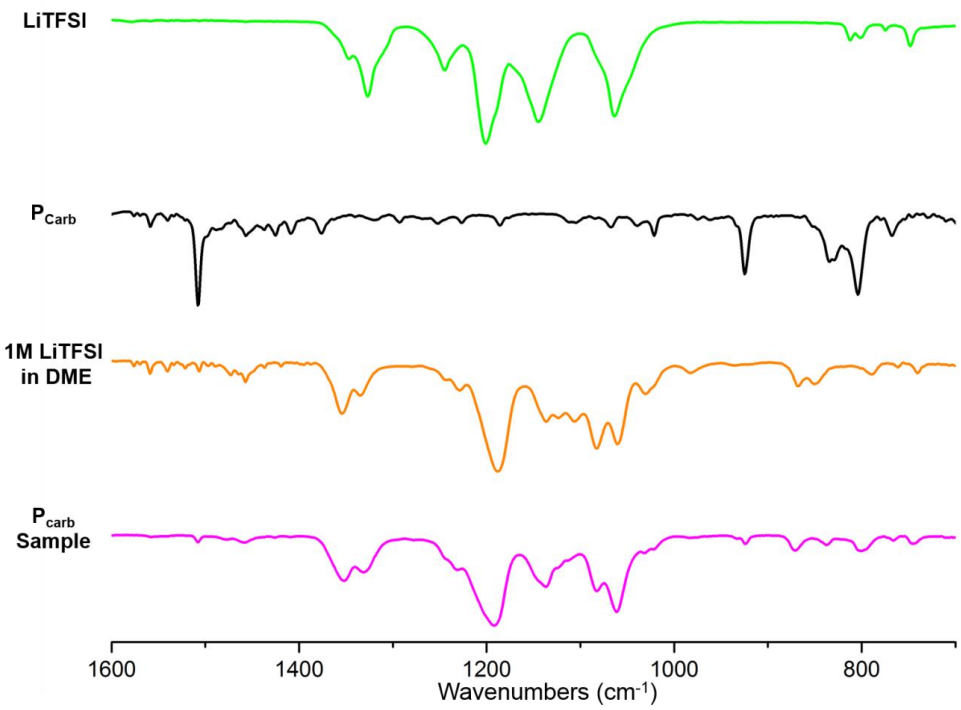

***Figure 4.17**: FTIR of LiTFSI, P_{carb}, 1 M LiTFSI in DME solution, and the P_{carb} composite.*

Determination of SLEN Lithium Ion Transference Number

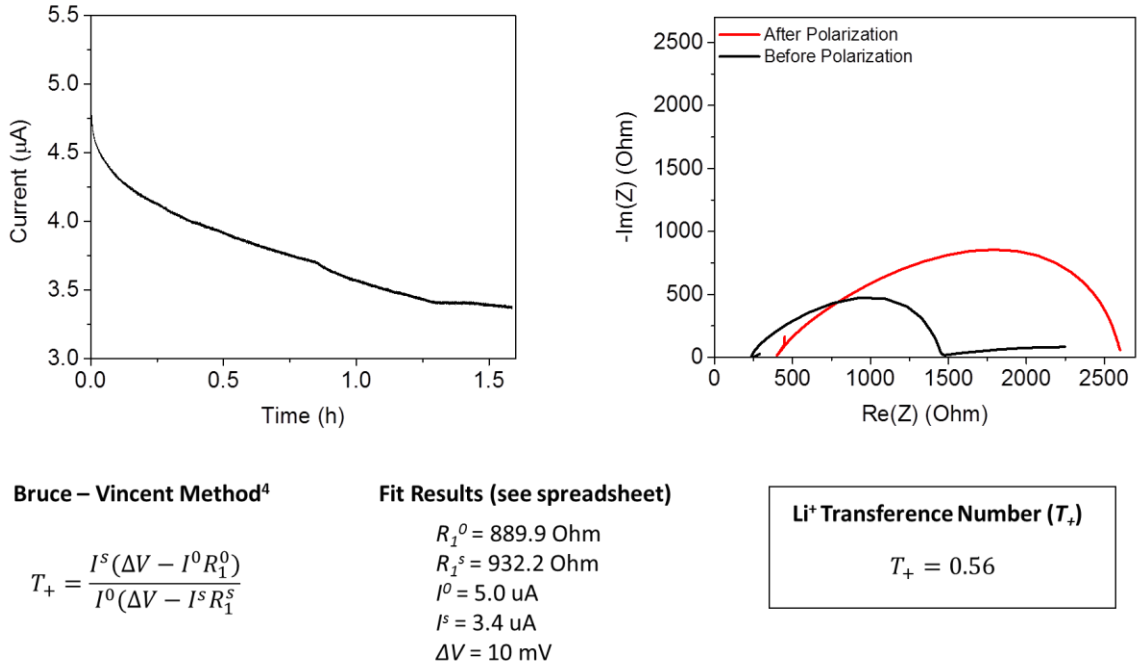

***Figure 4.18**: Determination of SLEN lithium ion transference number.*

4.7 References

Notes: †This chapter is adapted from Petronico, A.; Moneypenny, II, T. P.; Nicolau, B. G.; Moore, J. S.; Nuzzo, R. G.; Gewirth, A. A. *J. Am. Chem. Soc.* **2018**, *140*, 7504-7509. The materials are reproduced/adapted with permission. Copyright © 2018 American Chemical Society. This was a collaborative work with Aaron Petronico and Bruno Nicolau. T. P. M. II synthesized Td_A and P_{Carb} and performed materials characterization of the SLEN including FTIR, TGA, SEM, EDS, and NMR of both the SLEN and precursor composite samples. A. P. performed the electrochemical characterization including EIS, cyclic voltammetry, and T_+ experiment, and performed the SS NMR experiments. B. N. performed linear sweep voltammetry.

(1) Goodenough, J. B.; Park, K.-S. *J. Am. Chem. Soc.* **2013**, *135*, 1167.

(2) Goodenough, J. B.; Kim, Y. *Chem. Mater.* **2010**, *22*, 587.

(3) Nitta, N.; Wu, F.; Lee, J. T.; Yushin, G. *Mater. Today* **2015**, *18*, 252.

(4) Tarascon, J. M.; Armand, M. *Nature* **2001**, *414*, 359.

(5) Bachman, J. C.; Muy, S.; Grimaud, A.; Chang, H.-H.; Pour, N.; Lux, S. F.; Paschos, O.; Maglia, F.; Lupart, S.; Lamp, P.; Giordano, L.; Shao-Horn, Y. *Chem. Rev.* **2016**, *116*, 140.

(6) Thackeray, M. M.; Wolverton, C.; Isaacs, E. D. *Energy Environ. Sci.* **2012**, *5*, 7854.

(7) Li, Q.; Chen, J.; Fan, L.; Kong, X.; Lu, Y. *Green Energy & Environment* **2016**, *1*, 18.

(8) Long, L.; Wang, S.; Xiao, M.; Meng, Y. *J. Mater.Chem. A* **2016**, *4*, 10038.

(9) Sang, L.; Haasch, R. T.; Gewirth, A. A.; Nuzzo, R. G. *Chem. Mater.* **2017**, *29*, 3029.

(10) Richards, W. D.; Miara, L. J.; Wang, Y.; Kim, J. C.; Ceder, G. *Chem. Mater.* **2016**, *28*, 266.

(11) Takada, K.; Ohta, N.; Zhang, L.; Xu, X.; Thi Hang, B.; Ohnishi, T.; Osada, M.; Sasaki, T. *Interfacial phenomena in solid-state lithium battery with sulfide solid electrolyte*, 2012; Vol. 225.

(12) Wiers, B. M.; Foo, M.-L.; Balsara, N. P.; Long, J. R. *J. Am. Chem. Soc.* **2011**, *133*, 14522.

(13) Vazquez-Molina, D. A.; Mohammad-Pour, G. S.; Lee, C.; Logan, M. W.; Duan, X.; Harper, J. K.; Uribe-Romo, F. J. *J. Am. Chem. Soc.* **2016**, *138*, 9767.

(14) Du, Y.; Yang, H.; Whiteley, J. M.; Wan, S.; Jin, Y.; Lee, S.-H.; Zhang, W. *Angew. Chem. Int. Ed.* **2016**, *55*, 1737.

(15) Van Humbeck, J. F.; Aubrey, M. L.; Alsbaiee, A.; Ameloot, R.; Coates, G. W.; Dichtel, W. R.; Long, J. R. *Chem. Sci.* **2015**, *6*, 5499.

(16) Park, J. H.; Suh, K.; Rohman, M. R.; Hwang, W.; Yoon, M.; Kim, K. *Chem. Commun.* **2015**, *51*, 9313.

(17) Moneypenny, T. P.; Walter, N. P.; Cai, Z.; Miao, Y.-R.; Gray, D. L.; Hinman, J. J.; Lee, S.; Zhang, Y.; Moore, J. S. *J. Am. Chem. Soc.* **2017**, *139*, 3259.

(18) Lee, S.; Yang, A.; Moneypenny, T. P.; Moore, J. S. *J. Am. Chem. Soc.* **2016**, *138*, 2182.

(19) Zhang, G.; Presly, O.; White, F.; Oppel, I. M.; Mastalerz, M. *Angew. Chem. Int. Ed.* **2014**, *53*, 1516.

(20) Hasell, T.; Culshaw, J. L.; Chong, S. Y.; Schmidtmann, M.; Little, M. A.; Jelfs, K. E.; Pyzer-Knapp, E. O.; Shepherd, H.; Adams, D. J.; Day, G. M.; Cooper, A. I. *J. Am. Chem. Soc.* **2014**, *136*, 1438.

(21) Zhang, C.; Wang, Q.; Long, H.; Zhang, W. *J. Am. Chem. Soc.* **2011**, *133*, 20995.

(22) Liu, M.; Chen, L.; Lewis, S.; Chong, S. Y.; Little, M. A.; Hasell, T.; Aldous, I. M.; Brown, C. M.; Smith, M. W.; Morrison, C. A.; Hardwick, L. J.; Cooper, A. I. *Nat. Commun.* **2016**, *7*, 12750.

(23) McGrath, K. J.; Weiss, R. G. *Langmuir* **1997**, *13*, 4474.

(24) Arvai, R.; Toulgoat, F.; Langlois, B. R.; Sanchez, J.-Y.; Médebielle, M. *Tetrahedron* **2009**, *65*, 5361.

(25) Archer, W. I.; Armstrong, R. D. In *Electrochemistry: Volume 7*; Thirsk, H. R., Ed.; The Royal Society of Chemistry: 1980; Vol. 7, p 157.

(26) *Impedance Spectroscopy: Theory, Experiment, and Applications*; 1 ed.; John Wiley & Sons, Inc: Hoboken, New Jersey., 2005.

(27) Gao, H.; Guo, B.; Song, J.; Park, K.; Goodenough, J. B. *Adv. Energy Mater.* **2015**, *5*, 1402235.

(28) Saikia, D.; Kumar, A. *Electrochim. Acta* **2004**, *49*, 2581.

(29) Panero, S.; Scrosati, B. *J. Power Sources* **2000**, *90*, 13.

(30) Appetecchi, G. B.; Croce, F.; De Paolis, A.; Scrosati, B. *J. Electroanal. Chem.* **1999**, *463*, 248.

(31) Kamaya, N.; Homma, K.; Yamakawa, Y.; Hirayama, M.; Kanno, R.; Yonemura, M.; Kamiyama, T.; Kato, Y.; Hama, S.; Kawamoto, K.; Mitsui, A. *Nat. Mater.* **2011**, *10*, 682.

(32) Zheng, J.; Lochala, J. A.; Kwok, A.; Deng, Z. D.; Xiao, J. *Adv. Sci.* **2017**, *4*, 1700032.

(33) McOwen, D. W.; Seo, D. M.; Borodin, O.; Vatamanu, J.; Boyle, P. D.; Henderson, W. A. *Energy Environ. Sci.* **2014**, *7*, 416.

(34) Matsumoto, K.; Inoue, K.; Nakahara, K.; Yuge, R.; Noguchi, T.; Utsugi, K. *J. Power Sources* **2013**, *231*, 234.

(35) Li, L.-F.; Totir, D.; Gofer, Y.; Chottiner, G. S.; Scherson, D. A. *Electrochim. Acta* **1998**, *44*, 949.

(36) Liu, Z.; Fu, W.; Payzant, E. A.; Yu, X.; Wu, Z.; Dudney, N. J.; Kiggans, J.; Hong, K.; Rondinone, A. J.; Liang, C. *J. Am. Chem. Soc.* **2013**, *135*, 975.

(37) Seino, Y.; Ota, T.; Takada, K.; Hayashi, A.; Tatsumisago, M. *Energy Environ. Sci.* **2014**, *7*, 627.

(38) Wu, H.-L.; Huff, L. A.; Esbenshade, J. L.; Gewirth, A. A. *ACS Appl. Mater. Interfaces* **2015**, *7*, 20820.